

D* Meson Production in Deep Inelastic Electron-Proton Scattering with the Forward and Backward Silicon Trackers of the H1 Experiment at HERA

DISSERTATION

zur Erlangung des akademischen Grades
doctor rerum naturalium
(Dr. rer. nat.)
im Fach Physik

eingereicht an der
Mathematisch-Naturwissenschaftlichen Fakultät I
Humboldt-Universität zu Berlin

von
Herrn Dipl.-Phys. **Ivan Glushkov**
geboren am 27.03.1978 in Ruse, Bulgarien

Präsident der Humboldt-Universität zu Berlin:
Prof. Dr. Christoph Marksches

Dekan der Mathematisch-Naturwissenschaftlichen Fakultät I:
Prof. Dr. Christian Limberg

Gutachter:

1.
2.
3.

eingereicht am:	Dezember 2007
Tag der mündlichen Prüfung:	März 2008

Abstract

In this thesis, the measurement of the inclusive $D^*(2010)^\pm$ meson production cross section in deep inelastic electron-proton scattering at HERA is extended to higher and lower values of pseudorapidity. The scattering kinematics is defined by $5 \leq Q^2 \leq 100 \text{ GeV}^2$ and $0.05 \leq y \leq 0.6$. D^* mesons with $p_t > 1.5 \text{ GeV}$ and pseudorapidity $-2.5 < \eta < 2.5$ are reconstructed utilizing the decay channel $D^{*\pm} \rightarrow K^\mp \pi^\pm \pi_s^\pm$. The data was collected by the H1 experiment in 2006 and 2007 and corresponds to an integrated luminosity of $\mathcal{L} = 150 \text{ pb}^{-1}$.

For the first time in H1, a combined central-backward-forward tracking analysis is performed, using the H1 Backward and Forward Silicon Trackers BST and FST. This results in a nearly two times larger η acceptance compared to previous HERA analyses. The hardware, software, data quality and tracking performance of both detectors are reviewed.

Based on a good agreement of this analysis with the official H1 results in the central region a continuous drop of the cross section in the forward and backward regions is observed. The results are compared with the predictions of the leading order Monte Carlo generator RAPGAP and a reasonable agreement is observed.

Keywords:

Silicon, H1, D^* , Charm

Zusammenfassung

Diese Arbeit erweitert die Messung des Produktionsquerschnitts von D^* (2010) Mesonen in tief-inelastischer Elektron-Proton-Streuung bei HERA auf höhere und niedrigere Werte der Pseudorapidität. Die Streukinematik ist definiert durch $5 \leq Q^2 \leq 100 \text{ GeV}^2$ und $0.05 < y < 0.6$. Die D^* Mesonen werden im Zerfallskanal $D^{*\pm} \rightarrow K^\mp \pi^\pm \pi_s^\pm$ mit $p_t > 1.5 \text{ GeV}$ und im Rapiditätsbereich $-2.5 < \eta < 2.5$ rekonstruiert. Die Daten wurden im H1 Experiment in den Jahren 2006 und 2007 genommen und entsprechen einer integrierten Luminosität von $\mathcal{L} = 150 \text{ pb}^{-1}$.

Erstmals bei H1 wurde unter Benutzung der Vorwärts- und Rückwärts-Siliziumdetektoren FST und BST eine kombinierte Analyse im Zentral-, Vorwärts- und Rückwärtsbereich durchgeführt. Verglichen mit vorherigen HERA-Analysen konnte auf diese Weise die Akzeptanz in der Pseudorapidität fast verdoppelt werden. In der Arbeit werden Hardware, Software, Datenqualität und Spurnachweis beider Detektoren ausführlich dargestellt.

Gestützt auf eine gute Übereinstimmung dieser Analyse mit den offiziellen H1-Resultaten in der zentralen Region wird beobachtet, dass sich der Abfall des Wirkungsquerschnitts in Vorwärts- und Rückwärtsrichtung fortsetzt. Die Resultate werden mit den Vorhersagen des Leading Order Monte Carlo Generators RAPGAP verglichen und eine gute Übereinstimmung festgestellt.

Schlagwörter:

Silizium, H1, D^* , Charm

Contents

Introduction	6
1 Theoretical Overview	8
1.1 Kinematics of the Electron-Proton Scattering	8
1.2 Scattering Cross Section and Structure Functions	13
1.3 The Quark Parton Model	14
1.4 Quantum Chromodynamics	15
1.5 Running Coupling Constant α_s	16
1.5.1 Factorization	18
1.5.2 QCD Evolution Equations	19
1.6 Heavy Quark Production	22
1.6.1 Production	25
1.6.2 Fragmentation	26
1.7 Monte Carlo Generators	28
1.7.1 RAPGAP	30
2 The H1 Experiment at the HERA Accelerator	32
2.1 The HERA Accelerator	32
2.2 The H1 Experiment	34
2.2.1 Overview	34
2.2.2 Central Tracking Detectors	38
2.2.3 Backward Tracking Detectors	42
2.2.4 Forward Tracking Detector	42
2.2.5 Calorimeters	43
2.2.6 Luminosity System	46
2.2.7 Triggering and Data Taking	47
2.2.8 The H1 Data Structure	49
2.2.9 Track Reconstruction	50

3	The H1 Forward and Backward Silicon Trackers	56
3.1	Silicon Properties	57
3.2	Detecting Particles with Silicon	60
3.3	Silicon Sensors	63
3.4	Detector Geometry	67
3.5	Data Acquisition	73
3.6	Silicon Stand-alone Track and Vertex Reconstruction	77
3.6.1	Hit Finding	79
3.6.2	Track and Vertex Fit	82
3.6.3	Alignment	87
3.6.4	Data Quality	90
4	D* Selection	97
4.1	Event Selection	97
4.2	Trigger Selection	98
4.3	Luminosity	98
4.4	Kinematics Determination	103
4.5	D* Reconstruction	105
4.5.1	Track Selection	107
4.5.2	D* Finding	116
4.5.3	Signal Extraction	135
4.5.4	Statistical Subtraction	139
5	Measurement of the D* Meson Cross Section	140
5.1	Systematic Errors	142
5.2	The Total Cross Section	143
5.3	The Single Differential Cross Section	144
6	Conclusions and Outlook	149
A	H1 and Zeus Preliminary Results	151

Introduction

In elementary physics, all particles and their interactions, except for gravity, are successfully described by a common $SU(3) \times SU(2) \times U(1)$ gauge field theory - the "*Standard Model*" [1]. The part of the Standard Model which deals with strong interaction between quarks and gluons is named *Quantum Chromodynamics (QCD)*. Heavy quarks provide a mass scale that allows to test QCD and to extend the applicability range of its predictions. The charm quark as the lightest of the heavy quarks, is abundantly produced at HERA and thus creates conditions for precise investigations of parton dynamics. Due to confinement no free quark can be observed. Hence, the charm quarks can be observed only in a bound state with another quark, forming a charmed hadron. Thus, the investigation of the production cross section of charmed hadrons like the D^* meson is of vital importance.

This thesis investigates the D^* meson production in deep inelastic scattering with the H1 experiment at the HERA electron-proton accelerator. The topic of this thesis was set early in 2004, according to the main physics goal of the Forward Silicon Tracker FST newly introduced for the HERA II running period [2]. The ambitious FST physics program became partially unachievable, when due to technical problems the detector had to be removed from the experiment in 2004 for more than one year. As a consequence, this analysis is restricted to a data sample with an integrated luminosity of $\mathcal{L} = 150 \text{ Pb}^{-1}$ collected in 2006 and 2007 during nominal proton energy running. Both FST and BST increase the tracking acceptance of the H1 experiment and allow to extend the acceptance of this analysis to the pseudorapidity range of $-2.5 < \eta < 2.5$, or from three to five units compared to previous HERA analyses, which were restricted by the acceptance of the central drift chambers.

This thesis is organized as follows: Chapter 1 gives an overview of the theoretical approach to D^* meson production. Next, in Chapter 2 a concise description of the HERA accelerator and the H1 detector systems relevant to this analysis is given. Chapter 3 describes in detail both detectors essential for this analysis: the Forward Silicon Tracker and the Backward Silicon

Tracker - their functionality, hardware, software and data quality. The selection criteria and the D^* extraction algorithm are outlined in Chapter 4. In Chapter 5 the D^* cross section calculation and the final results are presented. Finally, Chapter 6 gives the conclusions and the outlook.

Chapter 1

Theoretical Overview

In this chapter a theoretical overview of the electron¹-proton (ep) scattering processes relevant to D^* meson production at HERA (Hadron Electron Ring Anlage) accelerator is presented. First, the kinematic variables used to describe ep scattering are introduced. The proton structure and its description in the framework of Quantum Chromodynamics are described. Different evolution schemes are shortly outlined. In the end, charm production mechanisms and the transition of quarks to visible hadrons is explained. The chapter can only provide a short overview of the individual topics. A detailed discussion can be found in [3, 4].

1.1 Kinematics of the Electron-Proton Scattering

The electron-proton scattering (ep scattering) to leading order takes place by exchanging a gauge boson between the interacting electron and a quark from the proton (see Fig. 1.1). In this process generally two categories of events can be distinguished depending on the type of the boson exchanged. When a neutral boson is exchanged $ep \rightarrow eX$ (a virtual photon or a Z^0), the event is referred to as *Neutral Current (NC)* event. For virtualities $Q^2 \ll M_Z^2$, where $M_Z = 91.19$ GeV [5] is the mass of the Z^0 boson, the cross section is dominated by single photon exchange since the weak interaction is suppressed by a factor of M_Z^2 in the Z^0 boson propagator. A definitive feature of a NC event is that the initial lepton type is conserved and found in the final state.

If the boson involved is a charged one (a W^\pm boson), then the event is of

¹Unless otherwise stated, the term 'electron' is used in this thesis to generically denote positron or electron.

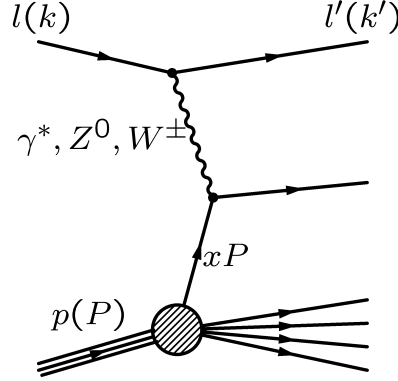


Figure 1.1: Schematics of the lepton-proton interaction process.

the type $ep \rightarrow \nu X$ and is defined to be a *Charged Current (CC)* event. The CC cross section (see Fig. 1.2) is purely weak and much lower than the NC one for $Q^2 \ll M_W^2$ where $M_W = 80.40$ GeV [5] is the mass of W^\pm boson. This comes again due to the suppression factor of M_W^2 in the gauge boson propagator. Both NC and CC are precisely measured at HERA [6, 7, 8].

Due to the kinematic region considered, contributions from weak interactions are neglected in this thesis. The kinematics of ep scattering is fully described by the following three Lorentz invariant variables defined as²:

$$\begin{aligned} Q^2 &= -q^2 = (k - k')^2 \\ x &= \frac{Q^2}{2P \cdot q} \\ y &= \frac{P \cdot q}{P \cdot k} \end{aligned} \tag{1.1}$$

where k is the momentum of the incoming lepton, k' - the momentum of the outgoing and P - the momentum of the initial proton as depicted on Fig. 1.1. The four-momentum transferred squared Q^2 from the incoming to the outgoing electron represents the virtuality of the exchanged boson.

The interpretation of the so-called Björken x in the framework of the Quark Parton Model (QPM) [9] is the following: If we assume that x is the fraction of the proton momentum carried by the interacting quark, and using the QPM quarks with masses zero (i.e. $(xP)^2 = p'^2 = 0$), where p' is the momentum of the outgoing quark, then $p'^2 - (xP + q)^2 = -2xP \cdot q = -Q^2 = 0$. Thus in the QPM x is the fraction of the proton momentum carried by the struck massless quark. It is a dimensionless parameter, limited to the

²Throughout this thesis the natural unit system is used in which $c = \hbar = 1$. Thus, the unit used for energy, momentum and mass is eV

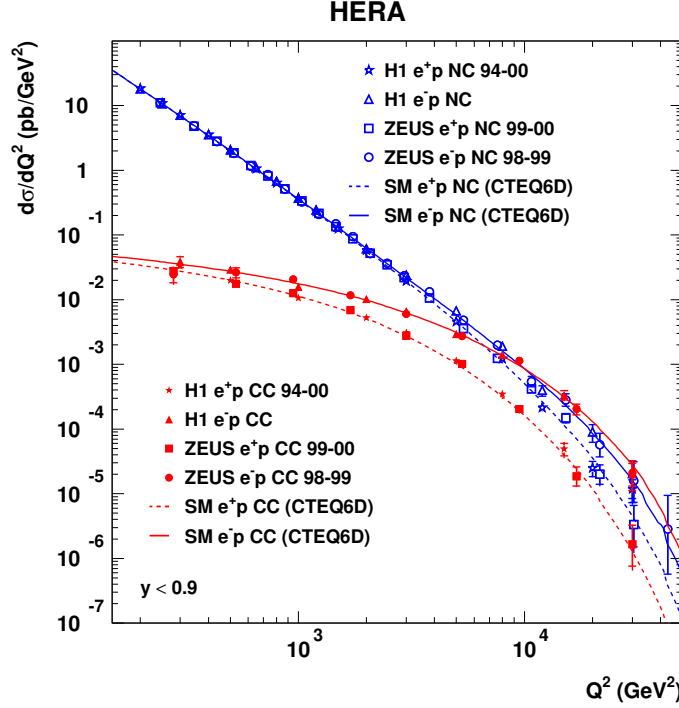


Figure 1.2: Single differential cross sections $d\sigma_{NC}/dQ^2$ and $d\sigma_{CC}/dQ^2$ for e^-p and e^+p data as measured by the experiments H1 and Zeus at HERA.

range $(0, 1)$. The *inelasticity* y is also a dimensionless parameter, limited to the range $(0, 1)$, identical to the fraction of the incoming lepton energy lost in the interaction in the proton rest frame.

The initial state in case of unpolarized particle scattering is described by 8 variables representing the initial 4-momentum of the particles. Taking into account the 4-momentum conservation law and the φ -symmetry three of these are independent. In case of constant beam energies, only two kinematic variables out of the three parameters are independent. Convenient choices are (E, θ) , as Rutherford did one hundred years ago [10], or (x, Q^2) , as used today and defined in (1.1). The following relation holds:

$$Q^2 = xys, \quad (1.2)$$

where \sqrt{s} is the total energy of the colliding particles in the center of mass system (CMS) defined as:

$$s = (k + P)^2 \quad (1.3)$$

$$s \approx 4E_e E_p \quad (1.4)$$

where E_e and E_p are the energies of the incident particles. The relation (1.4) is true if the electron and proton masses are neglected. Additionally, the Lorentz-invariant variable W is introduced as:

$$W^2 = (q + P)^2 = \left(\frac{1}{x} - 1\right) Q^2 + M_p^2 = ys - Q^2 + M_p^2 \quad (1.5)$$

which represents the total invariant mass of the hadronic final state or in other words the total energy of the boson-proton system. Here M_p is the rest mass of the proton

The ep events are kinematically classified based on the resolving power of the interaction. Thus, three groups of events in Q^2 are considered:

- **Photoproduction** is defined as the class of events with $Q^2 \approx 0 \text{ GeV}^2$. The exchanged gauge boson in this case is an almost real photon. It either fluctuates into a vector meson which interacts subsequently with the nucleon or interacts directly with a quark. Both processes are referred to as resolved and direct photoproduction respectively.
- **Low/Moderate Q^2 DIS** events are defined as Deep ($Q^2 \gg M_p^2$) Inelastic ($W^2 \gg M_p^2$) Scattering (DIS) events in the region $1 \text{ GeV}^2 < Q^2 < 100 \text{ GeV}^2$. This kinematic region is dominated by one photon exchange NC events, as can be judged from Fig. 1.2. The precise Q^2 limits are defined by the detector acceptance.
- **High Q^2 DIS** events with $Q^2 > 100 \text{ GeV}^2$, where the weak interaction becomes important.

Another frequently used kinematic quantity is the *rapidity* \hat{y} , defined as:

$$\hat{y} = \frac{1}{2} \ln \frac{E + p_z}{E - p_z} \quad (1.6)$$

where E is the energy of the particle, and p_z its longitudinal momentum. Neglecting the rest mass of the particle ($m \ll p$), the *pseudorapidity* η is defined as:

$$\eta \equiv \hat{y} \Big|_{m=0} = \frac{1}{2} \ln \frac{p + p_z}{p - p_z} = -\ln \left(\tan \frac{\theta}{2} \right) \quad (1.7)$$

The pseudorapidity η is usually preferred to θ , since pseudorapidity differences are independent under longitudinal Lorentz transformations.

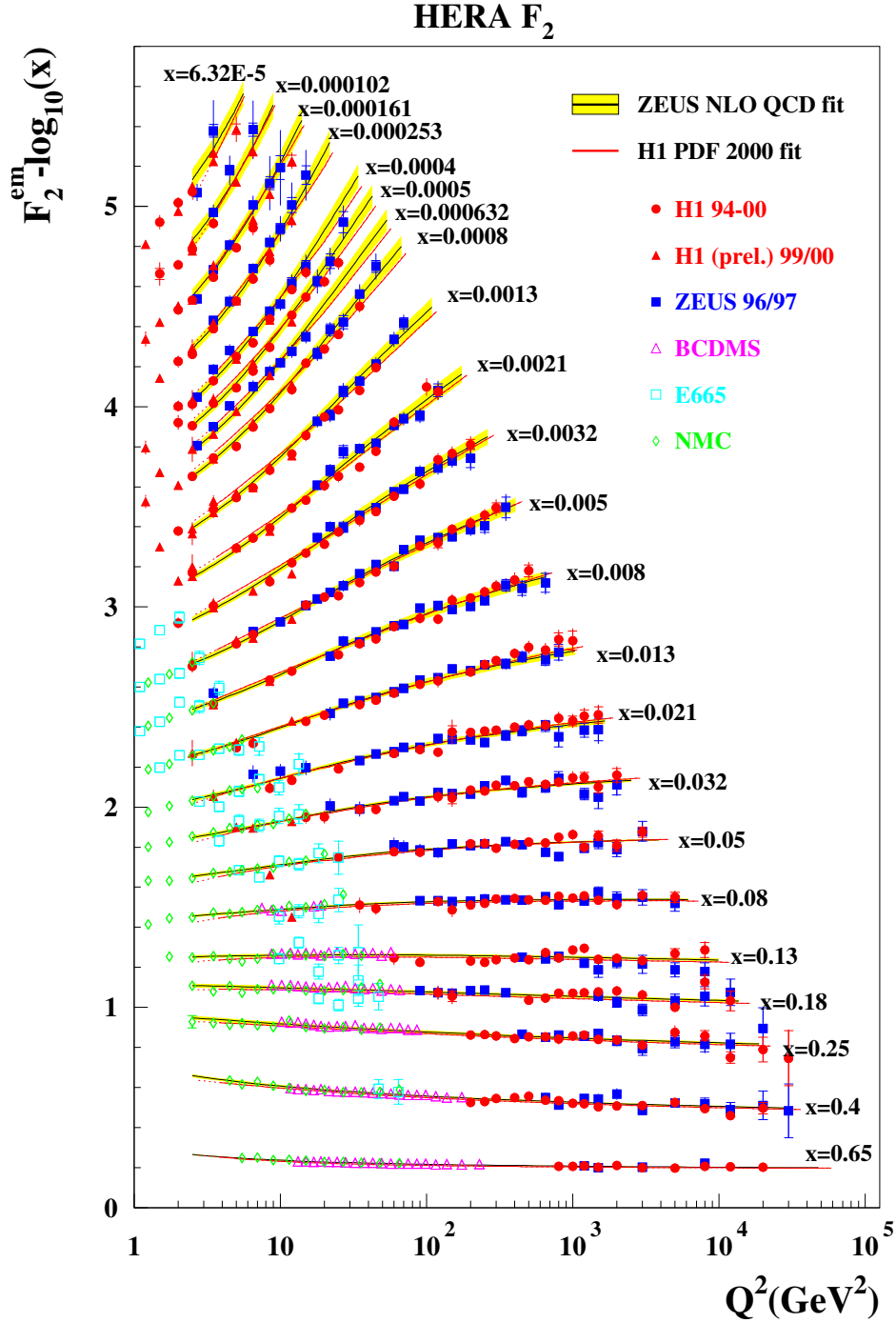


Figure 1.3: Measurement of the proton structure function $F_2(x, Q^2)$ as a function of Q^2 in bins of x by various fixed target and collider experiments. Lines correspond to NLO QCD fits by the Zeuss (black) and the H1 (red) experiments.

1.2 Scattering Cross Section and Structure Functions

The inclusive NC DIS cross section for $ep \rightarrow eX$ can be expressed in terms of the proton structure functions $F_1(x, Q^2)$ and $F_2(x, Q^2)$. The double differential DIS NC cross section is then represented as:

$$\frac{d^2\sigma(x, Q^2)}{dx dQ^2} = \frac{4\pi\alpha^2}{xQ^4} (xy^2 F_1(x, Q^2) + (1-y) F_2(x, Q^2)), \quad (1.8)$$

where α is the electromagnetic coupling constant. A further structure function term $xF_3(x, Q^2)$ can be added in equation (1.8) to account for Z^0 exchange and the γZ interference. Since this term contributes to the cross section only at $Q^2 \sim M_Z^2$, it is neglected here.

As a consequence of the gauge invariance of electrodynamics, the mass of the real photons are constrained to zero. A photon with a non-vanishing virtuality Q^2 can be either transversely or longitudinally polarized, whereas a real photon has a transverse polarization only. A longitudinally polarized virtual photon can probe the transverse momentum of the partons - purely QCD parton property, not observable in QPM, and quantitatively represented by the *longitudinal structure function* F_L defined as:

$$F_L(x, Q^2) = F_2(x, Q^2) - 2xF_1(x, Q^2). \quad (1.9)$$

Taking into account equation (1.9), the DIS NC differential cross section is written as a function of $F_2(x, Q^2)$ and $F_L(x, Q^2)$ conventionally as:

$$\frac{d^2\sigma(x, Q^2)}{dx dQ^2} = \frac{2\pi\alpha^2}{xQ^4} Y_+ \left[F_2(x, Q^2) - \frac{y^2}{Y_+} F_L(x, Q^2) \right], \quad Y_+ = 1 + (1-y)^2 \quad (1.10)$$

where the term in brackets is often denoted as *reduced cross section*.

The structure functions are related to the longitudinally and transversely polarized virtual photon absorption cross sections σ_L and σ_T as:

$$F_2(x, Q^2) = \frac{Q^2}{4\pi^2\alpha} (\sigma_T(x, Q^2) + \sigma_L(x, Q^2)) \quad (1.11)$$

$$F_L(x, Q^2) = \frac{Q^2}{4\pi^2\alpha} \sigma_L(x, Q^2). \quad (1.12)$$

Equations (1.11), (1.12) and the condition that σ_L and σ_T are always positive definite constrain the structure functions as $0 \leq F_L(x, Q^2) \leq F_2(x, Q^2)$. In most of the kinematic regions accessible by HERA, the NC cross section is proportional to the F_2 structure function. Due to the kinematic term y^2/Y_+ in (1.10), only at very high values of inelasticity y , contributions from a non-zero longitudinal structure function F_L starts playing role.

1.3 The Quark Parton Model

The Quark Parton Model (QPM) was proposed in 1968 by Richard Feynman [11]. It is the simplest model trying to explain the proton as combined object and its interactions as such with external fields. In this model the proton consists only from three point-like, spin 1/2 particles named *partons*. The partons are free particles inside the proton. Thus, the the lepton-proton scattering simplifies to lepton-parton scattering. QPM works in a reference frame in which the proton has infinite momentum. In such a reference frame, the transverse moment of the partons can be neglected with respect to their longitudinal one, and the momentum of each of them is $p' = xP$, where (if we neglect the particle masses) x is the Björken x and P is the momentum of the proton. In DIS the scattering cross section can then be represented as an *incoherent sum* of cross sections of scattering from individual charged partons. If we consider DIS at $Q^2 \gg M_P^2$, and neglect F_L , one can write the double differential cross section as:

$$\frac{d^2\sigma}{dx dQ^2} = \frac{4\pi\alpha^2}{Q^4} \frac{F_2(x, Q^2)}{x} \quad (1.13)$$

The differential cross section of elastic scattering from a point-like electric charge e is:

$$\frac{d^2\sigma}{dx dQ^2} = \frac{4\pi\alpha^2}{Q^4} e^2 \quad (1.14)$$

If we compare (1.13) with (1.14), take the proton as a sum of partons and denote the probability to find a parton i with charge e_i carrying a fraction x of the proton momentum with the parton density $d_i(x)$, then $F_2(x, Q^2)$ can be represented as:

$$\frac{F_2(x)}{x} = \sum_i e_i^2 d_i(x) \quad \text{or} \quad F_2(x) = \sum_i e_i^2 x d_i(x) \quad (1.15)$$

Representing with $q_i(x)$ and $\bar{q}_i(x)$ the parton density functions for quarks and anti-quarks, F_2 in terms of quark densities is written as:

$$F_2(x) = \sum_{i=1}^{n_f} e_i^2 x (q_i(x) + \bar{q}_i(x)), \quad (1.16)$$

where the sum $i = 1 \dots n_f$ runs over all quark flavours contributing to the proton structure. Due to helicity and momentum conservation and neglecting the intrinsic transverse momentum of partons, longitudinally polarized photons cannot be absorbed by massless spin 1/2 partons [12], which is expressed

in the Callan-Gross relation:

$$F_L(x) = F_2(x) - 2xF_1(x) = 0 \quad (1.17)$$

The QPM has the following implications:

1. The proton structure function F_2 depends only on x and is completely independent from the scale Q^2 . Thus, F_2 is said to be *scale invariant*, and its behaviour is called *scaling* [13, 14].
2. The integral over all momenta summed over all quark flavours in a proton should sum up to the proton momentum. This can be expressed as

$$\sum_{i=1}^{n_f} \int_0^1 x (q_i(x) + \bar{q}_i(x)) = 1. \quad (1.18)$$

In the later experiments (1970s) both predictions were proven not to be experimentally true. It was observed in neutrino-nucleon experiments that the quarks carry only about one half of the momentum of the nucleon. This was evidence that there are additional constituents in the proton which carry the rest of the proton momentum and do not interact with the leptonic probe. Furthermore, scaling violations were observed: F_2 has a logarithmic dependence on Q^2 , and F_L is non-vanishing (see Fig. 1.3). Another phenomenon that the QPM could not explain was the non-observation of quarks in the final state. This observation conceptionally contradicts the QPM, since it implies a strong interaction between the quarks, and the QPM states that there is no interaction between the partons. Hence, a more advanced theory was needed to explain the experimental results.

1.4 Quantum Chromodynamics

Quantum Chromodynamics (QCD) as a part of the Standard Model is the quantum field theory of the strong interactions [15, 16, 17]. It is a gauge field theory acting in a $SU(3)$ color space. Its gauge bosons are eight massless *gluons* mediating the interaction between quarks. QCD introduces a new quantum number and charge called *color*. Each quark carries color charge, conventionally denoted as r (red), g (green) and b (blue), while anti-quarks carry one of the corresponding anti-colors: \bar{r} (anti-red), \bar{g} (anti-green) and \bar{b} (anti-blue). Due to the non-Abelian³ structure of the $SU(3)$ group, the

³Non-Abelian means that the elements of the corresponding algebra do not commute with each other

gluons carry the charge of the interaction and have two colors - the color and the anticolor of the interacting quarks. This allows them to self interact. This is a fundamental difference from QED, and its $U(1)$ symmetry in which the photon has no charge and no selfcoupling.

The QPM treats the quarks as quasi-free particles, hence implying that at small distance or high momentum transfer the coupling strength is small. This property is referred to as *asymptotic freedom* [18, 19] of the quarks. On the other hand, there are no free quark observed implying that at large distances, i.e. low momentum scales the coupling strength is large. This strong coupling ultimately leads to *confinement*. This variation of the coupling strength implies that the coupling constant α_s is running. This behaviour is a direct consequence of the gauge-boson self-coupling and is explained in the quantum field theory with additional gluon loops in the boson propagators, where the momentum is not fixed by energy conservation.

1.5 Running Coupling Constant α_s

The *ultraviolet (UV) divergences* are removed from in the quantum field theory via the so-called *renormalization* procedure. The renormalization requests introduction of an arbitrary renormalization scale μ_r^2 , which can be regarded as the momentum at which the subtraction removing the divergences is performed. After applying the renormalization procedure, the UV are dealt with, but the coupling constant of the interaction α_s depends on the renormalization scale μ_r^2 . However, the physical observables should not depend on the renormalization scale μ_r^2 , when calculated to all orders of pQCD. Thus, every explicit dependence of any physical observable R on the renormalization scale μ_r^2 must be cancelled by a dependence of α_s on μ_r^2 . This requirement is mathematically expressed by the *Renormalization Group Equation (RGE)*:

$$\mu_r^2 \frac{dR}{d\mu_r^2} = \mu_r^2 \frac{\partial R}{\partial \mu_r^2} + \mu_r^2 \frac{\partial \alpha_s}{\partial \mu_r^2} \frac{\partial R}{\partial \alpha_s} = 0 \quad (1.19)$$

The logarithmic derivation $\partial \alpha_s / \partial \ln \mu_r^2$ from the second term in equation (1.19) can be expressed as a power series in α_s with coefficients, called β functions, which can be calculated in quantum field theory:

$$\frac{\partial \alpha_s}{\partial \ln \mu^2} = \alpha_s \beta(\alpha_s) = -\frac{\beta_0}{4\pi} \alpha_s^2 - \frac{\beta_1}{8\pi^2} \alpha_s^3 - \frac{\beta_2}{128\pi^3} \alpha_s^4 - \dots \quad (1.20)$$

The leading order coefficient β_0 is:

$$\beta_0 = \frac{11}{3} n_c - \frac{2}{3} n_f$$

where n_c is the number of colors, and n_f denotes the number of active quark flavours i.e. those with a mass less than the mass of the renormalization scale ($m_q^2 < \mu_r^2$).

Usually the renormalization scale μ_r is chosen to be the typical energy scale of the hard process. In solving the differential equation for α_s a constant of integration is introduced. The scale μ_r which has become a standard to choose is the Z^0 boson mass m_Z i.e. $\mu_r = m_Z$.

Solving equation (1.20) in one-loop approximation, i.e. considering only the leading order (LO) β_0 term gives:

$$\alpha_s(\mu_r^2) = \frac{\alpha_s(\mu_0^2)}{1 - \frac{\beta_0}{4\pi} \alpha_s(\mu_0) \ln\left(\frac{\mu_r^2}{\mu_0^2}\right)}. \quad (1.21)$$

From (1.20) it is visible that β_0 consists of two terms with opposite sign. The first term $\frac{11}{3}n_c$ contains the gluon self-coupling. It gives rise to anti-screening effects and hence to the rise of α_s towards low μ_r^2 . Such a term is absent in QED. The second one ($\frac{2}{3}n_f$) is due to quark loops and causes the screening effects in QED. It would eventually give rise to α_s towards high μ_r^2 if the number of quark flavours was $n_f > 33/2$.

It is also convenient to introduce a dimensionless parameter Λ_{QCD} , since this provides a parametrization of the μ dependence of α_s . In other words Λ_{QCD} determines the characteristic scale of QCD.

At leading order we can write:

$$\alpha_s(\mu_r^2) = \frac{4\pi}{\beta_0 \ln(\mu_r^2/\Lambda_{QCD}^2)} \quad (1.22)$$

$$\ln(\Lambda_{QCD}^2) = \ln(\mu_0^2) - \frac{4\pi}{\beta_0 \alpha_s(\mu_0^2)}. \quad (1.23)$$

Λ_{QCD} is a fundamental constant in QCD, which depends only on the number of the quark flavours considered at lower order of α_s . Its value in the $\overline{\text{MS}}$ renormalization scheme in NLO is 520 MeV [20]. It is visible from (1.22) that at $\mu_r^2 \gg \Lambda_{QCD}^2$ α_s becomes small, which describes properly the asymptotic freedom of the quarks. Approaching with $\mu_r^2 \rightarrow \Lambda_{QCD}^2$ from above gives an increase of α_s , which ultimately leads to the confinement of the quarks. In *hard* processes ($\mu > Q^2$) or at small interaction distance perturbative calculations can be applied, which is not possible for $\mu \ll Q^2$.

It has become customary to specify experimentally the strong coupling constant α_s at the mass of the Z boson instead of using Λ_{QCD} as a reference scale. The present world average is $\alpha_s(M_Z) = 0.1176 \pm 0.002$ [5].

1.5.1 Factorization

Processes like $q \rightarrow qg$ (gluon radiated off quarks), $g \rightarrow gg$ (gluon splitting to gluons) and $g \rightarrow q\bar{q}$ (gluon splitting into quark-antiquark pair) are taking place, at all orders and momentum scales, which are difficult to be calculated in pQCD. This problem is solved by the *factorization theorem* of DIS. It states that for the general case of lepton-hadron scattering the interaction of the exchanged vector boson with the hadron can be divided into two independent parts, a *short distance* part, which is perturbatively calculable and a *long distance* part, which is to be determined experimentally. Formally, factorization expresses the structure function $F_2^{V,h}$ as a convolution of a hard scattering process (calculable in pQCD), represented by *coefficient functions* $C^{V,i}$ and a *running parton density function (PDF)* $f_{i/h}$, summing over all partons i (quarks q , anti-quarks \bar{q} and gluons g):

$$F_2^{V,h}(x, Q^2) = \sum_{i=q,\bar{q},g} \int_x^1 dz C^{V,i} \left(\frac{x}{z}, \frac{Q^2}{\mu_r^2}, \frac{\mu_f^2}{\mu_r^2}, \alpha_s(\mu_r^2) \right) f_{i/h}(z, \mu_r^2, \mu_f^2) \quad (1.24)$$

The coefficient function $C^{V,i}$ describes the interaction of the exchanged vector boson V with a parton i . It is independent of the long distance effects and in particular independent of the identity of the hadron h . For a particular exchanged boson V it can be expanded in a power series of α_s and perturbatively calculated. The parton density $f_{i/h}(z)$ is the probability to find a parton i carrying a fraction z of the hadron's momentum. It is specific to the hadron h , but universal, that is, independent of the particular hard scattering process. Therefore it should be possible to use parton densities, which are determined at HERA, make predictions for other collisions involving protons, for example at LHC.

The processes at large scale $\mu^2 > \mu_f^2$ are referred to as hard processes and due to the small α_s are calculable in pQCD. On the other hand, soft processes with $\mu^2 \leq \mu_f^2$ are absorbed in the renormalized parton densities. Such separation to 'soft' and 'hard' processes is called factorization and μ_f^2 is called *factorization scale*. Since the PDFs also depend on the factorization scale μ_f^2 , they are also "running", in analogy to the coupling constant α_s .

The separation between the coefficient functions and parton density functions is not unique. To eliminate this ambiguity, a specific factorization scheme has to be applied. The two most commonly used schemes are the DIS [21] and the modified minimal subtraction scheme $\overline{\text{MS}}$ [20] scheme. In the DIS scheme the structure function F_2 is given by the QPM equation (1.16) to all orders in perturbation theory, in such a way that the quark

densities are scale dependent. Choosing $\mu_r = \mu_f = Q$ one obtains:

$$F_2(x, Q^2) = \sum_{i=q, \bar{q}} e_i^2 x f_i(x, Q^2) \quad (1.25)$$

In case of the $\overline{\text{MS}}$ scheme the parton density functions are defined directly in terms of hadronic matrix elements. The latter scheme is more useful for theoretical calculations while the former is the natural choice for DIS experiments.

1.5.2 QCD Evolution Equations

The dependence of the parton densities on the factorization scale can be understood by considering that at large momentum scales, small structures are resolved and the probability is large that the photon probes a quark, which has already emitted a gluon or which comes from gluon splitting. In those cases however, the momentum of the quark is smaller than the momentum of the original parton in the proton. The quark densities therefore, with increasing scale μ_f^2 , becomes progressively larger at smaller x and progressively smaller at large x . Thus, the scaling behaviour expected in the naive QPM, is observed only for values of Björken $x \approx 0.13$ (see Fig. 1.3). In all other x -regions F_2 depends about logarithmically on Q^2 .

The pQCD does not give any prediction on the dependence of the PDFs on the Björken x . However, having the PDFs at one scale μ allows their prediction for any other scale μ' given that both scales are large enough for α_s at each of them to be small. This is referred to as *evolution* of the parton densities. The underlying evolution equations can be derived from equation (1.24) by requiring that the structure functions as measurable quantities should be independent of the factorization and renormalization scale.

Three approximate evaluation models will be discussed: DGLAP and BFKL, which model the evolution of parton densities with Q^2 and x respectively. Finally the CCFM approach, which attempts to combine features from both DGLAP and BFKL is briefly mentioned.

The DGLAP Equations

The DGLAP⁴ [22, 23, 24] approach is the most common to describe the evolution of the quark density function $q(x, Q^2)$ and the gluon density function $g(x, Q^2)$ in Q^2 . The main approximation here is that consecutively radiated gluons (Fig. 1.4) are strongly ordered in transverse momenta squared - from

⁴Yu. L. Dokshitzer, V.N. Gribov, L.N. Lipatov, G. Altarelli and G. Parisi

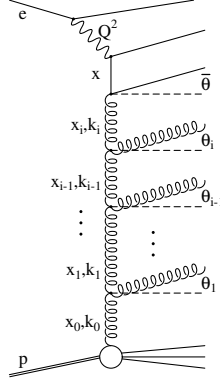


Figure 1.4: General gluon ladder with the momentum fractions x_i , the virtualities k_i^2 and gluon emission angles θ_i .

very small momenta for the initial emissions in the proton to larger momenta for emissions closer to the hard interaction with the photon. Additionally, weak ordering is also used:

$$\begin{aligned} Q^2 \gg k_{T,n}^2 \gg k_{T,n-1}^2 \gg \dots \gg k_2^2 \gg k_{T,1}^2 \gg Q_0^2 \\ x < x_n < \dots < x_2 < x_1, \end{aligned} \quad (1.26)$$

where $k_{T,i}^2$ is the norm of the transverse momentum of the i -th gluon in the ladder, $x_i P$ is its longitudinal momentum and Q_0^2 is the starting scale, typically in order of a few GeV. Furthermore, the longitudinal momenta $x_i P$ are supposed to be larger than the transverse momenta, which is valid for not too small x . Factorization within this approximation is called *collinear factorization*, since all dependencies of the parton densities on the transverse momentum of the partons are integrated out.

Within this approach, the DGLAP evolution equations are given by:

$$\frac{dq_i(x, Q^2)}{d \ln Q^2} = \frac{\alpha_s(Q^2)}{2\pi} \int_x^1 \frac{dz}{z} \left[\sum_j q_j(z, Q^2) P_{q_i q_j} \left(\frac{x}{z} \right) + g(z, Q^2) P_{q_i g} \left(\frac{x}{z} \right) \right] \quad (1.27)$$

$$\frac{dg(x, Q^2)}{d \ln Q^2} = \frac{\alpha_s(Q^2)}{2\pi} \int_x^1 \frac{dz}{z} \left[\sum_j q_j(z, Q^2) P_{g q_j} \left(\frac{x}{z} \right) + g(z, Q^2) P_{g g} \left(\frac{x}{z} \right) \right], \quad (1.28)$$

where the functions $P_{\alpha\beta}(x/z)$ are the *splitting functions*. They are calculable in pQCD as a power series of α_s :

$$P_{\alpha\beta}(z, \alpha_s(Q^2)) = P_{\alpha\beta}^{(0)}(z) + \frac{\alpha_s}{2\pi} P_{\alpha\beta}^{(1)}(z) + \dots \quad (1.29)$$

In the leading order the splitting functions correspond to the probability that a lepton α carrying a fraction x of the proton's momentum originates from a parton β with a momentum fraction z . The splitting functions $P_{\alpha\beta}^{(n)}$ are currently known up to order $n = 2$ in α_s , in the so-called next-to-next-to-leading order (NNLO) approximation.

In the DGLAP approximation, only powers of $\alpha_s \ln(Q^2/Q_0^2)$ from the perturbative expansion are considered in the *Leading Logarithmic Approximation (LLA)*. Thus, this approximation is valid only at large enough Q^2 , where α_s is small and $\ln(1/x)$ terms are not important and the only divergency left to be "resummed" in the parton distributions is the $\ln(Q^2)$. This is given by:

$$\begin{aligned}\alpha_s(Q^2) &\ll 1 \\ \alpha_s(Q^2) \ln(Q^2) &\approx 1 \\ \alpha_s(Q^2) \ln(1/x) &\ll 1.\end{aligned}\tag{1.30}$$

The BFKL Equations

At very low x and large enough Q^2 to work with reasonably small values of $\alpha_s(Q^2)$ the divergency comes from the $\ln(1/x)$ term, and (1.30) becomes:

$$\begin{aligned}\alpha_s(Q^2) &\ll 1 \\ \alpha_s(Q^2) \ln(Q^2) &\ll 1 \\ \alpha_s(Q^2) \ln(1/x) &\approx 1.\end{aligned}\tag{1.31}$$

The "resummation" of the $(\alpha_s \ln(1/x))^n$ terms independently of Q^2 was developed in the BFKL⁵ theory [25, 26]. Gluon ladders are considered with strong ordering in longitudinal momenta and soft ordering in transverse momenta:

$$\begin{aligned}Q^2 &> k_{T,n}^2 > \dots > k_{T,2}^2 > k_{T,1}^2 \\ x &\ll x_n \ll \dots \ll x_2 \ll x_1\end{aligned}\tag{1.32}$$

The *unintegrated gluon distribution* $f(x, k_T^2)$ is for $k_T^2 \neq 0$ defined as:

$$xg(x, Q^2) = \int_0^{Q^2} \frac{dk_T^2}{k_T^2} f(x, k_T^2).\tag{1.33}$$

This results in the BFKL evolution equation [25, 26]:

$$\frac{df(x, k_T^2)}{d \ln(1/x)} = \int dk_T'^2 K_L(k_T^2, k_T'^2) f(k_T^2, k_T'^2) = K_L \otimes f = \lambda f,\tag{1.34}$$

⁵Ya. Ya. Balitskii, V. S. Fadin, E. A. Kuraev, L. N. Lipatov

where \otimes stands for convolution, and K_L is the *Lipatov kernel* representing the sum over powers of $\alpha_s \ln(1/x)$ terms. From the equation (1.34) it is obvious that the function f follows a power law behaviour in the variable x . The resulting gluon distribution can be expressed as

$$xg(x, Q^2) \sim f(Q^2) x^{-\lambda}. \quad (1.35)$$

Hence, the behaviour of the structure function is predicted to be proportional to $x^{-\lambda}$, although the constant λ is not constrained.

The CCFM Equations

The parton evolution in the CCFM⁶ [27, 28, 29, 30] scheme is an attempt to describe both small and high x regions. If both $\ln(1/x)$ and $\ln(Q^2)$ terms yield divergences, (1.30) becomes:

$$\begin{aligned} \alpha_s(Q^2) &\ll 1 \\ \alpha_s(Q^2) \ln(Q^2) &\approx 1 \\ \alpha_s(Q^2) \ln(1/x) &\approx 1. \end{aligned} \quad (1.36)$$

The CCFM formalism, a general treatment of the gluon ladder within the *Double Leading Logarithmic Approximation (DLA)* is done, based on an angular ordering of the gluon emission - from small angles for the initial emissions to larger angles closer to the hard interaction:

$$\xi_0 < \xi_1 < \dots < \xi_n. \quad (1.37)$$

In the CCFM formalism the $\ln(Q^2)$ and $\ln(1/x)$ are "resummed" in the parton densities. Therefore it is expected to be valid for all values of x and Q^2 . For $x \rightarrow 0$ the CCFM evolution equation is equivalent to the BFKL evolution equation and for large x it reproduces the standard DGLAP equations.

1.6 Heavy Quark Production

The three heaviest quarks - charm, beauty and top - are often referred to as heavy flavours. At the energies considered in this work the heaviest of all quarks - the top quark - can not be pair-produced due to its large mass. For charm and beauty the energy available is large enough for pair-production to be observed. The Feynman diagrams of the leading order production mechanisms are shown in Fig. 1.5. Both charm and beauty in both DIS and

⁶M. Ciafaloni, S. Catani, F. Fiorani, G. Marchesini

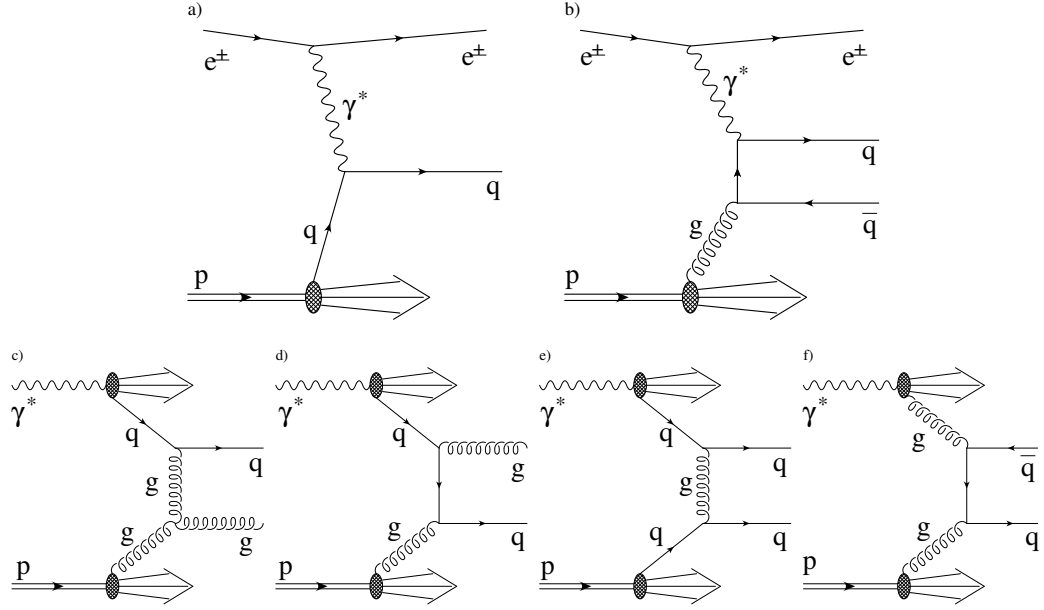


Figure 1.5: Leading order heavy quark production in ep collisions: Direct photon processes: *a)* - see quark interaction, and *b)* - boson-gluon fusion (BGF). Resolved photon processes: *c)*, *d)*, *e)* - Charm excitation. Here the photon fluctuates in a $c\bar{c}$ -pair. One of those takes part into the hard interaction process. Charm excitation via a quark propagator is strongly suppressed compared to the diagram with a gluon propagator shown in *f)* referred to as normal or hadron-like resolved process. Note that the separation to direct and resolved process is valid only in LO and becomes ambiguous in NLO approximation.

photoproduction are experimentally well studied at H1 [31, 32, 33, 34, 35]. The inclusive beauty cross section is two orders of magnitude lower than the charm cross section due to the larger mass ($M_b = 4.2$ GeV vs. $M_c = 1.25$ GeV [5]) and smaller charge squared ($q_b^2 = (\frac{1}{3}e)^2$ vs. $q_c^2 = (\frac{2}{3}e)^2$) of the beauty quark. In this work heavy quark production is discussed in the context of charm only.

Charm quarks are observed via their characteristic decay particles. The possible observable states are either a $c\bar{c}$ bound state (for example a J/Ψ [36, 37]) or in a combined state of charm with other type of quark referred to as *open charm*. The main advantage of considering a heavy flavour process is that the mass of the heavy quark provides an additional hard energy scale. On the other hand, the existence of at least one additional hard scale complicates the calculations significantly [38].

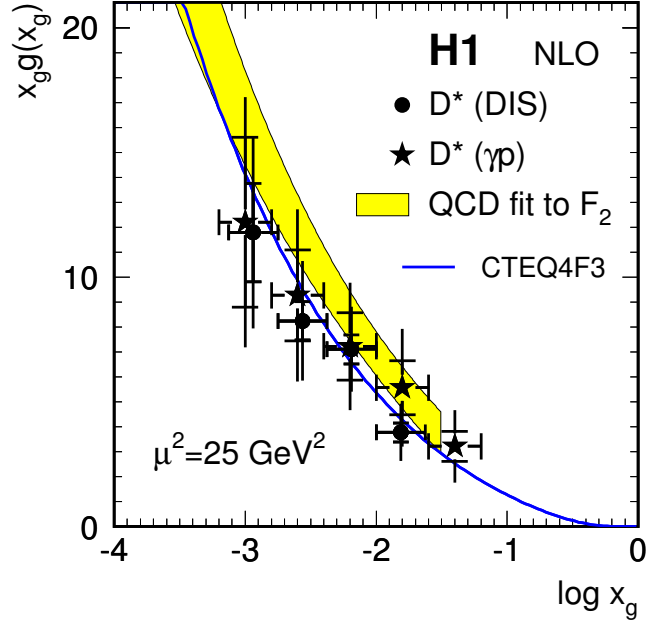


Figure 1.6: Gluon density obtained from H1 charm analysis and compared with the QCD analysis of the inclusive F_2 measurement at $\mu^2 = 25 \text{ GeV}^2$ [39].

In analogy to the inclusive structure functions, the charm pair production cross section in DIS can be written in terms of charm structure functions $F_{2,L}^{c\bar{c}}$ as:

$$\frac{d\sigma^{c\bar{c}}(x, Q^2)}{dx dQ^2} = \frac{2\pi\alpha^2}{xQ^4} \left\{ \left[1 + (1-y)^2 F_2^{c\bar{c}}(x, Q^2) - y^2 F_L^{c\bar{c}}(x, Q^2) \right] \right\} \quad (1.38)$$

The cross section depends directly on the parton densities and in particular on the gluon density in the proton. The gluon density $g(x, Q^2)$ can be obtained from the analysis of the scaling violations of the proton structure function F_2 . On the other hand, through the BGF process, the gluon density enters directly in the charm cross section and in the charm structure function. This gives a powerful cross-check of the PDFs and the pQCD calculations (see Fig. 1.6). Charm production consists of three different steps: production mechanisms, transition from charm quarks to charmed hadrons (*charm fragmentation*) and finally the decay of charmed hadrons. The first

two topics will be covered shortly, and the last one is explained considering the kinematic limitations of the current analysis in Chapter 4.

1.6.1 Production

Three different schemes have been developed to calculate the heavy quark processes, which are valid in different kinematic ranges:

The Massive Approach

In the 'massive' or Fixed Flavour Number Scheme (FFNS) [40, 41, 42], there are three active light flavours (u, d, s), considered as massless, and thus contained in density functions. The heavy flavours (charm or beauty) are considered to be massive and calculable perturbatively in QCD. The leading order process is the BGF shown on Fig. 1.5 b), and the NLO diagrams are of order α_S^2 , which can be calculated at $\alpha_S(\mu)$.

The Massless Approach

Like in the massive approach, in the massless approach [43], the light quark flavours are considered as massless, but unlike the massive scheme, here the charm is also considered to be massless. Thus, one can expect that this approach is reliable only far above the charm threshold $\mu^2 \gg M_c^2$. Below M_c , the charm is treated like infinitely massive. The dominant contribution comes from the leading order parton model process ($\gamma q \rightarrow q$) shown on Fig. 1.5, a). In the NLO processes with virtual corrections, QCD Compton ($\gamma q \rightarrow qg$) and BGF processes also contribute. This massless approach is adopted in Monte Carlo (MC) generators like RAPGAP (described in Chapter 1.7.1).

The Mixed Approach

In order to provide reliable pQCD predictions for the heavy flavour production over the whole range of μ^2 mixed approaches referred to as the Variable Flavour Number Scheme (VFNS) [44, 45, 46, 47] exist. They converge at small (large) energy scales to the massive (massless) scheme, offering different means to deal with the intermediate region. The mixed scheme is the one which is expected to describe the heavy flavour production over most of the kinematic phase space accessible at HERA ($\mu^2 \sim M_c^2$), which is the kinematic range of the present analysis.

1.6.2 Fragmentation

The fundamental scattering cross sections are calculated using pQCD raising color-charged partons. In the final state however, we observe only colorless *hadrons*. Hence, one can measure only the hadronic cross section. In order to be able to compare the results from measurements and calculation one needs to take into account the transition of partons to hadrons referred to as *fragmentation*. The impact of the fragmentation on the hadronic cross section can be represented as:

$$d\sigma_h(p) = \sum_{i=q,\bar{q},g} \int_0^1 D_i^h(z, \mu) d\sigma_i\left(\frac{p}{z}, \mu\right) \frac{dz}{z}, \quad (1.39)$$

where $d\sigma_h(p)$ is the inclusive production cross section for producing hadron h

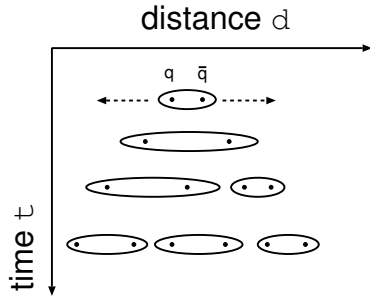


Figure 1.7: Lund string model color string string breaking scheme.

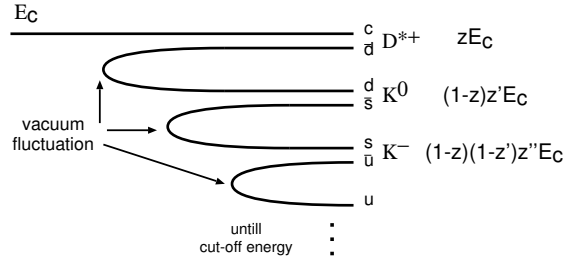


Figure 1.8: Peterson fragmentation hadronization scheme.

with momentum p , $d\sigma_i\left(\frac{p}{z}, \mu\right)$ is the hard cross section for producing a parton i with momentum p/z at the factorization scale μ and $D_i^h(z, \mu)$ is the so called *fragmentation function*, which gives the probability for the initial parton i to produce the hadron h , carrying a fraction z of its initial parton momentum at the factorization scale μ . The main property of the fragmentation functions is that they are universal, i.e. the fragmentation does not depend on the hard process. Hence, fragmentation functions measured in ee -collisions on LEP can be reused for ep - or pp -collisions.

The fragmentation process can be separated into two parts: a perturbative (D^p) and a non-perturbative (D_i^n) part:

$$D_i^h(z, \mu) = \int_z^1 D_i^n(x, \mu) D^p\left(\frac{z}{x}\right) \frac{dx}{x} \quad (1.40)$$

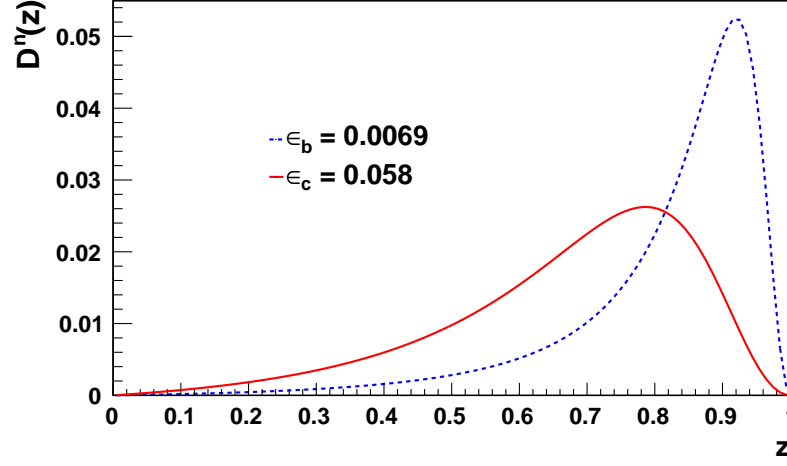


Figure 1.9: Peterson fragmentation function as used in [31] for parametrization of charm and beauty fragmentation.

The first part, referred to as *perturbative fragmentation function* is calculable in pQCD and describes the development of a parton shower from the initial factorization scale parton down to on-mass-shell quarks by means of gluon radiations ($q \rightarrow qg$) and quark-antiquark pair production ($g \rightarrow q\bar{q}$). The *non-perturbative fragmentation function* handles the transformation of quarks on the mass shell to colorless hadrons - a process often referred to as *hadronization*. It is a long-distance, low momentum transfer and thus highly non-perturbative process described by a number of phenomenological models. The most prominent of them is the *Lund string model* [48]. According to this model, the quark and the antiquark in a quark-antiquark pair are connected by one-dimensional color strings which are stretched proportionally to the distance between them. When the distance is large enough, the energy stored in the string is sufficient to create a new quark-antiquark pair, the string breaks up and two independent pairs are created. This sequence repeats (see Fig. 1.7) until the energy of the pairs is not sufficient for new pair production.

Another often used approach is the *Peterson fragmentation* [49]. In this model, the initial heavy quark is bound to a lighter quark in a colorless meson. To get this, a quark-antiquark pair is produced from a vacuum fluctuation (see Fig. 1.8) until the cut-off energy is reached. The Peterson fragmentation function (see Fig. 1.9) is given by:

$$D_i^n(z) = \frac{N}{z \left[1 - \frac{1}{z} - \frac{\epsilon}{1-z}\right]^2}, \quad (1.41)$$

where N is a normalization factor, and ϵ is a free parameter, depending on the order of the perturbative calculations. In LO it absorbs effects, which would be taken into account in the NLO. In fact ϵ is adjusted to describe the data.

Another parametrization used for fragmentation of heavy quarks is the *Bowler fragmentation* function [50]:

$$D_i^n = N \frac{1}{z^{1+bm^2}} (1-z)^a e^{-\frac{bm_\perp^2}{z}}, \quad (1.42)$$

where a and b are free parameters, the transverse mass m_\perp is defined via the mass m and the transverse momentum p_t as $m_\perp = \sqrt{p_t^2 + m^2}$. Recent studies show that the Bowler fragmentation function has advantages in describing charm hadrons in comparison with other parametrizations [51].

The most precise measurements of the fragmentation parameters come from e^+e^- experiments, where the knowledge of the initial state kinematics provides powerful constraints for the fragmentation measurement and effects from interaction between the final state and the beam are absent. On the other hand, the charm quarks produced in ep scattering have a broader energy spectrum which is not the case in the e^+e^- collisions. Therefore, in ep scattering the uncertainty on the parametrization of the fragmentation is one of the biggest theoretical uncertainties in the measurement of the heavy flavour cross sections. Moreover the uncertainty in the fragmentation process brings an uncertainty to the theoretical predictions.

1.7 Monte Carlo Generators

The Monte Carlo (MC) generators are physics event generating computer programs, used to simulate the final state of a system, knowing its initial state, calculating the probability for each of the set of processes, and randomly pick one of them, based on its relative probability. They are powerful analysis tools allowing direct comparison between theoretical models and experimental measurements. Additionally, they are widely used to investigate detector effects like resolution, efficiency, triggering and acceptance. The usual algorithm followed by a MC generator, used to generate a single ep event at HERA follows the following steps, displayed schematically in Fig. 1.10:

- In the beginning the interaction process in HERA consists of one incoming lepton and one incoming proton. The proton is characterized

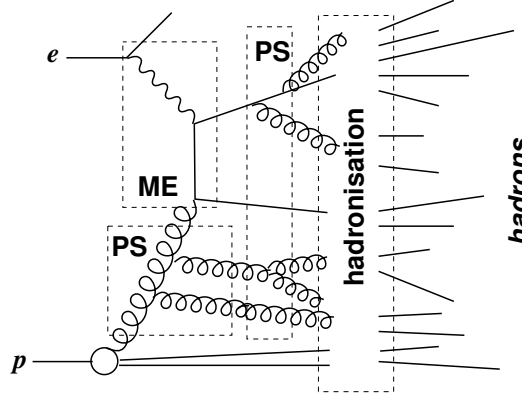


Figure 1.10: Schematic representation of the Monte Carlo event generation steps: A matrix element (ME) representing the hard subprocess, initial and final state parton showering (PS) and the final hadronization, resulting into a set of hadrons represented by corresponding set of four-vectors.

by a parton distribution functions (PDF), which describe the distribution of its energy between its partons. If a resolved process takes place, the photon is also described by a parton distribution functions.

- An initial state parton shower (PS) is initiated by a parton or gluon from the proton. In the case of a resolved process, a parton shower is initiated also from the photon. Both are referred as to initial state showers.
- One of the partons from the initial state parton shower performs a hard scatter with the photon. The cross section of this fundamental hard scattering process is calculated using matrix elements up to some order (LO, NLO or NNLO). This is the process, which defines the properties of the scattering. In the case of resolved processes, the interaction takes place between two partons - one from the proton initial state shower and one from the photon initial parton shower. Out of the process, usually two particles are produced.
- After this hard scattering process, the resulting particles start producing new partons in a shower, according to the probabilities given by the splitting functions (see eq. (1.29)), down to some cut off energy. The resulting showers are referred to as final state parton showers.
- Because of confinement in QCD, the resulting colored quarks and gluons can not directly be observed. At the next step, in order to get observable colorless hadrons, hadronization takes place. Since it cannot be

described by the QCD, it is conducted according to some phenomenological model. At the end of this step, a four-vector is produced for each particle of the final state.

- The produced short-living hadrons are decayed by the generator according to their branching ratios. The long-living particles are decayed on simulation level. In H1 all particles with a lifetime smaller than 10^{-8} seconds are decayed on generator level.
- Additionally the possibility of the initial or the scattered electron to emit photons before or after the hard interaction, and thus entering or exiting from the hard interaction with an energy different than measured is taken into account and referred to as *initial state radiation (ISR)* and *final state radiation (FSR)*, respectively.

The particles' four-vectors stored at this level are referred to as generated. The generated four-vectors are input to the full GEANT 3.15 [52] based H1 detector simulation H1SIM [53]. The GEANT reproduces the detector-induced effects on the generated particles like multiple scattering, bremsstrahlung, compton scattering etc. Additionally, the particles living longer then 10^{-8} seconds are decayed according to the corresponding branching ratios. The development of showers in the calorimeters is implemented using the fast parametrization H1FAST [54]. The simulation output is handed to the software module H1DIGI, which gives out the actual detector response to the simulated tracks, referred to as digitizations. The last step is to run the same, standard H1 reconstruction as the one used for actual data taking, to achieve the final data format, which is in the same format as the actual data, and allows direct comparison between both.

1.7.1 RAPGAP

RAPGAP [55] started off as a generator for diffractive ep events in DIS, which are characterized by large rapidity gap between the photon and proton final states, where actually its name comes from. Nowadays, RAPGAP, in its current version 3.1032 has been developed into a multi-purpose Monte Carlo event generator. The creation of heavy quarks in RAPGAP is implemented by a convolution of the leading order BGF matrix elements, calculated on-shell, with the parton distributions. The proton parton distribution functions used in this analysis through the Les Houches Accord PDF (LHAPDF) interface package [56] is CTEQ6L [57]. The photon parton distribution parametrization used is SaS-G 2D [58]. Higher order effects are simulated using parton showering model. It calculates hard gluon radiation

using QCD matrix elements, and soft gluon radiation using the leading log method. In the latter, the charm quark is treated as a massive parton with mass $m_c = 1.5$ GeV, and renormalization scale as $\mu_r = Q^2 + p_t^2$. The following fragmentation is implemented via the JETSET program [59] using the Lund string fragmentation model for light quark flavours, and the Bowler fragmentation function with parameters $a = 0.437$ and $b = 0.85$ for the heavy quarks. Both models have been discussed in Chapter 1.6.2.

For acceptance and resolutions in the current analysis, a RAPGAP 3.1032 neutral current Monte Carlo event sample was used. The total integrated luminosity of the sample is $\mathcal{L} = 1696.88$ pb⁻¹. On the generator level only events with $Q^2 > 0.5$ GeV², containing at least one D^* meson decaying in the decay chain $D^{*\pm} \rightarrow K^\mp \pi^\pm \pi^\pm$ were selected. This reduced the sample to 1843724 selected events, which required significantly less processing time.

Chapter 2

The H1 Experiment at the HERA Accelerator

This chapter describes the experimental setup with which the data in this work was taken in years 2004 and 2006. Protons and electrons are accelerated to nominal energies and brought to collision by the HERA (Hadron Electron Ring Anlage) accelerator which is described first. The four HERA experiments and their physics tasks are shortly described next. Next, the H1 detector, relevant for this work is described. Further on, the detector subsystems, relevant for this thesis are considered. The silicon detectors of H1, which are critical for this thesis are described in a separate chapter.

2.1 The HERA Accelerator

HERA [60, 61] is the only electron-proton colliding beam facility worldwide, built in DESY (Deutsches Elektronen-Synchrotron) research laboratory in Hamburg, Germany. It is housed in a closed fourfold symmetric underground tunnel, which consists of four straight tunnels each 360 m long, connected by four quarters of circular tunnels with a radius of 797 m. The overall length of the structure is 6336 m. Inside the tunnel, HERA consists of two independent storage rings, producing counter-circulating electrons and protons with nominal energies 27.55 GeV and 920 GeV (820 GeV before the HERA upgrade in 2000). The acceleration of electrons starts in a 500 MeV linear accelerator (e-linac), from which the electrons are injected in a small storage ring, accumulated into a single bunch, injected into DESY II, accelerated to 7 GeV, transferred to the PETRA ring, accelerated to 12 GeV and injected in HERA for final acceleration. The protons are stripped out from negatively charged hydrogen ions, accelerated in a 50 MeV linear

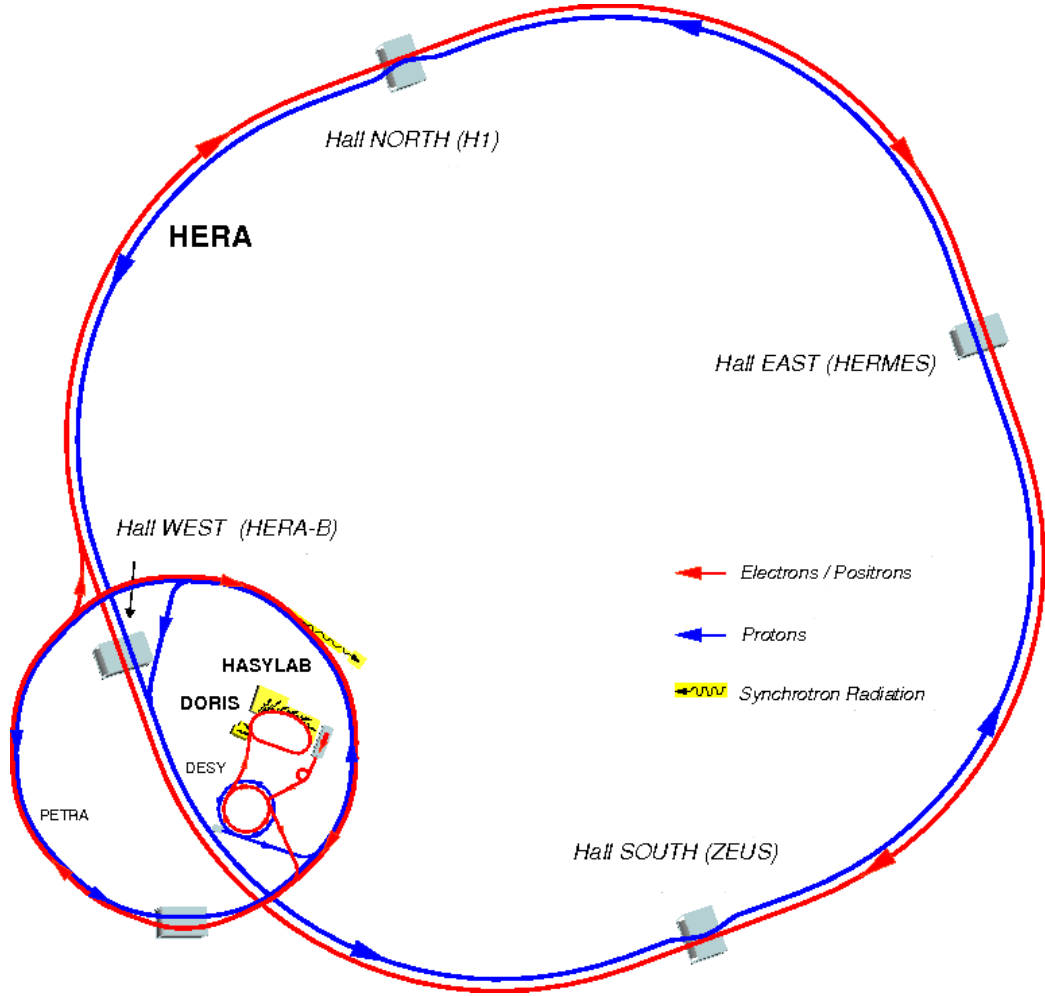


Figure 2.1: HERA accelerator complex

accelerator, upon their injection in DESY III. Later on they are accelerated to 8 GeV, transferred in PETRA, accelerated to 40 GeV, injected to the HERA proton ring and accelerated there to 920 GeV. HERA was approved in 1984, finished in 1990 and since then several times upgraded [62, 63]. The most important upgrade took place in the year 2000. The period before that is often referred to as HERA I and after - as HERA II. The most important nominal parameters of HERA beams as in [64] are listed in Table 2.1. The maximum energy reachable is limited for the lepton beam by the accelerating power available, which has to compensate for the synchrotron radiation emitted. For the proton beam energy, the limiting factor is the magnetic field power needed to keep protons on their orbit.

Four experiments were built at HERA in order to take advantage of its

Parameter	Units	e-ring	p-ring
Beam energy, E	GeV	27.5	920
Beam current, I	mA	58	140
Number of particles per bunch, N_{ppb}	10^{10}	4.0	10.3
Total number of bunches, n_{tot}	-	189	180
Number of colliding bunches, n_{col}	-	174	174
Horizontal β -function at IP, β_x^*	m	0.63	2.45
Vertical β -function at IP, β_y^*	m	0.26	0.18
Emittance, ϵ_x	nm	20	$\frac{5000}{\beta_\gamma}$
Emittance ratio, ϵ_y/ϵ_x	-	0.17	1
Horizontal beam size at IP, σ_x	μm	112	112
Vertical beam size at IP, σ_y	μm	30	30
Beam length at IP, σ_z	mm	10.3	191
Horizontal beam-beam tune shift at IP, $2\Delta\nu_x$	-	0.068	0.0031
Horizontal beam-beam tune shift at IP, $2\Delta\nu_y$	-	0.103	0.0009
Polarization	%	45	0
Luminosity, \mathcal{L}	$\text{cm}^{-2}\text{s}^{-1}$	$7.57 \cdot 10^{31}$	
Specific luminosity, \mathcal{L}_s	$\text{cm}^{-2}\text{s}^{-1}\text{mA}^{-2}$	$1.82 \cdot 10^{30}$	

Table 2.1: HERA nominal beam parameters

beams, namely H1, Zeus, Hermes and HERA-B (see Fig. 2.1). H1 [65] and Zeus [66] are both typical collider experiments, where leptons and protons are brought to collision in a center of mass energy $\sqrt{s} = 318.4$ GeV every 96 nsec leading to a bunch crossing rate of 10.4 MHz. Both Hermes [67] and Hera-B [68] are fixed target experiments using only one of the beams. Hermes uses polarized electron beam to study the spin structure of the nucleons in a gas target. Hera-B collided the proton beam with wire targets and searched for CP-violation over a background twelve orders of magnitude higher than the signal investigated. Hera-B stopped data taking in 2002.

2.2 The H1 Experiment

2.2.1 Overview

The H1 detector [69, 70, 71], is one of the two multipurpose detectors built to investigate ep scattering physics phenomena at high energies possible in HERA. It was commissioned in 1991, and since then has undergone a few

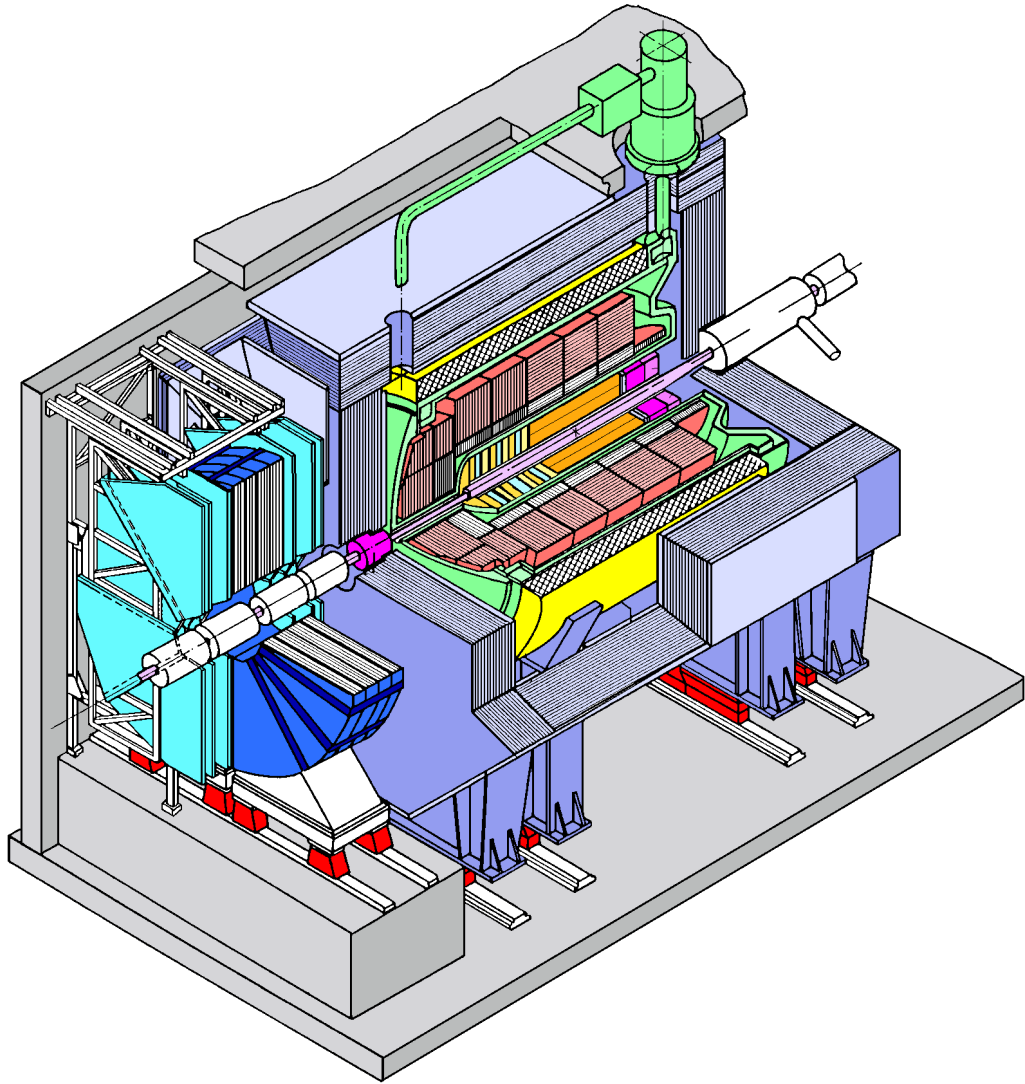


Figure 2.2: Schematic drawing of the H1 Experiment (3D view, 1993)

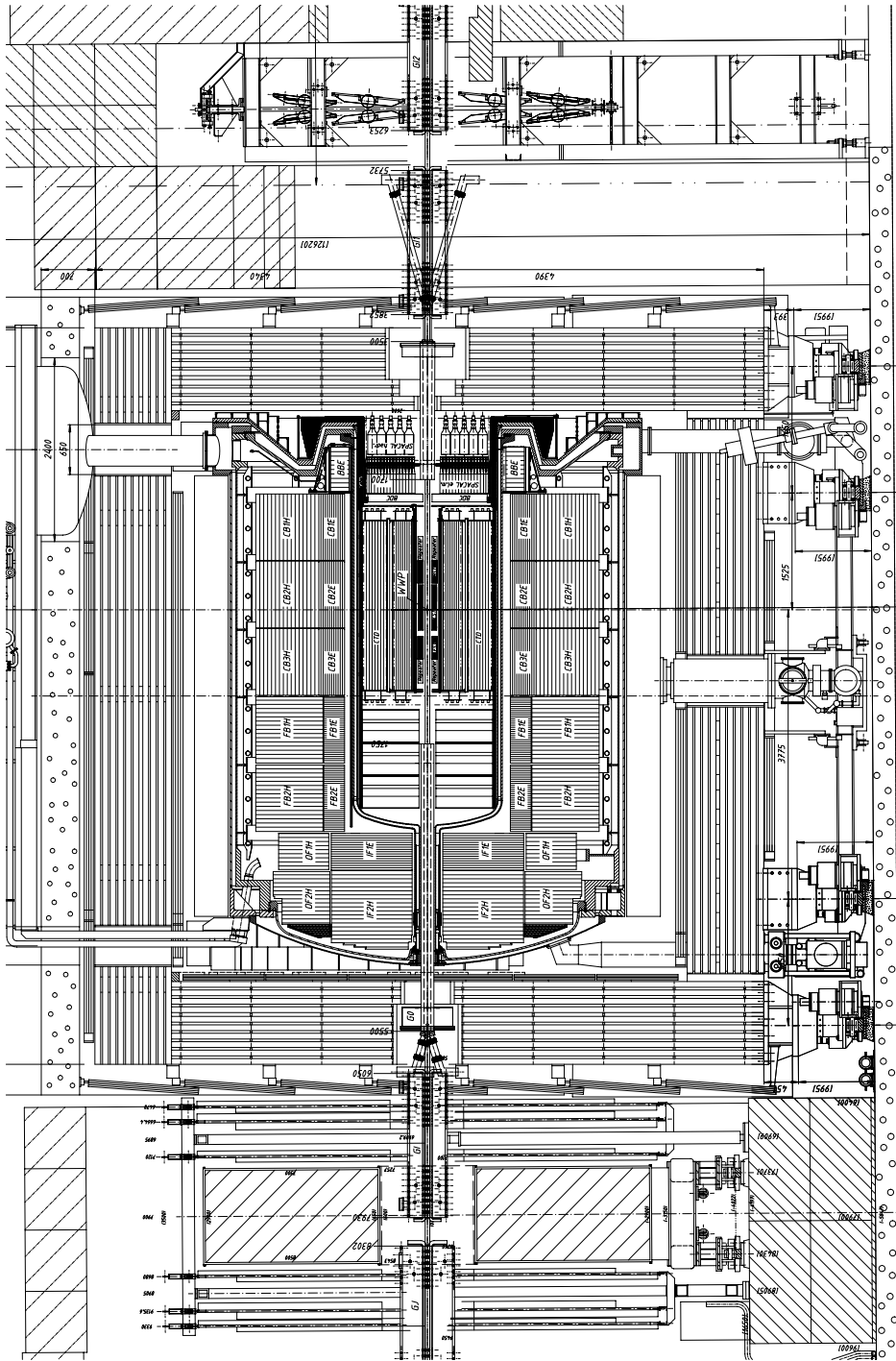


Figure 2.3: The H1 Experiment - Technical Drawing (side view, 2006). Only detector systems to be found in radius ~ 10 m around the nominal interaction point are visible.

upgrades [72, 73]. It is situated in the North Hall of the HERA ring (see Fig. 2.1).

The coordinate system used in H1 is defined as a right handed Cartesian coordinate system starting from the nominal ep collision point for HERA I. The x axis - pointing to the center of the HERA ring, the y axis - pointing upwards, and the z axis pointing along the proton beam direction. Parameters from a spherical coordinate system attached to (0, 0, 0) point are often used in H1: the *polar angle* θ - defined as the angle with respect to z-axis ($\theta \in [0, \pi]$) and the *azimuthal angle* (φ) - defined as the angle in the x - y plane with respect to the x-axis ($\varphi \in [-\pi, \pi]$). The x - y plane is referred also as r - φ plane, or transverse plane.

The main body of the H1 detector (see Fig. 2.3) weighs approximately 2800 tons and has dimensions 12 m \times 10 m \times 15 m. The detector geometry is azimuthally symmetric with respect to the beams, and centered around the nominal ep interaction point (IP)¹. This detector geometry allows H1 to detect outgoing particles in almost all possible directions. The instrumentation of the detector, however, is enhanced in proton direction, taking into account that due to the higher proton energy, the center of mass of the collision in the laboratory frame is moving in this direction, and thus most of the secondary particles are to be expected there. This defines the proton beam direction as "forward", the lepton beam direction as "backward" and as "central" the region between them.

Like all modern high energy collider physics experiments, H1 consists of the following subsystems:

- **Tracking detectors** - closest to the interaction point are the silicon trackers followed by proportional and drift chambers. In H1, because of the beam asymmetry, and to maintain reconstruction efficiency, the tracking is divided into a central and a forward part. It is designed with the main task to reconstruct tracks in the region $5^\circ < \theta < 175^\circ$, and measure their momentum and angles with a momentum precision of $\sigma_p/p^2 \approx 3 \times 10^{-3} \text{ GeV}^{-1}$ and a polar angular precision of $\sigma_\theta \approx 1 \text{ mrad}$. Additionally vertex information, trigger signals and particle identification data is supplied by the trackers.
- **Calorimeters** - surround the tracking system in H1, and provide precise energy measurement. The forward and central region is covered by Liquid-Argon Calorimeter (LAR), and the backward region, where bet-

¹For HERA II all detector systems close to the beam were redesigned to house the beryllium-aluminium elliptical beampipe introduced and thus they are not anymore symmetric.

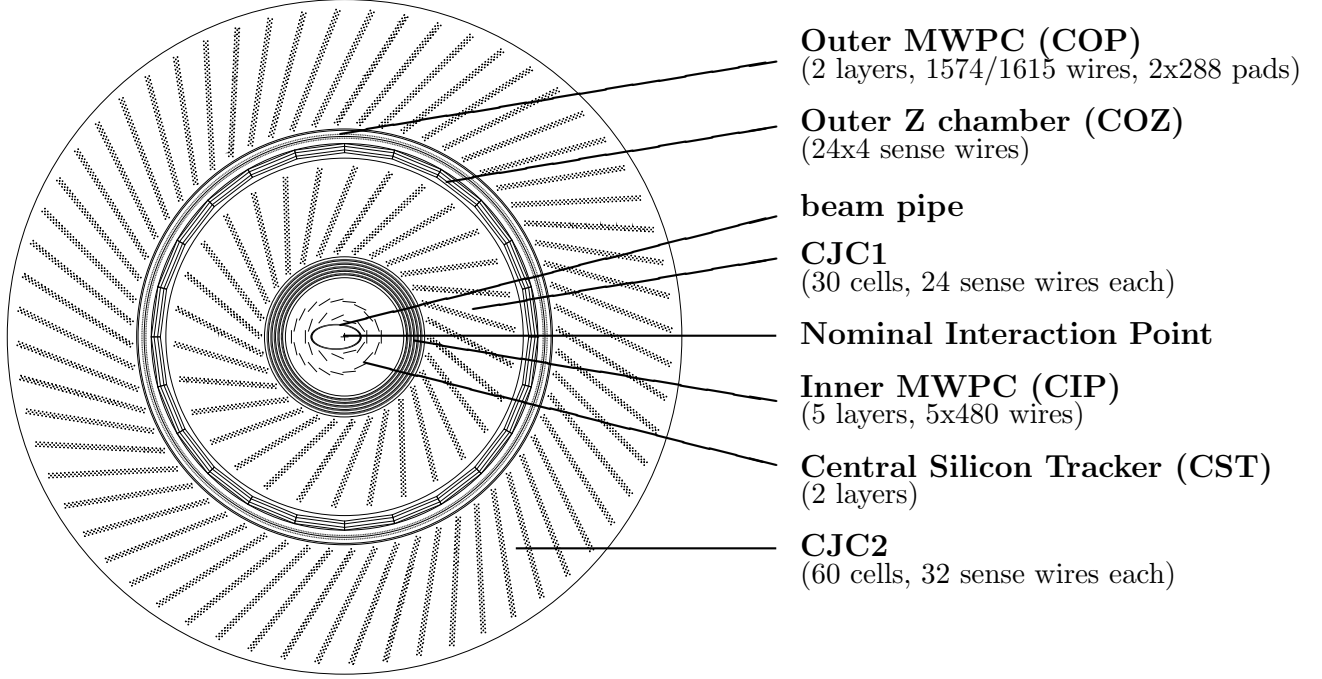
ter energy resolution is needed for scattered electron energy reconstruction, is instrumented with a Pb-fibre Spaghetti Calorimeter (SpaCal). In order to complete the hermeticity of H1 energy measurement, a Plug calorimeter is installed in forward direction.

- **Magnet** - A superconducting coil surrounds the calorimeters, and the tracking system, supplying a 1.16 T homogeneous magnetic field, needed for particle momentum measurement.
- **Muon System** - the outermost system of the main H1 body. Its purpose is to detect particles that survived after passing the superconducting solenoid - mostly muons.
- **Tunnel Systems** - installed in forward direction to investigate the details of proton diffraction and in the backward region - to trigger photoproduction events.
- **Luminosity System** - used for precise measurement of luminosity.
- **Trigger System** - used to extract the ep events from the background, and reduce the rate of data taken from processes with high cross section.

The initial proton and lepton are colliding in a point referred to as *primary vertex*, from which various particles emerge, called *primary particles*. Neutral particles can be detected by the energy deposit in the calorimeters, whereas those with charge - by the trace in the trackers (referred to as *track*) and the energy deposition in the calorimeters. Muons are detected by coincident signals from trackers, calorimeter and muon chambers. Decaying particles are reconstructed by detecting their decay particles. They leave tracks, which do not fit to the primary vertex, but fit well to another *secondary vertex*. Looking at the displacement between secondary and primary vertex allows measuring the lifetime of primary, short living particles.

2.2.2 Central Tracking Detectors

The Central tracking in H1 consists of two large concentric drift chambers, the Central Jet Chambers CJC1 and CJC2. There are two proportional chambers, the Central Inner Proportional chamber (CIP) and the Central Outer Proportional chamber (COP), one thin drift chamber, the Central Outer Z-chamber (COZ), and the Central Silicon Tracker (CST) (see Fig. 2.4). All chambers have independent gas volumes and separate electronics shielding. The complete central tracking system is housed in a 4 mm thick aluminium cylinder.

Figure 2.4: The Central Tracking Detectors in H1 (r - φ , $+z$ view)

Central Jet Chambers

The two coaxial Central Jet Chambers [74] are the main tracking devices in the H1 experiment. They provide precise measurement of the momentum and the type of the particle, using the information of the charge disposed in the chamber volume. The parameters of both chambers are summarized in Table 2.2. The inner chamber CJC1 (see Fig. 2.4) has 720 readout anode wires strung parallel to the beamline. It is divided into 30 jet cells in φ , and in 24 layers in radial direction. The outer chamber CJC2 has 1920 readout wires, distributed in 32 layers over 60 cells. Each two cells are separated by a plane of cathode wires, creating the electric field needed for secondary drift electron acceleration. To improve the uniformity of the field, the distance between the readout wire and the cathode wire is taken into account, when the cathode voltage is correspondingly adjusted. Field wires are placed on the inner and outer edge of each cell, to ensure sufficient uniformity of the field at the end of the chambers. In a cell, the drift field and the gas amplification

Dimensions	Units	CJC1	CJC2	CIP	COP	COZ	CST	FTD
Active Length	mm	2200	2200	2190	2190	2160	442	114
Active zone starts at z	mm	-1125	-1125	-1127	-1127	-1105	-221	1420
Active zone ends at z	mm	1075	1075	1043	1043	1055	221	2440
Active zone starts at θ	$^\circ$	11	26	9	26	25	7	4
Active zone ends at θ	$^\circ$	169	154	171	155	155	173	30
Inner radius	mm	203	530	157	520	460	-	1850
Outer radius	mm	451	844	193	491	485	-	7900
r- φ resolution	mm	0.17	0.17	-	-	58	0.012	-
z resolution	mm	22	22	-	-	0.2	0.022	-

Table 2.2: Summary of H1 Tracking Detectors' design parameters

are steered almost independently for each anode wire due to four potential wires, forming a square around it, connected to ground. Additionally, the readout wires are staggered by $\pm 150 \mu\text{m}$ with respect to the nominal anode wire plane. Staggering helps resolve ambiguities and minimizes electrostatic interactions between neighboring wires, leading to systematic shifts in r - φ wire positions. The nominal gas mixture used in the CJC consists of 49.3% Argon, 49.3% Ethane 1.2% Ethanol and 0.2% N_2 .

The jet cells are tilted by 30° in the r - φ plane. This allows a high energetic track originating from the nominal vertex to pass through more cells on average. Increasing the number of cells crossed per track helps to resolve the left-right ambiguity of a drift chamber. A passing particle in a drift chamber creates electron-ion pairs. Ions move in cathode direction, and electrons - towards anode wire. On their way they are accelerated by the electric field, up to energies at which they start to cause secondary ionization. In the end an avalanche of electrons reaches the anode wire and its charge is deposited and read out. From this charge alone one cannot judge from which side of the anode wire the initial particle has passed. If the jet cells were not inclined, out of the signals coming from one cell, two tracks would be reconstructed from one passing particle, a real and the so called "ghost track". In case of the CJC, a stiff track passes through at least 2 jet cells per jet chamber, creating short tracks, referred to as *track segments*. Only segments caused by real particles fit to a common track. Thus, the ghost tracks are rejected at an early stage. The second advantage given by the cell shift is the Lorentz angle compensation. Secondary drift electrons are moving towards the anode wire, but are deflected by the Lorentz force of the magnetic field. The resulting shift is approximately compensated by the inclination of the jet cell.

Central Z Chamber

The COZ (see Fig. 2.4) was designed and produced in DESY Zeuthen. Its main parameters are briefly outlined in Table 2.2. COZ is a cylindrical drift chamber, composed of 24 rings in z , each 9 cm wide. The side walls of each cylinder is a cathode, with holes in it, allowing gas flow through the chamber. The rings are subdivided in φ in 24 cells, each with four layers of sense and four pairs of potential wires in each ring strung perpendicular to the beam line. Thus, the drift velocity is in the z direction. In order to keep the chamber thickness low ($0.7\%X_0$ for the active zone of COZ), the gas volume is closed by the outer CJC1 capton ring. Further details can be found in [71, 75].

Central Proportional Chambers

The CIP and COP are complementary cylindrical multiwire proportional chambers, used to supply fast trigger signals based on the z position of the primary vertex. The COP is divided in 18 sectors with length 12.1 cm in z , and in 16 sectors in φ . During the H1 2000 upgrade, a new, 5-layer CIP [76, 77] took the place of the old 2-layer CIP [78] and the Central Inner Z-chamber (CIZ). It consists of 5 cathode planes, divided in φ in 8 sectors (16 for plane number 3) and in 240 pads in z direction. 480 anode wires per plane are strung 6 mm away from the cathode planes. Both anode and cathode signals are read out, giving the possibility to reconstruct track segments with resolution $\sigma_\varphi = 5$ mrad per plane. The main parameters of the CIP and COP are presented in Table 2.2, and an r - φ view of the chambers can be seen on Fig. 2.4.

Central Silicon Detector

The CST [79] is a silicon vertex detector equipped with double-layer, double-sided, double-metal silicon sensors. Due to the elliptical shape of the beam pipe introduced in the HERA II upgrade, a major rearrangement of the detector geometry was done [80]. The 12 ladders from the inner layer are placed as close as possible to the beam pipe, following its geometry, and assuring at least $450\ \mu\text{m}$ overlap between neighboring ladders to facilitate internal alignment using high energetic cosmic tracks. The outer plane of the CST consists of 20 ladders, situated as far away as possible from the interaction point. The r - φ position of the ladders was designed to ensure best resolution, i.e. such, that an incidenting, high energetic track coming from the interaction point would pass them at normal incidence. Two neighboring ladders share the same supply voltages, and are read out sequentially. A

ladder consists of 6 silicon sensors, grouped in two separate electrical units called half-ladders. Each half-ladder has three sensors. Each sensor has 640 p -type strips, parallel to the beam direction and 640 n -type strips both implanted on the both sides of high resistivity ($\rho > 6 \text{ k}\Omega$) n -bulk silicon. The strips are DC coupled to the metal strip, bonded to the same charge sensitive APC128 chip used in the FST and the BST readout [81]. The signal-to-noise ratio (S/N) achieved is 19 for p -side and 8 for the n -side. The p -side S/N results in a hit resolution in $r\text{-}\varphi = 12 \text{ }\mu\text{m}$, which allows precise reconstruction of secondary vertices e.g. from D0 decays [82].

The n -side S/N is too small, and it is therefore presently not used for the reconstruction of the primary vertex z position supplied by the CJC reconstruction (see Chapter 2.2.9).

2.2.3 Backward Tracking Detectors

Due to the difference in the beam energies, the track multiplicity in the backward region of H1 is lower than in the forward region. On the other hand, there is particular interest in the measurement of the inclusive scattered electron which defines the DIS kinematics. The two tracking detectors in the backward region - the Backward Silicon Tracker (BST) and the Backward Proportional Chamber (BPC) - have been adopted for that. The BST as a key device for this analysis will be discussed in more detail Chapter 3.

Backward Proportional Chamber

The Backward Proportional Chamber is a proportional gas chamber, mounted on the electromagnetic Spaghetti Calorimeter (SpaCal). It consists of 6 wire upper coordinate planes and of 6 wire down coordinate planes named Y(Y1,Y2), U(U1,U2), V(V1,V2) rotated in the $r\text{-}\varphi$ plane by 0, +60 and -60 degrees correspondingly. A wire plane consists of 296 long and 37 short wires for Y planes and of 494 wires for U and V planes, with a spacing of 2.5 mm.

2.2.4 Forward Tracking Detector

Forward tracking in H1 consists of the Forward Tracking Detector (FTD), and the Forward Silicon Detector (FST). The latter will be described in Chapter 3 together with BST.

The FTD [71] instruments the forward tracking of H1 with a high resolution tracker, supplying particle momentum, particle identification information and low level trigger data. Due to low track finding efficiency [83, 84, 85], the FTD was upgraded for the HERA II running period. During the upgrade,

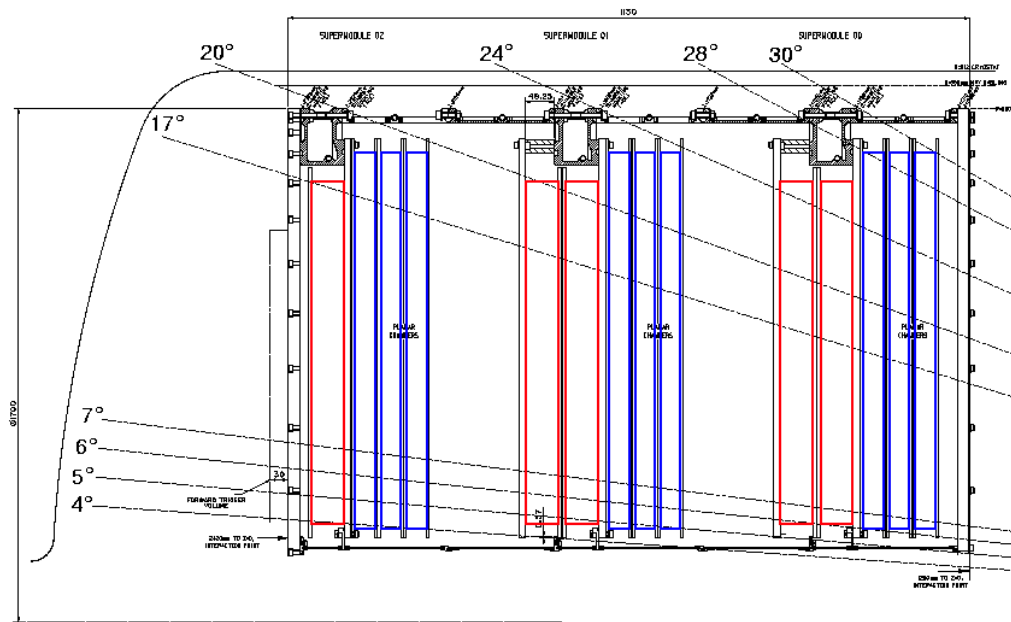


Figure 2.5: FTD - Technical Drawing (upper half, $r - z$ view)

the Radial Chambers, Forward Wire Proportional Chambers (FWPC), and the Transition Radiators (TR), which were all part of the FTD, were removed to lower the rate of secondary interactions in the detector material. Part of their place was taken by new Plane Chambers referred to as Q-chambers. These were intended to bring the redundancy needed to resolve the hodoscope ambiguities. In the current configuration FTD consists of 9 old planar chambers (P-chambers), and 5 Q-chambers, divided in 3 Super Modules, named SM0, SM1 and SM2 situated approximately 1.4, 1.8 and 2.2 m from the IP (see Fig. 2.5).

2.2.5 Calorimeters

The main purpose of the H1 Calorimetry system is to complete the momentum information from the tracking system described above by precise energy measurement, resulting in clear distinction, identification and measurement of electrons, muons, photons, neutral particles and jets in an environment of high particle densities. Following those requirements, the H1 collaboration decided for a calorimeter situated immediately behind the tracking system, surrounded by the superconducting coil - a concept chosen also for the high-energy experiments at the Large Hadron Collider (LHC) experiments at the European Organization for Nuclear Research (CERN). It minimizes the dead

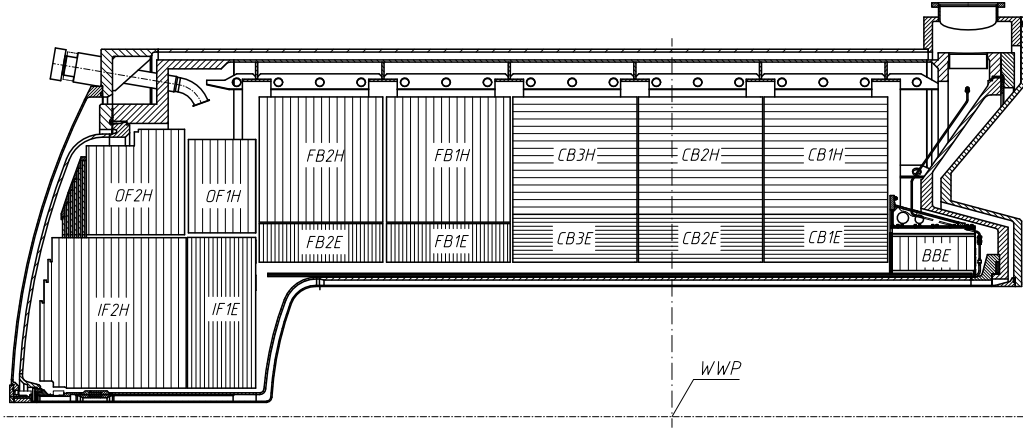


Figure 2.6: Liquid Argon calorimeter - Technical Drawing (upper half, $r - z$ view).

material in front of the electromagnetic calorimeter and reduces the size and the dimensions of the calorimeter. In the following, the calorimeters relevant for this analysis are described shortly.

Liquid Argon Calorimeter

The LAr calorimeter is the main calorimeter in H1. It covers the full azimuthal range of $4^\circ < \theta < 154^\circ$. It is a high granularity sampling calorimeter divided into an electromagnetic part (eLAr) and a hadronic part (hLAr). It is segmented in z into 8 self-supporting wheels, each of them segmented in φ into eight identical octants. Fig. 2.6 shows the LAr construction. The labels on the figure represent the position (F/C/B/ stand for forward / central / backward) and the type (E/H stand for electromagnetic / hadron part). Since in both eLAr and hLAr the active medium is liquid argon, the LAr calorimeter is placed in a cryostat cooled down by gaseous helium. The hLAr is made of a sandwich-like structure of 19 mm stainless steel absorber planes separated by double gaps of 2.4 mm liquid argon. In the middle of the gaps, a G10 (epoxy + glass fiber) board with pads is positioned in order to collect charges deposited in the LAr. The layers in the eLAr consist of 2.4 mm Pb absorber, 2.35 mm active material, a pad readout plane and a high voltage layer. The orientation of the planes is such that particles originating from the IP are incident on the calorimeter with angles not smaller than 45° . The total thickness of the eLAr varies between 20 and 30 radiation lengths for electrons and 1.0 - 1.4 interaction lengths for hadrons. The hadronic part has a thickness of 5 to 9 interaction lengths. The energy resolution of the

eLAr is $\sigma_E/E = 12\%/\sqrt{E/\text{GeV}} \oplus 1\%$ and $\sigma_E/E = 55\%/\sqrt{E/\text{GeV}} \oplus 2\%$ for the hLAr. More details can be found in [71, 86].

Spaghetti Calorimeter

The SpaCal calorimeter [87] was installed in the 1994/95 shutdown, replacing the previous backward calorimeter (BEMC [71]). It is a high resolution lead/scintillating-fiber detector completing the H1 calorimetric coverage in the polar angle range $153^\circ < \theta < 177.5^\circ$.

The SpaCal consists of an electromagnetic part, situated closer to the IP, and a hadronic part placed behind it. In both cases the same spaghetti production technology is used - scintillating fibers are pressed in z direction into suitably shaped lead plates. The electromagnetic (hadronic) SpaCal consists of 1180 (128) cells with an x - y surface $40.5 \times 40.5 \text{ mm}^2$ ($119.3 \times 119.3 \text{ mm}^2$). Each cell is made of 52 (65) lead plates containing 45 (54) fibers. The fibers used are 250 mm long, 0.5 mm (1.0 mm) in diameter and they have lead-to-fiber ratio of 2.3:1 (3.4:1). This corresponds to 27.8 (29.4) radiation lengths. The light from 2 (1) cells are mixed in an 80 mm long acrylic light mixer, and then read out by a single photomultiplier.

The energy resolution achieved for the electromagnetic and the hadronic part have been determined to be

$$\frac{\sigma_E}{E} = \frac{(7.1 \pm 0.2)\%}{\sqrt{E/\text{GeV}}} \oplus (1.0 \pm 0.1)\% \quad (2.1)$$

and

$$\frac{\sigma_E}{E} = \frac{(56.0 \pm 3.0)\%}{\sqrt{E/\text{GeV}}} \quad (2.2)$$

correspondingly. The main purpose of the SpaCal is to securely identify the scattered electron as such, and precisely measure its polar angle and energy as close as possible to the beampipe.

The design SpaCal acceptance is limited to $\theta = 177.5^\circ$, which allows to access Q^2 values down to 0.4 GeV^2 and Björken x values down to 10^{-5} . SpaCal has a reliable separation of charged hadrons and electrons at low energies, which is used to suppress photoproduction events. The photoproduction has a few orders of magnitude higher cross section than the DIS events, and is characterized by the scatter electron escaping through the beampipe. The scattered electron signal in the SpaCal would be faked via π^\pm from the hadronic system. The π^\pm rejection factor in the SpaCal is $\epsilon_e/(1 - \epsilon_\pi) > 100$, where ϵ_e and ϵ_π are the electron and pion identification efficiency respectively (for details see [88]). Finally, the SpaCal has a time resolution better than

1 nsec, which is fast enough to distinguish between upstream beam-induced background particles which have a time-of-flight delay of approximately 10 nsec with respect to the normal ep events [89].

For the HERA II period, the SpaCal had to be modified such that it could free space for the GG magnet [90]. A 20 cm hole, 2 cm shifted from the nominal beam position was freed by removing some of the innermost cells. This reduced the initial acceptance to $\theta \leq 174.5^\circ$ for the electromagnetic SpaCal and $\theta \leq 173^\circ$ for the hadronic SpaCal.

2.2.6 Luminosity System

The luminosity system in H1 [71, 91] consists of four detectors, near to the beampipe and behind H1, far away from the interaction point in backward direction, where collinearly radiated photons can be measured. The detectors are placed in the HERA tunnel behind H1 in the following order:

1. **Electron Tagger (ET6)** - at $z = -5.4$ m. It is a SpaCal type electromagnetic calorimeter made out of lead and scintillator-fiber planes. Its active area is 75.6×25 mm². It is 20 cm deep, resulting in 22 radiation lengths.
2. **Electron Tagger (ET40)** - at $z = -40.0$ m. It is a total absorption Cherenkov calorimeter, made of 2×2 cm² KRS₁₅ crystals, with a hodoscopic structure.
3. **Veto Counter (VC)** - at $z = -101.4$ m. It is a water Cherenkov detector, read out by two separate photomultipliers. One photomultiplier is working with nominal HV and is giving a spectroscopic channel, whilst the other is working under increased HV and is used as a veto.
4. **Photon Detector (PD)** - at $z = -101.8$ m. It is a 24 channel Cherenkov sampling calorimeter, made of tungsten absorber planes and quartz-fiber as active medium read out by photomultiplier tubes. It has an interaction area of 12×12 cm² and a depth of 25 radiation lengths. ET6 and PD are coupled in coincidence to measure online the luminosity with statistical precision of 2 %.

The main task of the luminosity system is to perform a fast relative luminosity measurement and to precisely determine the integrated luminosity for a given time period. It also tags photoproduction events and supplies energy measurement for electrons scattered at very small angles and initial state radiation photons. For the luminosity measurement the system exploits the bremsstrahlung process $ep \rightarrow ep\gamma$, for which the cross section is rather high

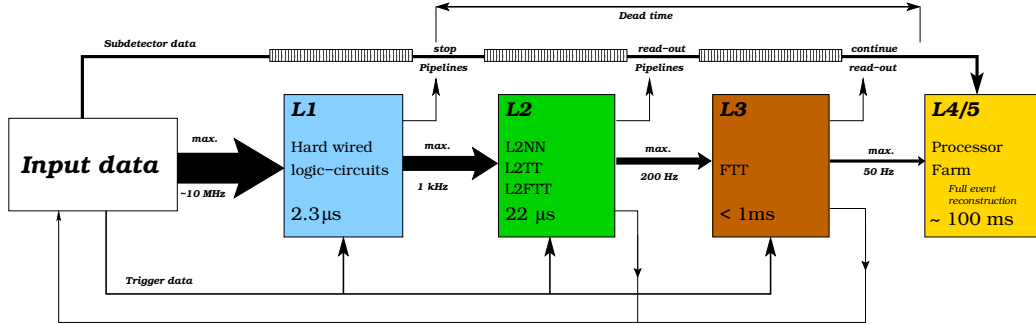


Figure 2.7: Overview of the trigger system

and well known. The instantaneous luminosity measurement is done by dividing the counting rate of gammas over a certain energy threshold detected in the photon detector by the visible bremsstrahlung cross section, which at the ultrarelativistic limit and in the small angle approximation is described by the Bethe-Heitler formula [92]. Thus, the accuracy of the luminosity measurement is about 5%.

2.2.7 Triggering and Data Taking

The task of the H1 trigger system [71] is to select the ep scattering events of interest and to reject the background based on the signals in the detector. The main background sources are synchrotron radiation from the electron beam, proton-gas interaction in the beampipe vacuum and beam-wall interactions produced by off-orbit protons, interacting with the beampipe and other parts of the accelerator and producing particle showers. Beam halo muons and cosmic ray muons play a role, too. The overall background rate is at the order of 100 kHz.

Only once per each thousand bunch crossings, an ep event takes place. The physics processes observed in ep -interactions have a wide variety of cross sections raging from a several μb to a fraction of pb . Depending on the luminosity this induces event rates ranging from tens of kHz for photoproduction down to less than one per week.

The maximum rate of data which H1 is able to store is 30 Hz. The trigger system reduces the initial rate of $\sim 10\text{MHz}$ down to 30 Hz by rejecting the background-induced events and prescaling the ep event rate depending on the physics process involved. The trigger system is divided into 4 different levels depicted on Fig. 2.7.

- **Level 1 (L1)** - On the first level (L1) the trigger decision is taken in $2.3\ \mu\text{s}$. It is phase-locked to the HERA accelerator clock (10.4 MHz),

and provides a trigger decision for each bunch crossing without causing dead time. The L1 trigger manages to reduce the input rate of ~ 10 MHz down to ~ 1 kHz. The input data from different subdetectors is encoded in 256 boolean variables referred to as raw trigger elements. The trigger elements are logically combined into 128 subtriggers. Each subtrigger can be prescaled to reduce the output rate to levels to which the deadtime is acceptable and the storage system is maximally loaded. A prescale of n for a given subtrigger would mean, that only one of n accepted events from this subtrigger will be accepted by L1. After prescaling the trigger elements are referred to as *actual trigger elements*. After the event was accepted by at least one from the subtriggers, the event is accepted on the L1 trigger level, and the central trigger sends to all subsystems the L1 trigger decision signal (called L1Keep signal). All subsystems keep their output data from the last few² bunch crossings temporally stored in pipelines. The L1Keep signal stops the the pipelines of all subsystems and prepares for readout. From this moment on, the detector does no longer record events, creating dead time until, after 1.2 ms the "Frontend Ready" signal reenables the pipelines.

- **Level 2 (L2)** - The second trigger level (L2), verifies the L1 trigger decision based on neural network (L2NN) [93], topological correlations (L2TT) [94] and fast tracking trigger (FTT) [95] signals. It must finish within maximum 22 μ s. If a positive L2 trigger decision was taken, an L2Keep signal is issued to all systems, and the reading of the data from the pipelines is started. If the event is rejected, L2Reject is issued, and H1 is ready to evaluate the next event on L1. The L2 reduces the input rate of ~ 1 kHz to ~ 100 Hz.
- **Level 3 (L3)** - Trigger level 3 (L3) is based on FTT and verifies the L2 trigger decisions. The FTT consists of a PowerPC based farm, which is used to combine tracks measured by FTT at trigger level 2. In 100 μ s a trigger decision is taken and the event is either rejected or sent to the Trigger Level 4 and the data taking is again resumed. L3 is the last trigger level contributing to the dead time of H1. It further reduces the event rate down to ~ 50 Hz.
- **Level 4 (L4)** - It is a software filter on which the full event reconstruction is done using the fortran77 software package H1REC [96]. Initial calibration and alignment for all detectors is applied. All events are

²up to 35 bunch crossings, depending on the subsystem

classified depending on the event topology. L4 trigger decision is taken asynchronously, depending on the time it takes to reconstruct the event (typically 500 ms). Finally, the events are stored as so-called POTs (Production Output Tapes) at a rate of 150 kB/event.

2.2.8 The H1 Data Structure

The data collected by H1 is grouped in time according to its physical properties. The events which are originating from the same beams are having the same initial particle properties and thus considered to belong to the same *luminosity fill*. Further division of the data into *luminosity runs* is done, depending on the current trigger prescales and subdetector systems' conditions. In general, the important database information in H1 is considered to be either run dependent or fill dependent. All data in H1 is distributed in BOS banks³. All data available for a given event, which had passed all trigger conditions and a minimum of quality requirements, is written on tapes, and often referred to as "raw data". A selected set of banks is extracted onto DST (Data Storage Tape), reducing by factor of 8 the amount of data per event down to 20 kB/event, and thus reducing the access time. Additionally, physics tools data processing is performed and the results are also saved in the DST. The data which is not event-based like run-based or fill-based calibration and alignment constants is written in a database. After software updates or new calibration data, H1 raw data is reprocessed, and new version of DST is produced called DST n , where n is the sequential number of the reprocessing. On top of the fortran framework, a C++ and ROOT [98] based framework is developed called h1oo [99]. Additional three data layers exist in the h1oo framework, namely ODS (Object Data Store), μ ODS (micro Object Data Store) and HAT (H1 Analysis Tag). The ODS files are usually not stored. They are created on-the-fly if some information is required from the user. They include almost all information from DST tapes, wrapped into ROOT classes. A basic BOS bank access is also implemented, making it possible to access every bank recorded from H1. To produce μ ODS, the next layer of files containing particle level information, a set of so called finders are run. They select only best defined tracks and clusters, combine them and create particle candidates - for example for the scattered electron - out of them. Dedicated finders are combining track candidates to heavier particles, like D^* or J/Ψ . All selected tracks, particle candidates, combined particles and links back to lower level information are saved in the μ ODS files. The

³BOS [97] is the H1 memory management system developed by V. Blobel at DESY and previously also used at the OPAL experiment at the LEP accelerator at CERN.

last abstraction level is the HAT files. In the HAT files only limited amount of variables are stored, providing a short event summary information. This reduces the amount of data tremendously, and allows a fast HAT-based event selection. H1 now extensively uses the h1oo framework.

2.2.9 Track Reconstruction

The main purpose of the track reconstruction is using the raw digitized detector information to reconstruct the tracks and the vertices from which they originate. The initial step is the *hit finding*. It is a procedure which uses as an input the raw detector data and based on the detector description and alignment information it finds the corresponding space coordinate where a particle interacted with the medium of the detector referred to as *space hit*. Depending on the detector geometry, the next stage is either fitting of parts of tracks (referred to as *track segments*) and then combining these segments to one track extending to the full acceptance of the detector or skipping segment finding and fitting directly a full track obeying an adequate track model. In both cases a fast, iterative pattern recognition fitting procedure is used in order to find from a significant number of hit combinations the ones coming most probably from physical particles and reject the rest of the combinations following a strict fit quality criterion. Finally based on the track information the most probable position of a primary and a set of secondary vertices is defined and each track is refitted to the corresponding vertex to which it is associated.

A short summary of the parametrizations, quality parameters and algorithms used follows.

The H1 Track Parametrization

A charged particle in a homogenous magnetic field moves along a helix with an axis in the direction of the magnetic field. There are various parametrizations possible for a helix. The usual parametrization is not suitable, since in case of high momentum, the radius becomes large. Thus in H1 the so called *dca parametrization* is chosen. The parameters for each non-vertex fitted track in dca parametrization are:

- κ - Signed curvature. It is defined as the signed inverse radius of the track ($\kappa = \pm 1/R$). The sign of κ is defined by the direction of movement of the particle on its track, projected on the x - y plane. If the particle moves counterclockwise, κ is positive, if not, κ is defined to be negative. If we define $\vec{p} = \vec{p}(t)$ as the momentum of the particle,

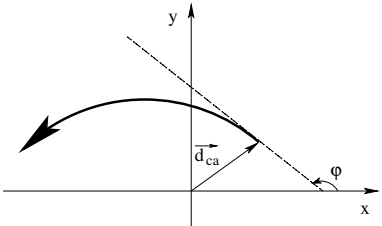
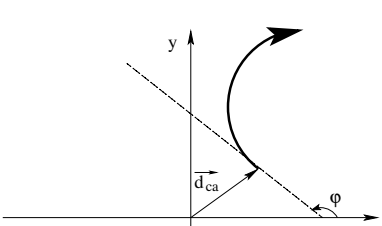
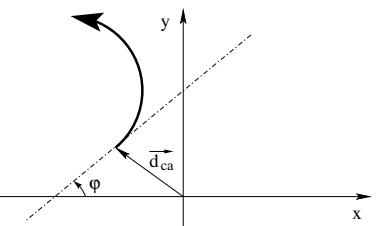
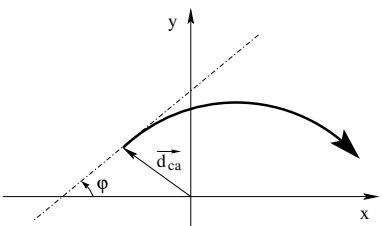
	$\kappa > 0$	$\kappa < 0$
$d_{ca} > 0$		
$d_{ca} < 0$		

Table 2.3: Definition of κ and d_{ca}

the κ definition can be presented as:

$$\left(\vec{p} \times \dot{\vec{p}} \right)_z > 0 \iff \kappa > 0 \quad (2.3)$$

- d_{ca} - distance of closest approach. A signed variable, the magnitude of which gives the closest distance in the x - y plane between the track and the H1 coordinate system origin. The point of the track which is closest to the coordinate system origin is referred to as the d_{ca} point. If in the x - y plane the vertex is on the left side of the track, then the d_{ca} is positive. If \vec{d}_{ca} is defined like the vector from the coordinate system origin to the d_{ca} point and \vec{p}_{ca} is the momentum vector in this point, then the d_{ca} definition can be presented as:

$$\left(\vec{d}_{ca} \times \vec{p}_{ca} \right)_z > 0 \iff d_{ca} > 0 \quad (2.4)$$

- z_0 - z position of the d_{ca} point.
- φ - Azimuthal angle. The angle defined by the direction of the positive x axis and the tangent to the track projection in the x - y plane at the d_{ca} point.

- θ - Polar angle. Defined as the angle between the direction of the positive z axis and the tangent to the track projection in the r - θ plane at the d_{ca} point.

With these parameters the coordinates of the particle can be described independently from the track length s . This track length s is given by a path integral over the track in the r - φ plane, starting from the d_{ca} point. The coordinates of any point on the helix can be presented as:

$$x(s) = x_0 + \sin(\varphi + \kappa s)/\kappa \quad (2.5)$$

$$y(s) = y_0 - \cos(\varphi + \kappa s)/\kappa \quad (2.6)$$

$$z(s) = z_0 + s \cdot \cot \theta \quad (2.7)$$

where (x_0, y_0) are the coordinates of the center of the circle representing the track in r - φ plane. They can be calculated using the dca parametrisation as:

$$x_0 = -(1/\kappa - d_{ca}) \sin \varphi \quad (2.8)$$

$$y_0 = (1/\kappa - d_{ca}) \cos \varphi \quad (2.9)$$

Using equation (2.7), one can represent the track in an s - z plane as a straight line with slope $\cot \theta$ crossing the z axis at z_0 , without further dependence on the r - φ measured track parameters i.e. κ , φ or d_{ca} . Thus, this parametrization suits best to H1 central tracking with a main tracking device as CJC - a drift chamber with two orders of magnitude different resolutions in x - y and along z .

The momentum of a particle can be calculated from the helix parameters as:

$$p_t = \sqrt{p_x^2 + p_y^2} = \frac{eB}{|\kappa|} = p \sin \theta \quad (2.10)$$

$$p_x = p_t \cos \varphi \quad (2.11)$$

$$p_y = p_t \sin \varphi \quad (2.12)$$

$$p_z = p_t / \tan \theta \quad (2.13)$$

$$p = \sqrt{p_x^2 + p_y^2 + p_z^2} = \sqrt{p_t^2 + p_z^2} = p_t / \sin \theta \quad (2.14)$$

where e is the particle charge, B - the magnetic field, p_t and p_l are the transverse and the longitudinal components of the particle 3-momentum $\vec{p} = (p_x, p_y, p_z)$.

In reality, deviations from an ideal helix are mainly due to:

- Magnetic field inhomogeneities.

- Multiple scattering in material - especially for low energy tracks. Results in change of initial direction of the track but preserves the total particle momentum.
- Energy loss due to bremsstrahlung.
- Kinks from one-prong decays.

Finally, a not perfect alignment or calibration spoils also the ideal track model

The H1 Tracking Scheme

The track reconstruction in H1 starts with reconstruction of central tracks in the CJC. The CJC hits are very precisely defined in the drift direction (i.e. r - φ plane). In z -direction, along the wire, however, the hit position is based on charge division along resistive wires, based on the equation:

$$z = L \frac{Q^+ - C_k Q^-}{Q^- + C_k Q^+} + z_0 \quad (2.15)$$

where L is the length of the anode wire, Q_- is the charge measured on the $-z$ end of the wire, Q_+ is the charge measured on the $+z$ end of the wire, C_k is a wire dependent factor, and z_0 is the position of the reference point on the z -axis. Thus, the central tracks are reconstructed in the CJC, and later corrected for COZ and CST information. The central reconstruction in H1 consist of the following major steps (for details, refer to [71, 100]):

1. **CJC r - φ fit** - The track finding is first performed in r - φ , since the spatial resolution of CJC is about two orders of magnitude better than in z . Initially, short track elements, consisting of three hits, in a distance $n \pm 2$ (n is the wire index number) are searched in every jet cell. From those triplets initial values of κ and φ are estimated. After selection of proper triplets, a circle fit is performed, using the non-iterative algorithm of Karimäki [101] from which the track segment parameters κ , d_{ca} and φ are defined. Combining track segments in a chamber and later on combining the information for CJC1 and CJC2 gives the track parameters and rejects ghost tracks. Based on long tracks, the moment of the ep interaction - the event $T0$ - is determined. The energy loss dE/dx for a given track is calculated from the mean single-hit values, taking into account only hits which are far enough from other hits from other tracks, using

$$1/\sqrt{k_i} = 1/\sqrt{dE/dx}. \quad (2.16)$$

Using the likelihood method, the dE/dx can be calculated to better than 10 % [102].

2. **CJC s - z fit** - Based on the circle fit per track, and corresponding z information for each hit along it, a linear least-squares fit of

$$z_i = z_0 + s_i (dz/ds) \quad (2.17)$$

is performed, where z_i is the z coordinate calculated using equation (2.15), $s_i (dz/ds)$ is the track length at point z_i . From the slope (dz/ds) the polar angle can be calculated like

$$\theta = \arctan(1/(dz/ds)) \quad (2.18)$$

After defining all five parameters per track, final corrections are made.

3. **Vertex Fit** - This is an iterative procedure which includes finding a primary vertex point, refitting of tracks to it, rejecting the tracks not fitting and trying to fit them to a secondary vertex. The procedure starts with the approximation of the vertex z position by combining information from good, high energetic tracks. Taking into account the beam tilts and the vertex information from previous events, an initial value for the x, y position of the vertex is calculated. A primary vertex fit is performed in r - φ . The tracks not fitting the primary vertex are used for secondary vertices reconstruction. The same procedure is repeated in s - z , rejecting non-fitting tracks. A track can be also tagged as a cosmic track if a matching track (with the same track parameters) is found.
4. **Adding COZ information** - The COZ reconstruction takes as input the tracks from the CJC and the raw COZ detector information and updates the initial track z information using the “Method of deformable templates” [103, 104]. With the updated tracks, new, more precise z vertex is fitted, and the tracks’ parameters are changed accordingly.
5. **Adding CST information** - The CST hit pick-up procedure starts from CJC non-vertex fitted tracks, looks for corresponding COZ-improved tracks, and uses those if available. The refitting procedure is done in two steps, taking into account the geometry of the detector and its significantly different performance in r - φ and r - z directions. The first step is improving the tracks in r - φ , picking up p-side hits. A track, together with its corresponding error matrix is extrapolated to the CST

planes. Hits which fit to the given track are searched in a space window of $300\ \mu\text{m}$ around the intersection point of the track with the CST plane. If more than one hit is found, the one with best χ^2 is taken, and the track is refitted. The updated track is extrapolated to the second plane, where the same procedure repeats. The best r - φ resolution can be achieved with 4 hits in the CST, possible in the places where two ladders of each layer are overlapping. A primary vertex refitting is done, using the updated tracks, followed by a secondary vertex fit. The second step for the CST reconstruction is z track refitting. It is not applied, due to the worse S/N performance of the n-side of the CST, mentioned in Chapter 2.2.2. The danger to pick up noise hits and distort the parameters of the initial track and thus leading to worse or even wrong vertex reconstruction does not allow using CST for improving the z-precision of the central tracks and vertices.

6. **FTD tracks and combining with CT** - the Forward Tracker reconstruction combines the information from its chambers into clusters, which are fitted into forward tracks (for details see [105]). The tracks are extrapolated to the CJC, the closest matching track is taken and a refitting to a common track is performed.

Steps 1-3, 4 and 5 are performed by the fortran packages CJCRC, CTREC and CSTREC, respectively of the standard H1 reconstruction program H1REC [96]. The last step is performed by the forward tracking, which is completely isolated from the central track reconstruction chain.

The best tracking information available in H1 for each event is summarized in three BOS banks, namely DTRA for vertex-fitted tracks, DTNV for non-vertex fitted tracks and DVER for the vertices. In all of them the output information from both forward and central track reconstruction is collected. There are a few weak points in the data stored in those banks. First of all, there are short forward and backward CJC tracks, which have too little number of hits in order to sufficiently define their track parameters. Usually in the standard analysis these tracks are not used for exclusive reconstruction of hadronic final state objects. A second weakness is the bad resolution of the primary vertex z position (for details see Chapter 2.2.2). An additional weakness of the forward tracks is that they are measured 150 cm away from the interaction point, and their parameters at the primary vertex position are suffering from large extrapolation errors.

In all of these cases, the FST and the BST, which are described in the next Chapter, can significantly improve the performance of the H1 detector.

Chapter 3

The H1 Forward and Backward Silicon Trackers

Precise detection and determination of charged particles properties is of vital importance for physicists ever since the radiation was first discovered by Henri Becquerel in 1896. Both are possible by means of observing the results of the charge particle interaction with its surrounding matter. Increasing the demands from simple detection of ionizing radiation to precise determination of the properties of quarks and leptons forced the detection techniques and detectors to evolve from photographic plates and Geiger counters to advanced gaseous and semiconductor detectors. The development of the semiconductor detectors (often referred to as solid-state detectors) was initiated in the seventies by the prediction [106] and discovery [107] of the charm quark. The open charm hadrons have relatively long lifetimes $\tau \sim 10^{-12}$ s and thus decay lengths of $c\tau \sim 300 \mu\text{m}$, which means that a distinct secondary vertex could be observed. This is possible only by high position resolution, fast semiconductor detectors. A semiconductor detector has ten times lower ionization energy than a gas detector (3.63 eV for silicon vs. ≈ 30 eV for a gas chamber) yielding an increased energy resolution making them appropriate for photodetectors or scintillation calorimeters. It is thin ($100 - 300 \mu\text{m}$), has higher density, achieves spacial resolutions of $\sim 10 \mu\text{m}$ and time response of ~ 10 nsec. Thus in the last decades silicon detectors became a key element of all high energy collider experiments as the measuring device closest to the interaction point providing vital track and vertex resolution improvement. The tracking of the collider experiments at LHC is also based partially [108] and - for the first time - also fully [109] on silicon detectors. Ongoing discussions [110, 111] claim that the silicon detectors are *the* tracking detectors of the far future high energy physics experiments. The only disadvantage of the semiconductor detectors worth mentioning is that since they are crys-

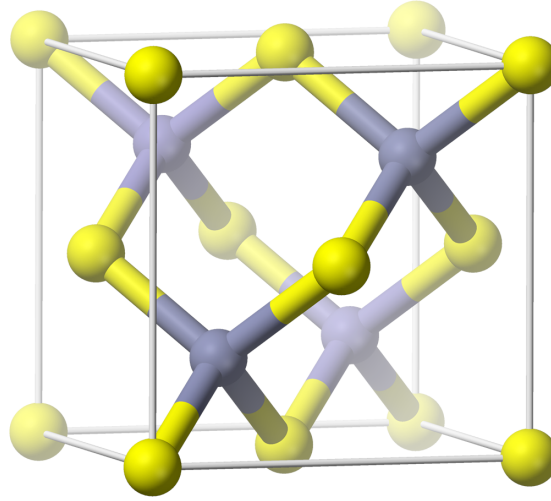


Figure 3.1: Diamond blende lattice.

talline materials, they are sensitive to radiation damage, which limits their long term use in high radiation environments.

In this chapter a comprehensive description of the Forward Silicon Tracker (FST) system and the Backward Silicon Tracker (BST) system is given. First shortly the silicon material and basic silicon detector functioning principles used in a tracking device will be discussed. An in-depth overview of the topic can be found in [112, 113]. Next, the mechanical properties and geometry of the Forward Silicon Tracker (FST) and the Backward Silicon Tracker (BST) at the H1 experiment are presented. Finally, the output detector data signals are traced from front-end electronics down to the final hit extraction, explaining the algorithms applied and electronics involved in each step.

3.1 Silicon Properties

Silicon (**Si**) is a tetravalent semiconductor metalloid with atomic number 14 in the periodic table of elements, part of group number 14 (carbon group). Despite being the second most spread chemical element on Earth, for semiconductor applications it is artificially grown due to the exceptionally high purity required. It is preferred as a semiconductor to germanium since it retains its semiconductor properties at higher temperatures and its native oxide is easily grown in oven producing the best possible interface with insulator. Moreover, the silicon production and processing technologies are

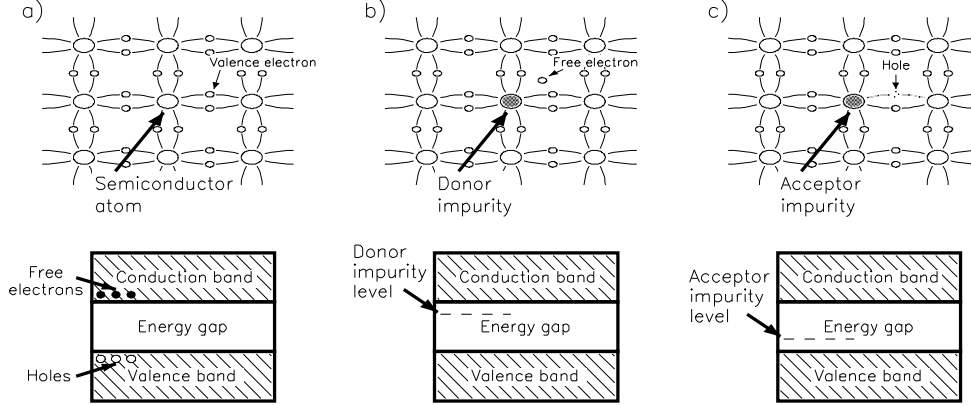


Figure 3.2: Corpuscular (up) and energy band (down) representation of the silicon crystalline lattice: a) Pure silicon at room temperature - the few free charge carriers available are depicted. b) Silicon doped with a pentavalent material, c) Silicon doped with an acceptor material. (Taken from [114], p. 24, Fig. 3.1)

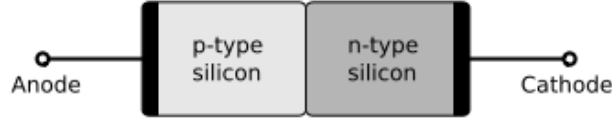
well developed and understood since silicon is since long time the main material used for integrated circuits and microchips mass-production. As all elements in the carbon group, it has four electrons in its outermost electron shell which readily form covalent bounds with neighboring atoms resulting in the case of a pure silicon crystal into a diamond blende lattice. Using the usual corpuscular description, at temperature 0° K the silicon lattice looks like the one shown on Fig. 3.1. In this state the semiconductor does not have free charges available for conduction and thus is an insulator. If one represents the different electron energy levels of the free atom as lines, in a crystal consisting of N atoms, the energy levels as a function of the lattice spacing split into multiple lines (because of the overlapping of the wave functions of electrons from different atoms) which in the case of $N \rightarrow \infty$ can be considered as bands depicted in Fig. 3.2. The energies of all electrons which are incorporated in the lattice via covalent bounds are represented by the valence band. The free electrons available for conductivity are represented by the conductivity band, and the minimum energy needed for an electron to escape from the lattice and join the free electrons is represented by the energy gap in Fig. 3.2. In the case of insulators, all electrons are in the valence band and the energy gap is around 6 eV. If an external electric field

is applied, due to lack of conductivity electrons and the large energy gap no current is observed. On the other hand, in case of conductors, the valence band and the conductivity bands are overlapping, thus the electrons can be easily excited into the conduction band, and when an external field is applied, an electrical current is observed. In the case of silicon a few electrons are in the conductivity band and the energy gap is 1.17 eV ([112]) which results in a weak conductivity. These few electrons are result of thermal vibrations.

At higher temperatures thermal vibration can break a covalent bond and thus release a free electron and leave a vacancy in the lattice. This vacancy is eventually filled by another electron which in turn frees a new vacancy. Following this pattern this vacancy is advancing through the lattice in a manner which can be described as a free positive charge particle referred to as a hole. In an absolutely pure semiconductor (referred to as *intrinsic*) the thermal excitation is the only reason for an electron-hole pair creation. In reality, no crystal is absolutely pure. In an impure semiconductor (referred to as *extrinsic*) the impurities are a cause for additional free charges in the semiconductor lattice which can limit or enhance the material properties. At room temperature the number of holes is always equal to the number of the electrons and they constantly recombine with each other which results in weak conductivity. To enhance the conductivity, a small amount of impurities ($\sim 10^{13}$ atoms/cm³ vs. $\sim 10^{22}$ atoms/cm³ for silicon) with different valence than the semiconductor one are added. They are usually incorporated in the lattice during the crystal growth or at a later stage by ion implantation while heating the crystal (referred to as *activation*).

If the material introduced has valence 5 (pentavalent, usually arsenic, phosphorus and antimony), it is referred to as *donor*. It has always one electron which does not participate in a covalent bond, thus it is readily available for conduction. All four valence electrons used in covalent bonds have energies in the valence band. The fifth electron has energy higher than the rest. The energy in the case of silicon is only ~ 0.05 eV lower than the minimum energy of the conductivity band. Since the concentration of donor atoms is 12 orders of magnitude less than the semiconductor atoms, the wave functions of electrons from separate atoms do not overlap and thus their energy level can be represented as a single additional line on the energy spectrum as on Fig. 3.2 b). The electrons on that level are easily excited to the conduction band which enhances the electron conductivity. Additionally they suppress the hole (positive) conductivity, since the free electrons recombine with the holes in the crystal. The semiconductors doped with donor atoms - meaning the one with minority carriers being electrons - are called *n-type* semiconductors.

If the dopant is trivalent (commonly used are gallium, boron and indium),

Figure 3.3: A silicon p - n junction scheme.

then it is called *acceptor*. Similarly to the previous case, the acceptor perturbs the band structure by creating an additional energy level in the energy gap ~ 0.05 eV above the valence band. The electrons easily couple on that level leaving behind free holes available for conduction. This type of semiconductor - doped with acceptor material and thus having holes as minority carriers - is referred to as *p-type* semiconductor.

Very often used are the so-called heavily doped semiconductors. These are semiconductors in which the concentration of doping material is $\sim 10^{22}$ atoms/cm³. They are highly conductive and widely used for electrical contacts for semiconductors. To distinguish them from the normally doped semiconductors, a heavily doped *p*-type semiconductor is labelled as p^+ and a heavily doped *n*-type semiconductor - as n^+ .

3.2 Detecting Particles with Silicon

Looking at a silicon from a single given type, it does not provide any special properties making it more interesting than the other materials. The properties which makes it the most used material in microelectronics are observed when two or more layers of different type of material including silicon are brought together. The simplest case consists of a *p*-type and an *n*-type silicon brought to a close contact as shown schematically on Fig. 3.3 and referred to as *p-n junction*. Such a close contact is produced by special technologies, like diffusion of one material onto the other in order to avoid third materials incorporation in the *p-n* junction. After creating the *p-n* junction, diffusion processes occur, trying to spread equally the electrons and holes over the whole structure to retain its thermodynamical equilibrium. Electrons start to float in the *p*-silicon, recombining with the holes. This captures them in the material lattice, building up negative charge in the initially neutral *p*-silicon. Similar processes start building positive charge in the contact zone of the *n*-silicon, out of recombining holes. The two charges create a potential difference of the order of 1 V known as *contact potential*. It is gradually rising with the newly coming charge carriers, but hindering diffusion up to a point where both effects come to equilibrium. The region in which the contact

potential is built is referred to as a *depletion zone*. Its width d as a function of the donor and acceptor concentrations N_D and N_A is given by [113]:

$$x_n = \left(\frac{2\varepsilon V_0}{eN_D(1 + N_D/N_A)} \right)^{1/2} \quad (3.1)$$

$$x_p = \left(\frac{2\varepsilon V_0}{eN_A(1 + N_A/N_D)} \right)^{1/2} \quad (3.2)$$

$$d = x_n + x_p = \left(\frac{2\varepsilon V_0}{e} \frac{N_A + N_D}{N_A N_D} \right)^{1/2}, \quad (3.3)$$

where x_n and x_p are the depletion zone width in the n -layer and in the p -layer, ε , e and V_0 are the dielectric constant of the material ($\varepsilon \approx 1$ pF/cm for silicon), the elementary charge and the contact potential, respectively. Usually in the silicon detectors an asymmetric structure is used, which in the H1 case consists of a highly doped p electrode and a lightly doped n region structure as schematically shown on Fig. 3.4. As following from (3.1) and (3.2), the depletion zone in this case is almost fully in the n bulk region and (3.3) transforms into:

$$d = \left(\frac{2\varepsilon V_0}{eN_D} \right)^{1/2} = (2\rho\mu\varepsilon V_0)^{1/2}, \quad (3.4)$$

where ρ is the specific resistivity of the semiconductor, μ is the charge carrier mobility ($\mu_e = 1350 \text{ cm}^2\text{V}^{-1}\text{s}^{-1}$ for electrons and $\mu_h = 450 \text{ cm}^2\text{V}^{-1}\text{s}^{-1}$ for holes), resulting for n -type and p -type materials correspondingly into:

$$d = 0.5[\mu m / \sqrt{\Omega cm \cdot V}] \times \sqrt{\rho V_0} \quad (3.5)$$

$$d = 0.3[\mu m / \sqrt{\Omega cm \cdot V}] \times \sqrt{\rho V_0} \quad (3.6)$$

The conductive p and n regions together with the free of mobile electrical charges depletion volume form a capacitor with capacitance

$$C = \varepsilon \frac{A}{d} \quad (3.7)$$

where A is the area of the depletion zone.

The fact that every newly created electron-hole pair in the depletion zone will be pulled out by the electric field is the main property of the p - n junction used to detect radiation. A minimum ionizing particle (mip) passing through the depletion zone will ionize the silicon by braking covalent bounds inside the lattice and freeing up about 22000 electron-hole pairs along a $300 \text{ }\mu\text{m}$ thick detector [5], which will be swept towards both ends of the p - n junction

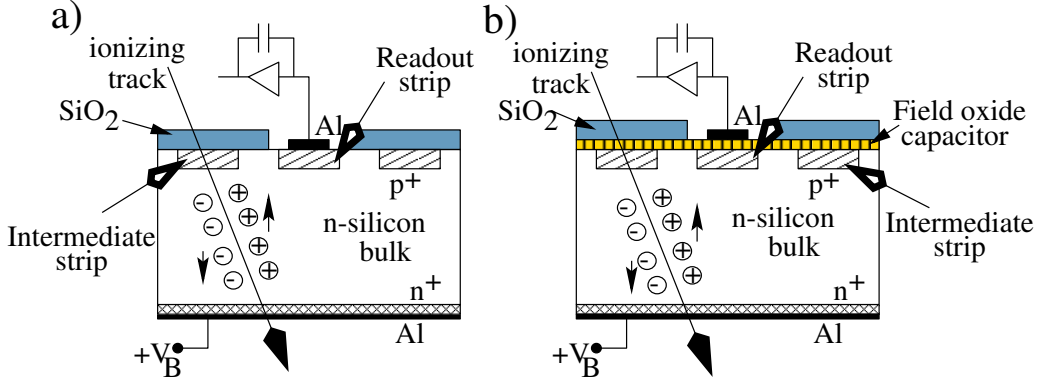


Figure 3.4: A silicon detector as a radiation detector. a) DC coupled readout, b) AC coupled readout.

withind ~ 10 nsec. The energy needed to produce an electron-hole pair is 3.67 eV. It is larger than the energy gap, since to preserve the momentum, additional energy is lost in phonon excitation. The charge induced as a function of time can be calculated as [113]:

$$Q(t) = Q_e(t) + Q_h(t) = \frac{e}{d} x_0 \left(\exp \frac{\sigma}{\varepsilon} t - \exp \frac{\mu_e}{\mu_h} t \right), \quad (3.8)$$

where σ is the silicon conductivity, x_0 in the coordinate of the point where the electron-hole pair was created (zero is at cathode) and $Q_e(t)$ and $Q_h(t)$ are the charges induced separately from electrons and holes. To collect the charge an ohmic contact with the ends of the p - n junction is needed. An ohmic contact is usually created using a layer of a highly doped semiconductor to contact the metal. Using directly normally doped silicon with metal would result in a Schottky barrier effect, which would obstruct the signal propagation.

In order to influence the depletion zone size an external voltage known as *bias voltage* is usually applied. If the p -side of a p - n junction is connected to the positive terminal of an electrical source, and the n -size to the negative one, the bias voltage is referred to as *forward bias voltage* and in the case of p -side connected to the negative terminal and n -side to the positive one - to as *reverse bias voltage*. In case of forward bias voltage, the electrons are pushed towards the holes and vice versa. The depletion zone shrinks with increasing voltage down to the point in which it disappears and the electrical current starts to flow freely through the p - n junction. The width of the depletion zone can be calculated from (3.4), if V_0 is to be replaced by $V_0 + V$, where V would be the bias voltage. If a reverse bias voltage is applied, the charge carriers are pulled out of the p - n junction, which increases the

depletion zone and additionally stops the free current flow through the p - n junction. The reverse bias voltage increases the sensitive volume available for radiation detection, decreases the capacitance of the junction, which decreases the input capacitance on the front-end charge-sensitive preamplifier, and thus decreases the noise level and speeds up the charge collection. The magnitude of the reverse voltage applied is limited only by the resistance of the semiconductor. At some point the junction will break down and become conducting. Thus, high-resistivity materials allowing maximum extension of the depletion zone are used and even higher-resistivity semiconductor materials are searched for. The charge pulse gathered on the strips can be read out either directly via a DC-coupled metal strip directly on top of the silicon strip or it can be used to induce charge on an AC-coupled one through an insulator metal strip as shown in Figs. 3.4 a) and b) respectively.

For the φ sensor design the latter was chosen, since the choice of the charge sensitive amplifier to which the aluminium strip is connected is dependent on the variations of its input capacitance. The capacitance in the AC case is dominated by the aluminium-fieldoxide-silicon capacitance which is only geometry dependent, while the capacitance in the DC case is given by the actual p - n -junction capacitance, which widely depends on the stability of the bias voltage. The bias voltage itself is experimentally defined for each sensor, which in the case of DC-coupling would mean designing a custom preamplifier for every single sensor.

3.3 Silicon Sensors

FST and BST were built from three types of wedge-shaped silicon sensors, namely φ sensors (Fig. 3.5, a)), r sensors (Fig. 3.5, b)) and pad sensors (Fig. 3.5, c)). Since the pad and r sensors are not used for this work they are only shortly mentioned. Further description of their properties, functional principles as well as physics aims and results can be found in [115, 116, 117] and [118, 119, 120, 121] correspondingly.

The φ sensor is made out of a six inch, 280 μm thick, high resistance (3-6 $\text{k}\Omega\text{cm}$) n -type silicon wafer (referred to as bulk silicon). On one of its surfaces, 1280 12.5 μm -wide parallel, equidistant strips made of heavily doped p^+ -type silicon are engraved by means of ion implantation. Thus, the active volume of the silicon detector is created. On the other surface of the bulk silicon, a common cathode for all bulk-strip p - n junctions is created by adding an additional layer of a heavily enriched n^+ silicon on the whole sensor through temperature diffusion and then covering it with an aluminium layer. In order to apply a depletion voltage to each strip, an individual negative

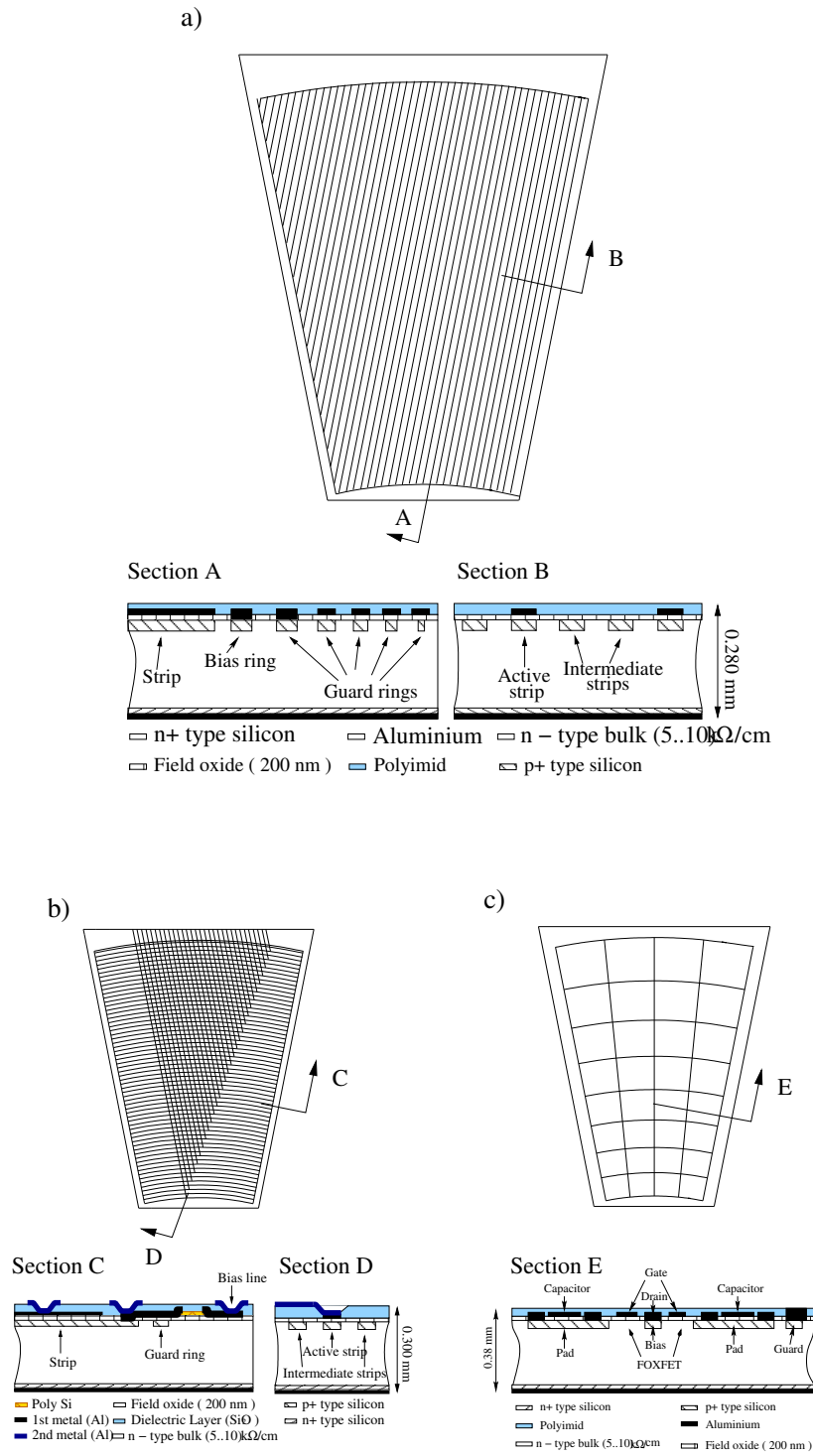


Figure 3.5: Silicon detector modules used for FST and BST: a) φ module, b) r module, c) pad module

voltage source should be applied to each single strip. This is realized by implementing a single additional p -silicon strip (referred to as *bias ring*) in immediate proximity of the far end of all strips. The bias ring on one hand provides a sink for all strip-bulk p - n junctions. On the other hand, it supplies each single strip with the bias voltage needed through the punch-through field-effect transistor (FET) formed by the strip p -silicon, the bulk n -silicon between the strip and the bias ring, and the p -silicon of the bias ring silicon itself, operating in punch off mode. In normal operation a bias voltage of 55-75 V depending on the properties of the particular sensor as shown in [122] is applied in order to stretch the depletion zone up to the full volume of the bulk region under the given strip. When the incident particle is nearly vertical, as in the BST and FST case, it releases a positive charge while passing through the depletion volume, which is typically collected on one or two strips. Through 200 nm of field oxide it induces a charge pulse into the AC-coupled aluminium strips, which leads the signal to the front-end electronics for further processing (discussed in more details in section 3.5). The capacitance of the overall structure is measured to be 10 - 15 pF/cm [122]. In order to get the signal properly registered and amplified and to avoid additional parasitic capacitance, the charge sensitive preamplifier should be situated as close as possible to the detector.

Finally, describing the φ sensors, it should be mentioned that measures are taken against the surface currents, resulting from the silicon atoms at the edge of the structure having uncoupled charge carriers. They are avoided by a group of additional p^+ strips parallel to the bias voltage ring and to the geometrical borders of the sensor, forming together with the bulk silicon series of a punch-through transistors starting from the bias ring and ending at the edge of the sensor, with the innermost strip connected to ground. The overall sensor strip structure is separated from the external environment by a layer of polyimide.

Every single sensor had to pass detailed tests and had to meet severe requirements to be approved for incorporation in the final silicon detector structure [122]. The sensor geometrical design, its motivation and parameters will be described in section 3.4.

If an ideal silicon detector is considered, the position resolution would be $\sim 1 \mu\text{m}$ - given by the size of the initial charge carriers born when the initial ionization particle crossed the depletion zone. During charge collection, the carriers acquire additional smearing from transverse thermal diffusion. It spreads the charge cloud transversely with an RMS width of [123]

$$\sigma_d \approx \sqrt{2 \frac{kT}{e} \frac{d^2}{V_b}}. \quad (3.9)$$

From equation (3.9), the best possible theoretical resolution for a particular silicon detector assuming no losses and independently of its architecture can be estimated. Knowing the geometrical parameters and the operating conditions of the φ sensor ($T \in (7 - 60)^\circ\text{C}$, $V \in (55 - 77) \text{ V}$) one can estimate it to be $7 - 9 \mu\text{m}$. In actual silicon detectors, the position resolution depends on the coordinate density of the information read out. The best two dimensional resolution would be acquired in a pixel detector, in which the charge pulse collected by every pixel is read out. In a strip detector only the coordinate perpendicular to the direction of the strip is measured. The best resolution in this case can be achieved by reading out every strip. If a particle passes through, the charge will be on one or two readout strips. Although there is a distance between the strips, they still manage to collect all charges, because the field remains constant almost up to the surface of the detector. If charge pulse height and charge division techniques are not considered, the position resolution is given by the distance between two strips. The minimum distance between two measurements (referred to as *detector pitch*) considering φ sensors is $p = 25 \mu\text{m}$. However, for tracks randomly aligned with respect to a given strip, the difference between the measured and the true position have a Gaussian distribution with standard deviation

$$\sigma_g^2 = \int_{-p/2}^{p/2} \frac{x^2}{p} dx = \frac{p^2}{12}, \quad (3.10)$$

which results in the considered case in a root mean square (RMS) purely geometrical resolution of $\sigma_g = 25 \mu\text{m}/\sqrt{12} \approx 7 \mu\text{m}$. In order to reduce the number of electronics channels while keeping the spatial resolution at acceptable level, the best technique is the use of a charge-division readout with intermediate strips [124]. Using this technique, in the φ sensors all strips are powered with bias voltage, but only every third one is read out, collecting part of the charge from the intermediate strips through the capacitive connection between neighboring strips formed by the strips themselves and the bulk silicon. Additionally, the intermediate strips maintain the uniformity of the electric field in the bulk region, thus improving the linearity of the charge division which leads to improved spatial resolution. Hence the actual readout pitch is $75 \mu\text{m}$ and the corresponding geometrical resolution is $\sigma_g = 75 \mu\text{m}/\sqrt{12} = 22 \mu\text{m}$. When using charge division, the thermal diffusion has actually a positive effect, since it spreads the charge between more strips, which always results in better position resolution than having the charge collected only on one readout strip. The final resolution is actually proportional only to the signal-to-noise (S/N) ratio: $\sigma \approx p/(S/N)$, [112]). This,

together with using charge weighting between adjacent strip according to the η method (Chapter 3.6.2) further improves the position resolution below the purely geometrical values.

3.4 Detector Geometry

In the initial H1 design [69, 70, 71] silicon detectors were not foreseen, but upgrades close to the beam pipe were envisaged by reserving limited space for further subdetector systems. In 1992 together with the CST (reviewed in short in Chapter 2.2.2) the first version of the BST was proposed [115] and in 1996 it was commissioned [125]. During the years the hardware configurations of FST and BST changed several times [2, 126, 127, 128, 129]. In Table 3.1 the major modifications, the year of the commissioning and the corresponding naming convention for different BST versions are shortly outlined. The FST was proposed in 1999 [2] and commissioned in 2001. Minor changes, shortly described in Table 3.2 were undertaken in 2005 [130]. All physics results and detector properties presented throughout this thesis are related to the 2006 geometry of both detectors.

Year	notion	Features
1996	BST1	4 r planes
1998	BST2	8 r planes, 2 sectors with φ modules
2001	BST3	6 double φ planes, 4 pad planes
2003		5 double and 1 single φ planes
		4 pad planes, radiation hard repeaters and subrepeaters
2005		6 double φ planes, 4 pad planes, radiation hard APC

Table 3.1: BST detector versions

Year	Features
2001	5 double φ planes, 2 r planes
2005	5 double φ planes, radiation hard front-end electronics

Table 3.2: FST detector versions

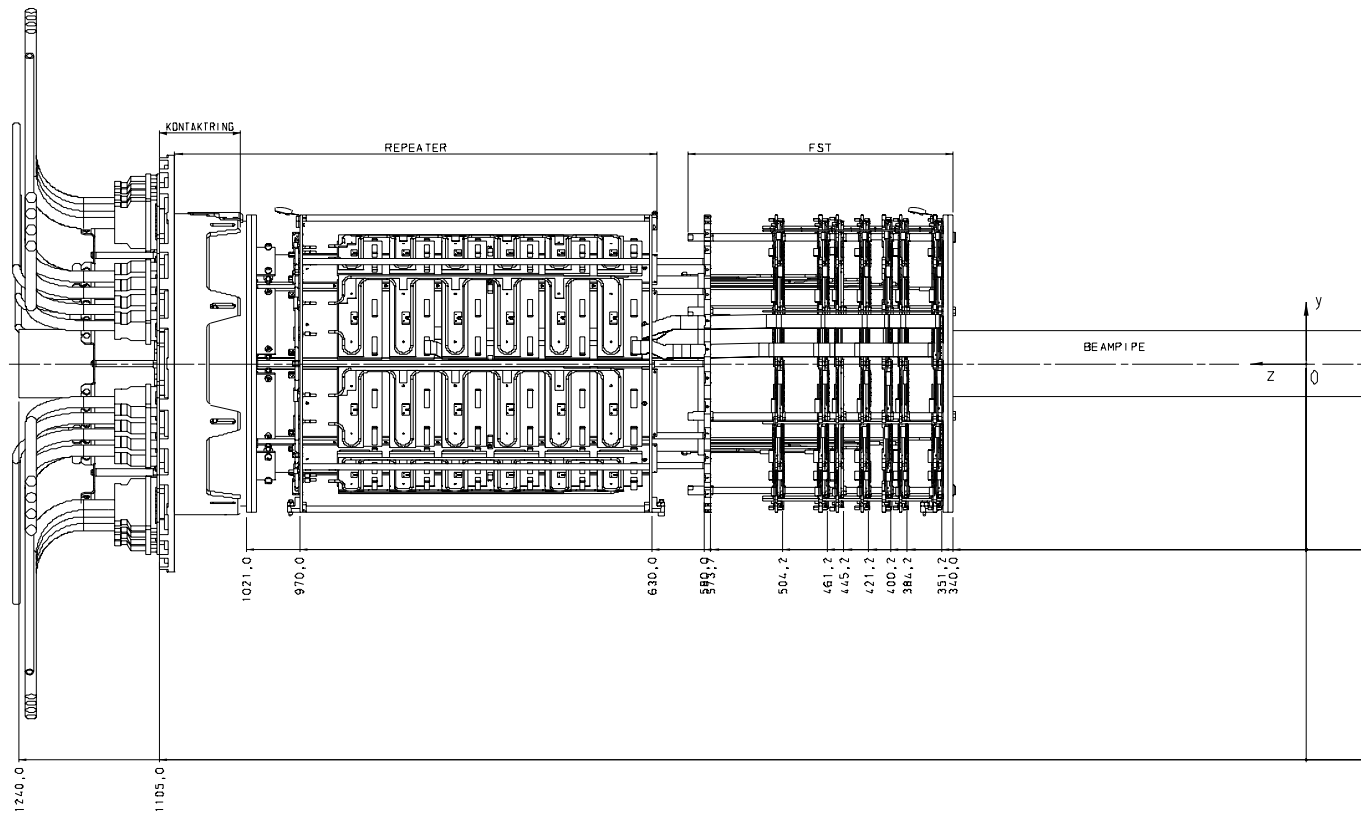


Figure 3.6: The Forward Silicon Tracker (FST). The silicon planes are facing the interaction point situated on the righthand side of the figure. The readout electronics, cables and cooling pipes are situated behind the silicon planes, pointing in the forward direction.

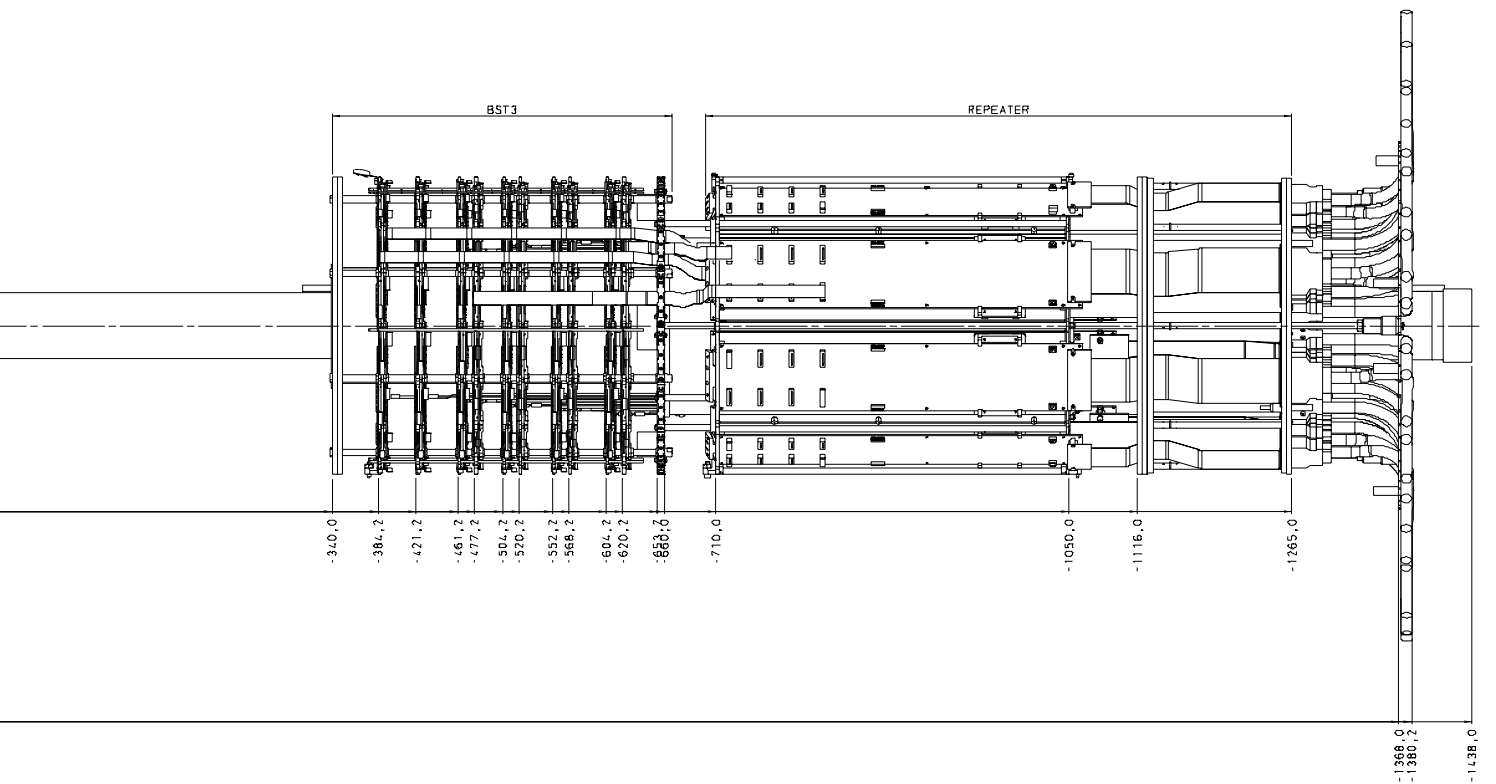


Figure 3.7: The Backward Silicon Tracker (BST). The silicon planes are facing the interaction point situated on the lefthand side of the figure. The readout electronics, cables and cooling pipes are situated behind the silicon planes, pointing in the backward direction.

The external geometrical dimensions of both devices, as well as the detector qualities depending on detector size are restricted by the positions of the adjacent H1 subdetector systems as visible from Fig. 3.6 and 3.7. Both FST and BST are cylindrical bodies with outer radius limited by the inner radius of the CIP, an inner radius limited by the beampipe and a length limited - on the vertex side - by the CST dimensions, in the opposite direction by the FTD and CIP edges and the SpaCal, respectively. Additional volume along the whole length of both detectors should be left free of detector components to house the beampipe. Maximizing the track efficiency and acceptance of both detectors requires an optimal number of coordinate measurements situated as close as possible to the nominal interaction point. The steering and readout of the silicon detectors requires a significant amount of electronics as close as possible to the active volume, without introducing too much additional dead material. The solution is a front-end integrated circuit (IC) directly glued to the sensor (referred to as *hybrid*) leaving the main electronics behind the active zone. Both parts of the electronics need cooling and a low humidity environment for proper operation. The cooling is realized by two separate systems of water tubes placed in immediate vicinity to the power dissipating part of the electronics - one for the hybrid and one for the repeater electronics. The humidity is vented out by constantly introducing nitrogen into the detector volume, thus preventing water condensation. Details on the cooling system can be found in [114].

The active part of FST (BST) consists of 7 (10) carbon-fiber wheels. In FST (BST) 5 (6) of them are occupied by double planes of φ sensors. The rest of the wheels in FST were left unoccupied after 2005, when the r sensors were removed. For the BST four wheels are occupied with pad-sensors, forming the BST pad trigger system described in detail elsewhere [120]. The numbering of the disks always starts from the interaction point with zero. As an example in Fig. 3.8 an FST φ disk is presented. The nominal geometrical parameters of FST and BST are summarized in Table 3.3. The frame of each wheel is made out of carbon-fiber composite (CFK) material. On the frame, 12 aluminium pads are embedded such that they are soldered directly to the copper tubes of the cooling system and provide cooling as well as a precise enough mounting plane for the 12 hybrids on each side of the frame. The hybrids are mounted with two screws (visible on Fig. 3.8). The left one fits precisely into its hole into the hybrid and thus allows only rotations around its axis, while the right one allows additional small translations in $(r-\varphi)$ plane. Onto each hybrid a silicon sensor is glued. Both together form a *silicon module*. One quarter of each disk is not occupied by sensors on order to leave empty space for the elliptical beam pipe. Populating this quarter would mean designing custom sensor modules, which would significantly increase the production

No.	Parameter	units	FST	BST
1.	U/V disks		5	6
2.	U disk 1, nominal z position	cm	35.19	-39.15
3.	U disk 2, nominal z position	cm	38.49	-42.85
4.	U disk 3, nominal z position	cm	42.19	-46.85
5.	U disk 4, nominal z position	cm	46.19	-51.15
6.	U disk 5, nominal z position	cm	50.49	-55.95
7.	U disk 6, nominal z position	cm	-	-61.15
8.	number of sectors per disk		12	12
9.	number of strips per module		640	640
10.	minimal sensitive radius	cm	5.877	5.900
11.	maximal sensitive radius	cm	11.966	12.044
12.	U modules pitch	cm	0.0075	0.0075
13.	U modules Silicon thickness	cm	0.030	0.030
14.	Approximate φ modules active zone overlap	deg	1.277	1.277
15.	φ modules active zone overlap	cm	0.18	0.18
16.	z offset between U and V planes	cm	0.81	0.842
17.	Stagger between odd and even sectors	cm	-0.18	0.18
18.	Offset of the first strip from $\rho = 0$	mm	-4.62	-4.62
19.	number of pad disks		0	4
20.	Pad plane offset from U plane	cm	-	-0.694
21.	Pad modules Silicon thickness	cm	-	0.040
22.	Pads per pad module		-	32

Table 3.3: FST and BST nominal geometry parameters as taken from the FGAS and BGAS data base banks and used in this thesis. All geometry related values are relative. The precise values are retrieved only after applying the correct alignment parameters.

expenses for both FST and BST. If a module is mounted facing (back to) the nominal vertex position it is referred to as a *u-module* (*v-module*). The nominal z-distance between both is 9.1 mm. The conventional numbering of the modules within a plane, goes from 0 to 11 sectors counted from the positive x -axis anti-clockwise.

Every hybrid is glued to the sensor ensuring the mechanical rigidity of the silicon module. The sensor active zone has an inner radius of 58.7 mm and an outer radius of 119.7 mm. The two azimuthal borders of the active zone form a 22.5° angle. When the sensor is positioned on the wheel, the vertex of this angle is shifted from the nominal x - y position in opposite direction to the position of the detector. This geometry solution ensures an overlap of 1.8 mm in the r - φ plane between the active zones of each two neighbouring sensors. To achieve that all odd-numbered sensors are positioned with a stagger of 1.8 mm behind the even-numbered sensors. All strips in the φ sensors are parallel to the right side border of the active zone. Thus, only approximately half of the strips have the same length (see Fig. 3.13). The strip length in the other half of the cases is limited by the left border of the active zone, thus linearly falling with the distance to the right border of the active zone. The actual geometrical borders of the sensor are 1.5 mm away from the sensor active zone borders.

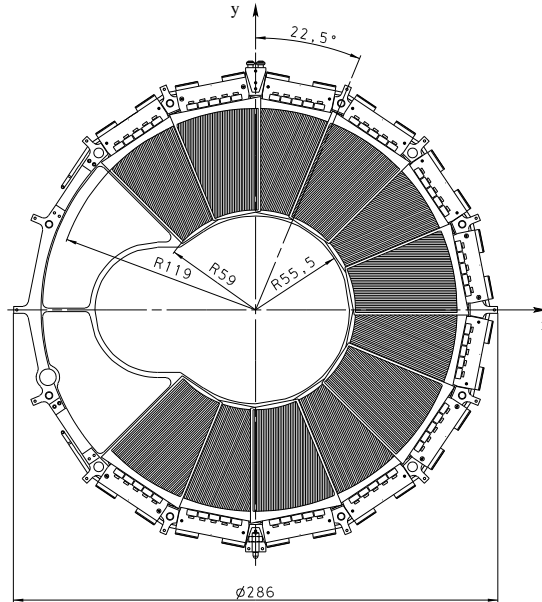


Figure 3.8: FST detector disk as mounted in the H1 experiment.

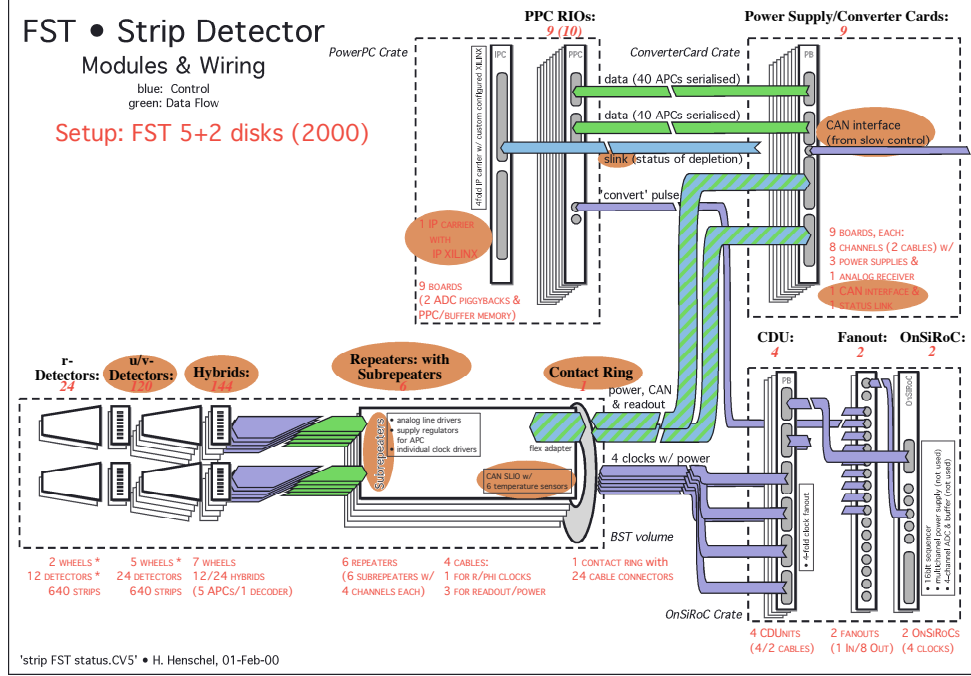


Figure 3.9: FST Data and control signal flow as in 2000. The main change in 2005 was removing of the r-detectors.

3.5 Data Acquisition

The data acquisition of both BST and FST are very similar. As an example, the data FST acquisition chain is sketched in Fig. 3.9. In the following section, the road of the information from the charge generated on the sensor strip to the filling of the data in raw data banks is followed. In short also the service voltage supplies and clocking signals are considered. A more detailed description can be found in [131], and more recently in [114].

The hybrid (Fig. 3.10) is in fact a printed circuit board (PCB), on which the ICs needed for bias voltage supply and analog data amplification, shaping and transmission are placed. On the PCB five analog readout APC128 chips [81] and one decoder chip [132] are glued and bonded. Both are radiation hard and produced using a special geometry deep submicron technology. As input to each APC128 chip 128 sensor strips are connected. Every strip ends with a small aluminium pad. The 640 pads are grouped in five groups, each group connected to a separate APC128 chip. The connections between the APC128 pins on the hybrid and the aluminium pads on the sensor are real-

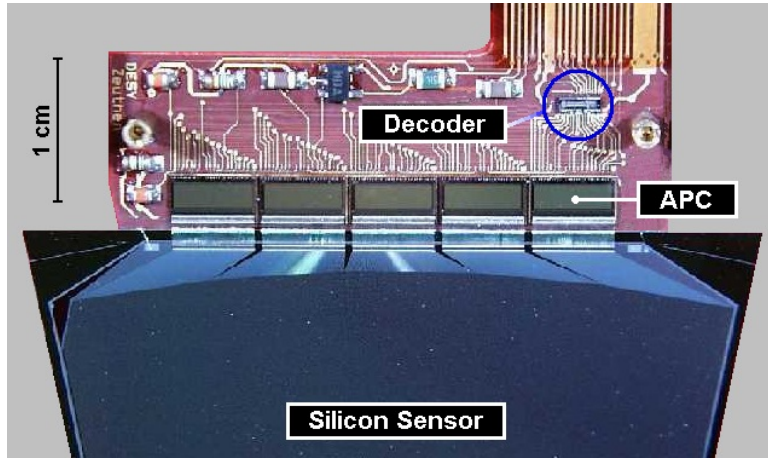


Figure 3.10: Hybrid

ized via about 2 mm long bonds. Similarly, the bias ring and the guard ring are connected via larger contact pads and bonds to the hybrid. The functionality of a APC128 chip is driven by the decoder chip, which on the other hand is externally driven by 4 digital clock signals. The APC128 is collecting in parallel the charge from every strip, amplifying it with a charge-sensitive preamplifier and storing it in a capacitor. This is done with the HERA clock frequency of 10.4 MHz with which the e-p collisions in H1 happen. When an L1 positive trigger decision is taken, the decoder stops the data taking and reads out sequentially the information from all strips, starting from the shortest one, and sends the information out for further processing. The hybrid communicates to the repeaters via a flexible capton stripline. Six repeaters as the one shown in Fig. 3.11) are mounted on an aluminium frame. On each repeater six subrepeaters are attached. On each subrepeater the striplines from the u and v modules from two neighboring sectors are connected. The subrepeaters receive sequentially the data from the two neighboring modules from the same type (u or v), forming from the 1280 strip signals one analog data channel. The data in the two channels handled by a given subrepeater is amplified and sent out through the repeater for further processing. The subrepeater takes care also of the power supply of the four modules. It supplies up to 100 V bias voltage for the p-n junction depletion, as well as the voltage and current needed to secure the proper decoder and APC128 operation: 5 V and 2.5 V digital voltage and analog current in the range 90-120 mA. Additionally, the subrepeater shapes the clock signals needed by the decoder chip to steer the APC128 operation. The clock signals needed for six subrepeaters servicing two neighboring sectors are shaped, amplified, properly

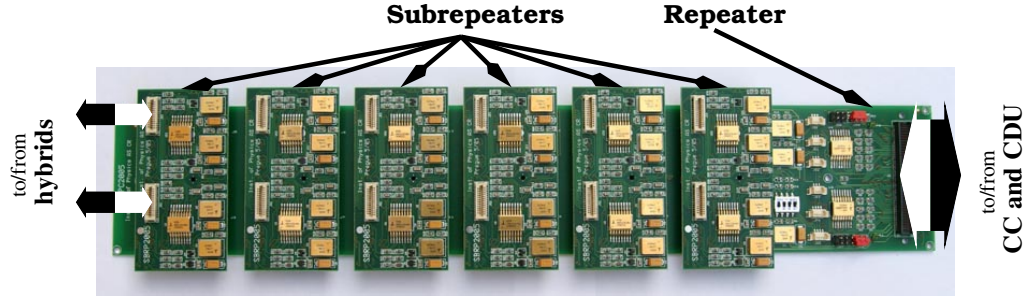


Figure 3.11: Repeater board with all subrepeater modules attached

transformed and distributed to each of them by their corresponding repeater. Additionally the repeater helps to diagnose the humidity and temperature in the detector by housing the Serial Linked I/O (SLIO) chip which provides the interface to the corresponding sensors. The main function of the repeater is to collect the information from all subrepeaters and to handle it to the exit of the detector where all signals are connected to terminals.

The overall detector is covered by a thin copper foil to protect it from interference with external electromagnetic noise sources. The terminals are mounted on an aluminium disk referred to as contact ring. In the case of FST the contact ring consist of two parts. One is fixed to the edge of the CIP and the other is fixed to the repeater aluminium frame. In operational condition the second part is fixed on the first one by screwing. Since the service cables for the FST come between CJC and FTD and no direct access from the forward part of H1 is available, the FST is installed from the backside. Taking this into account, this innovative contact ring design is the best technical solution to precisely fix the detector. For the BST no special treatment is needed, since it is directly accessible after removing the SpaCal.

From the contact ring two types of copper cables transfer all signals over some 30 meters away into the electronics trailer where the hit finding and the generation of the clock signals depending on the H1 trigger system takes place. The trailer electronics is depicted in Fig. 3.12. The first type of cables connects the repeater to the so-called Converter Card (CC). The second type supplies the detector with the clock signals from the Clock Distribution Unit (CDU). The CDU is a passive module, the main function of which is multiplication of one input clock signal into four output clock signals. It allows time delaying of the output signals with respect to the input signal as well as adding of capacitances compensating for the capacitance of the cable attached to the corresponding output. Usually three or more CDU serially connected modules (as schematically shown on Fig. 3.12) are needed

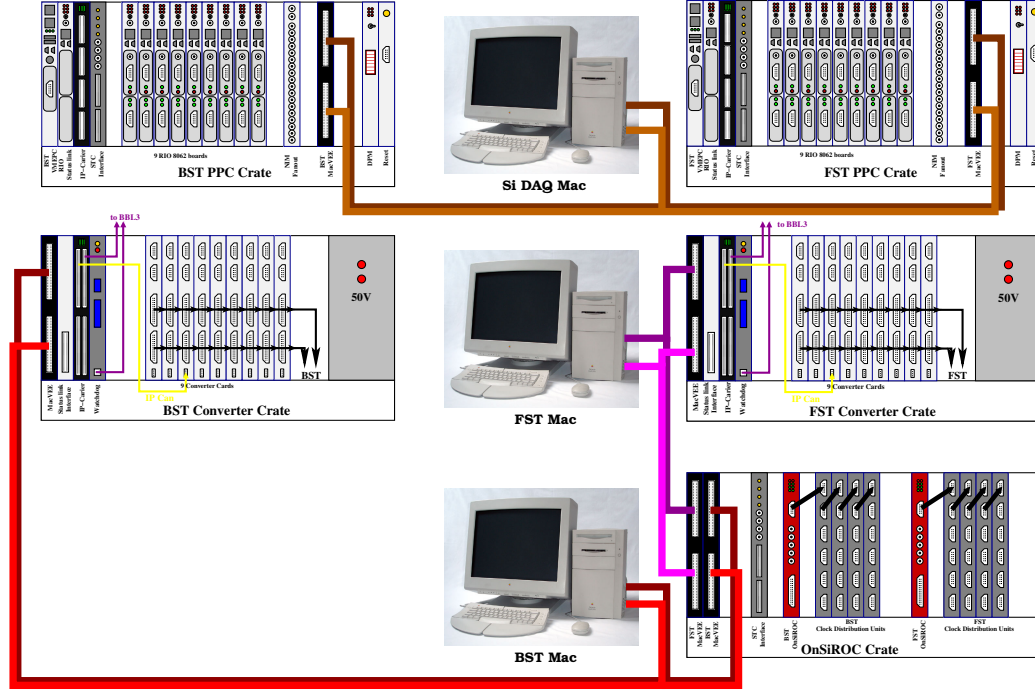


Figure 3.12: BST and FST trailer electronics chain.

to supply clock signals for data channels. The input clock signal for the CDUs is produced by a VMEbus module referred to as OnSiRoC. The OnSiRoC [133, 134] is a module developed for the H1 silicon data acquisition chain. It can digitize analog data, perform hit finding and generate the clock signals needed by the decoder chips in precise synchronization with the H1 trigger system. In the FST and BST data acquisition only the last property of the OnSiRoC is used. The clock sequence code (known as *sequencer code*) is generated externally using an especially developed high-level programming compiler [134], and then downloaded and executed on the OnSiRoC.

The data coming from both detectors comes via dedicated cables on the input of the converter cards. A converter card is a custom VMEbus [135] module which can handle the communication with 8 analog data signals (16 hybrids) over two 50-pin cables. It supplies from the VMEbus all the voltages needed by the hybrids connected to it. The bias voltage in the range 0 - 128 V is supplied with a step of 0.5 V from additional custom 50 V bus attached on the backplane in parallel to the standard VMEbus. The CC can also amplify the data signals from the hybrids to match the requirements of further processing. The data from the CC is fed via a pair of 20-pin custom designed cables to a PCI Mezzanine Card (PMC) embedded into a CES RIO

8062 VMEbus card [136]. The PMC board takes the analog signal and on an external NIM signal issued by the OnSiRoC it converts every strip signal amplitude to a 12 bit amplitude and in synchronization with the H1 trigger it hands it to the RIO 8062. There, the hit finding procedure described in Chapter 3.6.1 runs. The hit data packed into the SIFE (Silicon Front-End data) BOS bank is transferred via the VME bus to the corresponding VMEPC. The VMEPC is a VMEbus based personal computer (PC) running Linux Operating System (OS) and equipped with a fast Ethernet port. The data, packed in SIFE banks with different numbers from all silicon detectors are collected from their corresponding VMEPC by an industrial PC (referred to as *silicon event builder* or *silicon master*) via TCP/IP over Ethernet. The silicon master combines the data from all silicon detectors and sends it to the central H1 data acquisition system. Further on the H1 raw data from the event is processed using the H1REC package and the first version of the DST (referred to as DST1) is produced and stored for further physics analysis.

All modules described so far are housed in VMEbus crates, depicted in Fig. 3.12. The overall steering and monitoring of the system is required to be easily steerable for non-experts like the shift crew, with a user friendly interface. It is placed in the central H1 control room some 100 m away from the electronics trailer. Additionally, an expert should be able to fully access the system remotely via TCP/IP and internet in case it is needed. Taking into account that the system development was started in the beginning of the nineties, the only solution meeting this requirements was the one shown in Fig. 3.12. The steering is done via 3 Macintosh Quadra 800 computers. On two of them (FST Mac and BST Mac) a user-friendly LabView steering program dedicated to the corresponding detector is running. On each Macintosh a NuBus Micron interface card to a MacVEE bus [137, 138, 139] is attached. On each of the crates considered, a corresponding MacVEE VMEbus module is attached. This module allows instructions issued by the Macintosh and transferred via the MacVEE to control the modules attached to the given VMEbus. Moreover, all Macintoshes, and thus full control over FST and BST are available for experts via internet using the Timbuktu application [140].

3.6 Silicon Stand-alone Track and Vertex Reconstruction

The FST and BST data reconstruction is divided into two steps. The first step is performed only once during the H1 data taking and is referred to

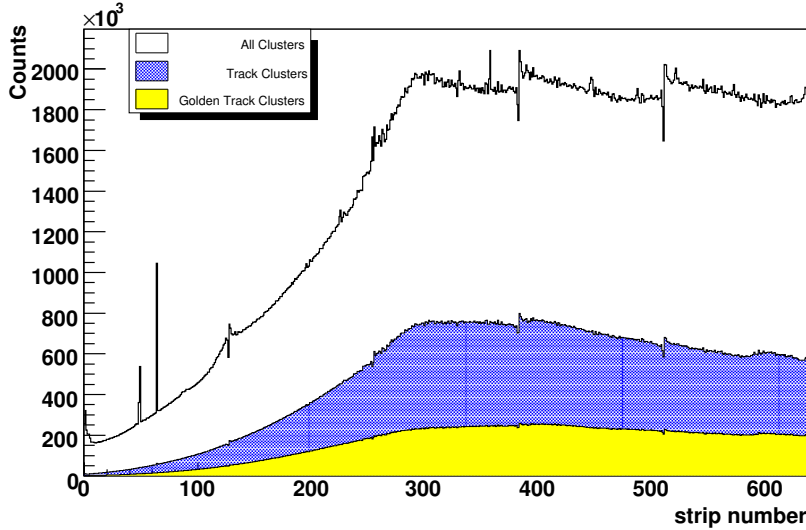


Figure 3.13: The digitized amplitudes from one silicon module. The distribution is divided to 5 parts indicating the different noise properties of the corresponding APCs. Its shapes reflects the lengths of the strips.

as on-line hit finding. The hit finding is an algorithm implemented in the C programming language and executed on the RIO 8062 boards during H1 data taking. The hit finding routine takes as input the digitized strip pulses from the PMC boards (shown on Fig. 3.13) and distinguishes the pulses coming from particles passing through the detector volume (referred to as *signals* or *hits*) from the pulses induced by various noise sources using the methods described in Chapter 3.6.1. After finding the hits, the routine writes out all the relevant hit information into a BOS bank (SIFE) ensuring its structure and integrity. All amplitudes being rejected as potential hits at this level are lost. This reduces the amount of data to a level which the H1 data acquisition can cope, without losing signal information and without adding dead time to the data taking process.

The second step is track and vertex finding. It is done by the C++ reconstruction package H1BSTREC (referred to as FBST reconstruction). It is a part of the official H1 reconstruction package H1REC [96]. The package utilizes a Kalman filter to reconstruct tracks and vertices based only on silicon strip data - an unique procedure in past high energy experiments.

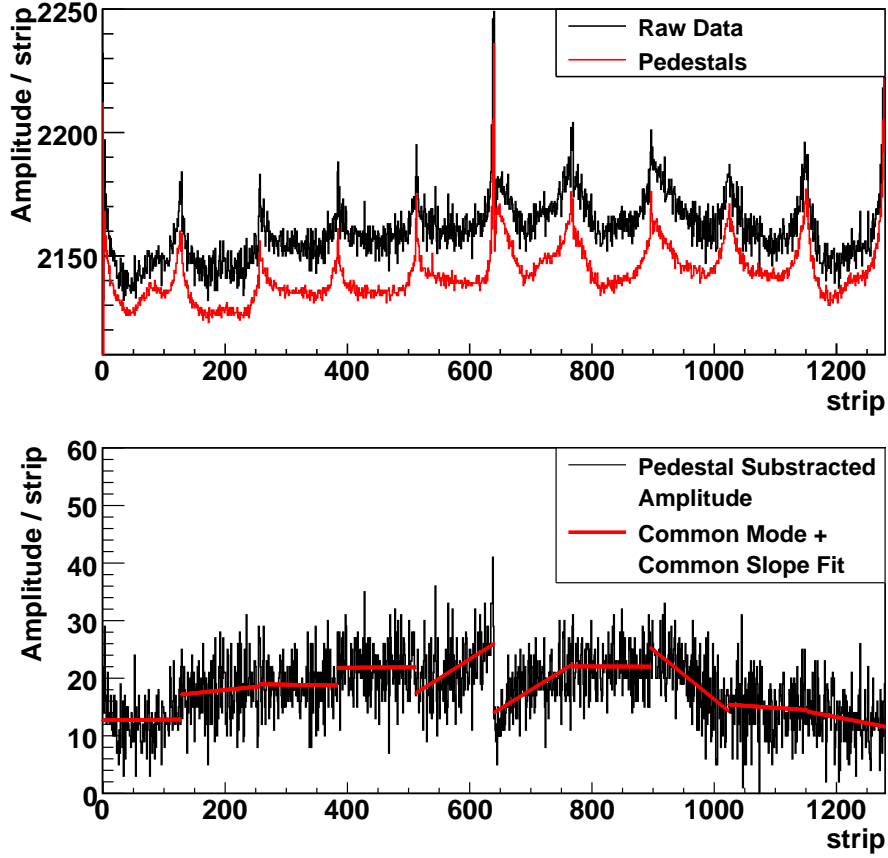


Figure 3.14: Example for a single data channel (1280 strips) main background contributions, depicted in red a) - pedestal on top of the initial ADC digitized amplitudes, b) - the common mode and common slope fits based on the pedestal subtracted amplitudes (depicted in black).

3.6.1 Hit Finding

The main task of the hit finding procedure is to use statistical methods to distinguish a particle induced signal by subtracting from the digitized raw data amplitudes the noise pulses originating from different sources. There are several noise components treated during the hit finding, namely:

- **Pedestal** - by far the largest contribution to the noise in the raw data. A sample pedestal distribution is shown as a red histogram on Fig. 3.14, a). The pedestal (P) accounts for the leakage current of every single strip as well as for the differences in the pipeline capacitances on the APC. Since there are 32 pipeline capacitors per APC input channel, the number of pedestal values needed per data channel is $1280 \times 32 = 40960$.

The magnitudes of the pedestals depend on different factors. Some of the factors are constant - like for example the relative geometrical position of the strip in the hybrid. Others are slowly changing during the data taking - like for example the temperature of the APCs and the sensors. This requires a constant update of the pedestals with time.

- **Common Mode and Common Slope** - a small noise contribution in comparison to the pedestal, but still comparable to the signal searched for. The Common Mode (CM) and the Common Slope (CS) in fact are the parameters in a linear function $f(i) = CM + CS * i$ fitted on the pedestal-subtracted APC amplitude spectra (see Fig. 3.14, b) and describing the noise contribution as a linear function of the number of the strip i in any given APC. The CM and the CS are actually accounting for short-termed fine fluctuations in the sensor depletion voltage and the supply voltage of the APC preamplifiers which lead to a common baseline shift per APC, which is nicely described by a straight line fit. To account for the CM and the CS, ten linear fits (one per APC) per event per data channel should be performed, ten values per CM and CS should be calculated and the value of $f(i)$ for every strip should be calculated and subtracted from the pedestal-subtracted amplitude.
- **Noise** - After subtracting the pedestal, the common mode and the common slope from the raw data in a strip without a hit, the only component left is a random electronic background noise mostly introduced by the charge-sensitive preamplifier on the APC128 chip. The standard deviation of this background distribution is referred to as *noise* (N).

Hit Identification

A proper hit identification in a given event is possible only if pedestals and noise are properly calculated. Their initialization and update procedure is described in the next subsection. For the moment we assume that the pedestals and noise are known from the previous events. Following the above, the magnitude of a possible signal hit amplitude S_i in a given event, using a pedestal P_{ip} for pipeline capacitor p at a strip i and a common mode CM_a and a common slope CS_a from APC128 chip number a can be represented as a function of all noise contributions and the initial ADC digitized amplitude a_i as:

$$S_i = A_i - P_{ip} - (CM_a + i \times CS_a). \quad (3.11)$$

To find the hits using equation (3.11) in a given event the CM and CS should be found. First a linear function is fitted per each ADC using all pedestal-

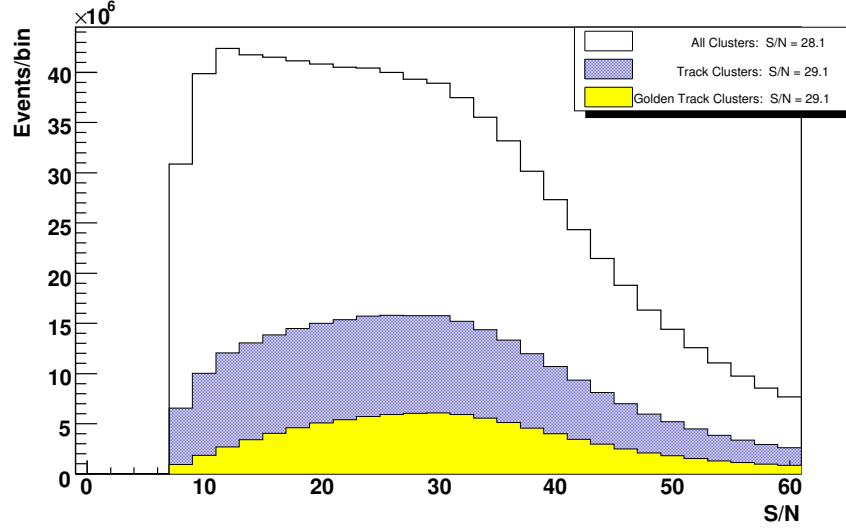


Figure 3.15: S/N distribution for all hits, hits used in reconstructed tracks, and hits used in the longest reconstructed tracks.

subtracted amplitudes, and then a signal is searched using equation (3.11)

and meeting the conditions:

$$\begin{aligned} S_i &> 0 \\ S_i^2 &> N^2 \times C, \end{aligned}$$

(3.12) where C is a confidence constant. If a signal on a given strip meets the

requirements (3.12), the signal, together with the corresponding noise and strip position information is packed and written out as a hit, and the corresponding strip is marked and not further considered in the event at hand. Next, once more CM and CS are fitted, but this time not considering the marked hits. This avoids the influence of the hits on the common mode and common mode calculation. Once more hits satisfying (3.12) are searched for and written out in BOS bank (SIFE). The signal-to-noise ratio distribution for all hits, hits used in tracks, and hits used in the longest possible tracks are presented in Fig. 3.15

Recursive Pedestal and Noise Calculation

The update of the noise and the pedestal for each event is done after the hit finding. The pedestal P_{ipj} and noise N_{ipj} calculated for a strip i , after

the current given event j with pipeline counter p is given by the recursive formula:

$$P_{ipj} = (w - 1) P_{ip(j-1)} + p_{ip} \quad (3.13)$$

$$N_{ipj}^2 = (w - 1) N_{ip(j-1)}^2 + n_{ip}^2 \quad (3.14)$$

where $P_{ip(j-1)}$ and $N_{ip(j-1)}$ are the corresponding values after the last event, and p_{ip} and n_{ip} are calculated from the current event, using only non-hit strips from APC128 number a according to:

$$p_{ip} = A_i - (CM_a + i \times CS_a) \quad (3.15)$$

$$n_{ip} = A_i - (CM_a + i \times CS_a) - p_{ip}. \quad (3.16)$$

The w in equations (3.13) and (3.14) stands for the weight of the average pedestal and noise in previous events with respect to the values calculated from the current event. In the usual data taking the value of w is 64. After a reset at least 64 events per given PIC for a pedestal and 64 events for noise determination are needed. During that time the weight w is changing dynamically from 2 up to 64. This implies a reliable hit finding available only after at least $(32 + 32) \times 64 = 4096$ events. On the other hand this ensures a dynamic determination of the pedestal and noise within a few minutes from scratch and without any a priori knowledge.

3.6.2 Track and Vertex Fit

The FST and the BST reconstructions form a common software package written in C++ named h1bfstrec. It is part of the H1 detector reconstruction software H1REC. The package contains a modular implementation of a C++ to BOS bank interface, a Kalman filter [141] and a fast 2D selection algorithm. Both reconstructions are essentially the same, and based only on FST (BST) information. The reconstruction works in two modes. In MC mode, it uses as input data the detector digitizations produced by a GEANT 3.15 [52] based H1 detector simulation module (H1SIM), which is followed by the digitization module H1DIGI. In data mode, either the raw amplitude information from the SIFE bank or the packed digitized information from FRSE/BRSE banks is used. The corresponding BOS bank descriptions can be found in Table 3.4. The reconstruction proceeds in the following steps:

1. Determination of the hit position.
2. 2D track reconstruction and filtering.
3. 3D non-vertex track finding.

FST	BST	Description	MC	Data
SIFE	SIFE	Raw data from the Silicon branch in H1	no	yes
FGAS	BGAS	Detector nominal geometry parameters	yes	yes
FSTC	BSTC	Detector modules alignment	no	yes
CGDF	CGDB	Dead material description	yes	no
FSTM	BSTM	Mapping of FST detectors to PowerPC	no	yes
FETA	BETA	η distribution	no	yes
FASY	BASY	Internal bank used for asymmetry calibration	no	yes
FSTR	BSTR	Reconstruction setting parameters	yes	yes
GTR	GTR	Generated particle four-vectors	yes	no
STR	STR	Simulated particle four-vectors	yes	no
FSUT	BSUT	U detectors simulated space hits	yes	no
FSVT	BSVT	V detectors simulated space hits	yes	no
FDSS	BDSS	Digitization parameters	yes	no
FSUX	BSUX	Pointers from FRSE (BRSE) to FSUT (BSUT)	yes	no
FSVX	BSVX	Pointers from FRSE (BRSE) to FSVT (BSVT)	yes	no
FJKY	BJKY	Pointers from FJKR (BJKR) to STR	yes	no
FRSE	BRSE	Packed hit information	yes	yes
FRXT	BRXT	Reconstructed 3D hits	yes	yes
FSPX	BSPX	Pointers from FJKR (BJKR) to FRSE (BRSE)	yes	yes
FJKR	BJKR	Reconstructed non-vertex fitted tracks	yes	yes
FJKX	BJKX	Tracks, fitted to x,y of run vertex	yes	yes
FJKT	BJKT	Reconstructed vertex fitted tracks	yes	yes
FJKV	BJKV	Reconstructed vertex	yes	yes

Table 3.4: Summary of the BOS banks relevant to FST and BST reconstruction.

4. Vertex finding.
5. Refitting the tracks to the vertex.

Hit position determination

To compute the precise impact point position of the particle through the detector, first the neighbouring hits strips are combined into *clusters*. For almost vertical incident tracks, the projection of the incident particle track along the coordinate measured by the strips in the active material is smaller than the readout pitch [142], and the charge is spread almost linearly over two strips. Hence, the clusters are limited to one- and two-strip clusters. If

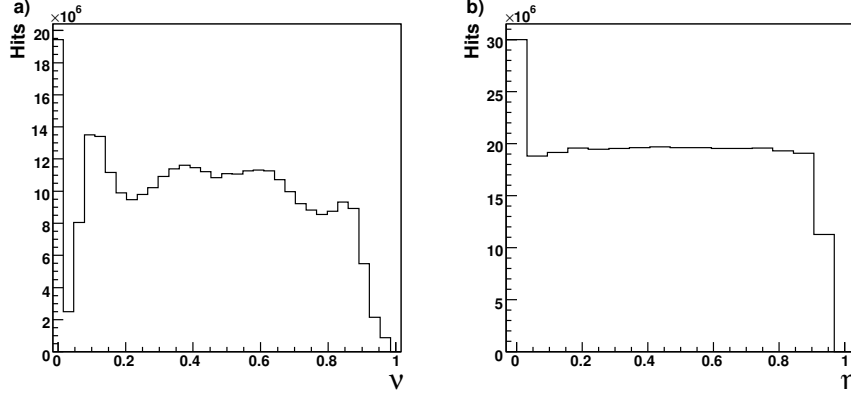


Figure 3.16: Distribution of the asymmetry a) Before correction b) After correction.

more strips are involved, the two strips with largest pulse height are taken into account. Remaining nonlinearities are compensated for using the so called η algorithm [143, 144]. This algorithm is based on the asymmetry η defined as:

$$\eta = \frac{R}{R + L}, \quad (3.17)$$

where R (L) are the charge pulse heights of the right (left) strips. The position correction of the impact position $d\xi$ with respect to the nearest strip can be calculated [145]:

$$d\xi = P \frac{\int_0^{\eta_0} \frac{dN}{d\eta} d\eta}{\int_0^1 \frac{dN}{d\eta} d\eta}, \quad (3.18)$$

where N denotes number of entries, P - the readout pitch, and η_0 is the η value calculated from equation (3.17) for the given hit. The absolute position of a hit in a projection (defined later in the current chapter) is defined as

$$\xi = (-1)^m [(n + d\xi) d - 4.62], \quad (3.19)$$

where $d = 75 \mu\text{m}$ is the readout pitch, n is the strip number, 4.62 is the coordinate of the longest strip in the module and the sign of the coordinate depends on the type of the detector module: for u-module (v-module) the parameter t is equal to 0 (1).

Track finding

Using the detector geometry information, corrected for sensor alignment (described in Chapter 3.6.3) one gets precise strip z position. Using z information and equation (3.18) one gets precise 2D space information in (u, z) or (v, z) space. To get a 3D space point one needs to combine information from two sensors hanging back to back on a silicon wheel. This is done only for possible use by external detectors and filled in FRXT (BRXT) bank. 3D hits are not used in the BST and FST reconstruction.

2D Track Estimation and Filtering

The 2D track finding algorithm (referred to as *2D finder*) works according to the following algorithm:

1. As shown in Fig. 3.17 a u -sector and its adjacent v -sector are considered together, since their strips are parallel and named *projections*. All possible projections are considered sequentially. U -sector 5 and v -sector 6 each form a projection on its own.
2. A parabola search is performed sequentially in each projection. The search in each projection starts between the first and last z -plane (in the FST case for example between planes number 0 and 4). Sequentially all combinations of two hits from the two planes are tested. A straight line search corridor of 0.5 mm is defined by each pair of hits. In the corridor, a matching hit in the intermediate planes is searched for. As soon as three hits are found a parabola is followed. A parabola is accepted if at minimum three hits are found. If no hits in the 4th plane are found, or all hits from plane 4 are already considered, then the same search is performed using planes 0 and 3. The parabola search is performed until all reconstructed 2D hits are used in at least one parabola. To distinguish two different parabolas, one different hit is sufficient at this stage of the fit.
3. An ordering based on the number of hits is performed. Parabolas are selected based on
 - **Curvature** - An approximation of the DCA parametrization (see chapter 2.2.9) is done to get a value for the curvature. If the curvature is too small (corresponding to less than 50 MeV), the parabola is rejected.
 - **Vertex Consistency** - All parabolas are extrapolated to the beam (x,y) position, and a z -position histogram is filled. The parabolas corresponding to outliers in this histogram are rejected.

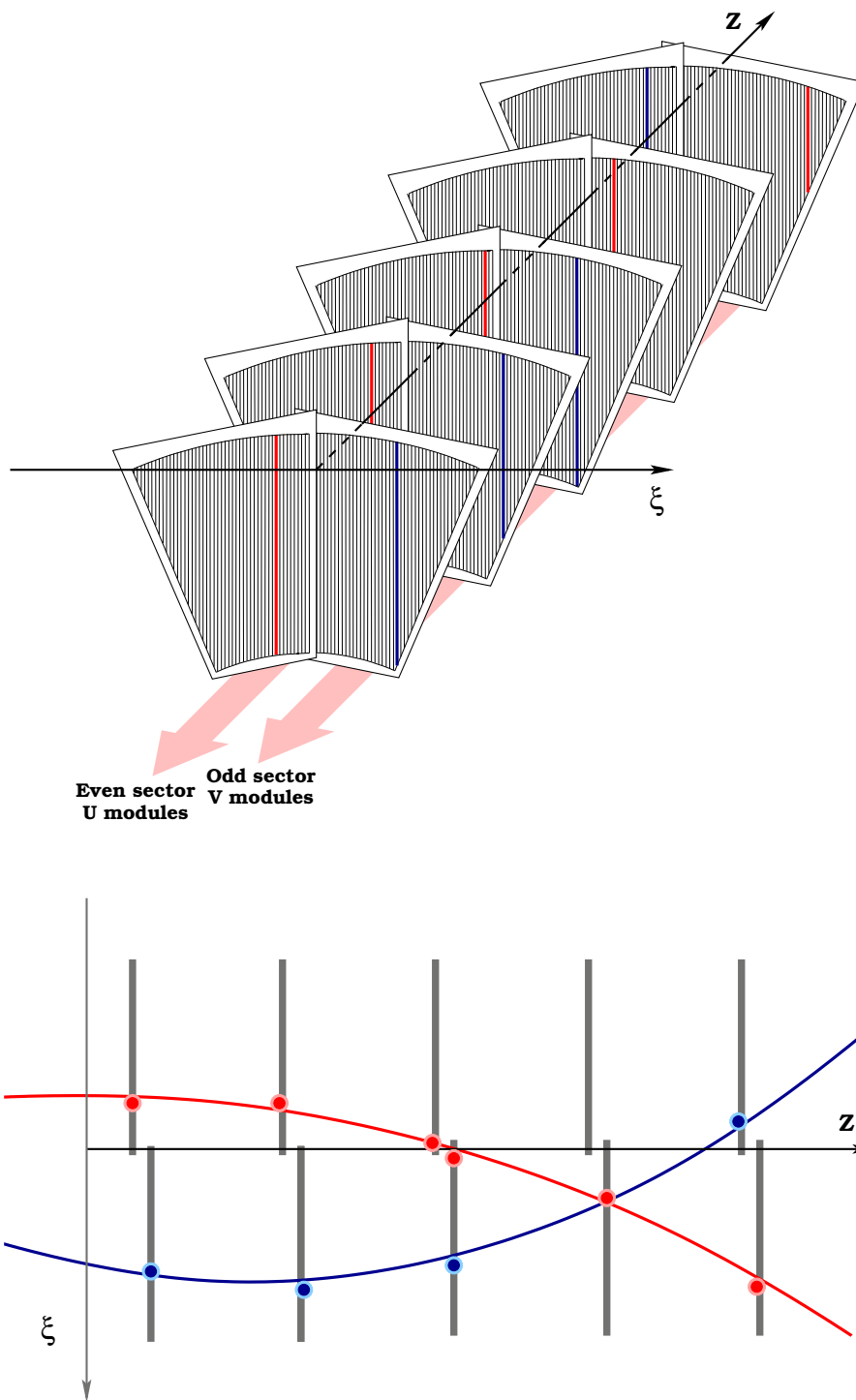


Figure 3.17: The 2D track finding scheme. ξ is the directly measured (u or v) coordinate.

3D track finding 3D tracks are fitted using a Kalman filtering procedure. Sequentially the hit information from each set of two parabolas is used as input to the Kalman filter, fitting a helix. If the χ^2/ndf of the fit is better than a certain limit (3.5 for the moment), the helix is saved, and all parabolas which are using the hits in the helix are removed from the input list. If the fit fails the χ^2/ndf condition, the parabolas are not rejected, but left for further consideration. This scheme is being repeated until parabola lists from both projections are exhausted. Only then, the same procedure is started on the next pair of projections.

Vertex Finding and Track Refitting

After the helix finding is completed, all helices are extrapolated, and the z position z_0 is found at which the distance between the beamline and the helix is shortest. A weighted z_0 histogram for all reconstructed helices is filled, where the weight of each helix is given by its number of hits. The mean value of the best cluster found in this histogram is taken as the vertex position, and all non-vertex fitted tracks fitting in this cluster are refitted using this space point as an additional measurement.

3.6.3 Alignment

Alignment is a mathematical procedure, which corrects each individual sensor spatial position via *alignment parameters* and determines precisely the most probable spatial position of the given detector module with respect to some reference system. When the alignment is performed on a detector module with respect to the other detector modules inside a detector, it is referred to as *internal alignment*. When the alignment of the whole detector as a single solid body is performed with respect to an other, independent detector, then an *external alignment* is performed.

In both FST and BST each sensor is individually aligned. The alignment parameters represent the shifts of every given module with respect to its mounting point (for details see Chapter 3.4). The possible deviations are two translations - one in the strip measuring direction, the other in z - and three rotations summing up to five parameters per detector module i referred to as $\Delta\xi_i, \Delta z_i, \Delta\varphi_i, \Delta\theta_i, \Delta\psi_i$. In the FST (BST) where the number of modules is 120 (144) the number of alignment parameters that has to found is 600 (720). To determine the alignment parameters a Kalman filter based iterative procedure was developed. The procedure takes as input all FST (BST) tracks with the maximum number of hits from all available data, as well as hits from

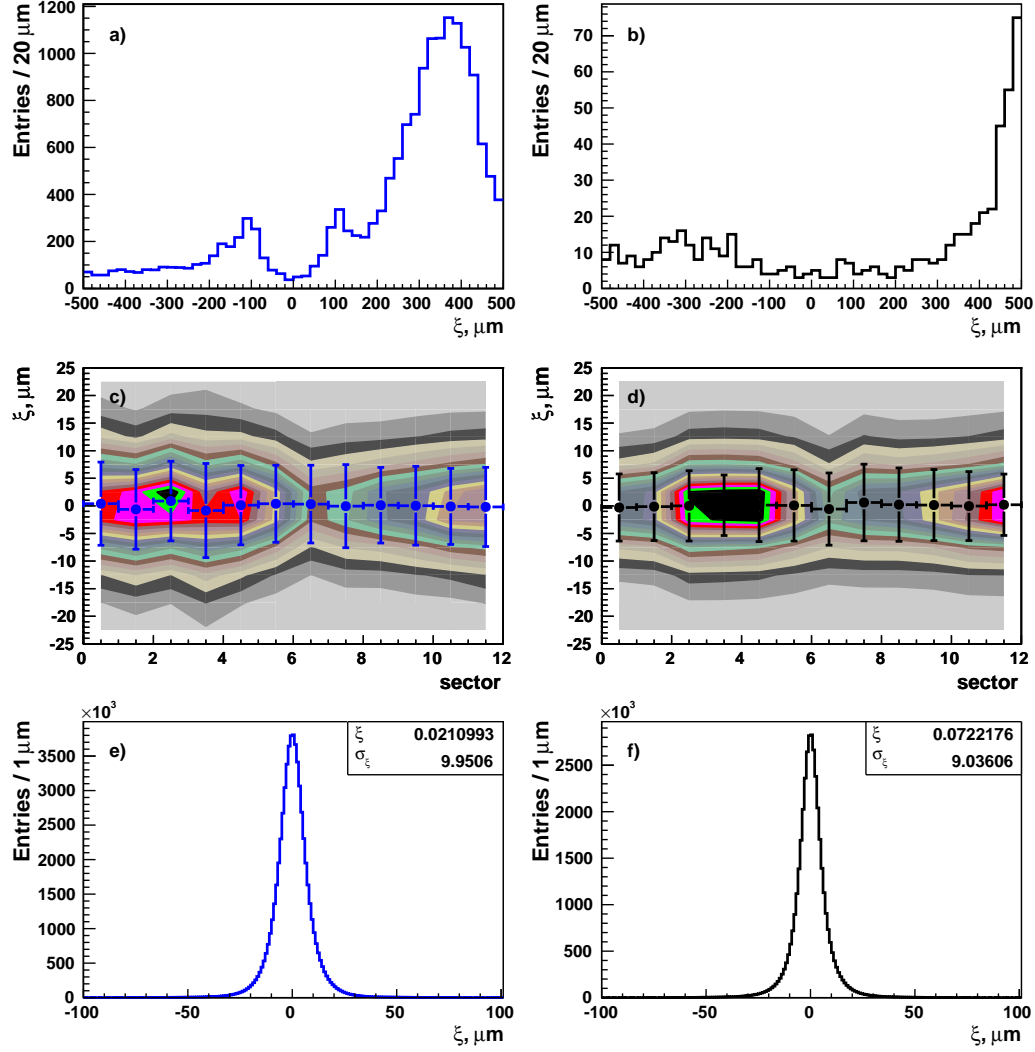


Figure 3.18: FST and BST hit residuals for the data sample used in the current analysis. The plots on the left (a) c) and e)) represent the FST residual, and the plots on the right (b), d) and f)) - the BST residual. The residuals as a function of φ of the track after alignment are presented in Fig. c) and d). The overall residuals for both detectors are represented before alignment in Fig. a) and b) and after the alignment in Fig. e) and Fig. f).

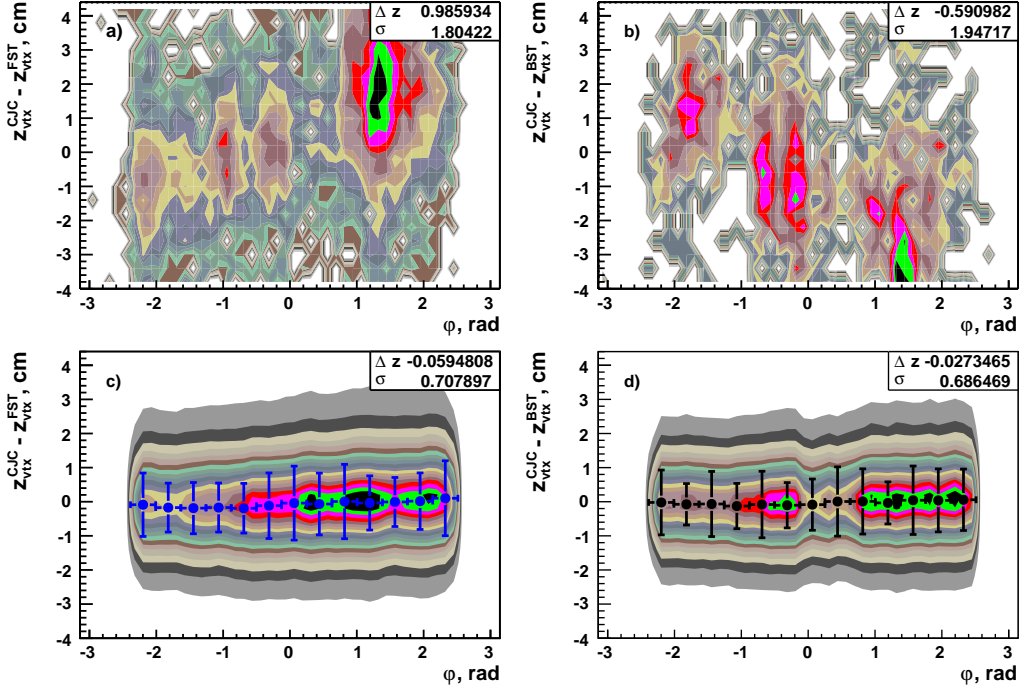


Figure 3.19: Difference between the z position of the vertex as it is reconstructed by the H1 central tracking and FST (a, c) and BST (b, d) before (a, b) and after (c, d) applying the detector alignment.

the CJC matching the tracks and - in case of the BST - matching SpaCal clusters. A measurement of the internal resolution is the width of the residual which for FST and BST case is presented in Fig. 3.18 e) and f), respectively. Since the residual is the signed difference between the hit position and the closest point of the corresponding track to it, its distribution (see Fig. 3.18, e) f)) directly reflects the quality of the alignment of each sensor and of the detector as a whole. Both residual distributions before and after alignment are presented on Fig. 3.18 a) and b) and Fig. 3.18 e) and f), respectively. It is visible that without alignment, the track reconstruction is largely disturbed. Moreover, in case of a significant noise contribution even the reconstruction of wrong tracks is possible. An additional check of the relative alignment between the detector sectors is presented by the dependence of residual versus φ shown of Fig 3.18 c) and d). The lack of characteristic shapes in the distribution shows no local shifts or rotations in the FST and BST.

The quality of the external alignment can be judged when a quantity measured by the internal reconstruction is compared with the measurement of the same quantity by an external, independent detector. In H1, the detector

defining the alignment reference system for all other detector components is the CJC. Thus, a comparison between an FST (BST) and a CJC measured quantity would prove the global alignment of both FST and BST. Such a comparison is provided by the difference of the CJC primary vertex z -measurement and the FST (BST) z -measurement depicted on Fig. 3.19. It is visible that a coincidence within the measurement error, dominated by the CJC z position resolution, of both measurements is possible only after applying the alignment procedure. Moreover, the φ dependence of the comparison proves that the local misalignments are successfully minimized due to the alignment procedure.

3.6.4 Data Quality

The quality of the tracking information provided by different detector devices used in this analysis is essential for determination of small signals. Lower track parameter resolution enters directly into the width of the signal distribution, smearing out completely the signal in the extreme case. The first important quality check is the hit resolution. The hit resolution for both FST and BST can be estimated from the residuals demonstrated in Fig. 3.18. The residual observed in the track fit does not directly represent the detector resolutions which are behind the physical process at hand. Depending on the number of associated hits and their distribution along the track, correction factors should be applied to translate the observed residuals into hardware resolution. The average correction factors for the track mix in the FST and BST is ~ 1.1 .

The next step is to estimate the internal efficiency of the FST and the BST. The internal efficiency is calculated by extrapolating every track to each possible detector module, constructing an intercept point and looking for the closest hit in the detector. Only if a close enough hit is found, the detector module is considered efficient. The internal efficiency of the FST as a function of the sensor number is presented in Fig. 3.20. It is visible that the internal efficiency of majority of the detectors, except for the malfunctioning ones is above 90 % on average.

Further on, the track parameter precision is investigated. To perform this task, an external reference measurement of the track parameters with a resolution comparable or better than the investigated device is needed. Since such a device is not available in this case, the Monte Carlo simulation is assumed to describe accurately the data sample.

For this study the Monte Carlo sample described in Chapter 1.7.1 is used. The reconstructed parameters for each track are compared with the parameters of the simulated particle. The results in the case of FST are

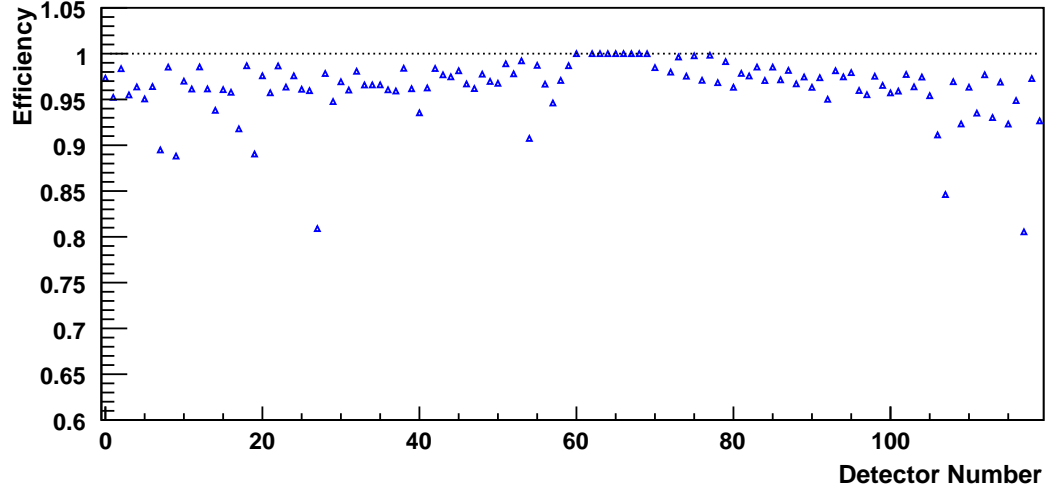


Figure 3.20: FST internal efficiency

presented in Fig. 3.21. For comparison the corresponding resolutions for the central tracks are presented on Fig. 3.22. For both detectors the resolutions as a function of the track's transverse momentum are presented in Fig. 3.24 and 3.23, respectively. From equation (2.10) follows that the uncertainty on the transverse component of the momentum p_t is directly proportional to the uncertainty of the curvature measurement $\delta\kappa$. The curvature error for uniformly spaced measurements on the trajectory of a charged particle in a uniform magnetic field can be approximated by [5]:

$$(\delta\kappa)^2 = (\delta\kappa_{\text{res}})^2 + (\delta\kappa_{\text{ms}})^2, \quad (3.20)$$

where κ_{res} is the curvature error due to finite measurement resolution and κ_{ms} is the curvature error due to multiple Coulomb scattering (MS). The term depending on the detector resolution is given by [5]:

$$\delta\kappa_{\text{res}} = \frac{\epsilon}{L_t^2} \sqrt{\frac{720}{N+4}}, \quad (3.21)$$

where N is the number of the points measured along the track, L_t is the length of the track in the $r - \varphi$ plane and ϵ is the measurement error for each point, perpendicular to the trajectory. If a vertex constraint is applied at the beginning of the track, the coefficient under the radical becomes 320. The contribution from the MS can be estimated as [5]:

$$\delta\kappa_{\text{ms}} \approx \frac{(0.016) (\text{GeV}/c) z}{L p \beta \cos^2 \lambda} \sqrt{\frac{L}{X_0}}, \quad (3.22)$$

where p and z are the momentum and the charge in elementary charge units correspondingly. The total length of the track is given by L , X_0 is the radiation length of the scattering medium and β is the kinematic variable $\beta = v/c$. λ is the pitch angle defined for a particle with a momentum p (in GeV/c) and charge ez in magnetic field \vec{B} with a radius of the curvature perpendicular to \vec{B} as $p \cos \lambda = 0.3zBR$.

Equations (3.21), (3.22) and (3.20) show the importance of the length of the track and its number of hits for the resolution of the curvature and the transverse momentum. Both of these parameters are restricted by the geometry of FST and BST and much smaller than the corresponding parameters in the central tracker. Thus, despite the better intrinsic silicon resolution, the final resolution expected cannot be better than the central one since the transverse momentum resolution is dominated by square of the length of the track and the number of hits.

In order to calculate the total momentum resolution of the detector, the polar angle θ precision should also be taken into account. At small angles the polar angle deviation of the particle from its initial direction is dominated by multiple scattering, the effect of which can be approximated by a Gaussian distribution with a width given by [5]:

$$\sigma_{\theta}^{\text{ms}} = \frac{13.6 \text{ MeV}}{\beta c p} z \sqrt{x/X_0} [1 + 0.038 \ln(x/X_0)]. \quad (3.23)$$

Here p , βc and z are the momentum, velocity and the charge of the particle, and x/X_0 is the total thickness of the material given in radiation lengths.

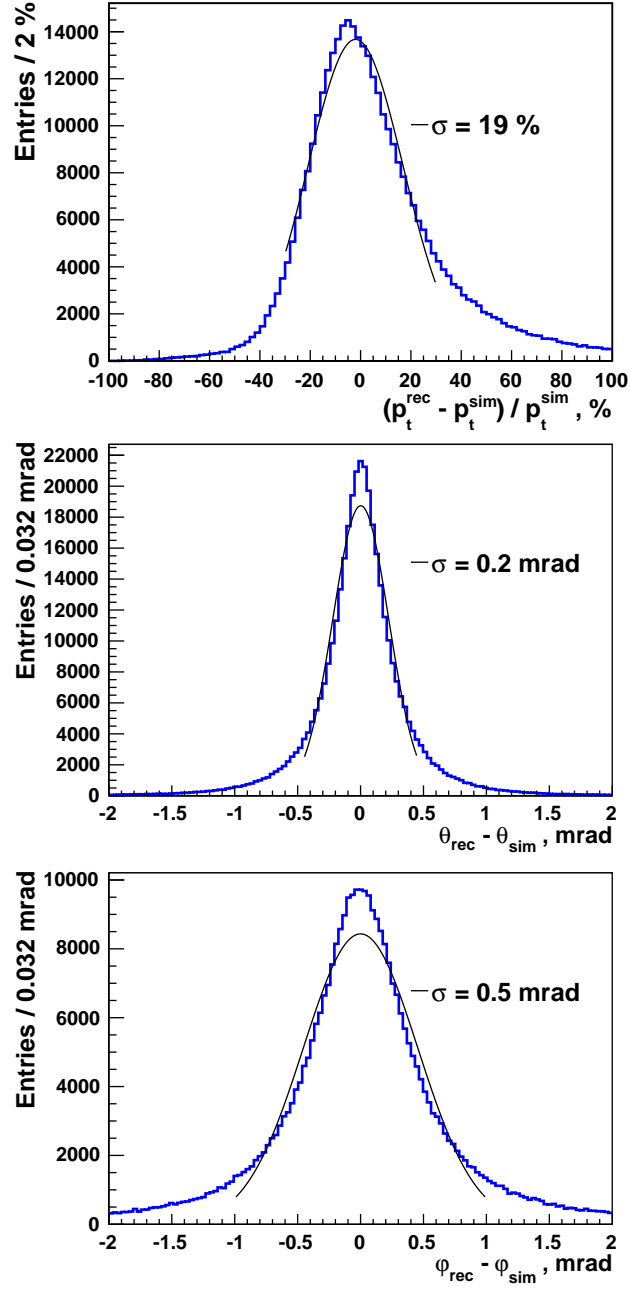


Figure 3.21: FST track parameter resolutions.

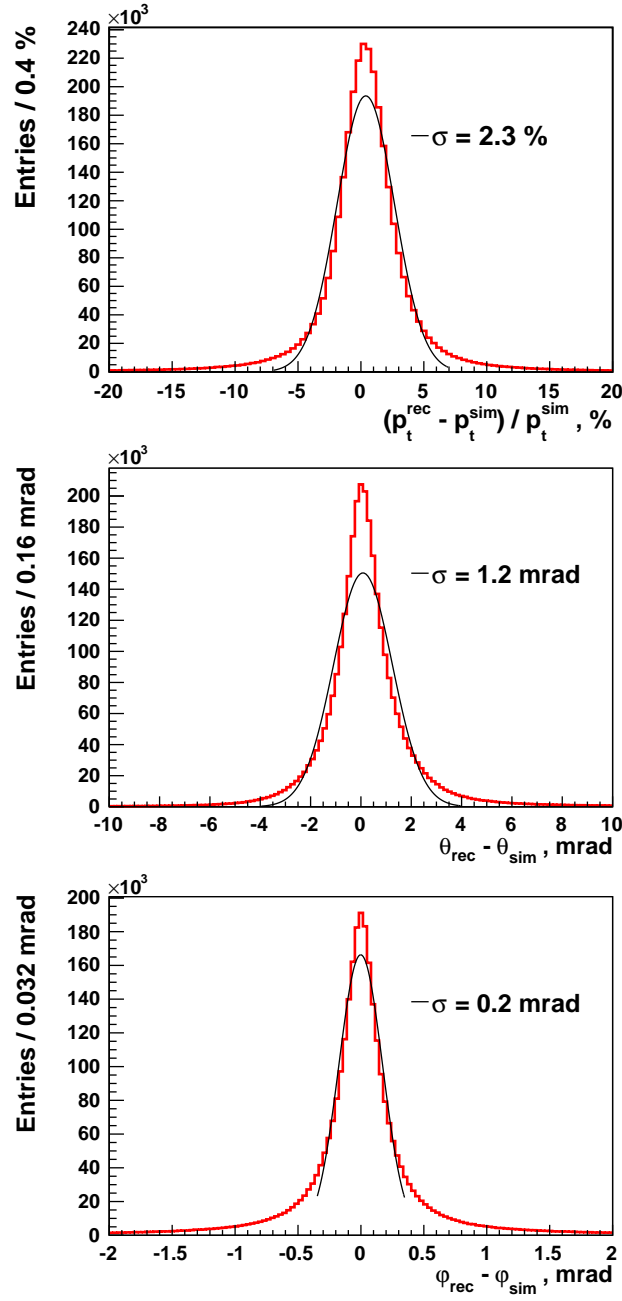


Figure 3.22: Central track parameter resolutions.

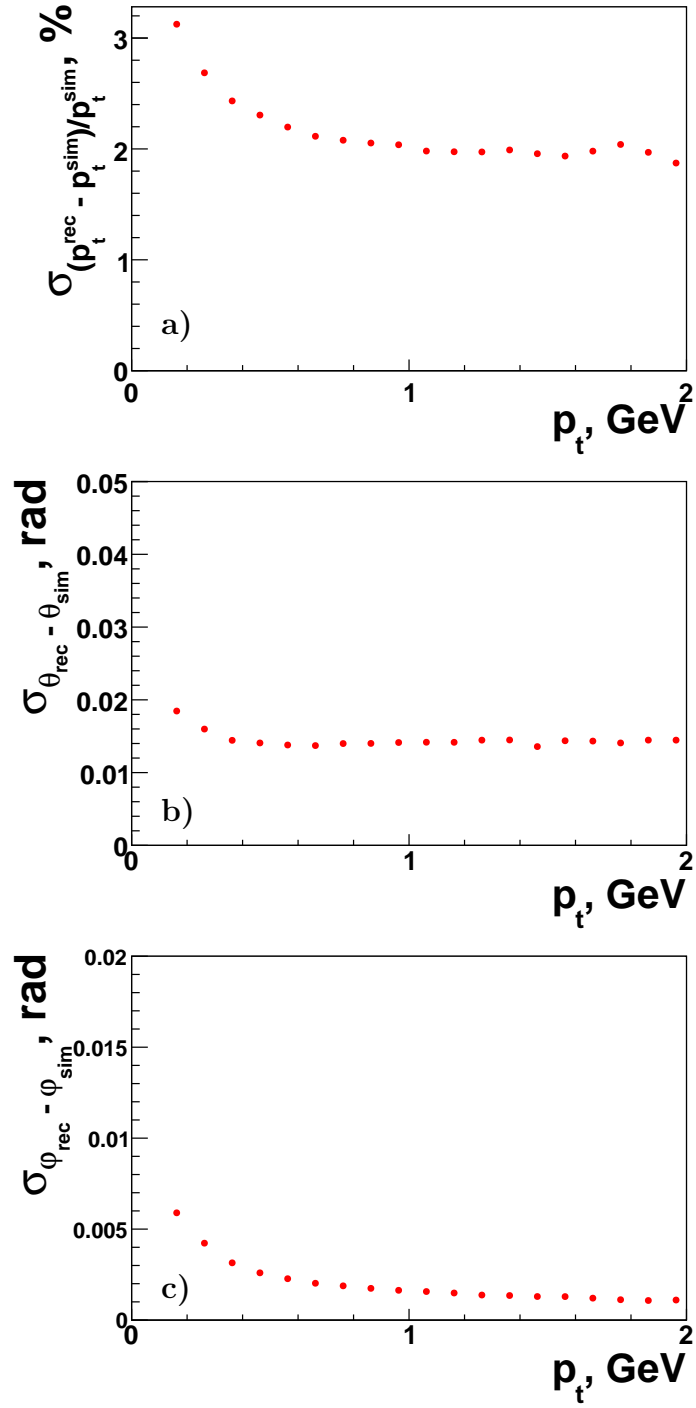


Figure 3.23: Central tracker track parameter resolutions as a function of the transverse momentum of the reconstructed track.

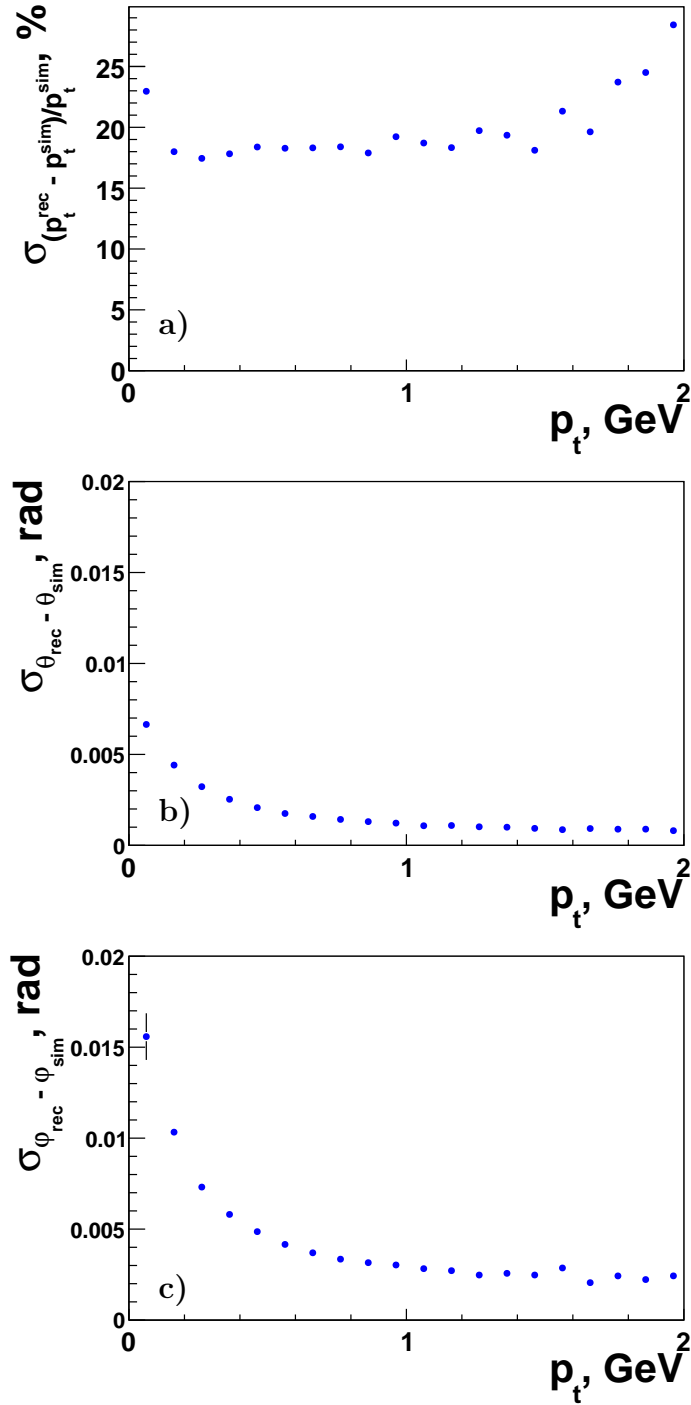


Figure 3.24: FST track parameter resolutions as a function of the transverse momentum of the reconstructed track.

Chapter 4

D* Selection

The aim of this analysis is the measurement of the visible production cross section for $D^*(2010)^\pm$ mesons. The D^* mesons are identified using the $\Delta m = D^* - D^0$ mass difference tagging technique [146, 147, 148] in the decay chain $D^{*+} \rightarrow D^0 \pi^+ \rightarrow (K^- \pi^+) \pi^+$ known as the "golden" channel¹. The golden channel is the most widely method used to detect D^* mesons at HERA [33, 148, 149, 150, 151].

In this chapter we describe step by step how the event sample considered in this analysis is selected. First, the inclusive data quality selection criteria is described. Next, the trigger selection conditions are described. Further on, the luminosity measured for the selected data sample is presented. A short description of the event kinematics determination is presented. Finally, in Chapter 4.5, the requirements imposed on the D^* candidates are described.

4.1 Event Selection

Initially, the data taking period for the current analysis was foreseen to consist of more than two years - from the beginning of 2004 to the end of HERA luminosity running. Due to a water leak in the FST and radiation damage in BST in 2004, after only $\sim 17 \text{ pb}^{-1}$ of data collected [114], both detectors had to cease operation due to a front-end electronics malfunction. Both detectors were dismantled from the H1 detector, repaired, upgraded and mounted back into the experiment in 2006 [130]. This reduced significantly the amount of data available for the current analysis.

The data used in this analysis was collected between 15.05.2006 and 20.03.2007, which corresponds to a run range 460649 - 500611. HERA operated until 25.06.2006 with electrons, and from 13.07.2007 (run 468530)

¹Henceforth, charge conjugate states are always implicitly included.

starting colliding positrons with protons. The beginning of the considered period is set by the start of the reliable FST and BST operation, and the end is determined by the end of HERA luminosity operation with 920 GeV protons.

Initial preselection of the data is performed based on the hardware status of the subdetector systems important for this analysis. An event is accepted only if CJC1, CJC2, CIP, LAr, TOF, FST and BST are powered on for the given event and are read out by the H1 DAQ system. In case of a technical problem in any of the mentioned systems, an alarm is issued during luminosity running, the events effected are marked and not considered further. Additionally, in each event, a primary vertex with $-35 \text{ cm} < z_{\text{vtx}} < 35 \text{ cm}$ is required, thus insuring that the event does not come from a beam-gas or a satellite bunch interaction.

4.2 Trigger Selection

Only trigger information from the first trigger level was used to select DIS events. The trigger element used is s61. Its functionality is based on the trigger information from two detector components, namely the SpaCal and the CJC. The trigger accepts an event only if the energy deposition in the SpaCal is at least 9 GeV ($\text{SPCLe_IET} > 2 \parallel \text{SPCLe_IET_Cen_3}$) and if there is at least one track with a transverse momentum of at least 900 MeV detected in the CJC1 and CJC2 ($\text{FTT_mul_Tc} > 1$). The average prescale factor of this trigger element for the data taking period investigated is 1.01. The trigger efficiency was estimated in [152] to be 97% with a systematic error of 1%. It is reasonable to assume for the current analysis that the SpaCal trigger element is independent of the pseudorapidity of the final state. Moreover, at least two tracks of the D^* plus more tracks from the accompanying jets are within the FTT acceptance. Thus, only small deviations on the percent level are expected in the trigger efficiency. Assuming that the deviation between the central and the current analysis is smaller than the statistical uncertainty of this analysis, no further trigger efficiency investigations were performed.

4.3 Luminosity

The integrated luminosity is calculated for each luminosity run, using the H1 luminosity system described in Chapter 2.2.6. To ensure a precise luminosity measurement, only runs with integrated luminosity $\mathcal{L} > 0.1 \text{ nb}^{-1}$ are considered. Adequate corrections in the luminosity calculation are implemented

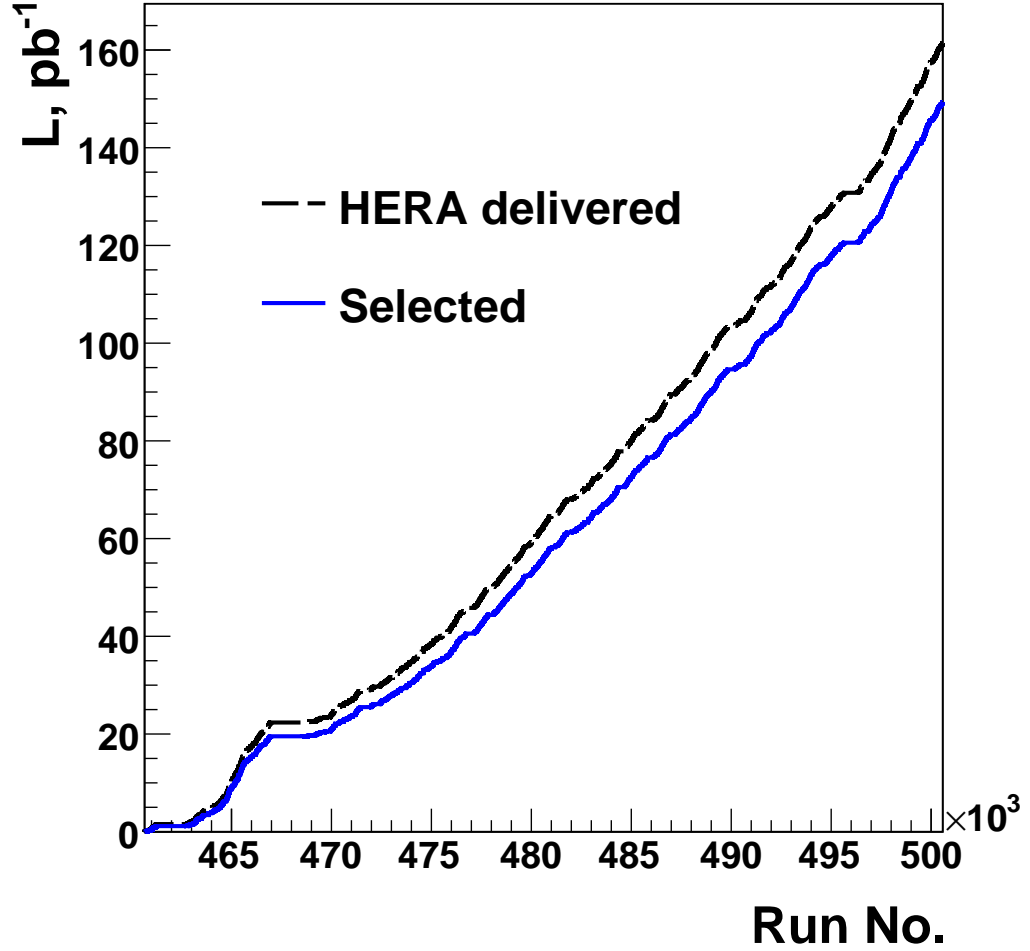


Figure 4.1: The evolution of the integrated luminosity delivered by HERA and the integrated luminosity selected for the current analysis vs. the run number.

reflecting the effects mentioned in Chapter 4.1, as well as for the subtrigger prescale factors. The evolution of the delivered integrated luminosity and the fraction selected for this analysis are depicted on Fig. 4.1. The total integrated luminosity for the considered running period under the conditions mentioned above is calculated to be $(149.6 \pm 1.9) \text{ pb}^{-1}$. The details of the data sample are summarized in Table 4.1

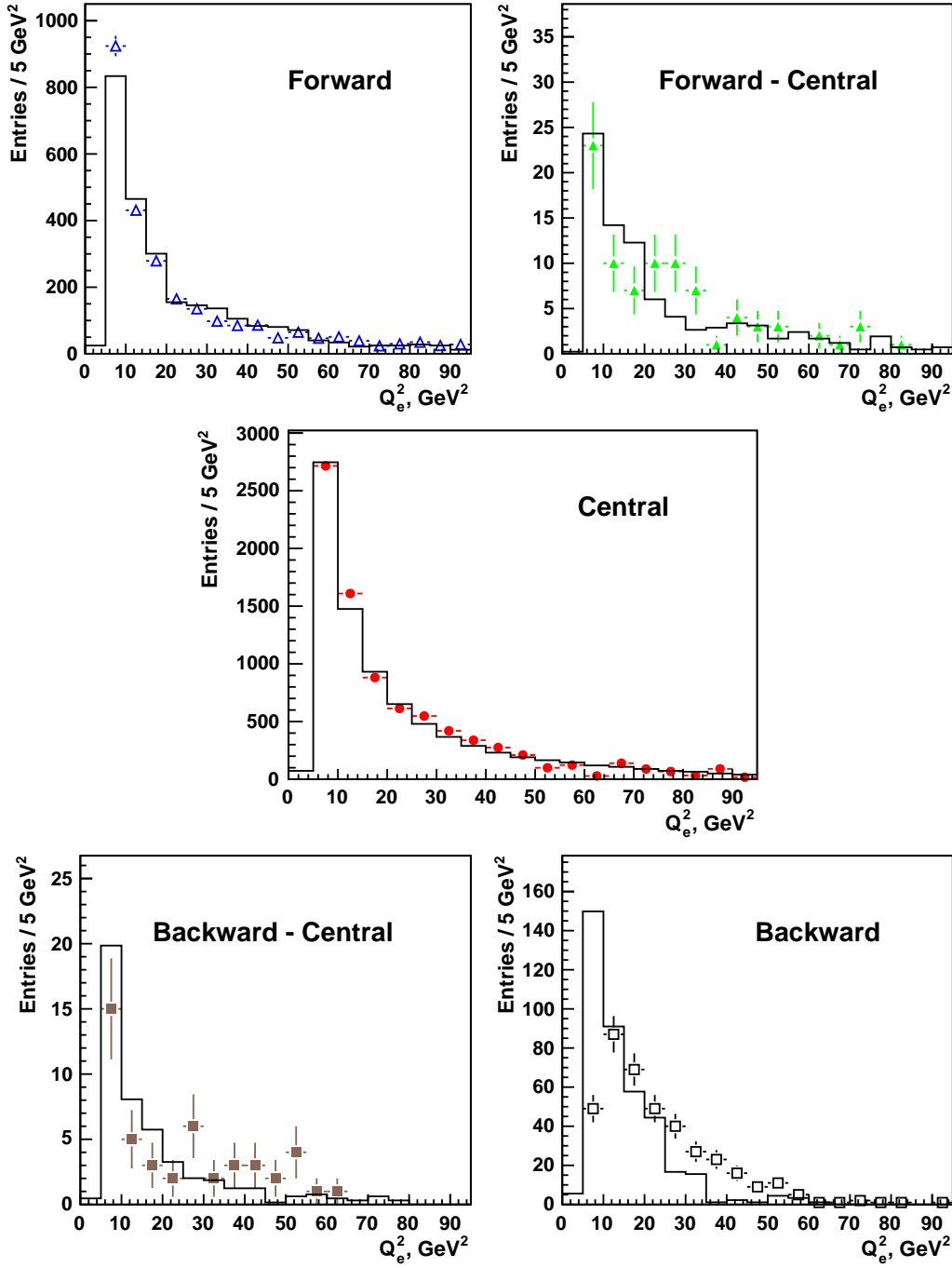


Figure 4.2: Comparison between data and Rapgap Monte Carlo (histogram) of the reconstruction of the four-momentum transfer Q^2 using the electron method for the different event categories as defined in Chapter 4.5.2. The statistical subtraction method is used for the central plot only.

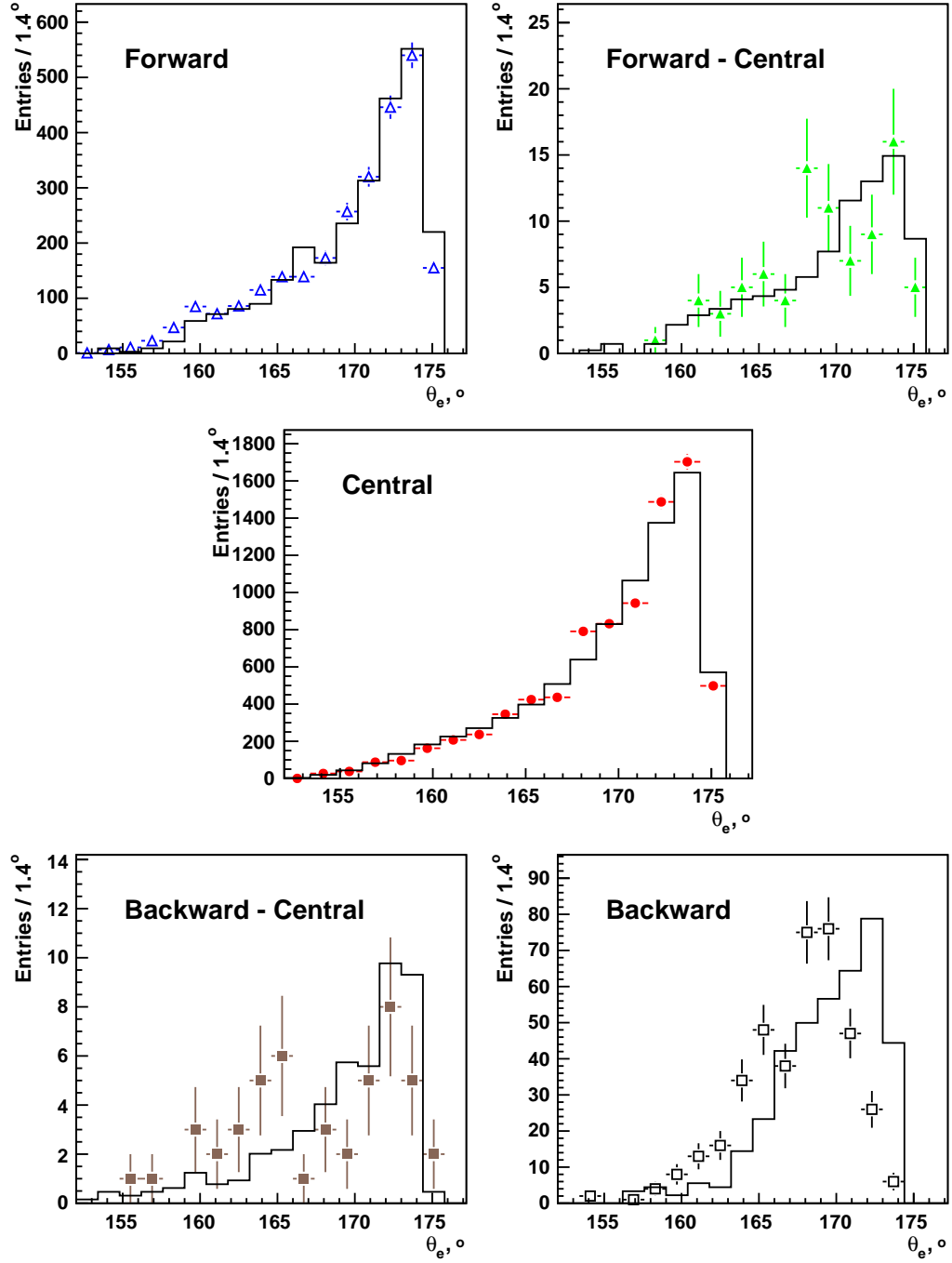


Figure 4.3: Comparison between data and Rapgap Monte Carlo (histogram) of the polar angle θ_e of the scattered electron, used for event kinematics determination. The different event categories are defined in Chapter 4.5.2. The statistical subtraction method is used for the central plot only.

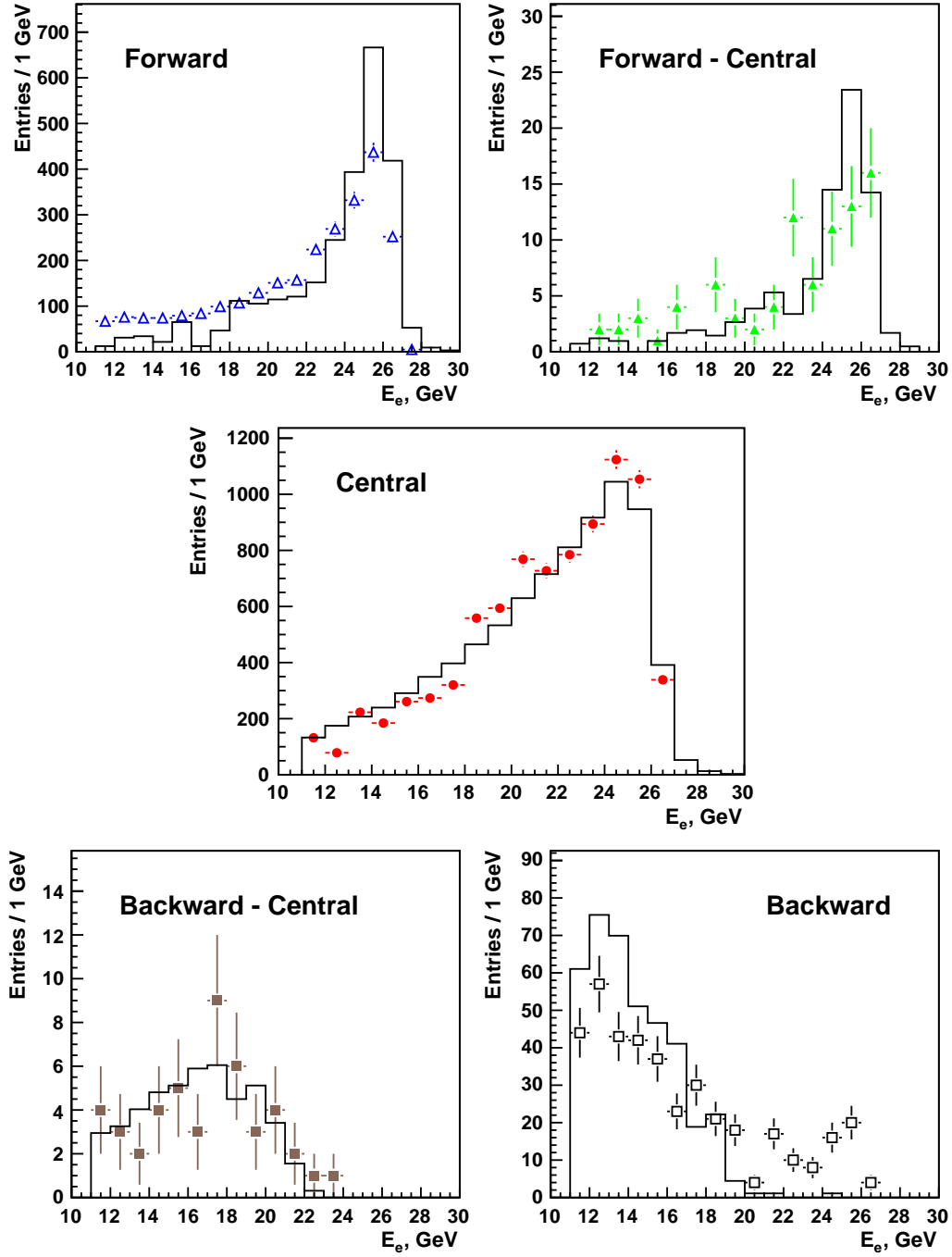


Figure 4.4: Comparison between data and Rapgap Monte Carlo (histogram) of for energy E_e of the scattered electron, used for event kinematics determination. The different event categories are defined in Chapter 4.5.2. The statistical subtraction method is used for the central plot only.

Data taking period	15.05.2006 - 20.03.2007
Run range	460649 - 465643
Lepton Type	e^- until 13.07.2007, afterwards - e^+
Subdetectors	CJC1, CJC2, FST, BST, CIP, LAr, TOF
Vertex Position	$-35 \text{ cm} < z_{vtx} < 35 \text{ cm}$
Minimal Luminosity	$\mathcal{L} > 0.1 \text{ nb}^{-1}$
Total Luminosity	$(149.58 \pm 1.94) \text{ pb}^{-1}$
s61 Luminosity	$(148.24 \pm 1.93) \text{ pb}^{-1}$

Table 4.1: Event selection and luminosity used in the current analysis.

4.4 Kinematics Determination

The precise determination of the event kinematics is of vital importance for precise DIS measurements. The main kinematics variables and the relations between them were already presented in Chapter 1.1. Various methods exist to determine the event kinematics depending either on the properties of the scattered electron, or on the properties of the hadronic final state, or both. These are

- **Electron method** - using the energy and the scattering angle of the scattered electron.
- **Hadron method** - reconstructs the event kinematics using only the hadronic final state (HFS) properties i.e. its angle and energy [153]. It has a worse resolution than the electron method and depends fully on the quality of the HFS reconstruction, but it is widely used for charge current event kinematics reconstruction where the electron method is inapplicable.
- **Σ method** - it utilizes both hadronic final state and scattered electron properties [154]. The inelasticity is calculated similarly to the electron method and Q^2 - to the electron method. The method does not use the incoming electron energy. Thus it is less sensitive to radiative corrections and energy calibration corrections.
- **Double angle method** - it is relying only on the polar angle measurement of both the HFS and the scattered electron [155]. Since the double angle method to the first approximation is not depending on energy measurement it is widely used in conjunction with the other methods for calorimeter energy calibration [104].

In the current analysis the electron method was chosen. It is defined using only the scattered electron properties as

$$Q_e^2 = 2E_e E'_e (1 + \cos \theta_e) = \frac{E_e'^2 \sin^2 \theta_e}{1 - y_e} \quad y_e = 1 - \frac{E'_e (1 + \cos \theta_e)}{2E_e}, \quad (4.1)$$

where E_e and E'_e are the energies of the incident and the scattered electron, θ_e is the polar angle of scattered electron and the subscript "e" denotes symbolically the electron method. The Bjorken-x can be calculated using equation (1.1) as $x = Q^2/ys$. The electron method has the advantage to be simple, and independent of the properties of the hadronic final state. The control plots representing the measured scattered electron energy and polar angle considered in this analysis are presented with markers for the different categories of events in Fig. 4.4 and Fig. 4.3. The corresponding Monte Carlo prediction is always represented by a continuous line. The bin contents for all central control plots are calculated using the statistical subtraction method described in Chapter 4.5.4.

If we define the operation $A \oplus B = \sqrt{A^2 + B^2}$, the errors on the kinematics measured using the electron method can be expressed directly from equations (4.1) as:

$$\begin{aligned} \frac{\delta Q^2}{Q^2} &= \frac{\delta E}{E} \oplus \tan \frac{\theta_e}{2} \delta \theta_e \\ \frac{\delta x}{x} &= \frac{1}{y} \frac{\delta E}{E} \oplus \tan \frac{\theta_e}{2} \left(x \frac{E_p}{E_e} - 1 \right) \delta \theta \\ \frac{\delta y}{y} &= \frac{1-y}{y} \left(\frac{\delta E}{E} \oplus \cot \frac{\theta_e}{2} \delta \theta_e \right). \end{aligned} \quad (4.2)$$

From equations (4.2) follows that at small scattering angles (large θ_e , low Q^2) the resolution is dominated by the the electron energy resolution, and diverges for low y as $1/y$. In order to ensure better resolution, a cut on the inelasticity is imposed, as well as a requirement on the angle θ_e of the scattered electron - it should be well inside the SpaCal acceptance and it should have an energy above a certain threshold. The cuts imposed to the data sample, determining the kinematic domain of this analysis are presented in Table 4.2. Further resolution studies of the methods mentioned above can be found in [104].

A comparison between data and Rapgap Monte Carlo for the the polar angle and the energy of the scattered electron and the resulting Q_e^2 are presented in Figs. 4.3, 4.4 and 4.2, respectively. Each of the MC plots is normalized to the corresponding data plot and represents the corresponding variable for events in which at least one D* meson from the matching

categories described in Chapter 4.5.2 is found. The reasonably good description of the data distributions by the MC distributions demonstrates how well detector resolutions and dead material are described.

Virtuality	$5 \text{ GeV}^2 < Q_e^2 < 100 \text{ GeV}^2$
Inelasticity	$0.05 < y_e < 0.6$
Electron scattering angle	$153^\circ < \theta_e < 177^\circ$
Electron cluster energy	$E_e > 11 \text{ GeV}$

Table 4.2: Kinematics domain selection cuts.

4.5 D^* Reconstruction

The $D^{*\pm}$ meson is an excited $c\bar{d}$ ($\bar{c}d$) quark state, decaying via strong interaction. The shape of its invariant mass distribution is a gaussian with a mean value representing the invariant mass of the particle and a width dominated by the momentum resolution of all particles. If one of the final state particles does not originate from the D^* , it creates a combinatorical background. Hence, the final distribution to be fitted is a sum of a gaussian and a shape for this background. The signal size is calculated as an integral over the gaussian function.

Searching for the optimal decay channel to use, one should take into account that H1 was not build to detect neutral particles i.e. decays with neutral decay products are disfavoured. Additionally, a decay channel with the minimum of charged decay particles should be considered, since every additional particle contributes its resolution to the mass resolution of the compound object. Thus, taking into account the branching fractions listed in Table 4.3 and Table 4.4, in this analysis the exclusive decay channel

$$D^{*\pm} \rightarrow D^0 \pi_s^\pm \rightarrow K^\mp \pi^\pm \pi_s^\pm \quad (4.3)$$

was chosen for reconstruction of the D^* mesons. The mass difference between

$D^* \rightarrow D^0 \pi^+$	$(67.7 \pm 0.5) \%$
$D^* \rightarrow D^+ \pi^0$	$(30.7 \pm 0.5) \%$
$D^* \rightarrow D^+ \gamma$	$(1.60 \pm 0.4) \%$

Table 4.3: D^* decay channels branching ratios from [5].

$D^0 \rightarrow K^- \pi^+ \pi^0$	$(14.1 \pm 0.50) \%$
$D^0 \rightarrow K^- \rho^+ \rightarrow K^- \pi^+ \pi^0$	$(11.0 \pm 0.70) \%$
$D^0 \rightarrow K^- \pi^+ \pi^+ \pi^-$	$(7.72 \pm 0.28) \%$
$D^0 \rightarrow K^- \pi^+ \pi^+ \pi^- \pi^0$	$(4.10 \pm 0.40) \%$
$D^0 \rightarrow K^- \pi^+$	$(3.80 \pm 0.07) \%$

Table 4.4: Selected D^0 branching ratios from [5].

$m(D^{*\pm})$, MeV	2010.0	± 0.4
$m(D^0)$, MeV	1864.5	± 0.4
$m(K^\pm)$, MeV	493.677	± 0.016
$m(\pi^\pm)$, MeV	139.5702	± 0.0003
Δm , MeV	145.421	± 0.010

Table 4.5: Invariant masses relevant to the current analysis taken from [5].

the mass of the D^* meson and the D^0 meson, labelled as Δm in Table 4.5 is only ~ 145 MeV. After producing a pion, the available free energy left (referred to as Q-value) is as little as 5.93 MeV. Thus, both D^0 and the slow pion π_s^\pm are produced almost at rest in the D^* rest frame. If we look at the decay from the laboratory frame, after the Lorentz transformations, the π_s^\pm momentum and the D^0 momentum are highly correlated. Moreover, the π_s^\pm will carry only a small fraction of the momentum of the D^* . Because of its low momentum the π_s^\pm is referred to as *slow pion* or *soft pion* and symbolically labelled with a "s" subscript. This tight kinematic constrain allows on approximately 25 times better [146] signal resolution of the mass difference

$$\Delta m = m_{K^\mp \pi^\pm \pi^\pm} - m_{K^\mp \pi^\pm} \quad (4.4)$$

(shown on Fig. 4.29, a), than the directly observable $D^{*\pm}$ and D^0 mass distributions. This is due to fact that the errors of the two D^0 decay particles largely cancel in the subtraction. The width of the signal peak in the Δm distribution is dominated by the momentum resolution of the slow pion. Additionally, the background of the distribution from combinations involving particles not related to the considered decay chain is suppressed at small mass differences. These are the main advantages turning the Δm method into the preferred technique for finding D^* mesons. A disadvantage, comparing to the life-time D^* tagging method [82], comes from the low branching ratio (\mathcal{BR}) for the exclusive decay chain (4.3), which using the data listed in Table 4.3

	θ_{track}	φ_{track}
FST	$8^\circ - 16^\circ$	$-135^\circ - 135^\circ$
BST	$165^\circ - 174^\circ$	$-135^\circ - 135^\circ$

Table 4.6: The nominal geometrical acceptance range of FST and BST.

and Table 4.4 results in

$$\mathcal{BR}(D^{*\pm} \rightarrow K^\mp \pi^\pm \pi^\pm) = (2.57 \pm 0.07) \%. \quad (4.5)$$

Fitting the Δm distribution, as explained later in Chapter 4.5.3, allows to extract the D^* signal, needed for final cross section calculation as outlined in Chapter 5.

4.5.1 Track Selection

The main purpose of the current analysis is to extend the acceptance of the central tracking by taking advantage on the BST and FST. Thus, the H1 standard tracks and quality cuts are not appropriate. The tracks available for mass reconstruction come from three independent reconstruction modules, namely central reconstruction (described in Chapter 2.2.9), FST reconstruction and BST reconstruction (both described in Chapter 3.6). All three of them produce its own set of non-vertex fitted and vertex fitted tracks and the corresponding vertices. A stand-alone reconstruction of all three D^* decays by FST or BST alone is not possible due to their geometrical acceptance limitations summarized in Table 4.6 and depicted in Fig. 4.5. The maximal theoretical track acceptance for FST and BST is 75% since their detector volume is limited to 3/4 of the full azimuthal angle. This value is achievable in the special case of muons coming from the nominal vertex position (see Fig. 4.6), which minimizes the influence of both vertex smearing and multiple scattering. Simple consideration of the three samples of tracks as one set of tracks is also not an option for the following two reasons:

Each set of primary vertex-fitted tracks produced by the three independent track reconstruction modules, namely *fstrec*, *bstrec* and *ctrec* are associated to their own "primary vertex" which, depending on the topology of the event, can be centimetres away from each other. Additionally, as mention in Chapter 2.2.9, the central vertex is well defined in the $(r - \varphi)$ plane, but it is not precisely defined in the $(r - z)$ plane, which leads also to a worse resolution of the $(r - z)$ - related central track parameters i.e. θ . Since in

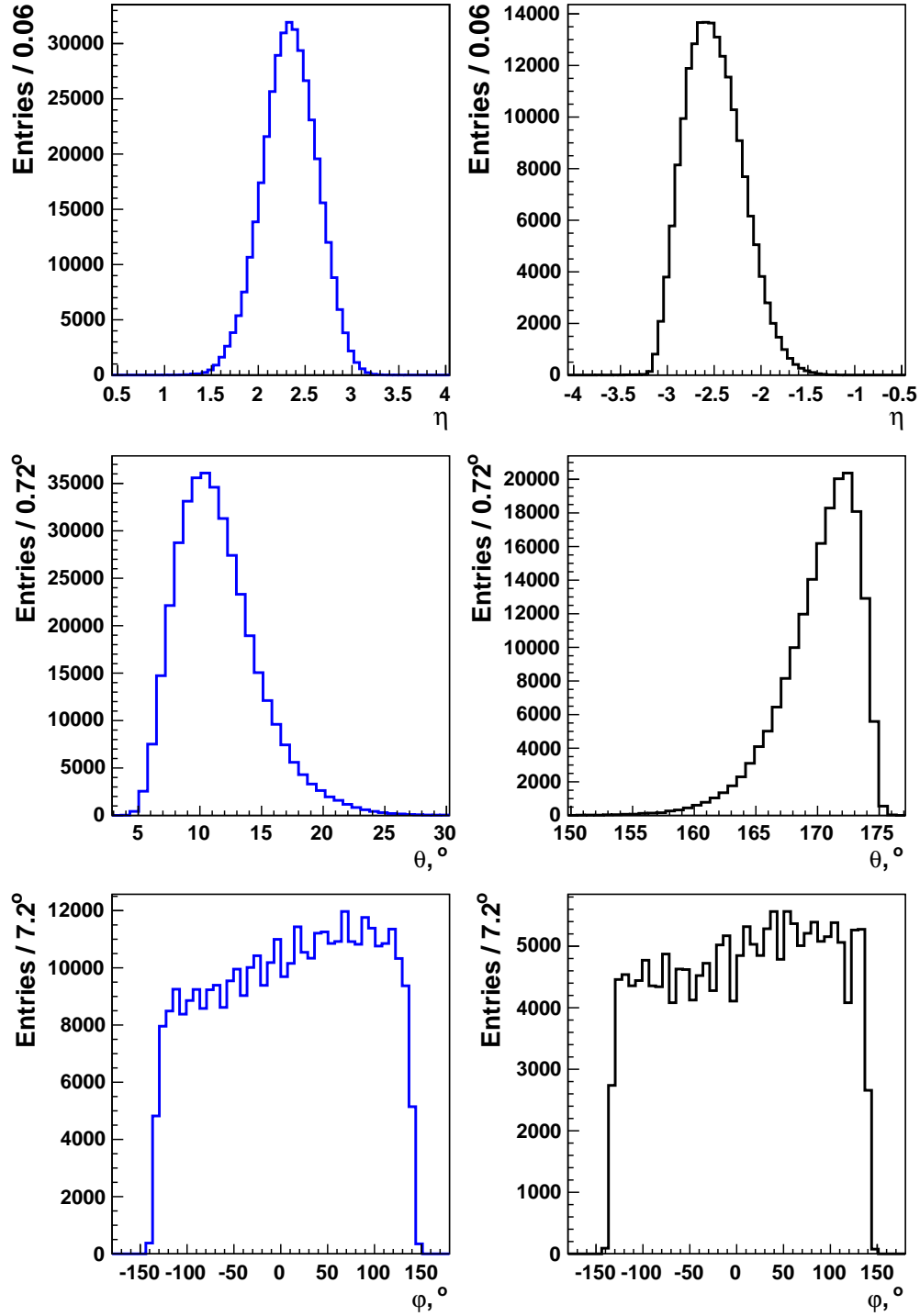


Figure 4.5: Geometrical acceptance region of FST (left) and BST (on the right).

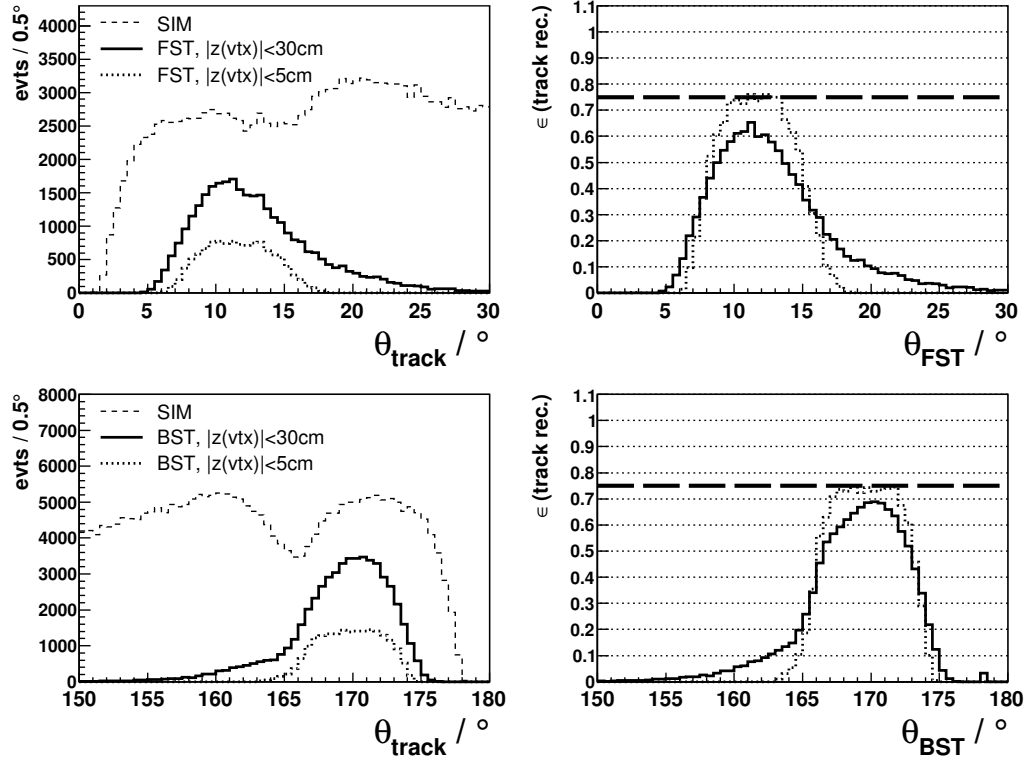


Figure 4.6: The geometrical track acceptance (left) for FST (top) and BST (bottom) taken from [156].

50% of the DIS events there is at least one track in the FST and in another 50% there is at least one track in the BST, and the vertex z -resolution achieved even from one FST or BST track is an order of magnitude better than the central reconstruction z -resolution without z information from the CST, a combination of the three sets of vertices was developed, and is shortly presented in the next two subsections.

As mentioned earlier, the CT reconstruction is not connected with the FST and the BST reconstruction. Thus, at the edges of the CJC near both silicon detectors, an acceptance gap exists. There, the CJC reconstruction reconstructs short, unprecise tracks, needing the silicon information from the silicon trackers, and on the other hand the FST and BST provide hits, not used in central tracks. To fill this acceptance gap, a fit of the central tracks using FST and BST information was developed.

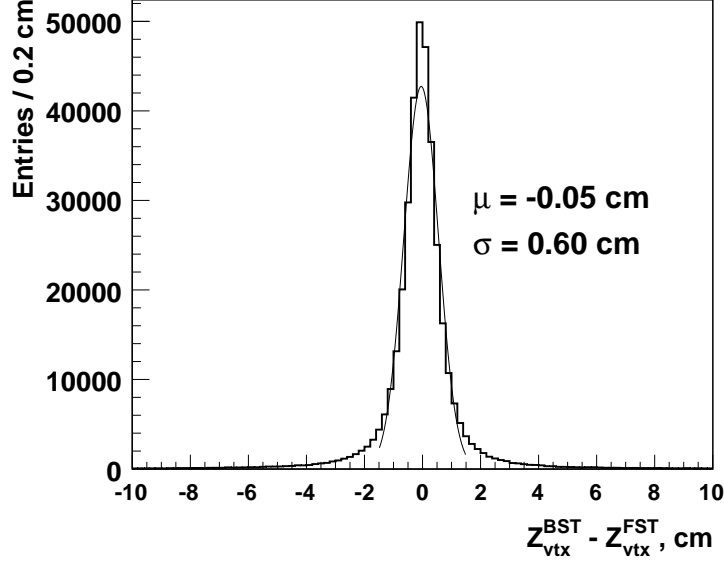


Figure 4.7: Difference of the z position of the vertex as determined independently from FST and BST.

Z Vertex Position Improvement

A stand-alone alignment procedure for FST and BST was developed and the FST and BST were properly aligned to each other and to the central tracker.

Following the procedure described in Chapter 3.6.2, both FST and BST provide a precise vertex measurement with a z precision of $0.60/\sqrt{2} \approx 0.43$ cm, determined from Fig. 4.7, which presents a comparison between the z of the vertex measured by the FST and the BST. The distribution proves also the relative alignment between both detectors, which is a better test than the comparison with the central tracking vertex shown on Fig. 3.19, since the silicon vertex is more precise than the central one.

The precision with respect to the central vertex is presented in Fig. 4.8. On top of a worse resolution to the central vertex, only a weak dependence on the number of CST z hits associated to the corresponding vertex is observed. To take advantage of the precise FST and BST vertex measurement, a procedure improving the H1 primary vertex z position measurement was developed. The procedure is performed only if at least one FST or BST vertex-fitted track (from here on referred to as *silicon track*) exist. The second condition is that the z position of the vertex to which a track is fitted (referred to as *silicon vertex*) is consistent with the z position of the central

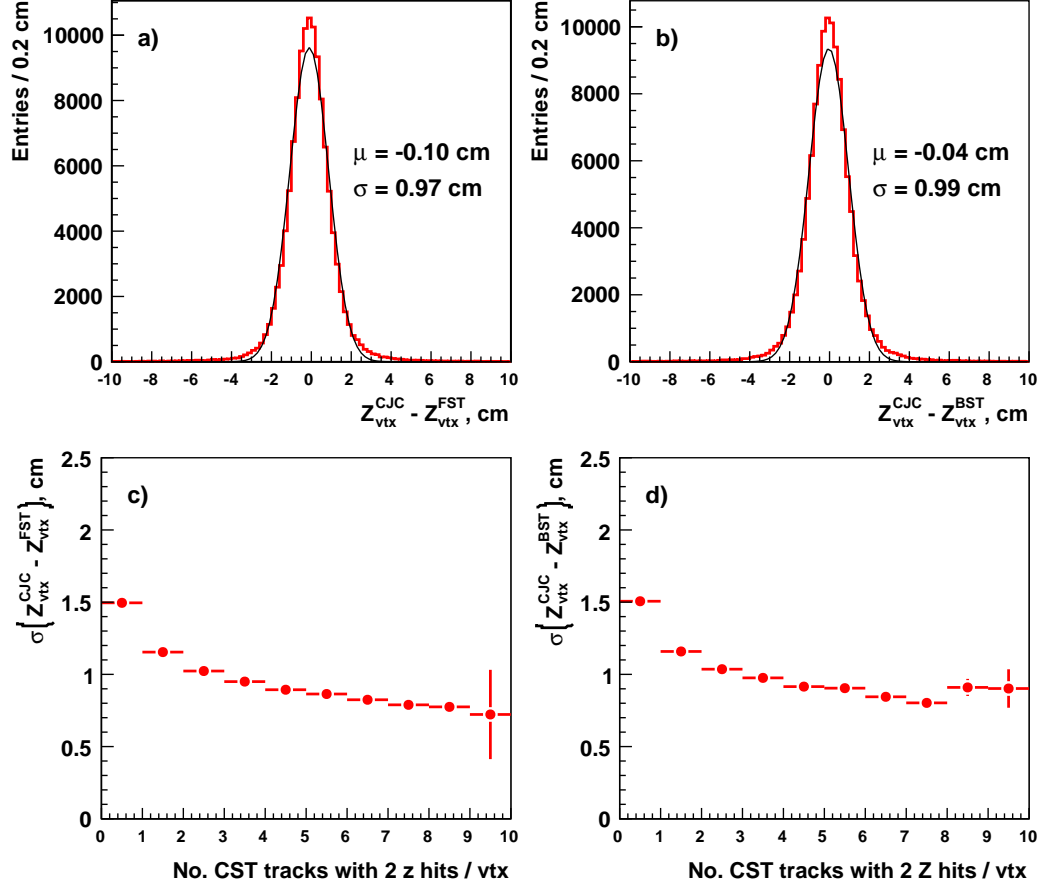


Figure 4.8: Difference of the z position of the vertex determined from the Central Trackers and the FST (a) or BST (b). In figures c) and d), the dependence of the z vertex position difference on the number of tracks with two CST z hits associated to the corresponding vertex is presented.

vertex within the error of the central vertex. If both conditions are met, and an FST (BST) vertex exists, then the z-position of the vertex and its error are updated with the information from the FST (BST) vertex according to the following expressions:

$$Z_{\text{vtx}} = Z_{\text{vtx}}^{\text{old}} + (\Delta Z_{\text{vtx}}^{\text{old}})^2 \frac{Z_{\text{vtx}}^{\text{Si}} - Z_{\text{vtx}}^{\text{old}}}{(\Delta Z_{\text{vtx}}^{\text{old}})^2 + (\Delta Z_{\text{vtx}}^{\text{Si}})^2} \quad (4.6)$$

$$\Delta Z_{\text{vtx}} = \frac{\Delta Z_{\text{vtx}}^{\text{old}} \Delta Z_{\text{vtx}}^{\text{Si}}}{\sqrt{(\Delta Z_{\text{vtx}}^{\text{old}})^2 + (\Delta Z_{\text{vtx}}^{\text{Si}})^2}}, \quad (4.7)$$

where the "Si" subscript stands for values from the FST and the "old" su-

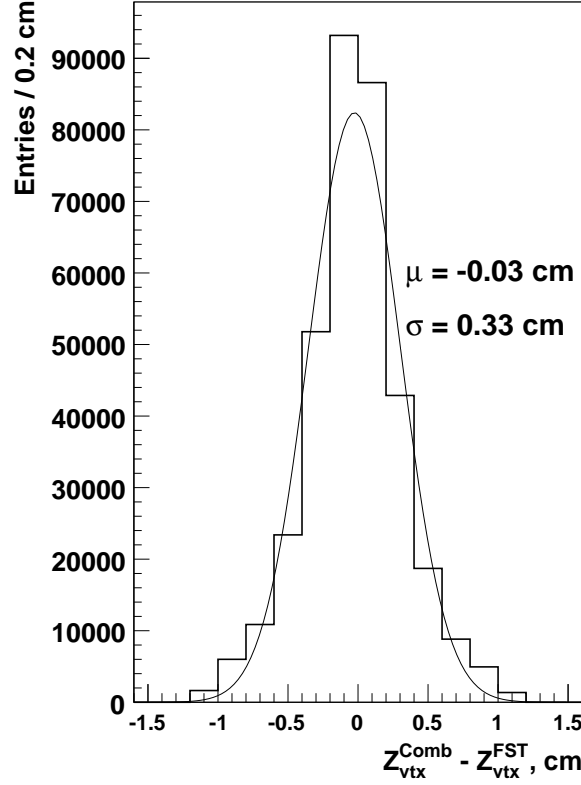


Figure 4.9: Difference of the z position of the combined and the FST vertex.

perscript denotes the values taken from the central reconstruction. The z-position of the corresponding vertex is denoted with Z_{vtx} and ΔZ_{vtx} gives its uncertainty. If both silicon vertices exist, first the vertex z position is updated with the FST information. Then, if the BST vertex is consistent with the z position of the updated vertex, it is once more updated using expressions (4.6) and (4.7), this time using BST information. In Fig. 4.9 the difference of the combined and FST vertex is shown. A clear improvement of $\sigma = 0.33 \text{ cm}$ is visible.

Polar Angle Improvement

As explained in Chapter 2.2.9, the θ and Z_0 parameters of the central non-vertex fitted tracks, depending on the $(r - z)$ CJC measurement are imprecise. This effect becomes more severe if the track polar angle starts getting out of the CJC acceptance of $\sim 40^\circ - 160^\circ$, and the number of hits associated to the track starts to diminish. At a later stage of the reconstruction, if these tracks are successfully fitted to a vertex, their track parameter quality,

mainly the polar angle resolution, depends on the z resolution of the vertex. Actually there is a direct linear dependence of the type $\sigma(\theta) = \sigma(Z) C_{\theta Z}$ between the theta measurement uncertainty $\sigma(\theta)$ and the uncertainty of the z position measurement of the vertex to which the track is associated $\sigma(Z)$, with an average correlation coefficient of $C_{\theta Z} = 0.9882$. Thus, after the update of the z position of the vertex explained in the previous paragraph, the polar angle of all tracks associated to the vertex updated are also updated, as well as the associated measured error of the polar angle at the vertex point using the following expressions:

$$\theta = \theta^{\text{old}} + C_{\theta Z} \frac{\Delta\theta^{\text{old}} \Delta Z_{\text{vtx}}^{\text{old}}}{(\Delta Z_{\text{vtx}}^{\text{old}})^2 + (\Delta Z_{\text{vtx}}^{\text{Si}})^2} (Z_{\text{vtx}}^{\text{Si}} - Z_{\text{vtx}}^{\text{old}}) \quad (4.8)$$

$$\Delta\theta = \Delta\theta^{\text{old}} \sqrt{\frac{(\Delta Z_{\text{vtx}}^{\text{Si}})^2 + (1 - C_{\theta Z}^2) (\Delta Z_{\text{vtx}}^{\text{old}})^2}{(\Delta Z_{\text{vtx}}^{\text{old}})^2 + (\Delta Z_{\text{vtx}}^{\text{Si}})^2}}. \quad (4.9)$$

The effect on the procedure is visible on the scattered plot of the θ_{sim} vs. θ_{rec} parameter of the tracks, presented in Fig. 4.10. A comparison between the reconstructed and the simulated polar angle of the central tracks before (green points) and after (red points) the improvement by the FST. A clear improvement of the central tracks' θ up to the precision of the pure silicon tracks depicted in blue is visible.

Improve CJC tracks with FST and BST

As discussed earlier it is impossible to find all three D* decay products in either FST or BST alone due to their small geometrical acceptance. Both detectors still offer an abundance of quality tracks in a highly interesting phase space, which are the key component needed to double the standard D* analysis. If one of the D* decay tracks is in the FST (BST) acceptance, then the other two tracks left should be measured in the CT, usually near the first track, and thus close to the edge of CJC acceptance. Exactly in that region, the probability for one of the tracks to be reconstructed by the CJC with large uncertainties, and later on to smear out the D* signal is high, which makes a procedure to improve the central tracks with FST and BST hit information vital.

The procedure of improving the central tracks is performed starting from the set of all central vertex-fitted tracks. If the track polar angle estimated by the CT reconstruction is smaller than 75° , the track is extrapolated to the nominal z-positions of each FST detector planes. The extrapolation procedure considers all planes with different positions: 5 silicon planes each

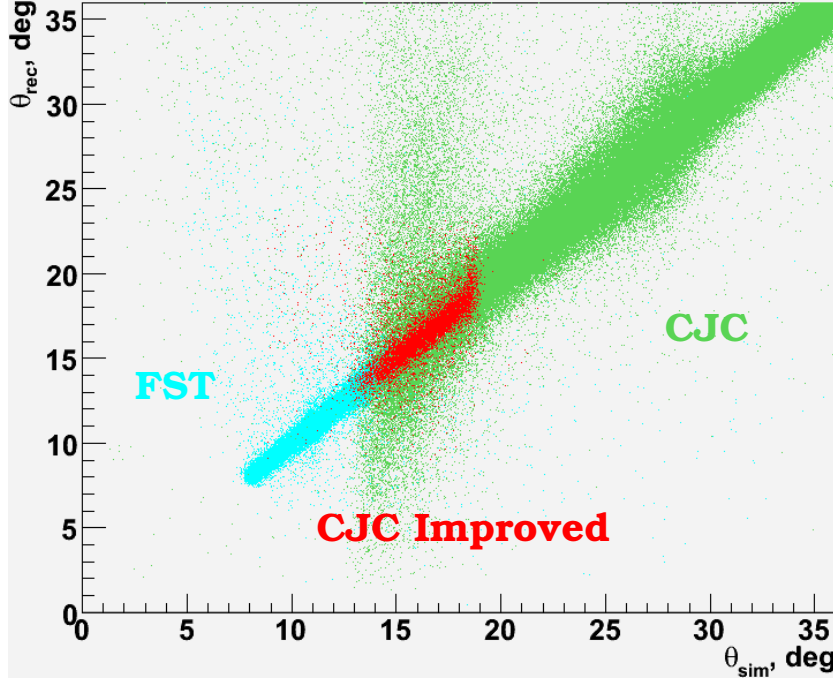


Figure 4.10: Simulated track polar angle θ_{sim} vs. reconstructed track polar angle θ_{rec} distribution.

consisting of one u-plane shifted from one v-plane, and each u or v plane having odd and even sectors staggered in z. All shifts are outlined in Table 3.3. If the track has a polar angle larger than 105° , the same procedure is performed using the BST. All the rest of the central tracks, which have $75^\circ < \theta < 105^\circ$ are not considered. After extrapolating a track to a given plane, if the extrapolated point is in the silicon sensitive acceptance (see Table 4.7) and there is a hit in the plane matching the r_{res} cut stated in Table 4.7, then the hit is accepted for the final refitting. If more than one hit is found in the given plane, the hit closest to the extrapolated point is taken. The same procedure is repeated for all planes, and finally ends with a set of hits found, selected for track refitting. The track is being refitted, using the Kalman Filter package included in the FST reconstruction package. A hit is rejected if it adds more than twice the average χ^2/ndf of the track. If the track is successfully updated with at least one hit, it is further on labelled as an FST improved or a BST improved track. The improvement achieved in track parameters can be seen on Fig. 4.11.

Throughout this thesis, five different categories of tracks are distinguished, depending on the origin of the track. To distinguish the corresponding plots for each type of tracks, a corresponding color is introduced for each one of

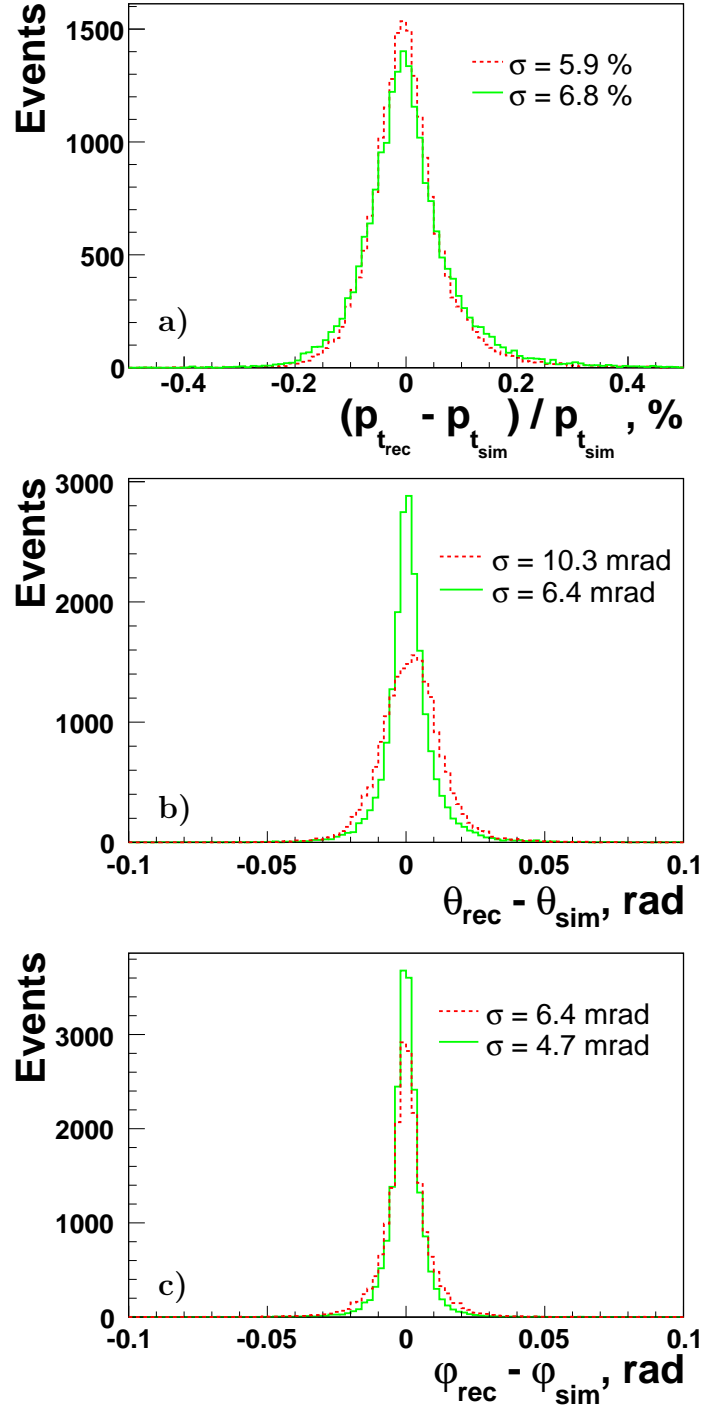


Figure 4.11: Central track parameter resolutions before (solid line) and after (dashed line) adding FST information.

minimal azimuthal angle, φ_{\min}	-130°
maximal azimuthal angle, φ_{\max}	130°
minimal radius, r_{\min}	$r_{\min}^{\text{Si}} + 0.3 \text{ cm}$
maximal radius, r_{\max}	$r_{\max}^{\text{Si}} - 0.3 \text{ cm}$
hit rejection criteria, r_{res}	2.0 cm

Table 4.7: Cuts on the extrapolated CJC tracks. The parameters r_{\min}^{Si} and r_{\max}^{Si} are the nominal radial limits of the silicon active area as given in rows 10 and 11 of Table 3.3.

them. The groups are the following:

- **FST Track** - A track produced from the FST reconstruction based only on FST information. The color chosen for the relevant histogram is blue.
- **FST Improved Track** - A track initiated by the central reconstruction, but improved by FST hits. The histograms for this set of tracks are green colored.
- **CJC Track** - A track, which is reconstructed fully in the central tracking system. The corresponding plots are red-colored.
- **BST Improved Track** - A track, which started as a central track, and was further improved by at least one BST hit. The properties related to this type of tracks are depicted using brown color.
- **BST Track** - A track fully reconstructed in BST, using only silicon information. For those histograms, the black color has been chosen.

4.5.2 D^* Finding

The $D^{*\pm}$ finding is performed over a given set of tracks. In the current analysis a combined set of tracks is formed from the five set of tracks mentioned in the previous subsection. Every combination is in the following referred to as D^* candidate. Depending on the type of tracks used for their reconstruction, the D^* candidates are unambiguously classified into five different categories as follows:

- **FST D^*** - A D^* candidate belongs to this group if one or more of its decay particles tracks are measured entirely by FST. The histograms concerning this type of candidates are styled in blue open triangles.

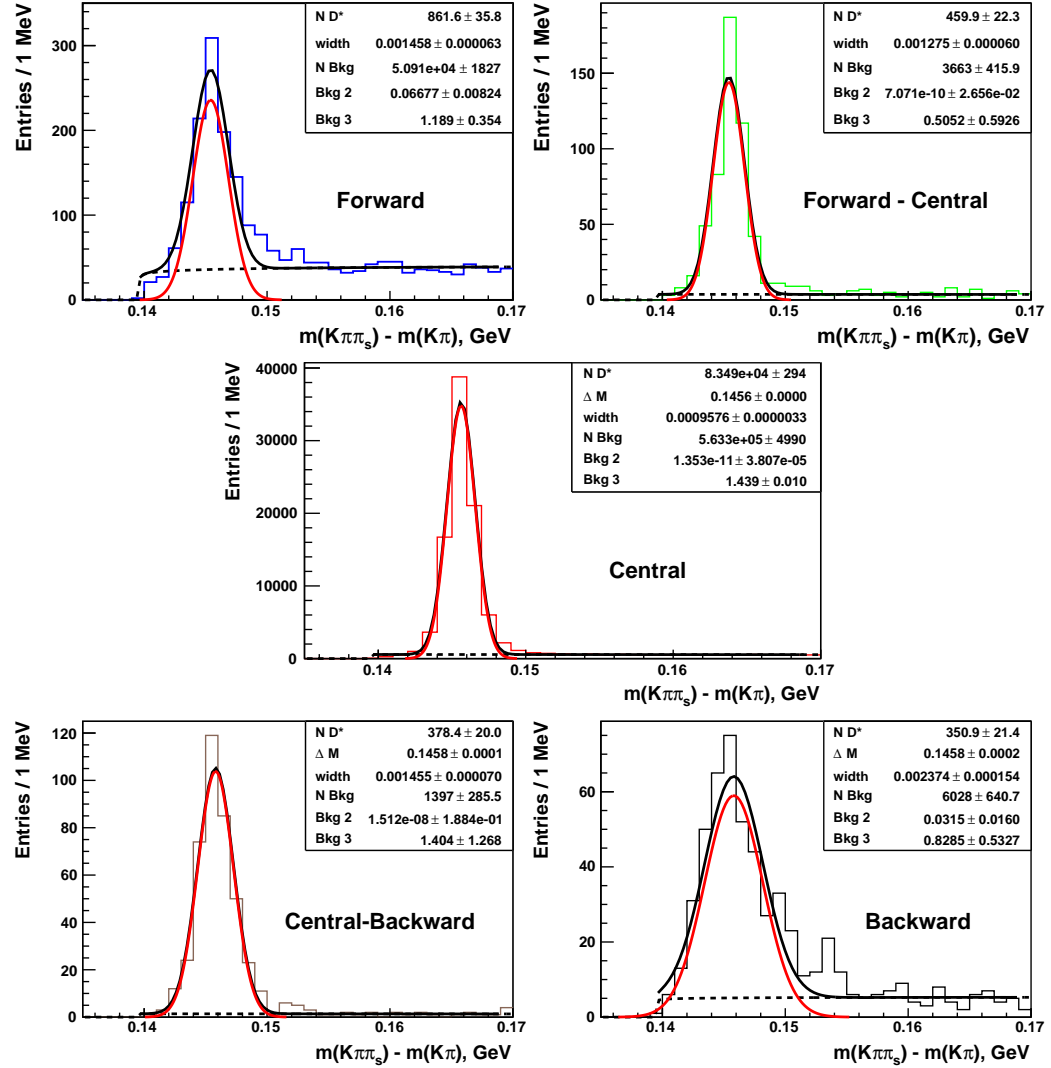


Figure 4.12: Rapgap Monte Carlo distribution of the difference Δm between the reconstructed invariant mass of the D^* candidate and the reconstructed D^0 candidate. Different histograms represent different D^* candidate classes defined in Chapter 4.5.1.

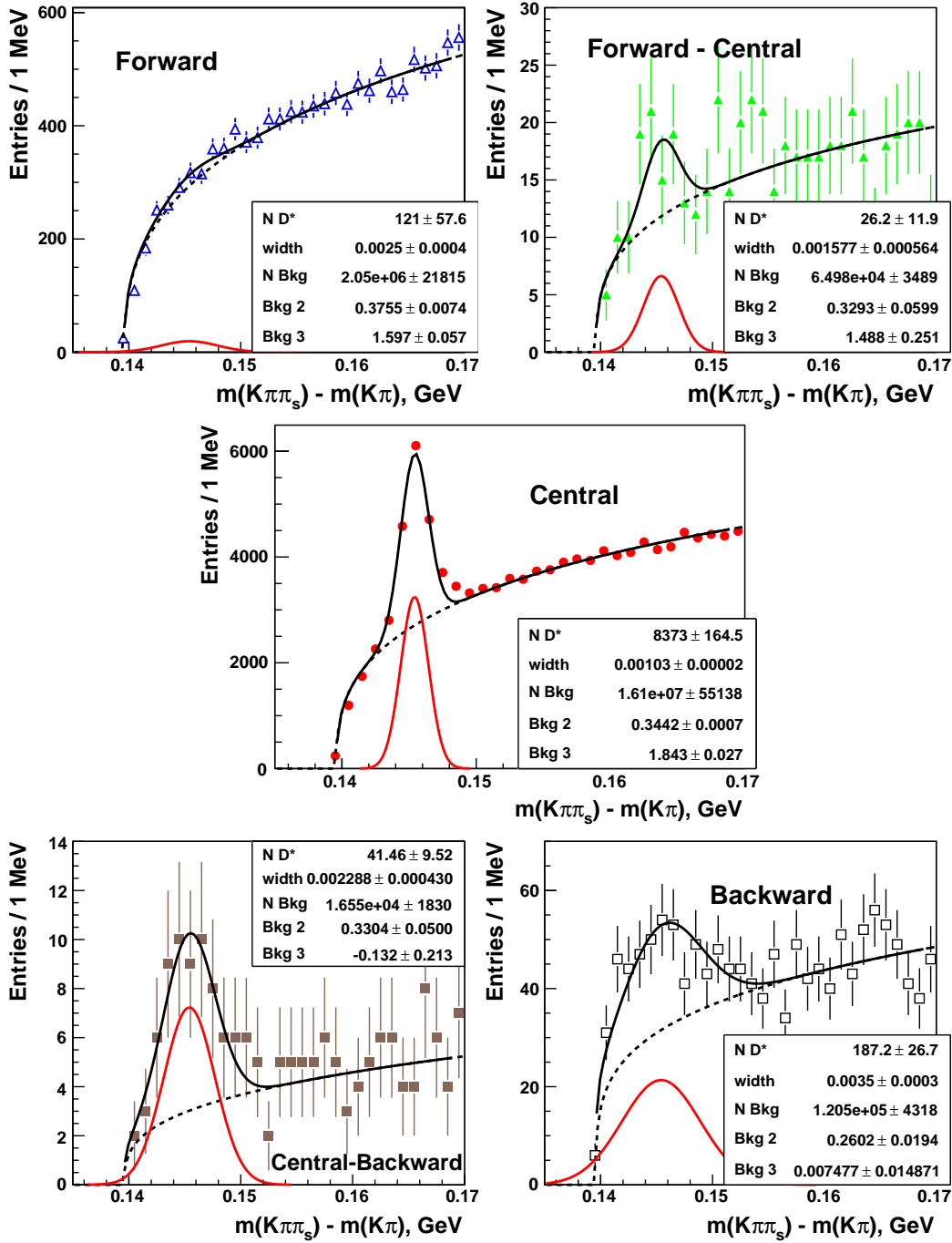


Figure 4.13: The difference Δm between the reconstructed invariant mass of the D^* candidate and the reconstructed D^0 candidate for real data. Figures a) - e) the different classes of candidates as explained earlier in the text.

	BST	BST Impr	CJC	FST Impr	FST
CJC hits	> 0	> 0	> 15	> 15	> 15
FST/BST hits	> 0	> 0	-	> 0	> 0
FST/BST improved hits	> 0	-	-	-	> 8
FST/BST track polar angle $\theta, ^\circ$	> 105	-	-	-	< 75
FST/BST or FST/BST improved track azimuthal angle $ \varphi , ^\circ$	< 130	< 130	-	< 130	< 130
$p_t(K^\mp), \text{ GeV}$	> 0.3	> 0.3	> 0.3	> 0.3	> 0.3
$p_t(\pi^\pm), \text{ GeV}$	> 0.3	> 0.3	> 0.3	> 0.3	> 0.3
$p_t(\pi_s^\pm), \text{ GeV}$	> 0.12	> 0.12	> 0.12	> 0.12	> 0.12
$p_t(K^\mp\pi^\pm), \text{ GeV}$	> 2.0	> 2.0	> 2.0	> 2.0	> 2.0
$p_t(D^*), \text{ GeV}$	> 1.5	> 1.5	> 1.5	> 1.5	> 1.5
$\eta_{min}(D^*)$	> -2.5	> -2.0	> -1.5	> 1.0	> 1.5
$\eta_{max}(D^*)$	< -1.5	< -1.0	< 1.5	< 2.0	< 2.5
$m(D^0) - m(K^\mp\pi^\pm), \text{ GeV}$	< 0.24	< 0.05	< 0.08	< 0.05	< 0.12
$m(D^*) - m(D^0) -$	< 7.5	< 4.5	< 3.0	< 4.5	< 7.5
$m(K^\mp\pi^\pm\pi_s^\pm) + m(K^\mp\pi^\pm),$ MeV					

Table 4.8: Conditions applied on different types of D^* candidates. For types definition see text.

- **FST Improved D^*** - Candidates in which at least one of the decay tracks is improved with FST hits, and none of them is reconstructed by FST only. The corresponding plots are styled in green full triangles.
- **CJC D^*** - All three decay tracks are reconstructed by the central tracking only. No information from FST or BST is used for these D^* candidates. The figures related to this type of D^* candidates are styled in red full circles.
- **BST Improved D^*** - In this case, at least one of the decay particle tracks are improved with BST hits. All other tracks are reconstructed by the central tracking system. The corresponding quantities are drawn styled in brown full squares.
- **BST D^*** - Candidates, with at least one track reconstructed by the

BST only. The plots concerning this category are plotted using black open squares.

First, sequentially all combinations of three tracks two of which are positive and one negative (D^{*+} candidate) or two negative and one positive track (D^{*-} candidate) are searched for. Next, depending on the origin of the tracks, the D^* candidate is associated to one of the categories described earlier. For each track the corresponding kaon or pion mass hypothesis is assumed. Next, depending on the category, the corresponding track quality cuts described in Table 4.8 are applied. Next, the kaon and pion pair invariant mass should fit to the D^0 nominal mass within the corresponding category limits as given in Table 4.8. All combinations failed are not considered further. A separate Δm distribution is made for each of the D^* candidates categories. The Monte Carlo distributions for all categories are presented in Fig. 4.12 and the corresponding distributions for the data is presented in Fig. 4.13. Out of both distribution, after considering the corresponding binning, the number of D^* mesons is extracted, as explained in the next section and used for acceptance and cross section calculation.

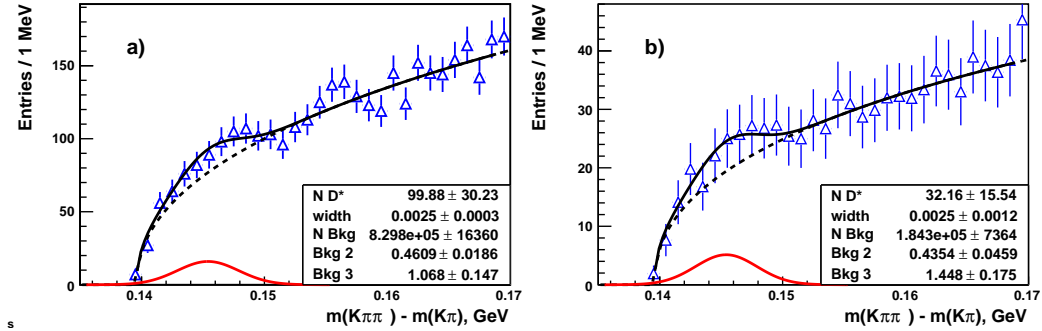


Figure 4.14: The forward data reconstructed Δm distribution under different conditions: a) $x < 0.001$, b) dE/dx wighted.

Several attempts were made to reduce the strong combinatorical background coming mainly from the proton remnants in the very forward FST region. First, through a low x cut $x < 0.001$ the hadronic system was forced to go into the backward direction. A better forward D^* signal is visible in Fig. 4.14 a). Second, track weights from the ionization dE/dx in the central tracker were applied in order to support the $K^\mp \pi^\pm \pi^\pm$ hypothesis. This results in the improved signal shown in Fig. 4.14 b). The efficiencies of dE/dx calculation are, however, not fully understood. Hence, this improved signal could not be used for cross section determination.

For all categories of D^* mesons defined earlier and their decay products, the reconstructed kinematic parameters from data and Monte Carlo simulation should reasonably agree in order to be allowed to use the Monte Carlo to calculate acceptance and efficiency. For the D^* meson the distributions of the momentum, its transverse component as well as its polar and azimuthal angles are compared for data and Monte Carlo in Fig. 4.15, 4.16, 4.17 and 4.18, respectively. The momentum distribution if the D^0 meson is presented on Fig. 4.19. Finally a comparison of the distributions of the momentum, the transverse momentum and the corresponding track length for all three D^* decay products is depicted on Fig. 4.20 to 4.28. In all cases the Monte Carlo describes reasonably the data.

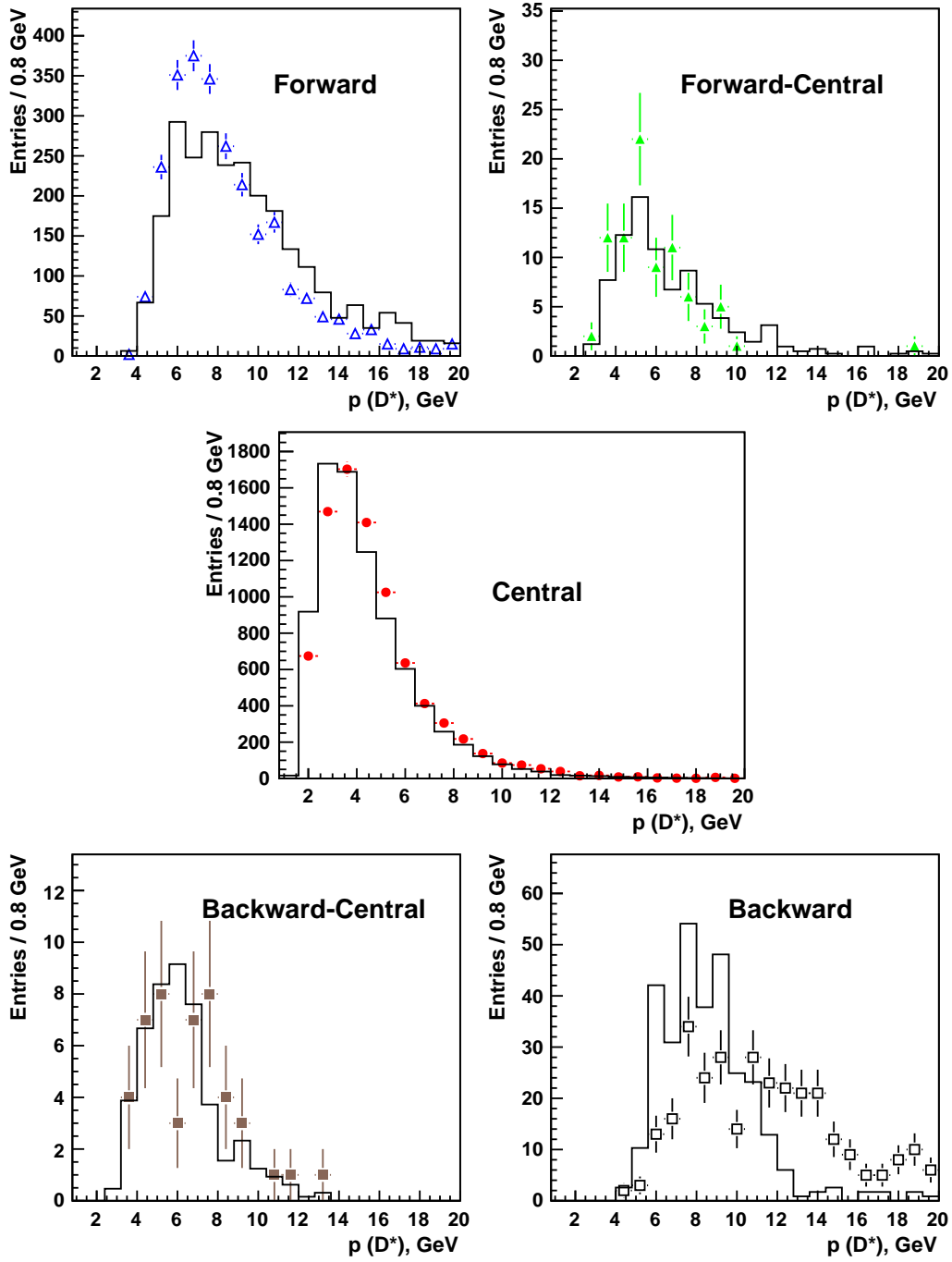


Figure 4.15: Comparison between data and Rapgap Monte Carlo histogram of the D^* meson reconstructed momentum $p(D^*)$ for the different D^* categories defined in Chapter 4.5.1. The statistical subtraction method is used for the central plot only.

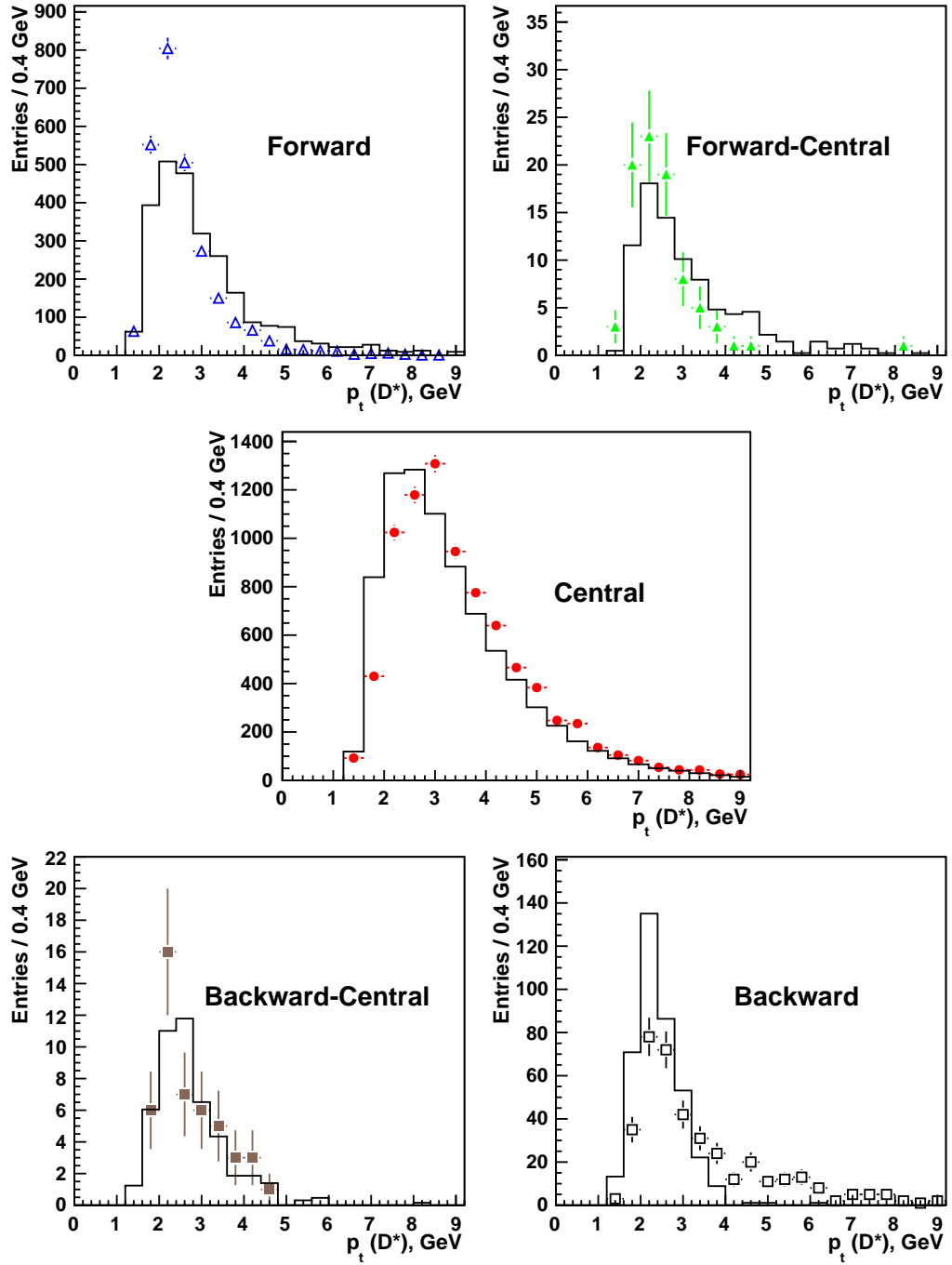


Figure 4.16: Comparison between data and Rapgap Monte Carlo histogram of the D^* meson reconstructed transverse momentum $p_t(D^*)$ for the different D^* categories defined in Chapter 4.5.1. The statistical subtraction method is used for the central plot only.

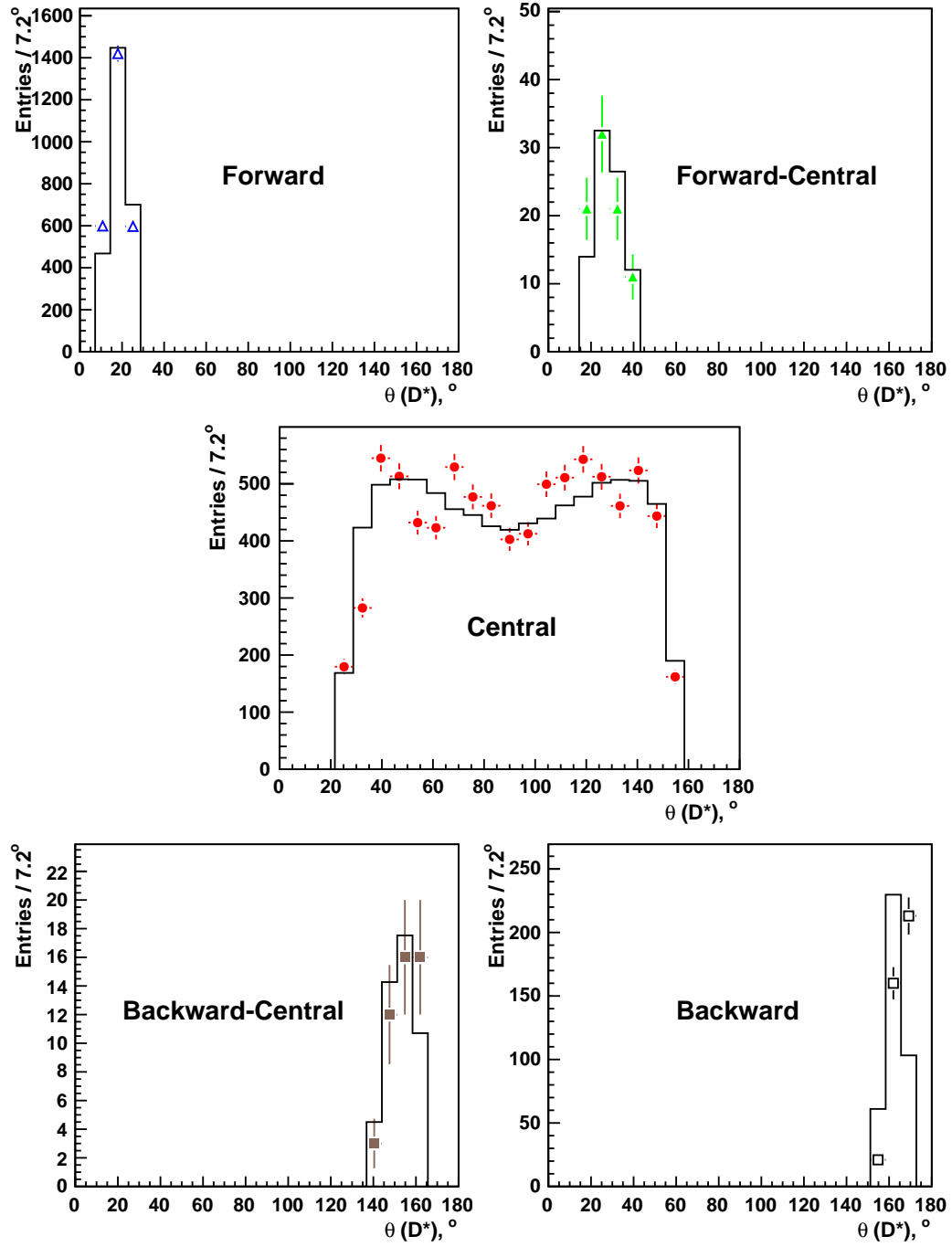


Figure 4.17: Comparison between data and Rapgap Monte Carlo histogram of the D^* meson reconstructed polar angle $\theta(D^*)$ for the different D^* categories defined in Chapter 4.5.1. The statistical subtraction method is used for the central plot only.

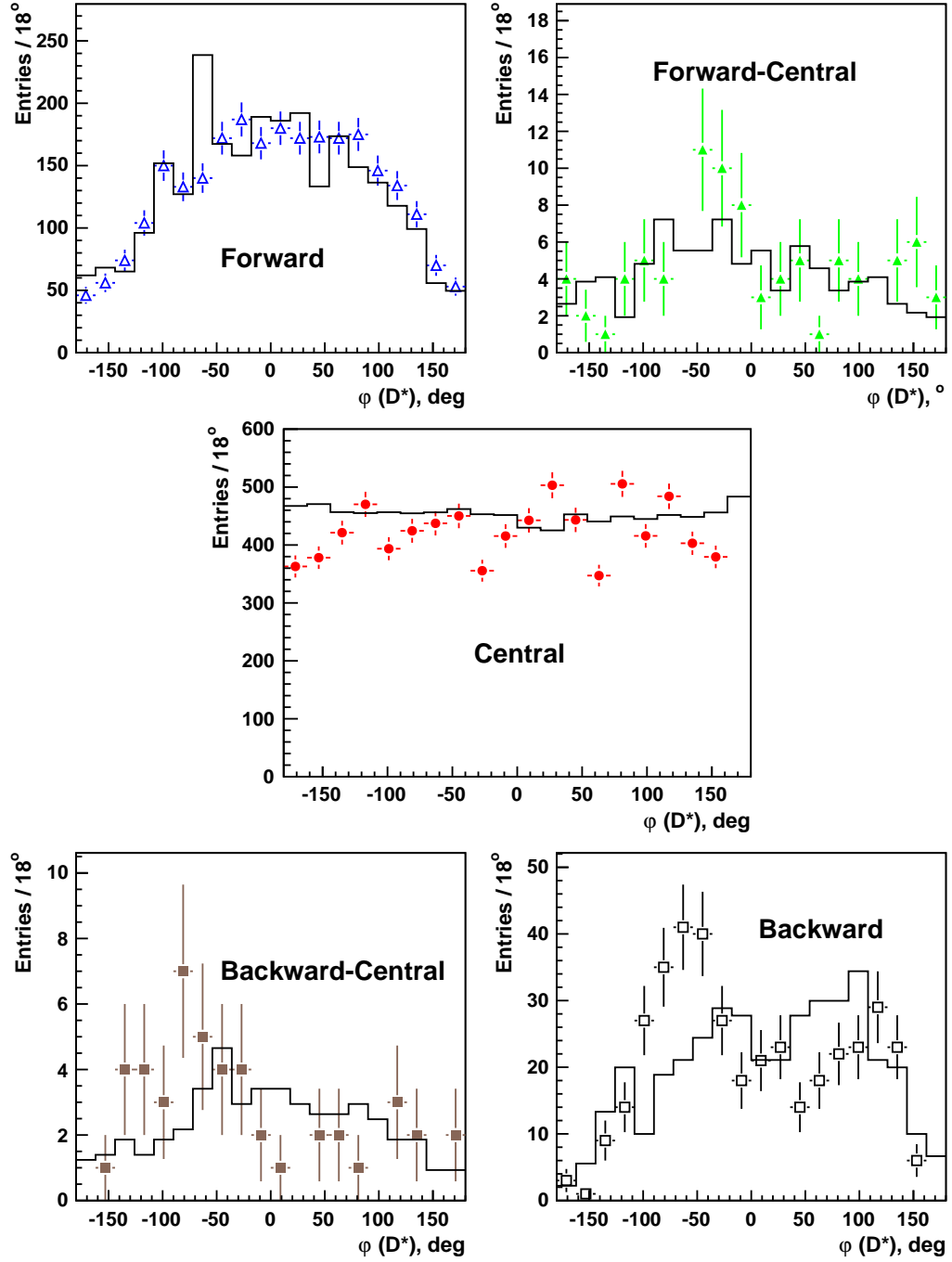


Figure 4.18: Comparison between data and Rapgap Monte Carlo histogram of the D^* meson reconstructed azimuthal angle $\varphi(D^*)$ for the different D^* categories defined in Chapter 4.5.1. The statistical subtraction method is used for the central plot only.

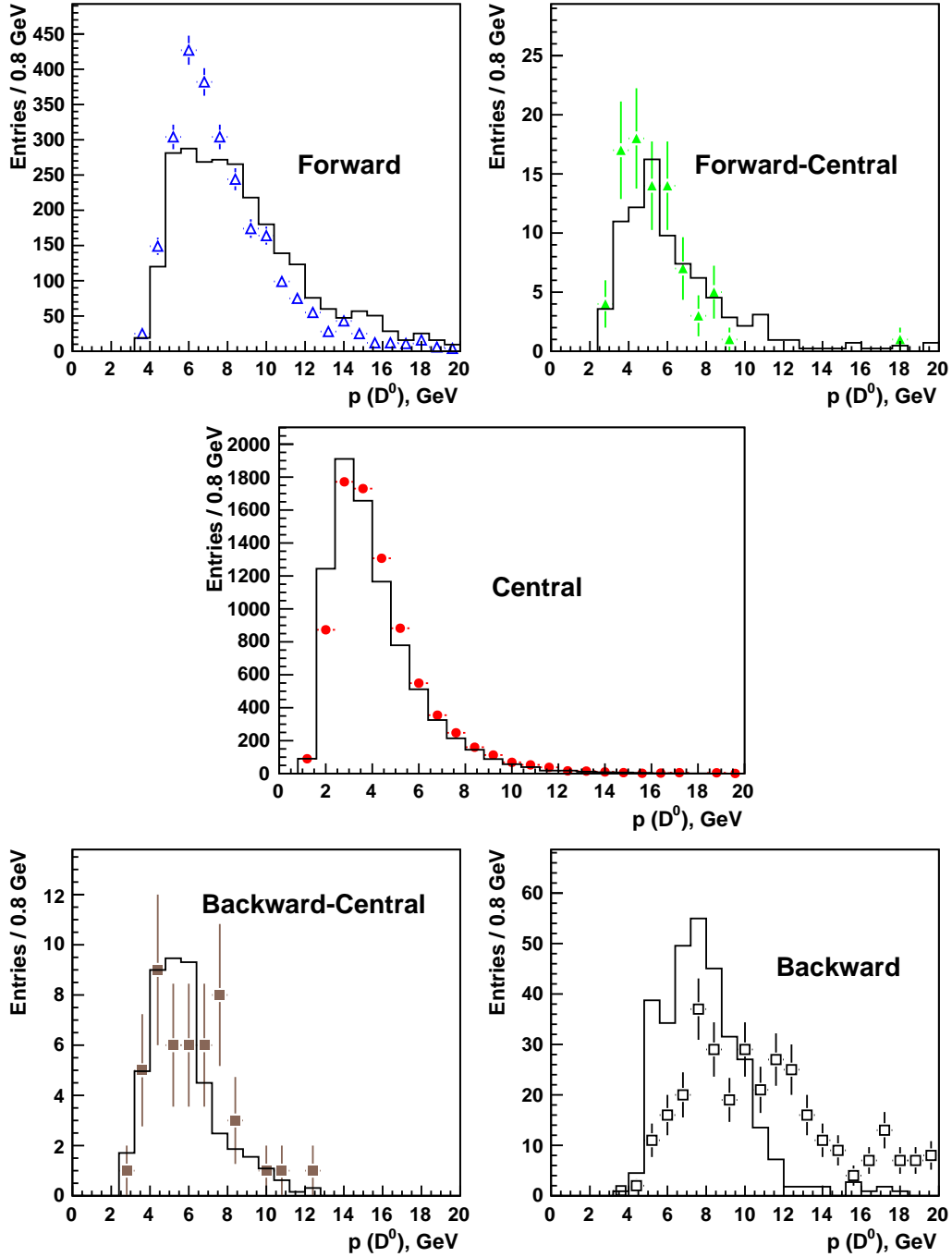


Figure 4.19: Comparison between data and Rapgap Monte Carlo histogram of the D^0 meson reconstructed momentum $p(D^0)$ for the different D^* categories defined in Chapter 4.5.1. The statistical subtraction method is used for the central plot only.

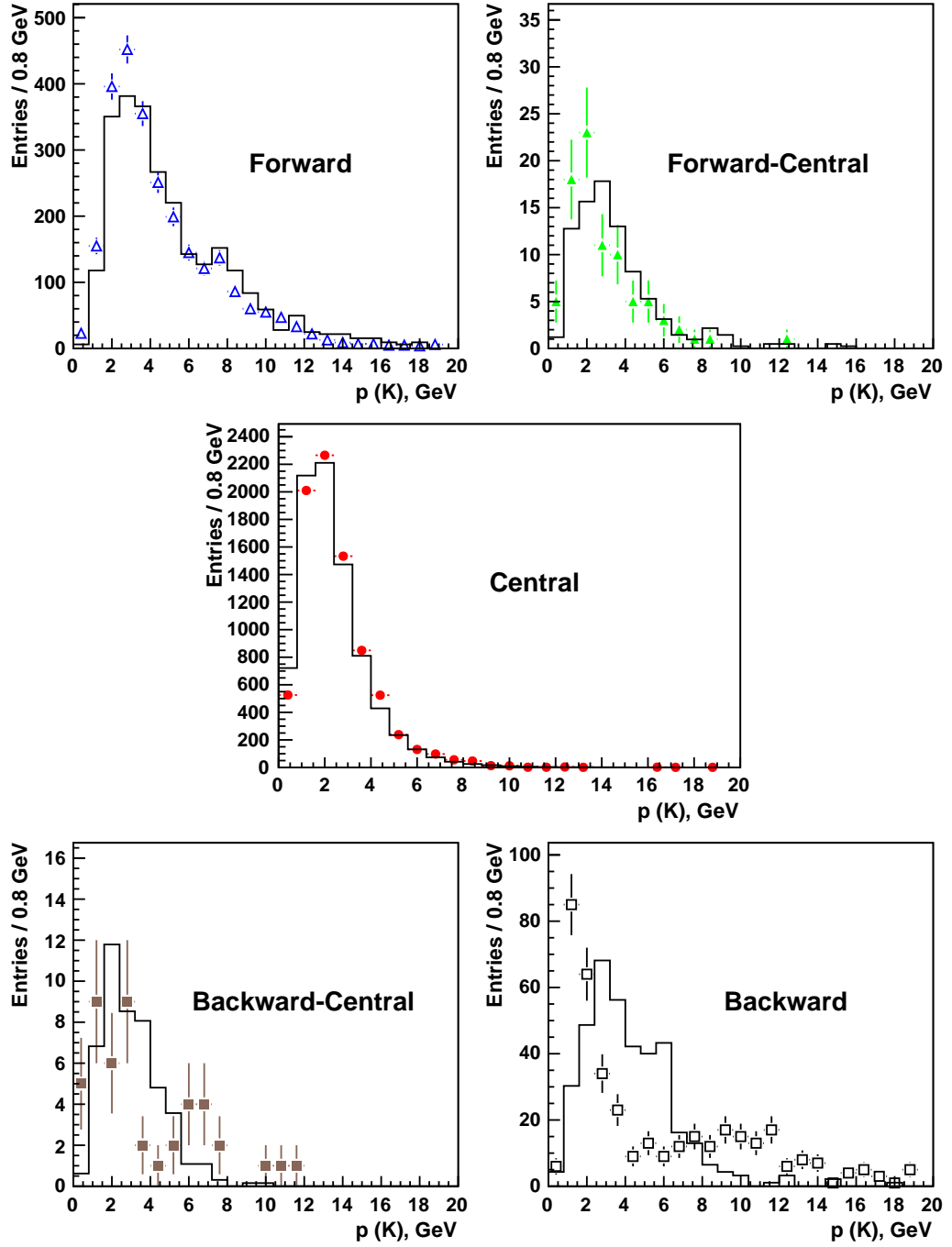


Figure 4.20: Comparison between data and Rapgap Monte Carlo histogram of the K meson reconstructed momentum $p(K)$ for the different D^* categories defined in Chapter 4.5.1. The statistical subtraction method is used for the central plot only.

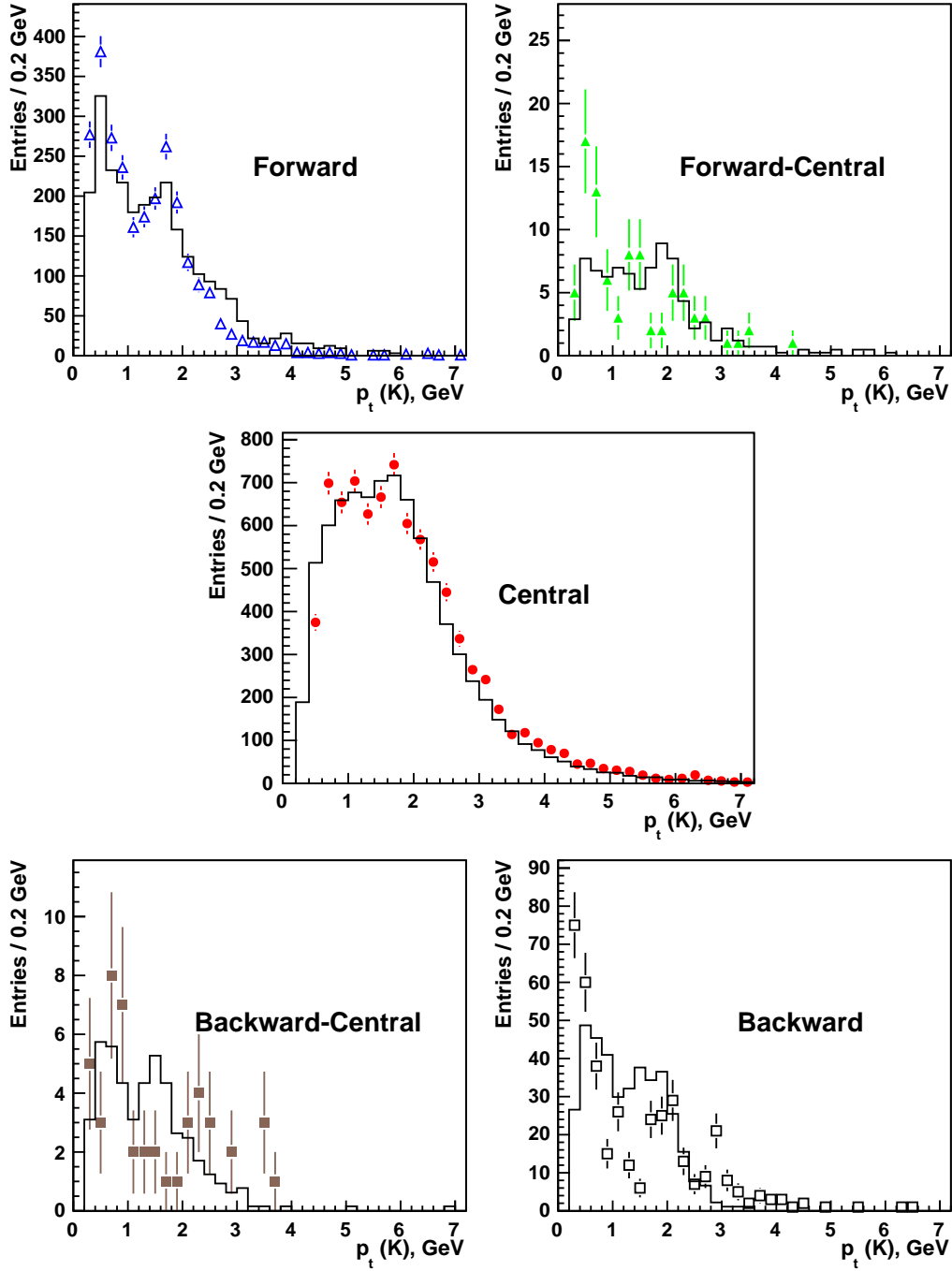


Figure 4.21: Comparison between data and Rapgap Monte Carlo histogram of the K meson reconstructed transverse momentum $p_t(K)$ for the different D^* categories defined in Chapter 4.5.1. The statistical subtraction method is used for the central plot only.

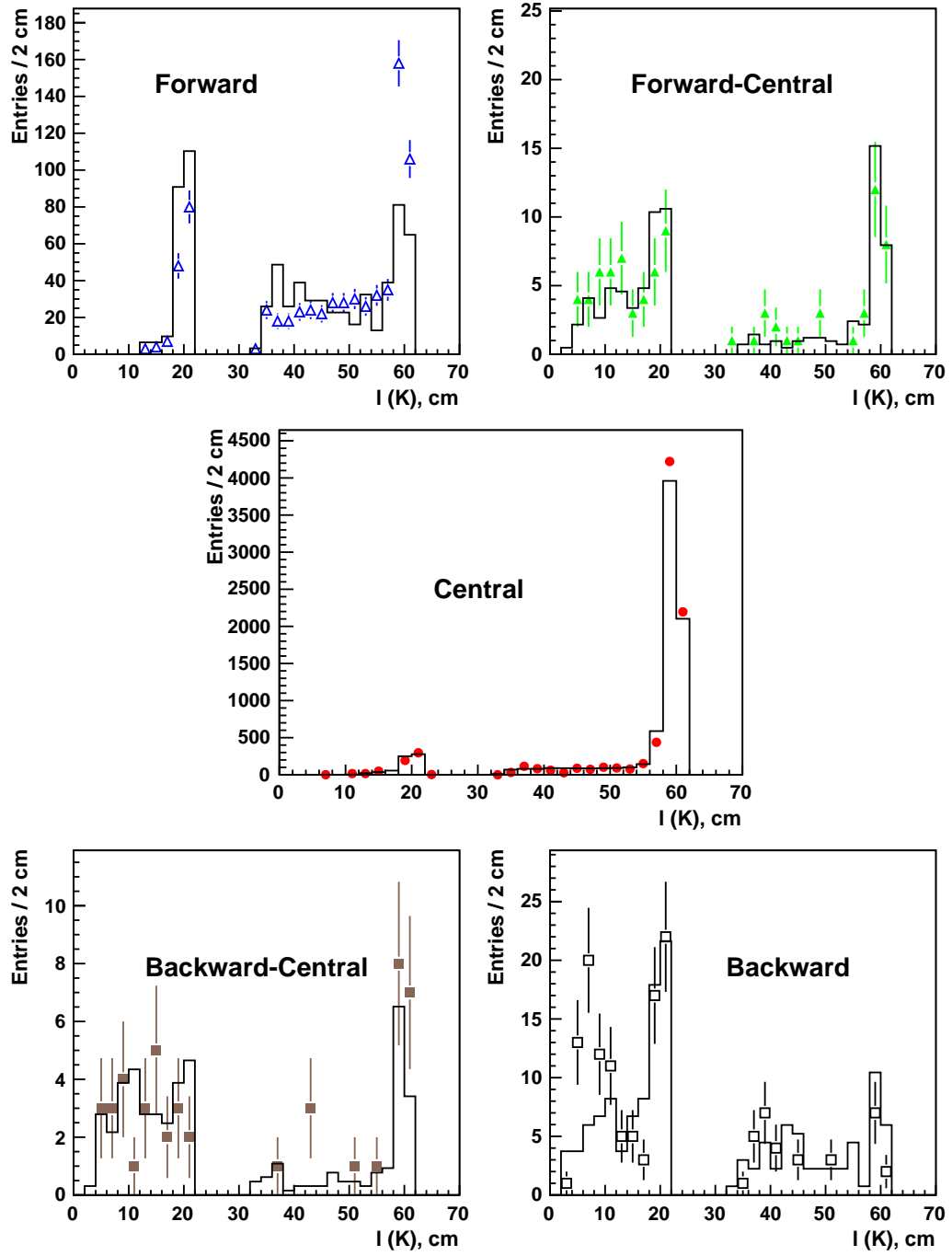


Figure 4.22: Comparison between data and Rapgap Monte Carlo histogram of the K meson reconstructed track length $l(K)$ for the different D^* categories defined in Chapter 4.5.1. The statistical subtraction method is used for the central plot only.

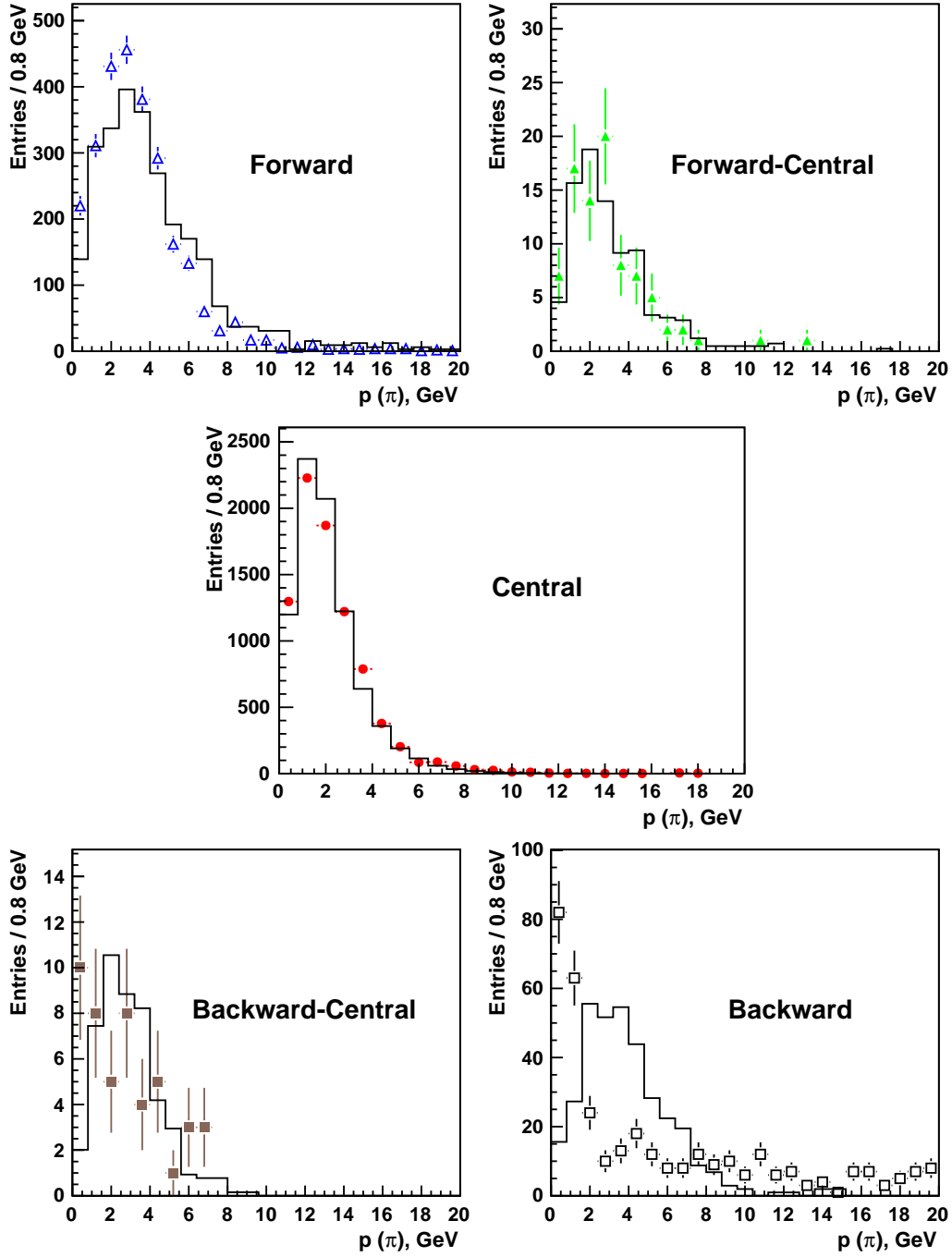


Figure 4.23: Comparison between data and Rapgap Monte Carlo histogram of the π meson reconstructed momentum $p(\pi)$ for the different D^* categories defined in Chapter 4.5.1. The statistical subtraction method is used for the central plot only.

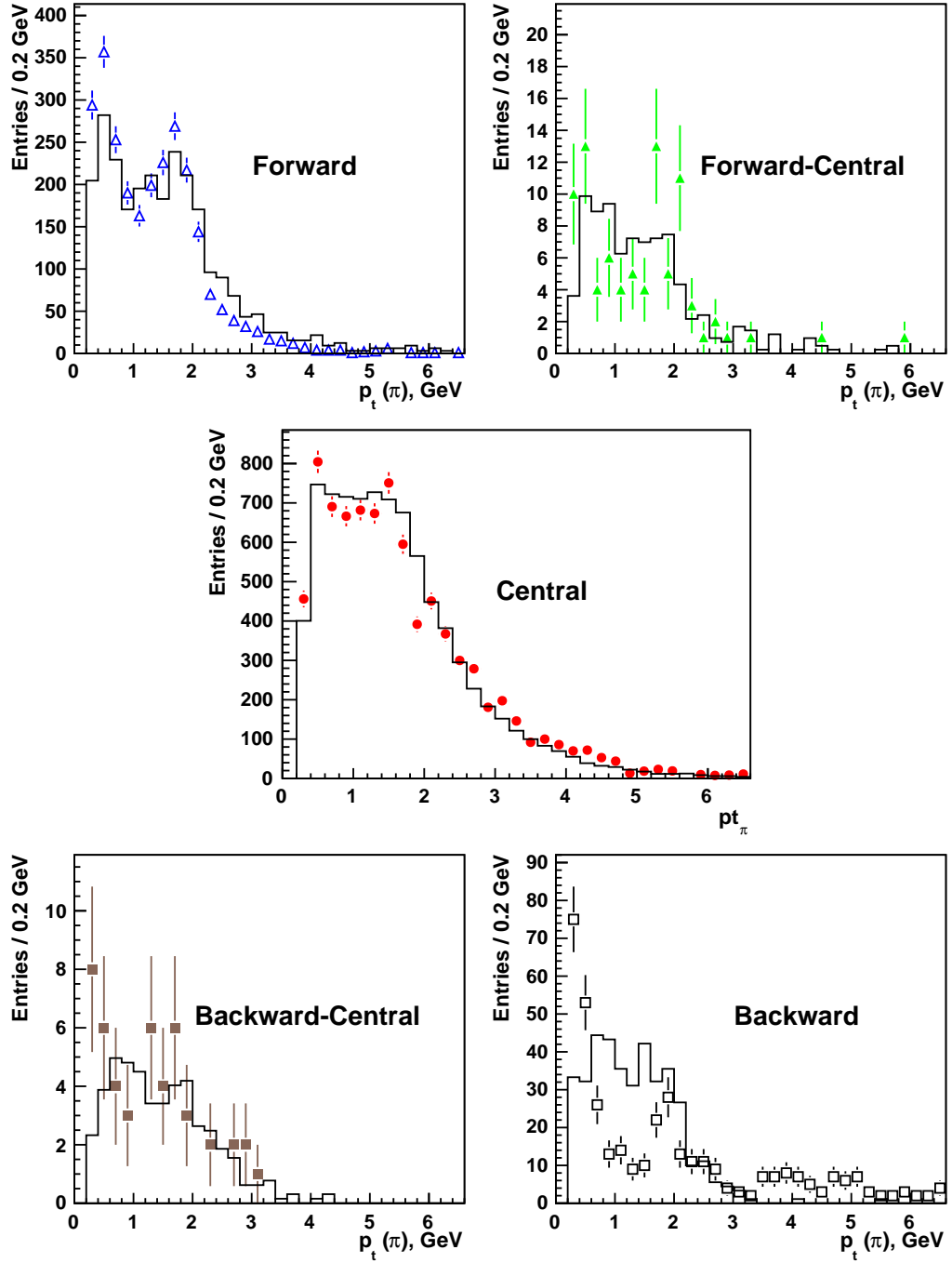


Figure 4.24: Comparison between data and Rapgap Monte Carlo histogram of the π meson reconstructed transverse momentum $p_t(\pi)$ for the different D^* categories defined in Chapter 4.5.1. The statistical subtraction method is used for the central plot only.

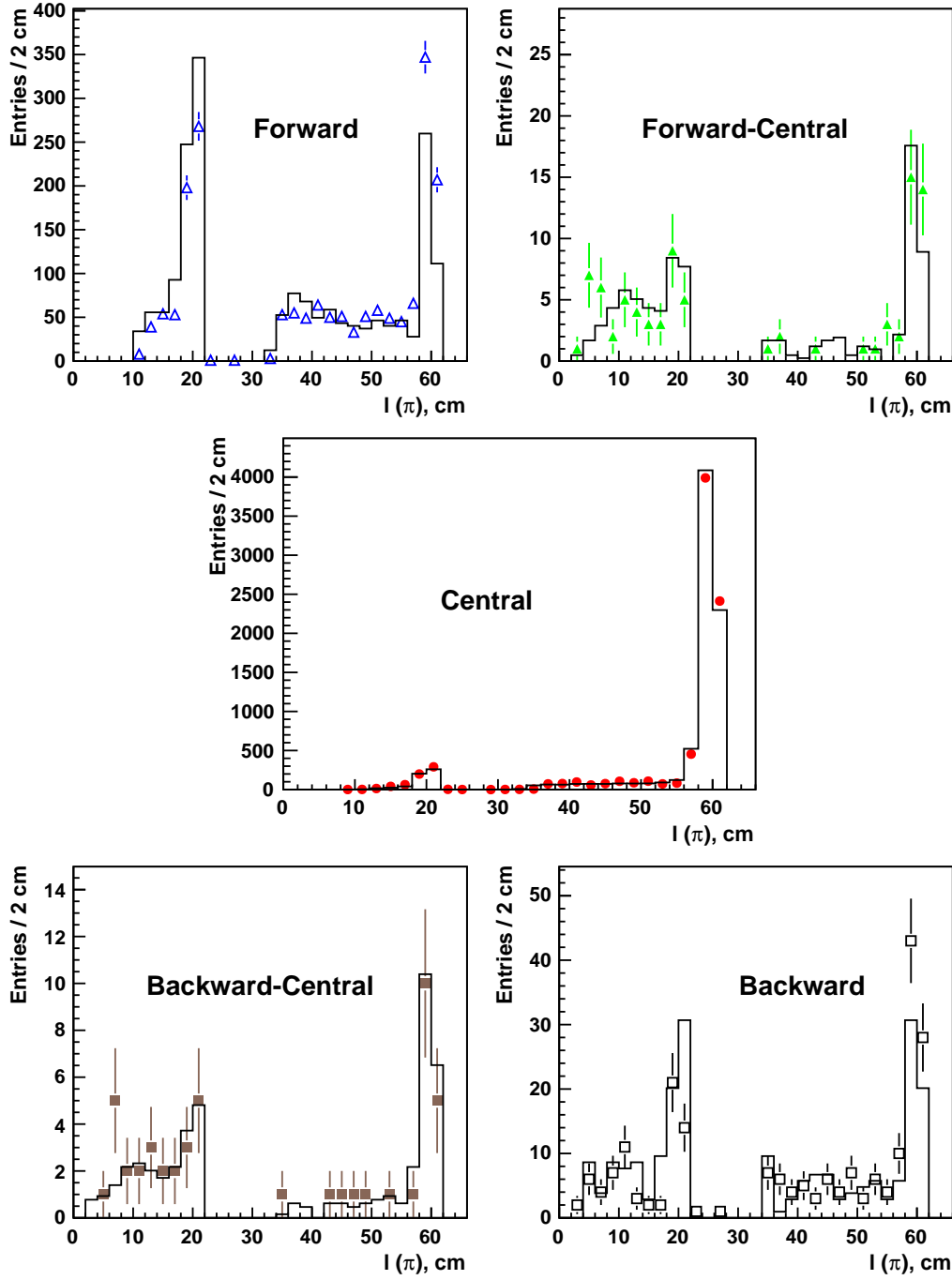


Figure 4.25: Comparison between data and Rapgap Monte Carlo histogram of the π meson. The reconstructed track length $l(\pi)$ for the different D^* categories defined in Chapter 4.5.1. The statistical subtraction method is used for the central plot only.

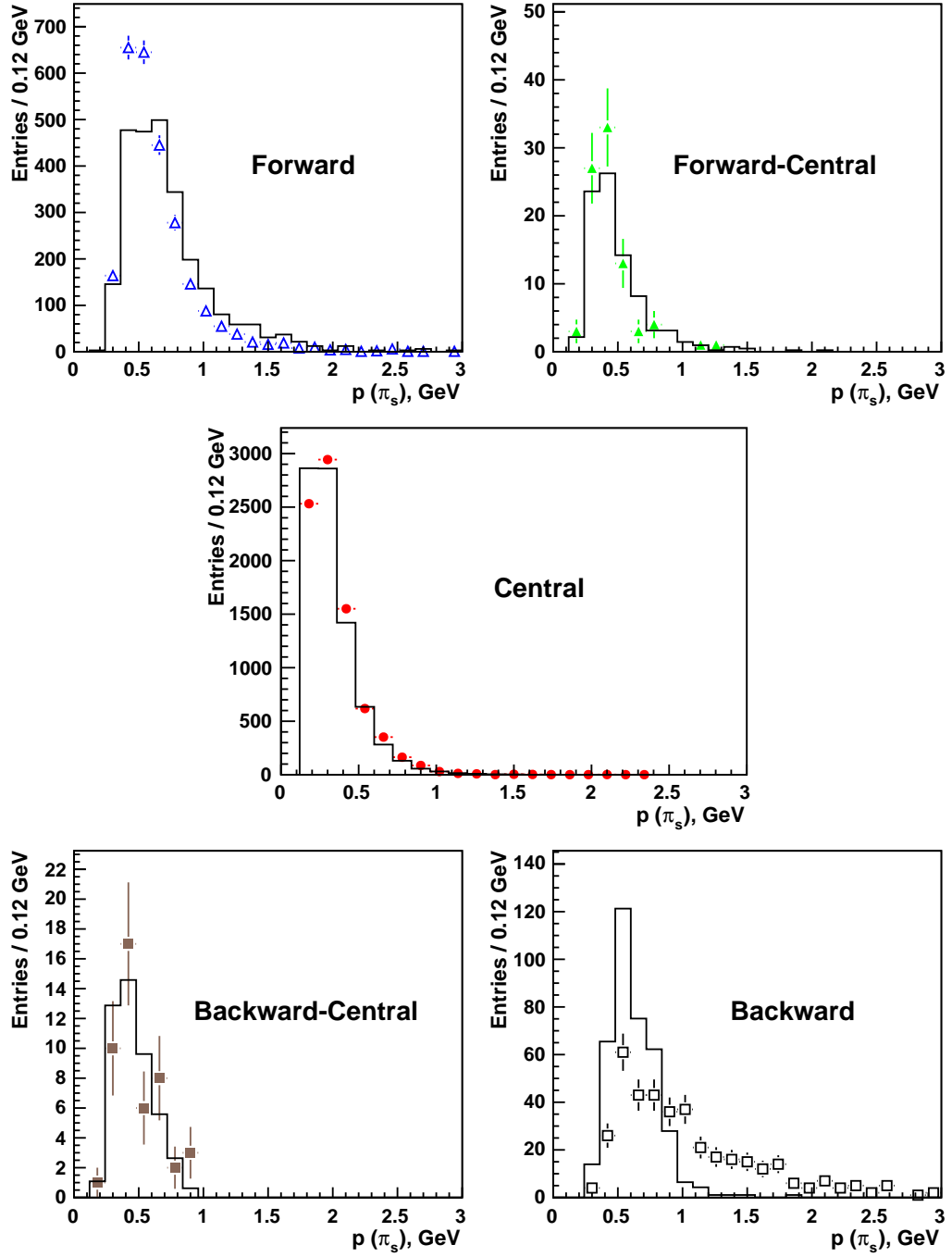


Figure 4.26: Comparison between data and Rapgap Monte Carlo histogram of the slow π meson reconstructed momentum $p(\pi_s)$ for the different D^* categories defined in Chapter 4.5.1. The statistical subtraction method is used for the central plot only.

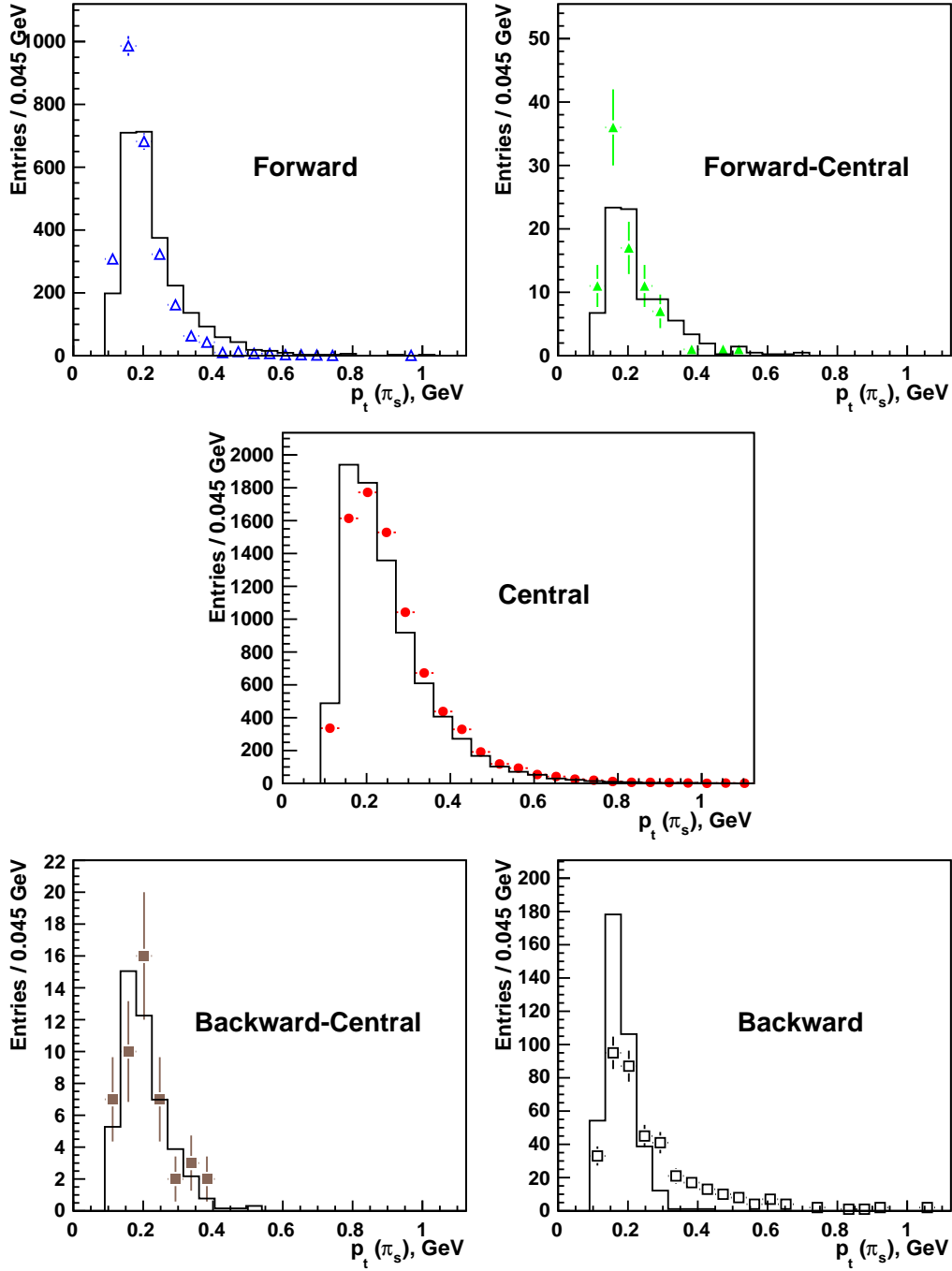


Figure 4.27: Comparison between data and Rapgap Monte Carlo histogram of the slow π meson reconstructed transverse momentum $p_t(\pi_s)$ for the different D^* categories defined in Chapter 4.5.1. The statistical subtraction method is used for the central plot only.

4.5.3 Signal Extraction

The number of produced D^* mesons is deduced by fitting the Δm distribution. In order to fit a resonant spectrum over a non-resonant combinatorical background from the Δm distribution, a combination of a signal and a background function is used. In some recent works, an asymmetric fitting of the Δm signal part of the distribution was used [152]. Since a measurement, influenced only by random and independent sources of errors, is described by a Gaussian function, and there is no good reason considering the opposite, in the current analysis the signal is described by the Gaussian function f_s as:

$$f_s(\Delta m) = \frac{N(D^*) w_{rc}}{\sqrt{2\pi}\sigma} e^{-\frac{(\Delta m - \mu)^2}{2\sigma^2}}, \quad (4.10)$$

where the free fit parameters are $N(D^*)$, μ and σ representing the number of fitted D^* s, the mean value of the distribution and its width respectively. The constant w_{rc} represents the bin width of the histogram. The background shape is fitted by the function f_b , representing a convolution of a polynomial and an exponential function given by

$$f_b(\Delta m) = \begin{cases} p_1 w_{wc} (\Delta m - m_\pi)^{p_2} e^{-p_3(\Delta m - m_\pi)} & \text{if } \Delta m > m_\pi \\ 0 & \text{if } \Delta m < m_\pi \end{cases} \quad (4.11)$$

The free parameters are denoted as p_1 , p_2 and p_3 , and the bin width is given by w_{wc} . To get the combinatorial background properly modelled close to the threshold and under the signal, a distribution referred to as *wrong charge* $\Delta m(D^*)$ distribution is used. The wrong charge D^* s are forbidden by the quark model and are searched following the algorithm and applying the cuts used for the D^* mesons (referred in this context to as *right charge* D^*) but searching for a three-particles combination of the type $K^\pm \pi^\pm \pi_s^\mp$. Under the tight kinematical conditions imposed by the Δm method, there is no physical object decaying into these combinations. Hence, the distribution represents the shape of the combinatorial background. Due to the smaller statistics in backward direction and higher background in forward direction in comparison with the central Δm distribution, a preciser estimation of the background shape is needed in the current analysis. To achieve this, the wrong charge distribution is fit with the function (4.11) in the range $(m_\pi, 0.52)$ GeV, which results in an order of magnitude more precise background fit parameter determination compared to the standard range (see Fig.4.29) being $(0.155, 0.1685)$ GeV [157].

After fitting the wrong charge combination, and the right charge combination with functions (4.10) and (4.11) respectively, a new fit with the function

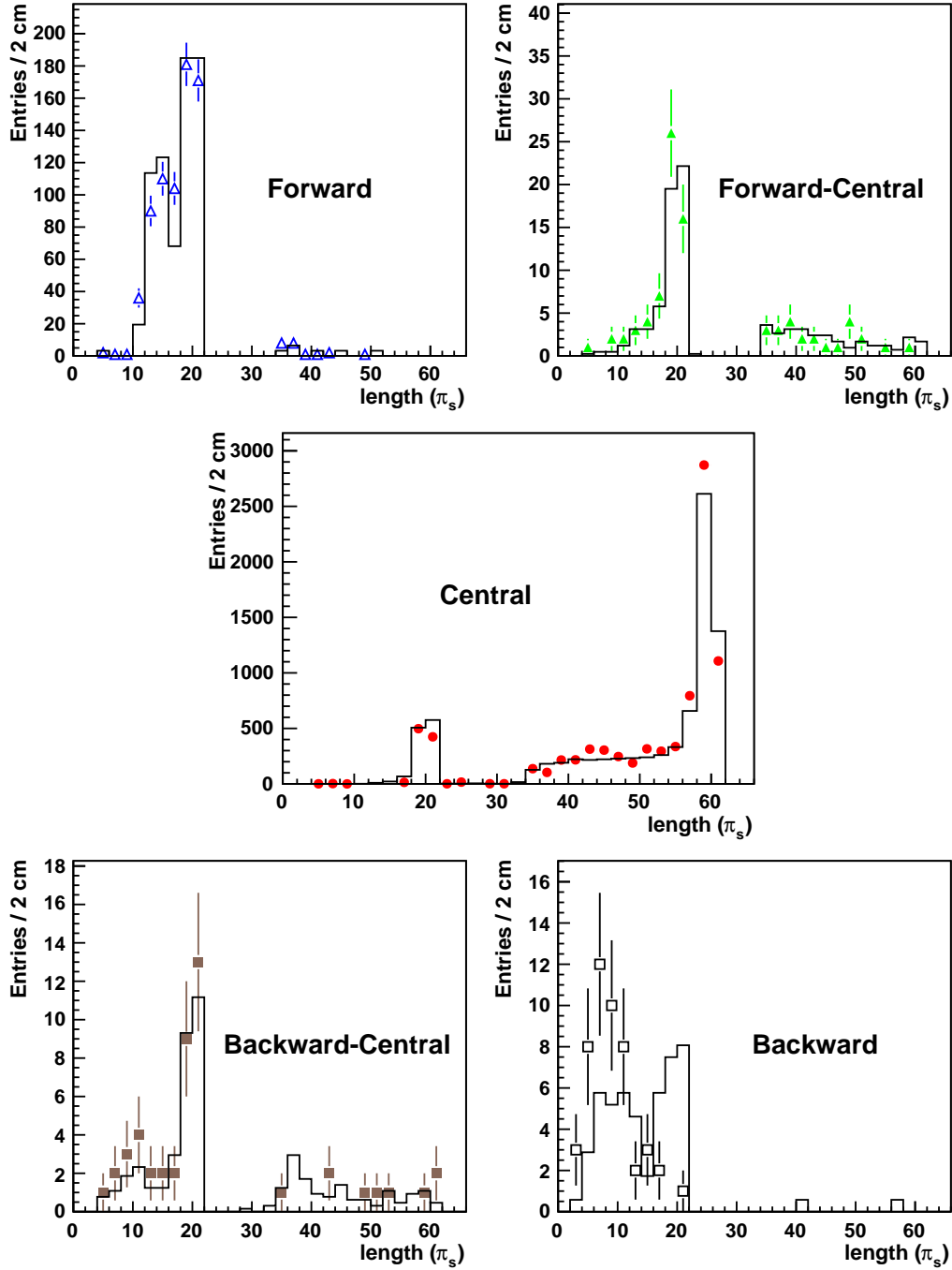


Figure 4.28: Comparison between data and Rapgap Monte Carlo histogram of the slow π meson reconstructed track length $l(\pi_s)$ for the different D^* categories defined in Chapter 4.5.1. The statistical subtraction method is used for the central plot only.

Parameter	Lower limit	Upper limit
$N(D^*)$	1	10^{10}
μ	0.14	0.15
σ	0.0008	0.0025
p_1	1	10^{10}
p_2	0	0.8
p_3	0	40.0

Table 4.9: Parameter limits applied to stabilize the Δm fitting procedure.

f_{sb} , representing a sum of both the signal and the background function as

$$\begin{aligned}
 f_{sb}(\Delta m) &= f_s + f_b = \\
 &= \frac{N(D^*) w_{rc}}{\sqrt{2\pi}\sigma} e^{-\frac{(x-\mu)^2}{2\sigma^2}} + p_1 w_{wc} (\Delta m - m_\pi)^{p_2} e^{-p_3(\Delta m - m_\pi)}.
 \end{aligned} \tag{4.12}$$

The initial values of the parameters are set to the corresponding values from the wrong charge and the right charge Δm fits. The background normalization parameter p_1 is left free, while the other two parameters are allowed to change only within the error from the wrong charge fit. The extension of the background fitting region allows to gain up to 30 % in signal significance (see Fig. 4.29). This is not so important for the standard central analysis, but at the edges of the acceptance, with marginal signals, such a gain is of vital importance.

For all Δm using information from FST or BST, additional measures are taken to stabilize the fit. The mean value of the gaussian (μ) is fixed to its nominal value of 145.421 MeV [5], and the width of the gaussian is limited to 2.5 MeV for the FST and 3.5 MeV for the BST D*s. In all other cases the parameters are left free in the limits given in Table 4.9. After final fitting, once more the combinatorial background function is formed, this time using the parameters p_1 , p_2 and p_3 from the final fitting. Using this function and the initial background function, fitted only from the wrong charge Δm distribution, the so-called background ratio (Br) is calculated. It is defined as the ratio between the integrals within the limits ($\mu - 2\sigma$, $\mu + 2\sigma$) of the two already mentioned background functions. The background ratio is used further for statistical subtraction method presented next.

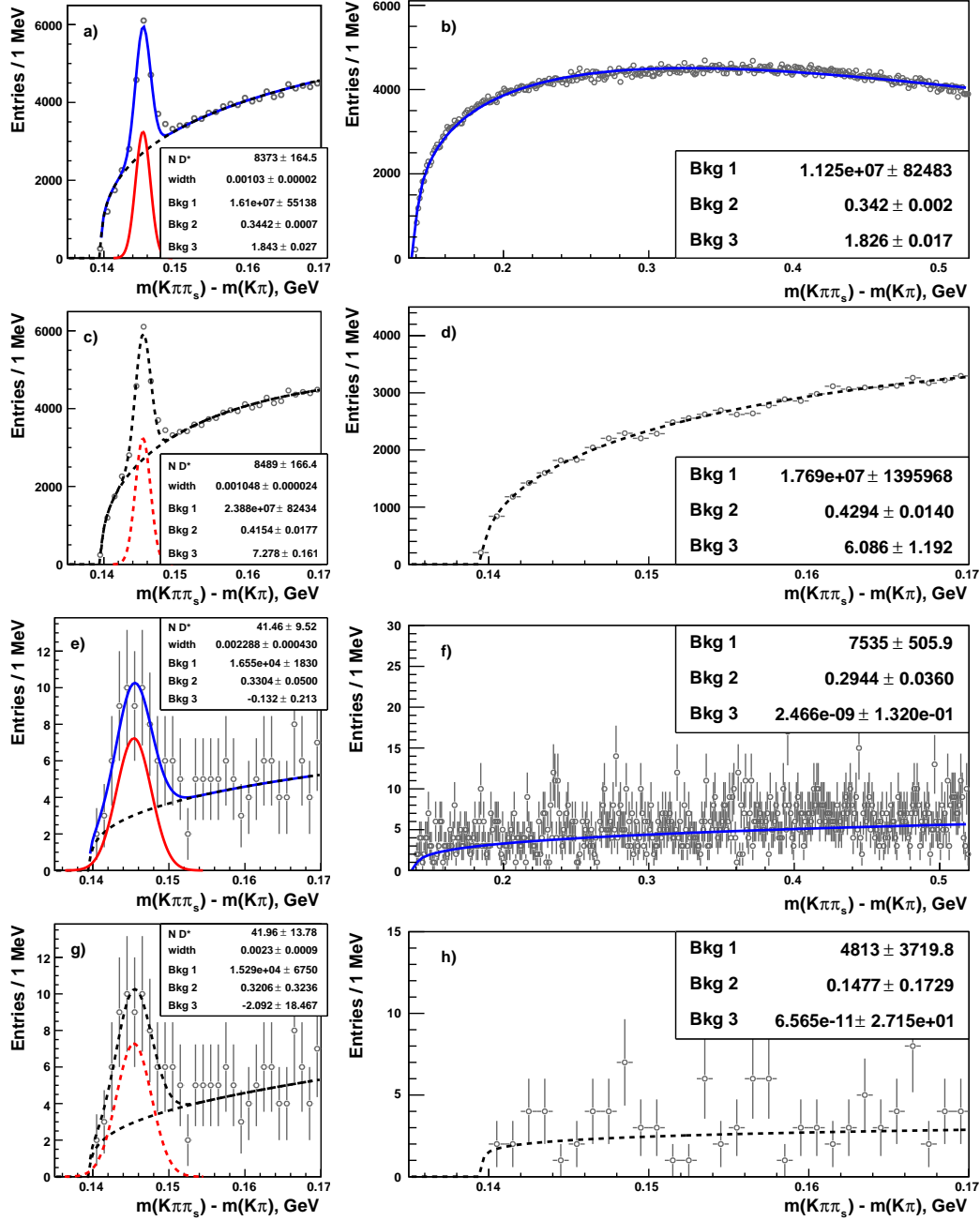


Figure 4.29: Improvement of the background fit parameter estimation for the right charge Δm distribution (left). The estimation is presented in two extreme cases: the low statistics case (Fig. e) - h)) and the high statistics case (Fig. a) - d)). For each case the parameters are estimated using the wrong charge Δm distributions (right) using the standard (Fig. d) and h)) and extended (Fig. b) and f)) fitting interval.

4.5.4 Statistical Subtraction

Taking into account that the number of D^* mesons is obtained as a result of fitting the Δm distribution, it is hard to estimate the properties of the D^* candidates coming from real D^* mesons and separate them from the properties of D^* candidates coming from a random combination of tracks. To separate both, the statistical subtraction method has been considered.

The method applied for a given D^* characteristic distribution - for example any kinematic variable, D^* or its decay particle properties - consist of the following steps. First the variable considered is histogrammed twice - once for the wrong charge combination (Fig. 4.30 b)) and once for the right charge combination (Fig. 4.30 a)) - for all D^* candidates with a Δm value in a 2σ window around the nominal Δm position. Next, the wrong charge distribution is scaled by the background ratio explained in the previous section, and then subtracted from the right charge histogram. The resulting histogram (Fig. 4.30 c)) is considered to statistically represent the distribution of the parameter for D^* mesons. Since the method precision depends on the statistical significance of the data sample, the method does not perform reliably on the new forward and backward measurements. Thus, the method is used only for the central region related variables.

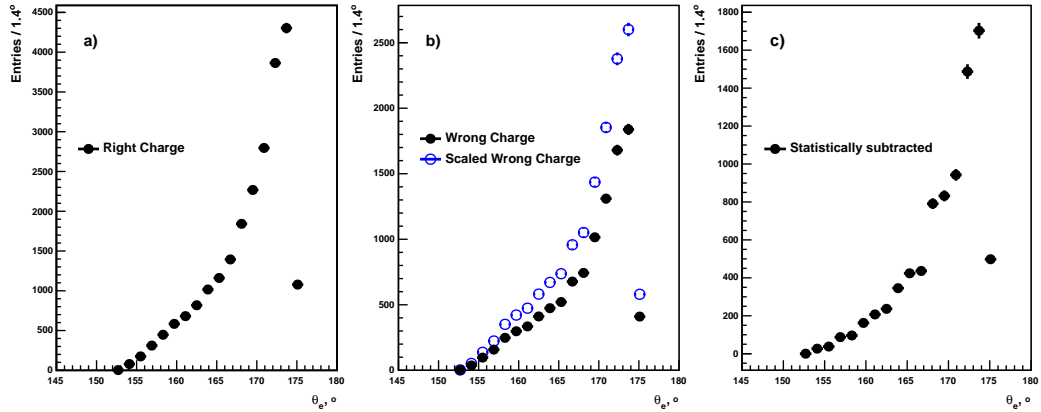


Figure 4.30: An example representing the steps of the statistical subtraction procedure.

Chapter 5

Measurement of the D^* Meson Cross Section

In this chapter the extraction of the differential cross section $d\sigma/d\eta$ from the D^{*+} analysis described in Chapter 4 is presented. The cross section is measured in the visible kinematic region defined by the limits presented in Table 5.1. The results are compared with the leading order Monte Carlo prediction, which describes the experimental results very good within the experimental error of the measurement. The sources of the systematic errors are also outlined.

Virtuality , GeV^2	$5 < Q^2 < 100$
Inelasticity	$0.05 < y < 0.6$
$p_t(D^*)$, GeV	> 1.5

Table 5.1: Visible kinematic range limits of this thesis.

In an ideal physical experiment, the total cross section of any physical process (σ) is defining the number of events N in which the process in consideration takes place, for a given integrated luminosity \mathcal{L} via the relation $N = \sigma \cdot \mathcal{L}$. In reality, when calculating the cross section for a given process, one has at disposal only an imperfect detector device, which has only limited acceptance, and a trigger system for the given type of events, which has an efficiency smaller than 100 %. Additionally, if many different event topologies for the given event type are possible, and only one of the possible topologies is considered, as in the current analysis, an external knowledge about the corresponding branching ratio is needed. The cross section which

is measured taking into account all these factors is referred to as *visible cross section* σ_{vis} . In the case of at least one D^* meson produced in electron-proton scattering it is given by

$$\sigma_{\text{vis}}^{\text{tot}}(ep \rightarrow e'D^*X) = \frac{N_{D^*}}{\mathcal{L} \cdot \mathcal{BR} \cdot A \cdot \varepsilon}, \quad (5.1)$$

where N_{D^*} is the number of D^* obtained from the fit to the Δm distribution (see Chapter 4.5.3). \mathcal{L} is the integrated luminosity, collected under conditions described in Chapter 4.3. The probability of the D^* to decay into the golden channel is given by the branching ratio \mathcal{BR} , the value of which was presented in Chapter 4.5. Losses, introduced by the trigger ability to select events with D^* mesons are represented by the trigger efficiency ε . All detector imperfections due to geometrical, efficiency, resolution or other limitations and leading to a loss of at least one of the decay particles and thus to the D^* meson are represented by the detector acceptance A , shown in Fig. 5.1. The acceptance is calculated dividing binwise the number of generated D^* obeying the kinematics cuts summarized in Table 5.1 by the fitted number of D^* mesons from the Δm distribution. The relatively low acceptance of both forward and backward measurements are explainable taking into account the geometrical details of FST and BST. Both detectors are covering only 3/4 from the full azimuthal angle and only a few degrees in the polar direction, which affects greatly detector acceptance taking into account the smearing of the vertex.

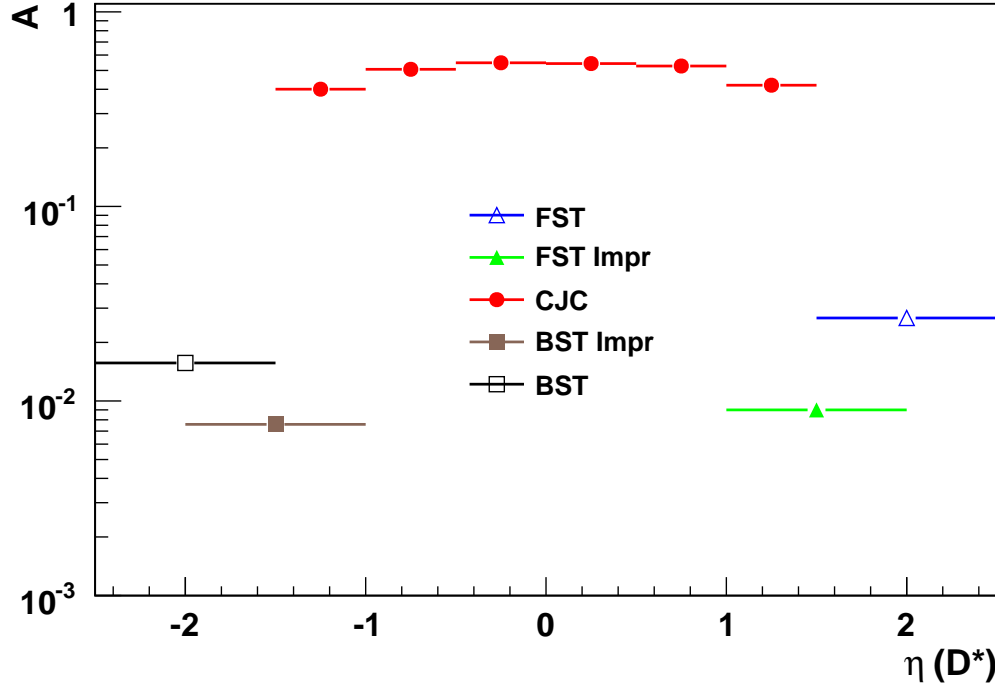
When the differential cross is searched as a function of some variable C , a single differential cross section is calculated analogically to the total cross section as

$$\frac{\sigma_{\text{vis}}(ep \rightarrow e'D^*X)}{dC} = \frac{N_{D^*}}{\Delta C \cdot \mathcal{L} \cdot \mathcal{BR} \cdot A \cdot \varepsilon}, \quad (5.2)$$

where the additional ΔC is representing the width of the bin in the given distribution.

For calculating the visible total and differential D^* production cross sections using the eqs. (5.1) and (5.2), besides the trigger efficiency (see Chapter 4.2), luminosity (see Chapter 4.3) and the branching ratio (see eq. (4.5)), also an estimation of the number of D^* lost due to detector imperfections is needed. All these effects are taken into account and included into the acceptance ε , which is estimated using a Monte Carlo simulation, and presented in Fig. 5.1. The acceptance is defined as the ratio between the number of reconstructed D^* mesons and the number of generated ones, which satisfy at

the generator level the kinematical conditions summarized in Table 5.1 and at reconstruction level additionally the cuts summarized in Table 4.8.

Figure 5.1: D^* meson detector acceptance and efficiency.

5.1 Systematic Errors

Most systematic errors are the same in the forward, central and backward region and thus taken from the H1 central D^* analysis [149]:

- **Luminosity** - Due to still unsolved problem with the H1 luminosity determination in 2006 and 2007, the systematic error on the luminosity measurement was taken to be 4% [158].
- **Trigger Efficiency** - The error coming from SpaCal and FTT trigger decision was estimated to be 1.4%.
- **Branching Ratio** - The contribution from the branching ratio is 2.57% [5].
- **Photoproduction Background** - The photoproduction background is estimated to be less than 1% at $E_e > 11$ GeV and $y < 0.6$ [149].
- **Reflections** - The contribution from other D^0 decay channels like

$$D^{*+} \rightarrow D^0 \pi_s^+ \rightarrow (KK, \pi\pi, \pi\pi\pi^0, Kl\nu_l) \pi_s^+ \quad (5.3)$$

are referred to as reflections. Their contribution is estimated to be less than 3.5% [149].

- **CT Track Finding Efficiency** - The difference in the data and MC track finding efficiency was calculated comparing the SpaCal cluster information with the track information from CT for electrons with energies >2 GeV. The difference is 2%. Since the kinematic region considered here and the particles considered here are much different, an error of 2% with uncertainty of 2 % for each track is applied.
- **CT Track Vertex Fit Efficiency** - The inefficiency of the CT vertex finding contributes with 2.5% to the common systematic error.
- **Nuclear Interactions** - The error on the CT π track finding efficiency is estimated to be $\sim 0.5\%$ after applying the proper dead material corrections. Since these corrections are not available yet for kaons, the corresponding error is increased to 1.5%. A combined error of 2.5% per D^* is applied.
- **D^0 Mass Cut** - The difference in this cut in data and MC is estimated to be 1%.
- **Electron Measurement** - The resolution of the electron scattering angle of the BST is ± 1 mrad resulting in an 1-2% systematic error contribution. Additionally, the energy resolution of the SpaCal contributes 1-2.5%.

5.2 The Total Cross Section

The total cross section is calculated integrating over the data points in Fig. 5.3 over the pseudorapidity range $-2.5 < \eta < 2.5$. In order to partially cross check the current analysis chain and its results with results from previous analysis, a D^* cross section calculation in the standard central H1 η range $-1.5 < \eta < 1.5$ was performed. The latest H1 preliminary results in this acceptance region are [152]:

$$\sigma_{\text{vis}}^{\text{tot}}(ep \rightarrow e' D^* X) = 4.23 \pm 0.09 \text{ (stat.)} \pm 0.37 \text{ (syst.) nb} \quad (5.4)$$

The current analysis in the same acceptance region gives

$$\sigma_{\text{vis}}^{\text{tot}}(ep \rightarrow e' D^* X) = 4.46 \pm 0.09 \text{ (stat.)} \pm 0.38 \text{ (syst.) nb}, \quad (5.5)$$

which is 5% higher than the standard analysis, but is well within the experimental errors of both measurements. The next step is to extend the cross

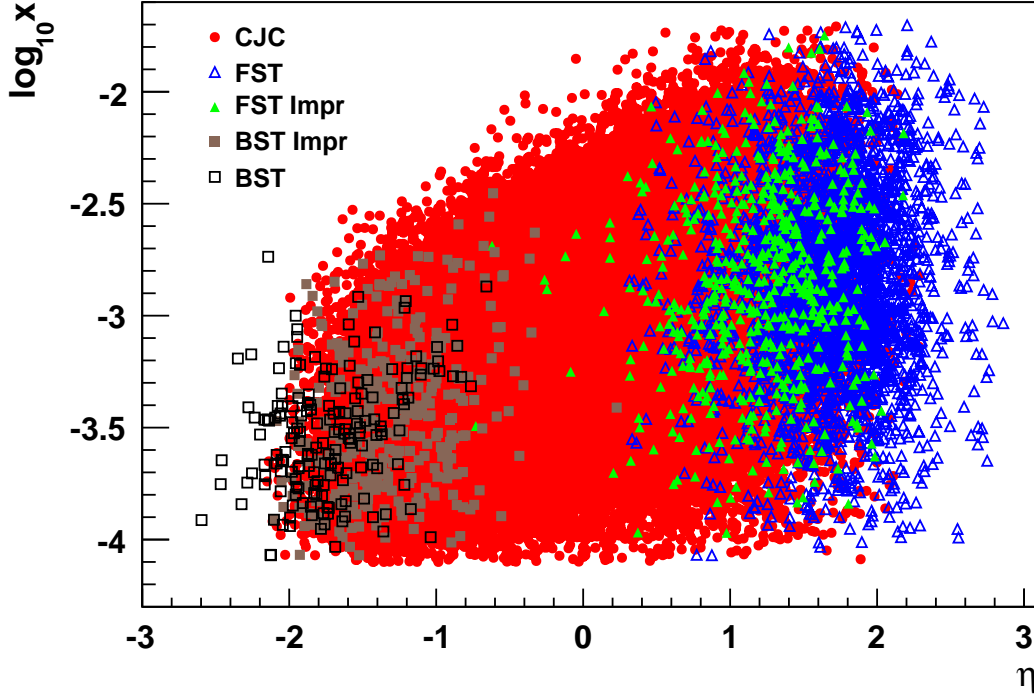


Figure 5.2: Monte Carlo D^* Meson distribution in $\log x - \eta$ phase space.

section measurement to the full acceptance of the current analysis, without double counting of data. This is done by integrating over the full acceptance region taking into account only D^* s either fully reconstructed in CJC, or having at least one FST or BST track (full circle, open triangle and open square measurement on Fig. 5.3), and ignoring the other two available measurements. The resulting cross section in the acceptance region $-2.5 < \eta < 2.5$ of the current analysis reads:

$$\sigma_{\text{vis}}^{\text{tot}}(ep \rightarrow e'D^*X) = 4.51 \pm 0.63 \text{ (stat.)} \pm 0.38 \text{ (syst.) nb.} \quad (5.6)$$

5.3 The Single Differential Cross Section

The single differential cross sections and their comparison with Monte Carlo predictions are much more informative. The standard single differential cross sections to be considered are for example $d\sigma/dQ^2$, $d\sigma/dx$, $d\sigma/dp_t(D^*)$ and $d\sigma/d\eta(D^*)$. In most of these cases, the information added by the FST and BST is statistically insignificant and disturbs the central measurement by introducing additional sources of uncertainty.

A common reason for both detectors is, that the data collected is much

η bin Low edge	η bin Upper edge	$d\sigma/d\eta (D^*)$ [nb]	σ_{stat} [nb]	σ_{syst} [nb]
-2.50	-1.50	0.6555	± 0.4266	± 0.0673
-2.00	-1.00	1.1754	± 0.2692	± 0.1208
-1.50	-1.00	1.1143	± 0.0593	± 0.1145
-1.00	-0.50	1.4670	± 0.0608	± 0.1508
-0.50	0.00	1.6446	± 0.0698	± 0.1690
0.00	0.50	1.7977	± 0.0755	± 0.1847
0.50	1.00	1.5777	± 0.0814	± 0.1621
1.00	1.50	1.3187	± 0.0944	± 0.1355
1.00	2.00	0.8570	± 0.3002	± 0.0881
1.50	2.50	0.6159	± 0.4537	± 0.0633

Table 5.2: The D^* differential cross section as a function of the pseudorapidity η measured in the current analysis.

less then foreseen, as explained earlier. In FST case, the proton induced background interferes with the D^* data sample and diminishes the statistical significance of the signal. In the BST case, the phase-space is much cleaner, but it is kinematically hardly achievable, which suppress the number of D^* candidates.

A noticeable FST and BST contribution to a differential cross section can be expected in the parts of the phase space where CJC losses acceptance, and cannot alone reconstruct D^* mesons. This condition as well as the track acceptance of the FST and BST defines $d\sigma/d\eta$ and $d\sigma/dx$ as the single differential cross section to which both detectors should contribute significantly to the H1 measurement. As visible from Fig. 5.2, both detectors are contributing to regions not achievable by the central reconstruction. In x, however, the BST, FST and CT cover almost the same range.

The $d\sigma/d\eta$ distribution calculated in this analysis using eq. (5.2) is presented in Fig. 5.3 stand-alone and in comparison with recent H1 and Zeus results. The results of the binwise calculations with the corresponding statistical and systematic errors are presented in Table 5.2. The preliminary results from both H1 and Zeus are also given for comparison in Appendix A. The first initial observation is that the new measurements at high and low η are consistent with the results from the central region. Moreover, the central points from the current analysis are consistent within the errors with the preliminary results from both H1 and Zeus - both received with the higher

statistics of the HERA II running period.

The points added thanks to the FST and BST information continues the decrease of the D^* production cross section towards high and low pseudorapidities. A comparison with the Rapgap leading order Monte Carlo sample described in Chapter 1.7.1 was also performed. Both distributions were normalized to each other in the central region. As visible from Fig. 5.4 the Monte Carlo describes well the data in the considered η range.

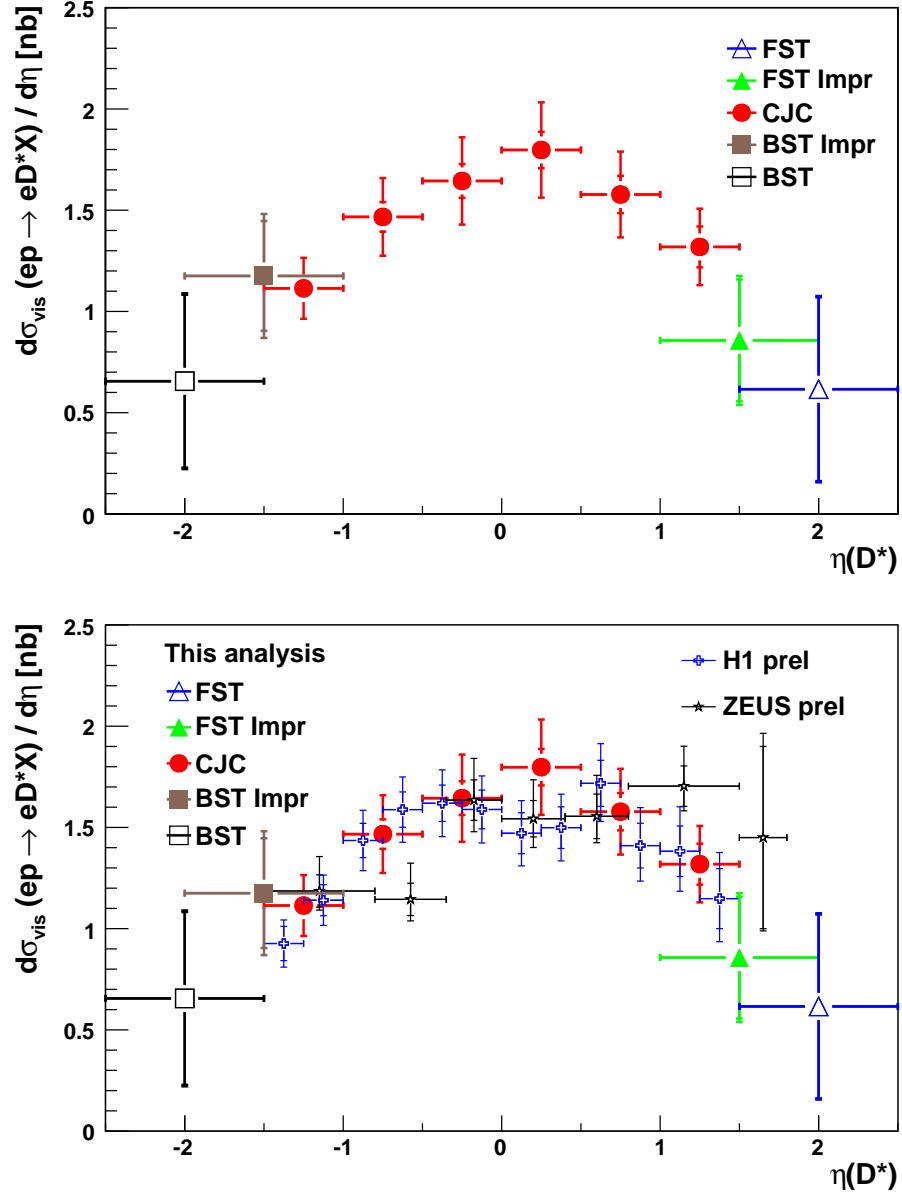


Figure 5.3: D^* production cross section as a function of the pseudorapidity η of the D^* mesons. The data points from the current analysis can be found in Table 5.2. The official preliminary data points from H1 and Zeus are also shown and summarized in Appendix A.

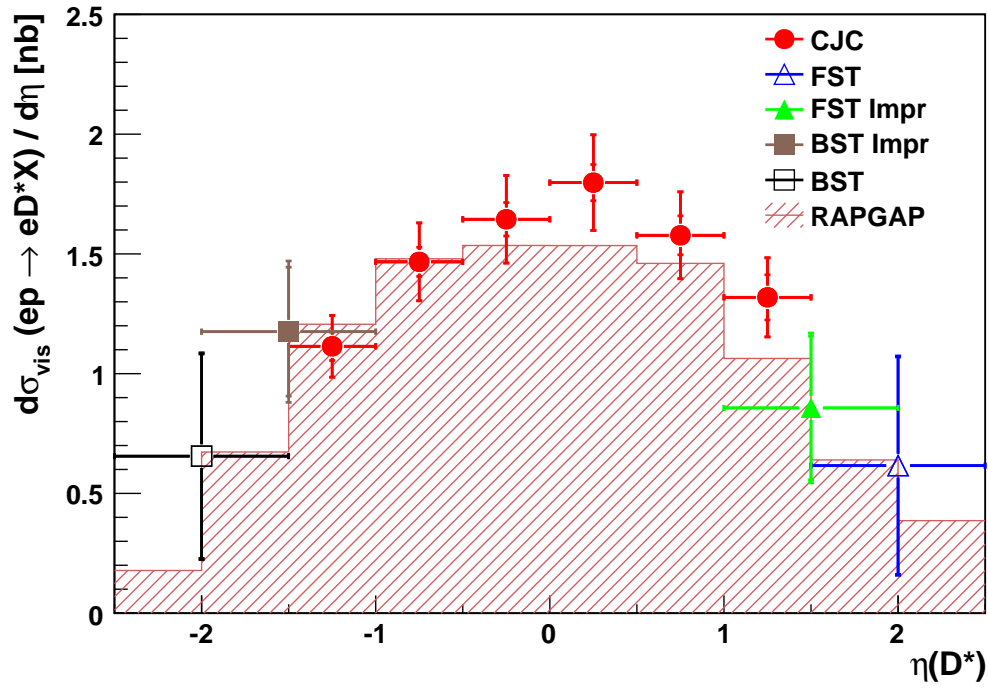


Figure 5.4: Differential D^* production cross section as a function of the pseudorapidity η of the D^* mesons. The data points from the current analysis as given in Table 5.2 are compared with the LO Rapgap prediction.

Chapter 6

Conclusions and Outlook

In this work, D^* meson production in deep inelastic ep scattering was studied. For the first time, the D^* cross section was measured in the forward and backward pseudorapidity regions of $1.5 < |\eta| < 2.5$. The increase of the acceptance by one unit in pseudorapidity was achieved due to the Backward Silicon Tracker (BST) and the Forward Silicon Tracker (FST). The data used for this analysis was collected in the time period between May 2006 and March 2007 and resulted in integrated luminosity of $\mathcal{L} = 150 \text{ pb}^{-1}$.

The introduction of the new forward silicon tracker and the upgrade of the existing backward silicon tracker were a significant part of the upgrade of the H1 experiment for the HERA II project. Both detectors together provide a significant extension in the H1 tracking towards large and small pseudorapidities, respectively.

In this thesis the design, the readout system and the track reconstruction of both devices were presented. The data quality of both detectors including detector internal and global alignment as well as hit and track parameters resolutions were investigated. In order to use standard central tracking information and the information from both FST and BST as a common data sample, additional improvements in the H1 standard tracking scheme were performed and are described within the current work.

In the data sample, D^* mesons in the golden decay channel $D^{*\pm} \rightarrow D^0 \pi_s^\pm \rightarrow K^\mp \pi^\pm \pi_s^\pm$ were searched using the mass difference between the D^* and D^0 mesons. The extracted cross section was compared to previous results as well as to the leading order Monte Carlo predictions. A reasonable agreement between previous H1 and Zeus results and the results from the current analysis was found. The new FST and BST measurements at high and low pseudorapidity show that the rapid decrease of the cross section at the of the pseudorapidity spectra continues. Moreover, the results are well described by the leading order Monte Carlo predictions within the experimental errors.

The current analysis has shown that both FST and BST are able to provide tracking information in corners of the phase space previously unreachable, and thus to contribute to a more precise heavy flavour structure function measurement by reducing the cross section extrapolation error.

To achieve this aim, the H1 tracking software should be carefully developed by fully combining the track and vertex information from all detectors in the forward and backward regions of H1. This would supply combined tracks, containing precise silicon information, needed for further heavy flavour studies at the edges of the H1 tracking acceptance.

Appendix A

H1 and Zeus Preliminary Results

In the following appendix, the preliminary results from the standard H1 and Zeus analysis are presented for comparison reasons. Both analysis are using larger statistics then the current analysis, which allows considerations of double differential cross sections and finer single differential binning, both not possible in the current analysis. On the other hand, both H1 and Zeus anal-

η bin Low edge	η bin Upper edge	$d\sigma/d\eta (D^*)$ [nb]	σ_{stat} [nb]	σ_{syst} [nb]
-1.50	-1.25	0.947	± 0.085	$\pm_{0.08}^{0.078}$
-1.25	-1.00	1.140	± 0.077	$\pm_{0.10}^{0.098}$
-1.00	-0.75	1.435	± 0.085	$\pm_{0.12}^{0.12}$
-0.75	-0.50	1.588	± 0.087	$\pm_{0.14}^{0.14}$
-0.50	-0.25	1.619	± 0.090	$\pm_{0.14}^{0.14}$
-0.25	0.00	1.589	± 0.096	$\pm_{0.14}^{0.14}$
0.00	0.25	1.47	± 0.10	$\pm_{0.13}^{0.13}$
0.25	0.50	1.50	± 0.10	$\pm_{0.13}^{0.13}$
0.50	0.75	1.72	± 0.11	$\pm_{0.15}^{0.16}$
0.75	1.00	1.41	± 0.11	$\pm_{0.14}^{0.15}$
1.00	1.25	1.38	± 0.12	$\pm_{0.15}^{0.18}$
1.25	1.50	1.15	± 0.15	$\pm_{0.15}^{0.17}$

Table A.1: The H1 HERA II preliminary D^* differential cross sections as a function of the pseudorapidity η . The results are cited from [152].

η bin Low edge	η bin Upper edge	$d\sigma/d\eta (D^*)$ [nb]	σ_{stat} [nb]	σ_{syst} [nb]
-1.50	-0.8	1.186	± 0.08	$\pm_{0.05}^{0.15}$
-0.8	-0.35	1.446	± 0.08	$\pm_{0.07}^{0.16}$
-0.35	0.00	1.635	± 0.10	$\pm_{0.12}^{0.18}$
0.00	0.40	1.543	± 0.09	$\pm_{0.11}^{0.17}$
0.40	0.80	1.555	± 0.11	$\pm_{0.07}^{0.17}$
0.80	1.50	1.704	± 0.10	$\pm_{0.07}^{0.17}$
1.50	1.80	1.45	± 0.45	$\pm_{0.1}^{0.25}$

Table A.2: The ZEUS HERA II preliminary D^* differential cross section as a function of the pseudorapidity η . The results are cited from [160], except for the bin $\eta > 1.5$, taken from [159].

ysis are taking advantage only of the corresponding central tracking systems and thus they are limited in acceptance in comparison with the current analysis. Both results are summarized in Tables A.1 and A.2 respectively, and compared with the current analysis depicted on Fig.5.3. For H1 the results are taken from [149, 152] and for Zeus - from [159, 160].

Bibliography

- [1] T.-P. Cheng and L.-F. Li. *Gauge theory of elementary particle physics*. Oxford University Press, New York, 2000. ISBN 0-19-851961-3.
- [2] H1 Collaboration. A Forward Silicon Detector for H1. *DESY PRC 99/01*, unpublished, 1999.
- [3] R. Devenish and A. Cooper-Sarkar. *Deep Inelastic Scattering*. Oxford University Press, New York, 1st edition, 2004. ISBN 0-198-50671-6.
- [4] (CTEQ Collaboration) R. Brock et al. Handbook of perturbative QCD. *Reviews of Modern Physics*, Volume 67:157–248, 1995.
- [5] W. M. Yao et al. Review of particle physics. *Journal of Physics G*, Volume 33:1–1231, 2006.
- [6] C. Adloff et al. (H1 Collaboration). Measurement and QCD analysis of neutral and charged current cross section at HERA. *The European Physics Journal C*, Volume 30:1–32, 2003. hep-ex/0606004.
- [7] J. Breitweg et al. (Zeus Collaboration). Measurement of high- Q^2 neutral-current e^+p deep inelastic scattering cross-section at HERA. *The European Physics Journal C*, Volume 11:427–445, 1999. hep-ex/9905032.
- [8] J. Breitweg et al. (Zeus Collaboration). Measurement of high- Q^2 charged-current e^+p deep inelastic scattering cross-section at HERA. *The European Physics Journal C*, Volume 12:411, 2000. hep-ex/9907010.
- [9] J. Kogut and L. Susskind. The parton picture of elementary particles. *Physics Reports*, Volume 8:76–172, 1973.
- [10] E. Rutherford. The Scattering of α and β Particles by Matter and the Structure of the Atom. *Philosophical Magazine*, Volume 6:669–688, 1911.

- [11] R. P. Feynman. *Photon-hadron interactions*. Benjamin, New York, 1st edition, 1972. ISBN 0-201-36074-8.
- [12] C. G. Callan and D. J. Gross. High-energy electroproduction and the constitution of the electric current. *Physical Review Letters*, Volume 22:156–159, 1969.
- [13] J. D. Bjorken. Inequality for electron and muon scattering from nucleons. *Physical Review Letters*, Volume 16:408, 1966.
- [14] J. D. Bjorken. Asymptotic sum rules at infinite momentum. *Physical Review*, Volume 179:1547–1553, 1969.
- [15] M. Gell-Mann H. Fritzsch and H. Leutwyler. Advantages of color octet gluon picture. *Physics Letters B*, Volume 47:365–368, 1973.
- [16] D. J. Gross and F. Wilczek. Asymptotically free gauge theories. *Physical Review D*, Volume 8:3633–3652, 1973.
- [17] S. Weinberg. Non-abelian gauge theories of the strong interactions. *Physical Review Letters*, Volume 31:494–497, 1973.
- [18] D. J. Gross and F. Wilczek. Ultraviolet behaviour of non-abelian gauge theories. *Physical Review Letters*, Volume 30:1343–1346, 1973.
- [19] H. D. Politzer. Reliable perturbative results from strong interactions? *Physical Review Letters*, Volume 30:1343–1346, 1973.
- [20] W. A. Bardeen et al. Deep Inelastic Scattering beyond the Leading Order in Asymptotically Free Gauge Theories. *Physical Reviews D*, Volume 18:3998–4017, 1978.
- [21] R. K. Ellis G. Altarelli and G. Martinelli. Large Perturbative Corrections to the Drell-Yan Process in QCD. *Nuclear Physics B*, Volume 157:461–497, 1979.
- [22] Yu. L. Dokshitzer. Calculation of structure functions of deep-inelastic scattering and e^+e^- annihilation by perturbation theory in quantum chromodynamics. *Sov. Phys JETP*, Volume 46:641–653, 1977.
- [23] V. N. Gribov and L. N. Lipatov. Deep inelastic ep scattering in perturbation theory. *Soviet Journal of Nuclear Physics*, Volume 15:438–450 and 675–684, 1972.

- [24] G. Altarelli and G. Parisi. Asymptotic freedom in parton language. *Nuclear Physics B*, Volume 126:298–318, 1977.
- [25] L. N. Lipatov E. A. Kuraev and V. S. Fadin. The Pomeranchuk singularity in nonabelian gauge theories. *Sov. Phys JETP*, Volume 46:199, 1972.
- [26] Ya. Ya. Balitsky and L. N. Lipatov. The Pomeranchuk singularity in quantum chromodynamics. *Sov. J. Nucl. Phys.*, Volume 28:282, 1978.
- [27] M. Ciafaloni. Coherence effects in initial jets at small Q^2/s . *Nuclear Physics B*, Volume 296:49–74, 1988.
- [28] F. Fiorani S. Catani and G. Marchesini. Small- x behaviour of initial state radiation in perturbative QCD. *Nuclear Physics B*, Volume 336: 18–85, 1990.
- [29] G. Marchesini. QCD coherence in the structure function and associated distributions in small x . *Nuclear Physics B*, Volume 445:49–78, 1995.
- [30] F. Fiorani S. Catani and G. Marchesini. QCD coherence in initial state radiation. *Physics Letters B*, Volume 234:339, 1990.
- [31] (H1 Collaboration) A. Aktas et al. Measurement of $F_2^{c\bar{c}}$ and $F_2^{b\bar{b}}$ at low Q^2 and x using the H1 Vertex Detector at HERA. *The European Physical Journal C*, Volume 45:23–33, 2006. hep-ex/0507081.
- [32] (H1 Collaboration) A. Aktas et al. Measurement of Charm and Beauty Dijet Cross Sections in Photoproduction at HERA using the H1 Vertex Detector. *The European Physical Journal C*, Volume 47:597–610, 2006. hep-ex/0605016.
- [33] (H1 Collaboration) A. Aktas et al. Measurement of Charm and Beauty Photoproduction at HERA using $D^* \mu$ Correlations. *Physics Letters B*, Volume 621:56–71, 2005. hep-ex/0503038.
- [34] (H1 Collaboration) A. Aktas et al. Measurement of Beauty Production at HERA Using Events with Muons and Jets. *The European Physical Journal C*, Volume 41:453–467, 2005. hep-ex/0502010.
- [35] (H1 Collaboration) A. Aktas et al. Measurement of $F_2^{c\bar{c}}$ and $F_2^{b\bar{b}}$ at High Q^2 using the H1 Vertex Detector at HERA. *The European Physical Journal C*, Volume 40:349–359, 2004. hep-ex/0411046.

- [36] (H1 Collaboration) A. Aktas et al. Elastic J/ψ Production at HERA. *The European Physical Journal C*, Volume 46:585–603, 2006. hep-ex/0510016.
- [37] (ZEUS Collaboration) S. Chekanov et al. Measurement of Inelastic J/ψ Production in Deep Inelastic Scattering at HERA. *The European Physical Journal C*, Volume 44:13–25, 2005. hep-ex/0505008.
- [38] C. Schmidt W. K. Tung, S. Kretzer. Open Heavy Flavour Production in QCD - Conceptual Framework and Implementation Issues. *Journal of Physics G*, Volume 28:983–995, 2002.
- [39] (H1 Collaboration) C. Adloff et al. Measurement of D^* Meson Cross Sections at HERA and Determination of the Gluon Density in the Proton. *Nuclear Physics B*, Volume 545:21–44, 1999. hep-ex/9812023.
- [40] J. Smith E. Laenen, S. Riemersma and W. L. van Neerven. Complete $O(\alpha_s)$ corrections to heavy-flavour structure functions in electroproduction. *Nuclear Physics B*, Volume 392:162–228, 1993.
- [41] J. Smith E. Laenen, S. Riemersma and W. L. van Neerven. $O(\alpha_s)$ corrections to heavy-flavour inclusive distributions in electroproduction. *Nuclear Physics B*, Volume 392:229–250, 1993.
- [42] J. Smith S. Riemersma and W. L. van Neerven. $O(\alpha_s)$ corrections to heavy-flavour inclusive distributions in electroproduction. *Nuclear Physics B*, Volume 347:143–151, 1995. hep-ph/9411431.
- [43] A. D. Martin and W. J. Stirling. Parton distributions of the proton. *Physical Review D*, Volume 50:6734–6752, 1994. hep-ph/9406315.
- [44] A. D. Martin and W. J. Stirling. When is a heavy quark not a parton? Charged Higgs production and heavy quark mass effects in the QCD-based parton model. *Nuclear Physics B*, Volume 308:813–832, 1988.
- [45] F. I. Olness M. A. G. Aivazis and W. K. Tung. Leptoproduction of heavy quarks. I. General formalism and kinematics of charged current and neutral current production processes. *Physical Review D*, Volume 50:3085–3101, 1994. hep-ph/9312318.
- [46] F. I. Olness M. A. G. Aivazis, J. C. Collins and W. K. Tung. Leptoproduction of heavy quarks. II. A unified QCD formulation of charged and neutral current processes from fixed-target to collider energies. *Physical Review D*, Volume 50:3102–3118, 1994. hep-ph/9312319.

- [47] F. I. Olness M. Krämer and D. E. Soper. Treatment of heavy quarks in deeply inelastic scattering. *Physical Review D*, Volume 62:096007, 2000. hep-ph/0003035.
- [48] G. Ingelman B. Andersson, G. Gustafson and T. Sjöstrand. Parton fragmentation and string dynamics. *Physics Reports*, Volume 97:31–145, 1983. hep-ph/0003035.
- [49] I. Schmitt C. Peterson, D. Schlatter and P. M. Zerwas. Scaling violations in inclusive e^+e^- annihilation spectra. *Physical Review D*, Volume 27:105–111, 1983.
- [50] M. G. Bowler. e^+e^- Production of Heavy Quarks in the String Model. *Zeitschrift für Physik C*, Volume 11:169–174, 1981.
- [51] R. Seuster et al. (Belle Collaboration). Charmed hadrons from fragmentation and b decays in e^+e^- annihilation at $\sqrt{s} = 10.6$ gev. *Physical Review D*, Volume 73:032002, 2006.
- [52] GEANT. Detector Description and Simulation Tool, March 1994. URL <http://wwwinfo.cern.ch/asdoc/pdfdir/geant.pdf>.
- [53] H1. Guide to simulation program H1SIM, 1991. URL <https://www-h1.desy.de/imc/h1sim/guide.html>.
- [54] G. Grinhammer et al. The fast simulation of electromagnetic and hadronic showers. *Nuclear Instruments and Methods in Physics Research A*, 290:469–488, 1990.
- [55] H. Jung. Hard diffractive scattering in high energy ep collisions and the Monte Carlo Generator RAPGAP. *Computer Physics Communications*, Volume 86:147–161, 1995. URL <http://www.desy.de/~jung/rapgap/>.
- [56] LHAPDF the Les Houches Accord PDF Interface, 2002. URL <http://projects.hepforge.org/lhapdf/manual>.
- [57] J. Pumplin et al. New generation of parton distributions with uncertainties from global QCD analysis. *Journal of High Energy Physics*, Volume 07, 2002. hep-ex/0201195.
- [58] G. A. Schuler and T. Sjöstrand. Parton distributions of the virtual photon. *Physics Letters B*, Volume 376:193–200, 1996.

- [59] T. Sjöstrand. The Lund monte carlo for jet fragmentation and e^+e^- physics - jetset version 6.2. *Computer Physics Communications*, Volume 39:347–407, 1986.
- [60] Deutsches Elektronen-Synchrotron. HERA: A Proposal for a Large Electron - Proton Colliding Beam Facility at DESY. DESY-HERA-81-10, 1981.
- [61] B. H. Wiik. HERA Status. In *Proceedings of the Workshop on Physics at HERA, Hamburg, Germany, October 29-30, 1991*, pages 1–16. HB-Druck, 1992.
- [62] Ferdinand J. Willeke. HERA performance and prospects. In *XII International Workshop on Deep Inelastic Scattering, Štrébské Pleso, Slovakia*, 2004. URL <http://www.saske.sk/dis04/proceedings/plenary/willeke.ps.gz>.
- [63] W. Bartel et al. HERA luminosity upgrade. In *Future Physics at HERA*, Hamburg, Germany, 1995/1996. URL <http://www.desy.de/~heraws96/HERAproc96.tar.gz>.
- [64] G. H. Hoffstaetter. Future possibilities for hera. In *Proceedings of the EPAC 2000*, pages 13–17, 2000. URL <http://epaper.kek.jp/e00/PAPERS/MOZE04.pdf>.
- [65] H1 Homepage, 2007. URL <http://www-h1.desy.de>.
- [66] U. Holm (ed.) (ZEUS Collaboration). The ZEUS Detector, 1993. URL <https://www-zeus.desy.de/bluebook/bluebook.html>.
- [67] Hermes Homepage, 2007. URL <http://www-hermes.desy.de>.
- [68] Hera-b Homepage, 2007. URL <http://www-hera-b.desy.de>.
- [69] H1 Collaboration. Technical proposal for the H1 detector. *DESY PRC-86/02, unpublished*, 1986.
- [70] I. Abt et al. (H1 Collaboration). The H1 detector at HERA. *Nuclear Instruments and Methods in Physics A*, Volume 386:310–347, 1997. URL <https://www-h1.desy.de/h1/www/h1det/detpaper/contents.html>.
- [71] I. Abt et al. (H1 Collaboration). The tracking, calorimeter and muon detectors of the H1 detector at HERA. *Nuclear Instruments and Methods in Physics A*, Volume 386:348–396, 1997. URL <https://www-h1.desy.de/h1/www/h1det/detpaper/contents.html>.

- [72] H1 for HERA II, 2006. URL <https://www-h1.desy.de/idet/upgrade/>.
- [73] H1 Collaboration. e-p Physics beyond 1999. *H1 internal report H-10/97-531*, 1997.
- [74] J. Bürger et al. The Central Jet Chamber of the H1 Experiment. *Nuclear Instruments and Methods in Physics Research A*, Volume 279: 217–222, 1989.
- [75] H. Bärwolff et al. Design and performance of a full-scale prototype of the outer z-Drift Chamber for the H1 experiment at HERA, 1988.
- [76] M. Cuje et al. H1 high luminosity upgrade 2000 CIP and level 1 vertex trigger. *DESY- 98/02 and H1 internal report H-10/98-535*, 1998.
- [77] M. Urban. *The new CIP2k z-vertex trigger for the H1 experiment at HERA*. PhD thesis, Universität Zürich, 2004. URL <https://www-h1.desy.de/psfiles/theses/h1th-366.ps>.
- [78] K. Müller et al. Construction and performance of a thin cylindrical multiwire proportional chamber with cathode pad readout for the H1 Experiment. *Nuclear Instruments and Methods in Physics Research A*, Volume 312:457–466, 1992.
- [79] D. Pitzl et al. (H1 Collaboration). The H1 Silicon Vertex Detector. *Nuclear Instruments and Methods in Physics Research A*, Volume 454: 334–349, 2000.
- [80] B. List et al. (H1 Collaboration). The H1 Central Silicon Tracker. *Nuclear Instruments and Methods in Physics Research A*, Volume 501: 49–53, 2001.
- [81] R. Horisberger et al. A novel readout chip for silicon strip detectors with analog pipeline and digitally controlled analog signal processing. *Nuclear Instruments and Methods in Physics Research A*, Volume 326: 92–99, 1993.
- [82] A. Aktas et al. (H1 Collaboration). Inclusive production of D^+ , D^0 , D_s^+ and D^{*+} Mesons in Deep Inelastic Scattering at HERA. *European Physics Journal C*, 38:447, 2005. hep-ex/0408149.
- [83] H1 Collaboration. Proposal for Upgrade of the H1 Forward Track Detector for HERA 2000. *DESY 98/06, unpublished*, June 1998.

- [84] C. Adloff et al. (H1 Collaboration). Measurement of charged particle transverse momentum spectra in deep inelastic scattering. *Nuclear Physics B*, 485:3–22, 1997.
- [85] C. Adloff et al. (H1 Collaboration). Evolution of ep fragmentation and multiplicity distributions in Breit frame. *Nuclear Physics B*, 504:3–23, 1997.
- [86] V. Korbel. The H1 LAr calorimeter at HERA, design, performance and status. *Nuclear Instruments and Methods in Physics Research A*, 327:209–211, 1993.
- [87] R.-D. Appuhn et al. (H1 SpaCal). The H1 lead/scintillating-fibre calorimeter. *Nuclear Instruments and Methods in Physics Research A*, 386:3–23, 1997.
- [88] R.-D. Appuhn et al. (H1 SpaCal). Hadronic response and e/π separation with the H1 lead/scintillating-fibre calorimeter. *Nuclear Instruments and Methods in Physics Research A*, 382:395–412, 1996.
- [89] F. Moreau (H1 Collaboration). The low noise L1 trigger of the H1 lead/scintillating-fibre calorimeter. *Nuclear Physics B*, 61:132–136, 1998.
- [90] D. Reyna. Modifications to SpaCal for H1 High Luminosity Operation and the Effect on Acceptance. *H1 report 11/98-555*, 1998.
- [91] V. Andreev et al. The new H1 luminosity system for HERA II. *Nuclear Instruments and Methods in Physics Research A*, 494:45–50, 2002.
- [92] H. A. Bethe and W. Heitler. On the stopping of fast particles and on the creation of positive electrons. *Proceedings of the Royal Society A*, 146:83, 1934.
- [93] C. Kiesling et al. The H1 Neural Network Trigger Project. *ACAD2000, Fermilab, USA*, 2000. URL http://www.h1.mppmu.mpg.de/projects/neuro/pub/acat2000_cmkn.ps.gz.
- [94] D. Hoffman et al. The Second Level Topological Trigger of the H1 Experiment at HERA I. *Submitted to Elsevier Preprint*, 2004.
- [95] A. Schöning. The Fast Track Trigger at the H1 experiment design concepts and algorithms. *Nuclear Instruments and Methods in Physics Research A*, 566:130–132, 2006.

- [96] H1. H1REC documentation page, 2005. URL <https://www-h1.desy.de/icas/imanuals/h1rec/h1rec9/h1rec.html>.
- [97] Volker Blobel. *The BOS System*. Universität Hamburg, Luruper Chaussee 149, fourth, updated edition, March 2001. URL <https://www.desy.de/~glushkov/documents/phd/references/BOS.ps.gz>.
- [98] ROOT. An Object-Oriented Data Analysis Framework, 2007. URL <http://root.cern.ch/>.
- [99] H1 OO Analysis Framework, 2007. URL <https://www-h1.desy.de/icas/oop/>.
- [100] V. Blobel. Central track reconstruction, November 2004. URL <https://www-h1.desy.de/idet/itracker/TrackingGroup/AgnMin/Meet041103/blobel041103.pdf>.
- [101] Veikko Karimäki. Fast code to fit circular arcs. *HU-SEFT-1991-10*, unpublished, 1991. URL http://www.helsinki.fi/~seft_www/ps/hu_seft_91_10.ps.
- [102] V. Lioubimov. Particle separation by likelihood analysis of dE/dx measurements in H1 tracking chambers. *H1 report 11/93-329*, 1993.
- [103] M. Ohlsson et. al. Track Finding with Deformable Templates - The Elastic Arms Approach. *LU TP 91-27*, 1991.
- [104] A. A. Glazov. *Measurement of the Proton Structure Function $F_2(x, Q^2)$ and $F_L(x, Q^2)$ with the H1 Detector at HERA*. PhD thesis, Humboldt-Universität zu Berlin, 1998. URL <https://www-h1.desy.de/psfiles/theses/h1th-116.ps>.
- [105] S. Burke et al. Track finding and fitting in the H1 Forward Track Detector. *Nuclear Instruments and Methods in Physics Research A*, 373:227–260, 1996.
- [106] J. Iliopoulos S. L. Glashow and L. Maiani. Weak interactions with lepton-hadron symmetry. *Physical Review D*, Volume 2:1285–1292, 1970.
- [107] J.-E. Augustin et al. Discovery of a narrow resonance in $e^+ e^-$ annihilation. *Physical Review Letters*, Volume 33:1406–1408, 1974.
- [108] R. Klingenberg et al. The ATLAS pixel detector. *Nuclear Instruments and Methods in Physics Research A*, Volume 579:664–668, 2007.

- [109] C. Civinini. The CMS silicon strip tracker. *Nuclear Instruments and Methods in Physics Research A*, Volume 579:726–730, 2007.
- [110] B. A. Schumm. Tracking at the ILC: Why silicon tracking is best, and how it might be optimized. *Nuclear Instruments and Methods in Physics Research A*, Volume 579:595–598, 2007.
- [111] J. E. Brau et al. Silicon detectors at the ILC. *Nuclear Instruments and Methods in Physics Research A*, Volume 579:567–571, 2007.
- [112] G. Lutz. *Semiconductor Radiation Detectors*. Springer, Berlin, 1st edition, 1999. ISBN 3-540-64859-3.
- [113] W. R. Leo. *Techniques for Nuclear and Particle Physics Experiments*. Springer-Verlag, Berlin, 1st edition, 1987. ISBN 3-540-17386-2.
- [114] M. Nožiča. *Forward Silicon Tracker of the H1 Experiment: Hardware and Study of D^* Meson Detection*. PhD thesis, Charles University in Prague, 2006.
- [115] H1 Collaboration. Technical proposal to build silicon tracking detectors for H1 detector. *DESY PRC 92/01, H1 internal note 06/92-226, unpublished*, 1992.
- [116] W. Eick et al. Development of the H1 backward silicon strip detector. *Nuclear Instruments and Methods in Physics Research A*, Volume 386: 81–86, 1997.
- [117] V. Arkadov. *Measurement of the Deep-Inelastic ep Scattering Cross Section using the Backward Silicon Tracker at the H1 Detector at HERA*. PhD thesis, Humboldt-Universität zu Berlin, 2000. URL <https://www-h1.desy.de/psfiles/theses/h1th-226.ps>.
- [118] H. Henschel et al. A Silicon Pad Detector L1 Trigger for Deep Inelastic Scattering at low x and Q^2 . *H1 internal note 04/92-221*, 1992.
- [119] I. Tsourine. Development of a fast H1 trigger using silicon pad detectors. *Nuclear Instruments and Methods in Physics Research A*, Volume 501:219–221, 2003.
- [120] I. Tsurin. *The Backward Silicon Track Trigger of the HERA Experiment H1*. PhD thesis, Humboldt-Universität zu Berlin, 2003. URL <https://www-h1.desy.de/psfiles/theses/h1th-397.pdf>.

- [121] J. Kretzschmar. A Trigger with the BST-PAD Detector for the H1 Experiment, dec 2003. URL [/afs/desy.de/group/h1/psfiles/theses/h1th-332.ps](https://afs.desy.de/group/h1/psfiles/theses/h1th-332.ps).
- [122] M. Nožička. Silicon detector for detection of inelastic scattering of electrons on protons in H1 experiment, aug 2000. URL <https://www-h1.desy.de/psfiles/theses/h1th-281.ps>.
- [123] G. Spieler. *Semiconductor Detector Systems*. Oxford University Press, Oxford, 1st edition, 2005. ISBN 0-19-852784-5.
- [124] W. Dabrowski et al. Study of spatial resolution and efficiency of silicon strip detectors with charge division readout. *Nuclear Instruments and Methods in Physics Research A*, Volume 383:137–143, 1996.
- [125] E. Peppel et al. First results with the H1 backward silicon strip detector. *Nuclear Instruments and Methods in Physics Research A*, Volume 409:201–203, 1998.
- [126] H1 Collaboration. Upgrade of the H1 Backward Silicon Tracker. *Addendum to DESY PRC 92/01, unpublished*, 1995.
- [127] C. Kiesling et al. Proposal to Complement the H1 Backward Silicon Tracker (BST) with ϕ -Strip Detectors. *Addendum 2 to DESY PRC 92/01, DESY PRC 98/01, H1 internal note 01/98-534, unpublished*, 1998.
- [128] H. Henschel et al. The backward silicon tracker of the H1 experiment at HERA. *Nuclear Instruments and Methods in Physics Research A*, Volume 453:93–97, 2000.
- [129] M. Nožička. The forward and backward silicon trackers of H1. *Nuclear Instruments and Methods in Physics Research A*, Volume 501:54–59, 2003.
- [130] V. Chekelyan et al. On the Repair of the H1 Forward Silicon Tracker. *H1 internal note 07/04-613, unpublished*, 2004.
- [131] W. J. Haynes et al. The H1 silicon tracker data acquisition system. *Nuclear Instruments and Methods in Physics Research A*, Volume 403:313–325, 1998.
- [132] W. Erdmann et al. Optical analog readout and control of the central silicon vertex detector of H1 at HERA. *Nuclear Instruments and Methods in Physics Research A*, Volume 372:188–194, 1996.

- [133] J. Bürger et al. Online readout and control unit for high-speed/high resolution readout of silicon tracking detectors. *Nuclear Instruments and Methods in Physics Research A*, Volume 386:269–279, 1997.
- [134] S. Prell. *Entwicklung des Steuer- und Auslesemoduls für die Silizium-streifendetektoren des H1-Detektors*. PhD thesis, Universität Hamburg, 1996. URL <https://www-h1.desy.de/psfiles/theses/h1th-081.ps.Z>.
- [135] IEEE standard 1014. VMEbus specification, 1987.
- [136] Creative Electronic System. RIO2 8062 powerpc based risc i/o Board, user's manual, may 2000.
- [137] IEEE standard 1196. NuBus specification, 1980.
- [138] B. G. Taylor. The MICRON User Manual, 1989.
- [139] B. G. Taylor. The MacVEE User Manual, 1989.
- [140] Motorola Inc. Timbuktu Pro Application, 2007. URL <http://www.netopia.com/software/products/tb2/>.
- [141] R. et al. Frühwirth. *Data analysis techniques for high-energy physics*. Cambridge University Press, Cambridge, UK, 2nd edition, 2000. ISBN 0-521-63548-9.
- [142] R. Brenner et al. Measurement of the spatial resolution of double-sided double-metal AC-coupled silicon microstrip detectors. *Nuclear Instruments and Methods in Physics Research A*, Volume 326:189–197, 1993.
- [143] E. Belau. Charge collection in silicon strip detectors. *Nuclear Instruments and Methods*, Volume 214:253–260, 1983.
- [144] J. Straver. One micron spatial resolution with silicon strip detectors. *Nuclear Instruments and Methods in Physics Research A*, Volume 348:485–490, 1994.
- [145] R. Turchetta. Spatial resolution of silicon microstrip detectors. *Nuclear Instruments and Methods in Physics Research A*, Volume 335:44–58, 1993.
- [146] G. Feldmann et al. Observation of the Decay $D^* \rightarrow D^0 \pi^+$. *Physics Review Letters*, Volume 38:1313–1314, 1977.

- [147] C. Adloff et al. (H1 Collaboration). Measurement of $D^{*\pm}$ meson production and F_2^c in deep-inelastic scattering at HERA. *Physics Letters B*, Volume 528:199–214, 2002. hep-ex/0108039.
- [148] (H1 Collaboration) C. Adloff et al. Inclusive D^0 and $D^{*\pm}$ Production in Deep Inelastic ep Scattering at HERA. *Zeitschrift für Physik C*, Volume 72:593–605, 1996. hep-ex/9607012.
- [149] (H1 Collaboration) M.-O. Bönig et al. D^* -Meson Production in Deep Inelastic Scattering at HERA. *H1prelim-07-072*, unpublished, 2007. URL <http://www-h1.desy.de/psfiles/confpap/EPS2007/H1prelim-07-072.ps>.
- [150] A. Aktas et al. (H1 Collaboration). Inclusive $D^{*\pm}$ meson and associated dijet production in deep-inelastic scattering at HERA. *The European Physical Journal C*, Volume 51:271–287, 2007. hep-ex/0701023.
- [151] A. Aktas et al. (H1 Collaboration). Diffractive open charm production in deep-inelastic scattering and photoproduction at HERA. *The European Physical Journal C*, Volume 50:1–20, 2007. hep-ex/0610076.
- [152] M.-O. Bönig. *Messung des D^* -Meson-Produktionsquerschnitts in tiefinelastischer Streuung mit dem H1-Experiment*. PhD thesis, Universität Dortmund, 2007. URL <https://www-h1.desy.de/psfiles/theses/h1th-457.pdf>.
- [153] F. Jacquet and A. Blondel. A method to study the structure functions. In *Proceedings of the Study for an ep Facility for Europe*, pages 391–394, Hamburg, 1979.
- [154] U. Bassler and G. Bernardi. On the kinematic reconstruction of deep inelastic scattering at HERA. *Nuclear Instruments and Methods in Physics Research A*, Volume 361:197–208, 1995.
- [155] S. Bentvelsen et al. Reconstruction of (x, Q^2) and extraction of structure functions in neutral current scattering at HERA. In *Physics at HERA*, pages 23–56, Hamburg, Germany, 1991.
- [156] P. Steinbach. Vector Meson Production in the Forward and Backward Region of the H1 Experiment at HERA, sept 2007. URL <https://www-h1.desy.de/psfiles/theses/h1th-472.ps>.
- [157] J. Wagner. *Charm and Beauty Production at HERA with D^* -Muon Events*. PhD thesis, Universität Hamburg, 2004. URL <https://www-h1.desy.de/psfiles/theses/h1th-346.ps>.

- [158] S. Levonian. The status of H1 luminosity precision, feb 2007. URL https://www-h1.desy.de/idet/ilumi/online/levonian/lumi_Feb07.pdf.
- [159] (Zeus Collaboration). Measurement of charm production in deep inelastic scattering at HERA II. *ZEUS-prel-06-021, XXII International Conference on High Energy Physics, July 26-August 2, Moscow, Russia*, 2006. URL <http://www-zeus.desy.de/physics/phch/conf/ichep06/hf1/8/ZEUS-prel-06-021.ps>.
- [160] W. M. Dunne. *Measurement of D^* Production in Deep Inelastic Scattering at HERA*. PhD thesis, University of Glasgow, 2007. URL <http://ppewww.physics.gla.ac.uk/~bdunne/thesis/thesis.pdf>.
- [161] P. Nason S. Frixione and G. Ridolfi. Differential distributions for heavy flavour production at HERA. *Nuclear Physics B*, Volume 454:3–24, 1995. hep-ph/9506226.
- [162] (H1 Collaboration) S. Aid et al. A measurement and QCD analysis of the proton structure function $F_2(x, q^2)$ at HERA. *Nuclear Physics B*, Volume 470:3–38, 1996. hep-ex/9603004.
- [163] (Zeus Collaboration) J. Breitweg et al. ZEUS results on the measurement and phenomenology of F_2 at low x and low Q^2 . *The European Physical Journal C*, Volume 7:609–630, 1999. hep-ex/9809005.
- [164] Sergej Gorbounov. FSTR bank description, aug 2003. URL <https://www.desy.de/~glushkov/documents/phd/references/FSTR.ps.gz>.
- [165] Sergej Gorbounov. FJKX bank description, aug 2003. URL <https://www.desy.de/~glushkov/documents/phd/references/FJKX.ps.gz>.

Abbreviations

AC	Analog Current
APC	Analog Pipeline Chip
BEMC	Backward ElectroMagnetic Calorimeter
BGF	Boson-Gluon Fusion
BPC	Backward Proportional Chamber
\mathcal{BR}	Branching Ratio
BST	Backward Silicon Tracker
CC	Charged Current Converter Card
CDU	Clock Distribution Unit
CERN	Conseil Européen pour la Recherche Nucléaire (European Organization for Nuclear Research)
CES	Creative Electronic Systems S. A.
CFK	Carbon-Fiber-Komposite
CIP	Central Inner Proportional chamber
CJC	Central Jet Chamber
CMS	Center of Mass System
COP	Central Outer Proportional chamber
COZ	Central Outer Z-chamber
CST	Central Silicon Tracker
DC	Direct Current
d_{ca}	Distance of closest approach
DESY	Deutsches Elektronen-Synchrotron
DGLAP	Yu. L. Dokshitser, V.N. Gribov, L.N. Lipatov, G. Altarelli and G. Parisi
DIS	Deep Inelastic Scattering
DLA	Double Leading Logarithmic Approximation
DST	Data Storage Tape
DIS	Deep Inelastic Scattering
ET40	Electron Tagger at 40 meters
ET6	Electron Tagger at 6 meters

FET	Fiel Effect Transistor
FFNS	Fixed Flavour Number Scheme
FNC	Forward Neutron Calorimeter
FSR	Final State Radiation
FST	Forward Silicon Tracker
FTD	Forward Tracking Detector
FTT	Fast Track Trigger
FWPC	Forward Wire Proportional Chambers
HAT	H1 Analysis Tag
HERA	Hadron Electron Ring Anlage
HFS	Hadronic Final State
IC	Integrated Circuit
ISR	Initial State Radiation
IP	Interaction Point
L1	Level 1 trigger
L2	Level 2 trigger
L2NN	Level 2 Neural Network Trigger
L2TT	Level 2 Topological Trigger
L3	Level 3 trigger
L4	Level 4 trigger
LAr	Liquid-Argon Calorimeter
LEP	Large Electron-Positron Collider
LHC	Large Hadron Collider
LHAPDF	Les Houches Accord PDF
LLA	Leading Logarithmic Approximation
LO	Leading Order
LST	Limited Streamer Tubes
MC	Monte Carlo simulation
MIP	Minimum Ionizing Particle
$\overline{\text{MS}}$	Minimal Subtraction Scheme
MS	Multiple Coulomb Scattering
NC	Neutral Current
NIM	Nuclear Instrumentation Module
NLO	Next to Leading Order
NNLO	Next to Next to Leading Order
ODS	Object Data Store
OnSiRoC	Online Silicon Readout Controller
OO	Object Oriented
OPAL	Omni-Purpose Apparatus at LEP
OS	Operating System

PC	P ersonal C omputer
PCB	P rinted C ircuit B oard
PCI	P eripheral C omponent I nterconnect
PD	P hoto D etector
PDF	P arton D ensity F unction
PETRA	P ositron E lectron T andem R ing A nlage
PIC	P ipeline C ounter
PMC	P CI M ezzanine C ard
POT	P roduction O utput T ape
pQCD	P erturbative Q uantum C hromodynamics
QCD	Q uantum C hromodynamics
QED	Q uantum E lectrodynamics
QPM	Q uark P arton M odel
RGE	R enormalization G roup E quation
RMS	R oot M ean S quare
Si	S ilicon
SIFE	S ilicon F ront- E nd data
SpaCal	S pacal C alorimeter
TC	T ail C atcher
TCP/IP	T ransmission C ontrol P rotocol / I nternet P rotocol
TR	T ransition R adiators
UV	U ltraviolet
ZMVFNS	Z ero M ass V ariable F lavor N umber S cheme
VC	V eto C ounter
μODS	μ icro O bject D ata S tore

Acknowledgments

The long list of names which should be mentioned in this part of my thesis definitely should start with the name of my supervisor Prof. Thomas Naumann. His permanent support, deep knowledge and patience were always vital for my progress over the last four years. I am grateful to Prof. Hermann Kolanoski and Dr. Andreas Meyer for evaluating this work.

I am grateful also to the leader of the H1-Zeuthen group Dr. Peter Kostka. Without his 24/7 work there would be neither FST nor BST and hence the major part of this work would not be possible. Next, I would like to thank Prof. Max Klein for letting me participate in the H1 Collaboration, and Dr. Leandar Litov for introducing me into the world of particle physics.

For his constant support, I am deeply grateful to my colleague and friend Dr. Miroslav Nožička. He is the one who is always ready for fruitful discussions - starting in the office hours from physics, silicon, hardware and software issues, through personal issues over the late afternoon coffee and sometimes ending over a six-pack of Czech beer discussing everyday topics, which made my stay in Germany much nicer. To Sergey Gorbounov I am thankful for the long discussions on the Kalman Filter and the particularities of the track and vertex reconstruction. I am grateful to Sasha Glazov for the ideas and knowledge I gained from him during our discussions on the physics phenomena at H1. I would also like to thank the students I was working with - Peter Steinbach, Nikolay Evtimov and Rositsa Gergova - through countless discussions, they taught me how to pass my knowledge on.

For the largest part of my nice, quiet, productive office environment I am indebted to Alexey Petrukhin. For the not-so-quiet, but very interesting and already legendary part of the same environment I should not miss to mention Ilya Tsurin. "Danke, Ilya!"

I would like to thank also all my Bulgarian friends: Pavlin, Chavdar, Dilyan with Katia, Boyan with Bistra, Ivo and Magi - with you around guys it always feels like home. On the top of the private part of this chapter I put my family. Without knowing that my brother, my parents and grandparents and my country are and always will be there for me when I need them, I

wouldn't be who I am and where I am.

Finally, I want to thank my wife Maria for supporting and loving me patiently through the years and the years to come.

Curriculum Vitae

Personal data

Name	Ivan Glushkov
Date of Birth	27 March 1978
Place of Birth	Ruse, Bulgaria
Nationality	Bulgarian
Marital status	Married

Contact information

Address	Bld. 1b/132 Notkestrasse 85 Deutsches Elektronen Synchrotron D-22607 Hamburg Germany
E-mail	Ivan.Glushkov@desy.de
Phone	+49 176 70029168 +49 40 89983293

Academic Education

2003 - 2007	PhD education in Physics - expected in winter 2007 Humboldt University, Berlin, Germany Deutsches Elektronen-Synchrotron DESY, Zeuthen
1997 - 2002	Master degree in Physics University of Sofia, Sofia, Bulgaria Major: Nuclear equipment and power engineering Specialization: Physics of nucleus and elementary particles
1992 - 1997	National High School of Mathematics and Science, Sofia, Bulgaria
1985 - 1992	Elementary School in Ruse and Sofia, Bulgaria

Summer Schools

September 2007	Herbstschule für Hochenergiephysik Maria Laach, Maria Laach Monastery, Germany
September 2001	Adriatic School of Particle Physics and Physics Informatics, Split, Croatia

Conferences

April 2002	Four Seas Conference, Thessaloniki, Greece
------------	--

Computer Skills

Physics software	ROOT, PAW
Programming	C/C++, Fortran 77, LabView, HTML, Make, bash
Operating Systems	
- administration	Linux (Debian, SuSE), Windows 98, ME, XP
- utilization	Linux, Unix, MacOS, MacOSX, Windows 98, ME, NT4, 2000, XP, Vista
Applications	Mathematica, L ^A T _E X 2 _ε , Emacs, Gimp, OpenOffice and wide variety of GPL Software

Languages

Bulgarian - native language
English - fluent
German - good spoken and understanding
Russian - good understanding
Italian - very basic

Statement of authorship

I hereby certify that this thesis had been composed by myself, and describes my own work, unless otherwise acknowledged in the text. All references and verbatim extracts have been quoted, and all sources of information have been specially acknowledged.

Ivan Glushkov
December 13, 2007